

**NASA CONTRACTOR  
REPORT**

NASA CR-2750



**NASA CR-2**



LOAN COPY: RETURN TO  
AFWL TECHNICAL LIBRARY  
KIRTLAND AFB, N. M.

**ATMOSPHERIC FLOW OVER TWO-DIMENSIONAL  
BLUFF SURFACE OBSTRUCTIONS**

*Juergen Bitte and Walter Frost*

*Prepared by*

**THE UNIVERSITY OF TENNESSEE SPACE INSTITUTE**

**Tullahoma, Tenn. 37388**

*for George C. Marshall Space Flight Center*



**NATIONAL AERONAUTICS AND SPACE ADMINISTRATION • WASHINGTON, D. C. • OCTOBER 1976**



0061410

## TECHNICAL REPORT STANDARD TITLE PAGE

1. REPORT NO. NASA CR-2750	2. GOVERNMENT ACCESSION NO.	3. RECIPIENT'S CATALOG NO.	
4. TITLE AND SUBTITLE Atmospheric Flow Over Two-Dimensional Bluff Surface Obstructions		5. REPORT DATE October 1976	
		6. PERFORMING ORGANIZATION CODE	
7. AUTHOR(S) Juergen Bitte and Walter Frost		8. PERFORMING ORGANIZATION REPORT # M-182	
9. PERFORMING ORGANIZATION NAME AND ADDRESS The University of Tennessee Space Institute Tullahoma, Tennessee 37388		10. WORK UNIT NO.	
		11. CONTRACT OR GRANT NO. NAS8-29584	
		13. TYPE OF REPORT & PERIOD COVERED Contractor Report	
12. SPONSORING AGENCY NAME AND ADDRESS National Aeronautics and Space Administration Washington, D. C. 20546		14. SPONSORING AGENCY CODE	
15. SUPPLEMENTARY NOTES This report was prepared under the technical monitorship of the Aerospace Environment Division, Space Sciences Laboratory, NASA Marshall Space Flight Center.			
16. ABSTRACT <p>The phenomenon of atmospheric flow over a two-dimensional surface obstruction, such as a building (modeled as a rectangular block, a fence or a forward-facing step), is analyzed by three methods: (1) an inviscid free streamline approach, (2) a turbulent boundary layer approach using an eddy viscosity turbulence model and a horizontal pressure gradient determined by the inviscid model, and (3) an approach using the full Navier-Stokes equations with three turbulence models; i.e., an eddy viscosity model, a turbulence kinetic-energy model and a two-equation model with an additional transport equation for the turbulence length scale.</p> <p>A comparison of the performance of the different turbulence models is given, indicating that only the two-equation model adequately accounts for the convective character of turbulence. Turbulence flow property predictions obtained from the turbulence kinetic-energy model with prescribed length scale are only insignificantly better than those obtained from the eddy viscosity model. A parametric study includes the effects of the variation of the characteristic parameters of the assumed logarithmic approach velocity profile. For the case of the forward-facing step, it is shown that in the downstream flow region an increase of the surface roughness <math>z_0</math> gives rise to higher turbulence levels in the shear layer originating from the step corner. This in turn results in higher shear stress, leading to faster reattachment of the separated flow. The typical eddy size in the shear layer increases with <math>z_0</math> and causes rapid spreading of a region of high stream-wise vorticity gradients. In the upstream flow region, changes in <math>z_0</math> have only moderate influence on the flow parameters. Except for very small surface roughnesses, the separation bubble in front of the step is found to grow in size.</p>			
17. KEY WORDS Wind shear Turbulence Turbulence flow Flow separation Wind profile Boundary layer flow		18. DISTRIBUTION STATEMENT  Category 02	
19. SECURITY CLASSIF. (of this report) Unclassified	20. SECURITY CLASSIF. (of this page) Unclassified	21. NO. OF PAGES 224	22. PRICE \$ 7.25

#### AUTHORS' ACKNOWLEDGMENTS

The work reported herein was supported by the National Aeronautics and Space Administration, Marshall Space Flight Center, Aerospace Environment Division, under contract number NAS8-29584.

The authors are indebted to Mr. John Enders, of the Aeronautical and Operating Systems Division, Office of Aeronautics and Space Technology, NASA, Washington, D.C., for his support of this research. Special thanks go to Dr. G.H. Fichtl of the Marshall Space Flight Center for his cooperation and valuable suggestions in carrying out the work.

## TABLE OF CONTENTS

CHAPTER	PAGE
I. INTRODUCTION . . . . .	1
II. INVISCID FLOW MODEL . . . . .	12
Introductory Remarks . . . . .	12
Development of Governing Equations for	
Inviscid Flow Over a Fence . . . . .	16
Required Empirical Input . . . . .	27
Discussion of Applicability of Fence Model	
to Rectangular Bodies . . . . .	28
Relation to Atmospheric Flows . . . . .	30
Results of Inviscid Model . . . . .	34
III. ANALYSIS OF ATMOSPHERIC FLOW OVER A BLUFF	
SURFACE OBSTRUCTION BY THE TURBULENT	
BOUNDARY LAYER APPROACH . . . . .	47
Governing Equations . . . . .	47
Incorporation of the Inviscid Solution . . . . .	49
Coordinate System . . . . .	51
Numerical Solution . . . . .	59
Results and Discussion . . . . .	62
IV. ANALYSIS OF ATMOSPHERIC FLOW OVER A BLUFF	
SURFACE OBSTRUCTION BY THE TURBULENT	
NAVIER-STOKES EQUATIONS . . . . .	82
Governing Equations . . . . .	82
Turbulence Models . . . . .	87

## CHAPTER

## PAGE

Mixing length model . . . . .	87
Turbulence kinetic energy model . . . . .	88
Two-Equation model of turbulence . . . . .	92
Numerical Solution . . . . .	94
Numerical procedure . . . . .	94
Physical and numerical coordinate system . . . . .	95
Boundary conditions . . . . .	95
Inflow . . . . .	98
Outflow . . . . .	100
Upper boundary . . . . .	103
Wall boundary . . . . .	103
Special treatment at step corner . . . . .	106
Accuracy, convergence and economy . . . . .	108
Influence of grid size on accuracy . . . . .	108
Factors affecting convergence . . . . .	125
Termination of computation . . . . .	128
Results and Discussion . . . . .	128
Factors influencing the solution . . . . .	129
Boundary conditions . . . . .	129
Empirical coefficients . . . . .	136
Comparison of different models . . . . .	151
Laminar solution . . . . .	151
Comparison of different turbulent solutions . . . . .	156
Effect of variation of the parameters of the approaching wind . . . . .	171

**CHAPTER****PAGE****BIBLIOGRAPHY . . . . . 202****VITA . . . . . 208**

## LIST OF TABLES

TABLE	PAGE
2.1. Typical Base Pressure Coefficients for Different Building Geometries . . . . .	31
3.1. Parameters for the Different Data Points Investigated . . . . .	68
3.2. Empirical Input and Resulting Calculation Parameters for Respective Data Points . . . . .	70
4.1. Coefficient Functions of Equation 4.11 or 4.12 . . . . .	86
4.2. Set of Empirical Constants Used in Trial Calculations . . . . .	138
4.3. Geometries of Separation Regions for Different Turbulence Models . . . . .	166

## LIST OF FIGURES

FIGURE		PAGE
2.1.	Physical- and Basic Transformation-Planes with Separation Points $S_1$ and $S_2$ as Critical Points [24] . . . . .	14
2.2.	Physical- and Transformation-Planes for Inviscid Parallel Shear Flow Over a Bluff Body Attached to a Wall [25] . . . . .	15
2.3.	Physical- and Transformation-Planes for Inviscid Parallel Shear Flow Over a Fence . . . . .	17
2.4.	Implementation of Different Body Geometries by Using Different Empirical Values $C_{p_b}$ and $x_R$ . .	29
2.5.	Graphical Representation of Equation 2.65 . . . .	33
2.6.	Streamlines for Inviscid Model . . . . .	36
2.7.	Streamline Pattern in Upstream Fence Region for Inviscid Model . . . . .	37
2.8.	Comparison of Analytically and Experimentally Determined Separation Streamline . . . . .	38
2.9.	Velocity Profiles for Various x-Stations . . . .	39
2.10.	Velocity Gradient along Different Streamlines . .	41
2.11.	$C_p$ Distribution along Various Streamlines . . . .	42
2.12.	Maximum Height of Recirculation Region in Dependence of the Parameters of the Approaching Wind . . . . .	43



2.13. Velocity Increase Due to the Presence of the Fence . . . . .	45
3.1. Coordinate System Used in Boundary Layer Approach for Flow Over a Fence . . . . .	52
3.2. Justification of First Order Analysis After Hunt [30] . . . . .	55
3.3. Matching of Boundary-Layer-Velocity Profile with Shear Layer- and Wake-Velocity Profile [31] . . . . .	57
3.4. Velocity Profiles for $\psi_{ns} = 0.2$ and Quadratic Pressure Decay Function . . . . .	64
3.5. Velocity Profiles for $\psi_{ns} = 0.05$ and Quadratic Pressure Decay Function . . . . .	65
3.6. Velocity Profiles for $\psi_{ns} = 0.05$ and Inviscid Pressure Decay Function . . . . .	66
3.7. Graphical Representation of Investigated Data Points . . . . .	69
3.8. Velocity Profiles for Case 1 . . . . .	71
3.9. Velocity Profiles for Case 2 . . . . .	72
3.10. Velocity Profiles for Case 3 . . . . .	73
3.11. Velocity Profiles for Case 4 . . . . .	74
3.12. Velocity Increase Due to the Presence of the Fence for Various Upstream Conditions . . . . .	76
3.13. Comparison of Velocity Profiles at $x = 1.0$ Obtained from Boundary Layer Model and Full Scale Experiments [32] . . . . .	78

3.14.	Comparison of Velocity Profiles at $x = 2.0$ Obtained from Boundary Layer Model and Wind Tunnel Experiments [27] . . . . .	79
4.1.	Description of Flow Region Considered . . . . .	83
4.2.	Assumed Mixing Length Distribution . . . . .	89
4.3.	Description of Physical $(x^*, z^*)$ and Numerical $(I, J)$ Coordinate System Used . . . . .	96
4.4.	Actual Grid Distribution . . . . .	97
4.5.	Investigated Boundary Conditions for Upper Step Corner Point . . . . .	107
4.6.	Stream Function Distribution at $x = -6.0$ for Different Grid Sizes . . . . .	110
4.7.	Vorticity Distribution at $x = -6.0$ for Different Grid Sizes . . . . .	111
4.8.	Stream Function Distribution at $x = 0.0$ for Different Grid Sizes . . . . .	112
4.9.	Vorticity Distribution at $x = 0.0$ for Different Grid Sizes . . . . .	113
4.10.	Stream Function Distribution at $x = 0.8$ for Different Grid Sizes . . . . .	114
4.11.	Vorticity Distribution at $x = 0.8$ for Different Grid Sizes . . . . .	115
4.12.	Near Wall Stream Function Distribution for Laminar Flow at $x = 1.6$ . . . . .	117
4.13.	Near Wall Vorticity Distribution for Laminar Flow at $x = 1.6$ . . . . .	118

FIGURE	PAGE
4.14. Near Wall Stream Function Distribution for Laminar Flow at $x = 3.0$ . . . . .	119
4.15. Streamline Plots for Laminar Flow; (a) Coarse Grid, (b) Finer Grid . . . . .	120
4.16. Explanation of Extrapolation of Second Zero of Stream Function Value . . . . .	124
4.17. Streamline Plots Using (a) Normal Linear Interpolation, and (b) Parabolic Extrapolation of the Separating Streamline . .	126
4.18. Influence of Outflow Boundary Condition on $k$ -Solution; (a) $k^* = (u_{*}^*/C_{\mu 0})^2$ and (b) $(\partial k^*/\partial x^*) = 0$ . . . . .	131
4.19. Influence of Outflow Boundary Condition on $k$ -Solution, $k^* = (u_{*out}^*/C_{\mu 0})^2$ . . . . .	133
4.20. Influence of Upper Boundary Condition on $k$ -Solution, $(\partial k^*/\partial x^*) = 0$ . . . . .	135
4.21. Streamline Pattern and Turbulence Kinetic Energy Contours for Case 1 ( $C_{\mu 0} = 1.0$ , $C_{D_0} = 1.0$ , $C_{S_0} = 1.0$ , $C_{B_0} = 1.0$ ) . . . . .	139
4.22. Streamline Pattern and Turbulence Kinetic Energy Contours for Case 3 ( $C_{\mu 0} = 1.0$ , $C_{D_0} = 0.1$ , $C_{S_0} = 1.0$ , $C_{B_0} = 1.0$ ) . . . . .	140
4.23. Streamline Pattern and Turbulence Kinetic Energy Contours for Case 5 ( $C_{\mu 0} = 1.0$ , $C_{D_0} = 1.0$ , $C_{S_0} = 1.0$ , $C_{B_0} = 0.1$ ) . . . . .	141

4.24.	Streamline Pattern and Turbulence Kinetic Energy Contours for Case 6 ( $C_{\mu_0} = 2.0$ , $C_{D_0} = 1.0$ , $C_{S_0} = 1.0$ , $C_{B_0} = 1.0$ ) . . . . .	142
4.25.	Streamline Pattern and Turbulence Kinetic Energy Contours for Case 7 ( $C_{\mu_0} = 1.74$ , $C_{D_0} = 1.18$ , $C_{S_0} = 0.27$ , $C_{B_0} = 0.14$ ) . . . . .	143
4.26.	Streamline Pattern and Turbulence Kinetic Energy Contours for Case 8 ( $C_{\mu_0} = 1.0$ , $C_{D_0} = 0.1$ , $C_{S_0} = 0.27$ , $C_{B_0} = 0.08$ ) . . . . .	144
4.27.	Length Scale Distribution for Case 1 (Lines of Constant $\ell^*$ ) . . . . .	145
4.28.	Lines of Constant Length Scale Passing through Point P for the Different Cases . . . . .	146
4.29.	Streamline Pattern for Laminar Flow Solution ( $Re_n = 3.9 \times 10^6$ ) . . . . .	153
4.30.	Velocity Profiles for Laminar Flow Solution . . . . .	154
4.31.	Streamline Pattern for Turbulent Flow Solution Using the Prandtl-Mixing-Length Concept ( $Re_n = 3.9 \times 10^6$ ) . . . . .	155
4.32.	Streamline Pattern for Turbulent Flow Solution Using the Turbulence Kinetic Energy Concept with Prescribed Length Scale; One-Equation Model ( $Re_n = 3.9 \times 10^6$ ) . . . . .	157
4.33.	Turbulence Kinetic Energy Contours for One-Equation Model . . . . .	158

4.34.	Streamline Pattern for Turbulent Flow Solution Using the Turbulence Kinetic Energy Concept with Calculated Length Scale; Two-Equation Model ( $Re_n = 3.9 \times 10^6$ ) . . . . .	159
4.35.	Turbulence Kinetic Energy Contours for Two-Equation Model . . . . .	160
4.36.	Length Scale Distribution for Two-Equation Model (Lines of Constant $\ell^*$ ) . . . . .	161
4.37.	Effective Viscosity Variation along Near Wall Nodes on the Top of the Step for the Different Turbulence Models . . . . .	162
4.38.	Effective Viscosity Variation along the Wall on the Top of the Step for Different Turbulence Models . . . . .	163
4.39.	Vorticity Distribution for Two-Equation Model . .	170
4.40.	Stream Function Pattern for (a) $z_0 = 0.005$ , (b) $z_0 = 0.045$ , (c) $z_0 = 0.1$ . . . . .	175
4.41.	Turbulence Kinetic Energy Contours for (a) $z_0 = 0.005$ , (b) $z_0 = 0.045$ , (c) $z_0 = 0.1$ . . . . .	178
4.42.	Lines of Constant Turbulence Length Scale for (a) $z_0 = 0.005$ , (b) $z_0 = 0.045$ , (c) $z_0 = 0.1$ . . . . .	181
4.43.	Reattachment Length of Top Separation Region in Dependence of $z_0$ . . . . .	185

4.44.	Forward Separation Region; (a) Geometry in Dependence of $z_0$ , (b) Maximum Vorticity in Dependence of $z_0$ . . . . .	186
4.45.	Velocity Profiles for Various $z_0$ ; (a) Approach Velocities, (b) Velocity Overshoot at $x = 0$ Due to the Step for Different $z_0$ . . . . .	188
4.46.	Velocity Distribution for $z_0 = 0.005$ ; (a) Ahead of the Step, (b) in the Vicinity of the Step .	193
4.47.	Turbulence Kinetic Energy Profiles at $x = 3.0$ for Different $z_0$ . . . . .	195
4.48.	Turbulence Kinetic Energy Distribution for $z_0 = 0.005$ ; (a) Ahead of the Step, (b) in the Vicinity of the Step . . . . .	196
4.49.	Turbulence Length Scale Profiles at $x = 3.0$ for Different $z_0$ . . . . .	199
4.50.	Variation of Outer Edge of Vorticity Wake Region for Different $z_0$ . . . . .	200

## NOMENCLATURE

$a, b, c$	Coefficient functions in the general elliptic equation (Equation 4.11)
$a$	Circle radius in Z-plane
$C_\mu$	Empirical function in expression for effective viscosity (Equation 4.16)
$C_D$	Empirical function in source term for TKE-equation (Equation 4.19)
$C_B, C_S$	Empirical functions in source term for $\ell$ -equation (Equation 4.23)
$C_g$	Geostrophic drag coefficient, $u_*^2/g$
$C_p$	Pressure coefficient $(p - p_\infty)/(\rho/2 U_{ref}^2)$
$d$	Source term in general elliptic equation (Equation 4.11)
$f$	Coriolis parameter
$F_\beta, F_\delta$	Functions defined by Equations 2.47 and 2.48
$G$	Geostrophic wind velocity
$h$	Height of fence or step
$H$	Characteristic height of recirculation region behind fence
$k$	Vorticity for the inviscid model as defined by Equation 2.2
$k$	Turbulence kinetic energy; $\frac{1}{2}(\overline{u'^2} + \overline{v'^2} + \overline{w'^2})$
$\ell$	Prandtl mixing length or local turbulence length scale

$L$	Characteristic length of disturbance caused by the fence
$n$	General normal coordinate
$\Delta n$	Numerical step size in $n$ -direction
$p$	Pressure
$\vec{q}$	Velocity vector, $u\vec{i} + v\vec{j}$
$q$	Pressure damping function
$Q$	Source- or sink-strength in inviscid model
$Re$	Reynolds number $(u_\infty \cdot h)/\nu$
$Re_n$	Reynolds number based on $u_n$ , $(u_n \cdot h)/\nu$
$Re_*$	Reynolds number based on $u_*$ , $(u_* \cdot h)/\nu$
$R_t$	Turbulent Reynolds number defined by Equation 4.20
$S_\omega, S_k, S_\epsilon$	Respective source terms in $\omega$ -, $k$ - and $\epsilon$ -transport equation and defined by Equations 4.9, 4.19 and 4.23
$u$	Velocity component in $x$ -direction
$\hat{u}$	Turbulence intensity, $[\frac{1}{3}(\overline{u'^2} + \overline{v'^2} + \overline{w'^2})]^{1/2}/u_*$
$u_*$	Friction velocity, $\sqrt{\tau_{wall}/\rho}$
$u_\infty$	Linear approach velocity profile in inviscid model (Equation 2.1)
$U_0$	Slip velocity near wall (Equation 2.1)
$U_{ref}$	Reference velocity
$U_e$	Velocity at outer edge of shear layer (Figure 3.3)
$U_\infty$	Characteristic velocity defined by Equation 3.1 at $z^* = 3.0 h^*$
$v$	Velocity component in $y$ -direction



$\dot{V}$	Volume flow
$w$	Velocity component in z-direction
$w$	Complex velocity in z-plane, $u - iv$
$W$	Complex potential, $\phi + i\psi$
$x$	Horizontal coordinate
$\Delta x$	Numerical step size in x-direction
$x_S$	Horizontal extent of forward separation region defined in Figure 4.44(a)
$x_R$	Reattachment length defined in Figure 4.43
$X$	Horizontal coordinate in Z-plane
$Y$	Vertical coordinate in z-plane
$Y_R$	Vertical extent of forward separation region defined in Figure 4.44(a)
$Y$	Vertical coordinate in Z-plane
$z$	Complex variable; $x + iy$
$z$	Vertical coordinate
$\Delta z$	Numerical step size in z-direction
$z_0$	Surface roughness
$Z$	Complex variable; $X + iY$

#### Greek Symbols

$\beta$	Parameter for location of source (Figure 2.3)
$\Gamma_{k,eff}$	Effective exchange coefficient for turbulence kinetic energy; $\mu_{eff}/\sigma_{k,eff}$
$\Gamma_{l,eff}$	Effective exchange coefficient for turbulence length scale; $\mu_{eff}/\sigma_{l,eff}$
$\delta$	Parameter for location of sink (Figure 2.3)
$\delta$	Boundary layer thickness

$\delta_i$	Thickness of internal boundary layer
$\epsilon$	Convergence criterion
$\zeta$	Complex variable; $\xi + i\eta$
$\eta$	Vertical coordinate in $\zeta$ -plane
$\kappa$	von Karman constant = 0.4
$\mu$	Dynamic viscosity of the flow
$\mu_t$	Turbulent viscosity of the flow
$\mu_{eff}$	Effective viscosity; $\mu + \mu_t$
$\nu$	Kinematic viscosity of the flow
$\xi$	Horizontal coordinate in $\zeta$ -plane
$\rho$	Density of the flow
$\rho_0$	Constant density of the flow
$\sigma_{k,eff}$	Schmidt number for turbulence kinetic energy based on effective viscosity
$\sigma_{l,eff}$	Schmidt number for turbulence length scale based on effective viscosity
$\tau$	Shear stress
$\tau_{wall}$	Shear stress at surface
$\phi$	Dependent variable in general elliptic equation (Equation 4.11)
$\Phi$	Potential function
$\psi$	Stream function
$\Psi$	Irrotational stream function
$\vec{\Omega}$	Vorticity vector, $\omega \vec{k}$
$\omega$	Vorticity as defined by Equation 4.7

## Superscripts

*	Dimensional quantity
'	Turbulent fluctuation about mean flow quantity
—	Mean flow quantity as ensemble average
N	Index of iteration

## Subscripts

b	Base or separation condition
eff	Effective transport property, comprising both molecular and turbulent contributions
in	Inflow condition
I, J, IN, JN	Finite difference indices as defined in Figure 4.3
max	Condition of point of maximum pressure on fence face
ns	Conditions along nonseparating streamline
out	Outflow condition
P	Pertains to node at which dependent variable is currently being calculated
NP	Refers to node lying adjacent to boundary node
R	Reattachment condition
ref	General reference condition
S	Separation condition
surf	Surface condition
t	Turbulent quantity

## CHAPTER I

### INTRODUCTION

Ground wind induced flow fields around surface obstructions such as buildings, bridges and other man-made structures have long been of interest in structural design. For many years wind loading has been the subject of studies in various wind tunnels. Most of these studies, however, have been related to specific problems rather than to the more general and systematic flow field investigation which can provide a code of practice for the building engineer.

More recently such fundamental investigations have attained new importance through environmental considerations, as well as through the many aerodynamical problems encountered in the design of airports for V/STOL aircraft or helicopter ports in large metropolitan areas. Operating low speed aircraft between buildings in regions of steep velocity gradients or large fluctuations through vortex fields or recirculation zones is very hazardous. A clear understanding and detailed knowledge of the flow field around typical buildings is therefore a necessary source of information to minimize the dangers of these problems. The need for analytical methods to predict local atmospheric motions influenced by buildings or similar bluff surface obstructions is then obvious.

In formulating an analytical model to completely describe this complicated flow situation, the complete equations of motion must be considered. However, practical methods for carrying out a solution of such equations are limited to numerical approaches which are presently in the development stage.

Some of the more recently developed methods which were quite successful shall be discussed here in brief. However, only very few methods incorporate the effects of turbulence. Most of them are applicable to laminar time-dependent two- or three-dimensional incompressible viscous flow problems with various boundary conditions. One of these methods, which uses pressure and velocities as primary variables, and which can be applied to confined flows as well as flows having free surfaces is the "marker-and-cell" (MAC) method developed by Harlow and Welch [1, 2]<sup>1</sup> at Los Alamos. Certain marker particles are introduced into the flow calculation to indicate the respective fluid configuration. The flow equations which are described in Eulerian space (full Navier-Stokes equations, incompressible) are formulated in finite difference form, in both space and time variables. The derivation of these finite-difference equations is based upon the following sequence of events by

---

<sup>1</sup>Numbers in brackets refer to similarly numbered references in the Bibliography.

which the whole configuration is advanced from one step to the next.

1. The velocity distribution is known at the beginning of the cycle either from an initial condition or from the previous cycle.
2. The corresponding field of pressure is calculated.
3. The components of acceleration are calculated; from these changes in velocity are computed and added to the previous values.
4. The marker particles are moved to new positions according to the velocity determined for their locations.

The method is capable of satisfying a free-slip or no-slip condition at a rigid wall and a pressure boundary condition at a free surface. Computations have indicated considerable numerical stability and comparisons with some experimental results showed very close agreement. However, finite difference approximations introduce truncation errors that can obscure the effects of real viscosity and influence the stability of the solution. If only the mean effects of turbulence on a flow are of interest, such difficulties can usually be avoided, because the effective turbulent viscosity is often larger than the molecular viscosity and is, therefore, not likely to be obscured by finite difference errors. A method of this type, proposing ZIP differencing [3] is presented by C. W. Hirt [4]. However, ZIP

differentiating cannot be readily incorporated into the marker-and-cell technique, since its variables are defined at different mesh points.

R. S. Hotchkiss [5] quite successfully employs an extension of the MAC method for his calculations of three-dimensional flows of air and particles around structures. The full nonlinear Navier-Stokes equations for incompressible flow with buoyancy are solved. The effect of turbulence is resolved through a constant eddy viscosity. The method is capable of satisfying five different kinds of boundary conditions, e.g., inflow, outflow and periodic boundaries, along with rigid walls that have either free-slip or no-slip conditions. In addition to the Navier-Stokes equations, the time dependent heat equation is solved to incorporate features of thermal buoyancy (Boussinesq approximation). The computer program also includes the simultaneous solution of a transport equation in order to determine distributions of particulate matter. The results are displayed as three-dimensional perspective views drawn by a computer. Similar equations, however, using a variable eddy viscosity have been used by J. W. Deardorff [6] for his numerical investigation of the idealized planetary boundary layer. The nonlinear equations of motion are solved for the ideal case of neutral stability, horizontal homogeneity of all dependent mean variables except the mean pressure. No buoyancy effects are considered. A discussion and details of the numerical method are given in [7].

Although it was possible in all these examples to study full three-dimensional problems with methods such as the MAC method, these calculations are still extremely time consuming and require the largest computers now available. A simplified marker-and-cell method (SMAC) has been given by A. A. Amsden and F. H. Harlow [8]. Another extension of the SMAC method is proposed by P. I. Nakayama and N. C. Romero [9] for the solution of incompressible transient flows that are almost three-dimensional. The equations of motion are two-dimensional but contain functions that account for the effects of a third dimension. The method may also be used for the simple incorporation of internal obstacles in two-dimensional flows.

Besides the MAC method and its numerous modifications, some other numerical experiments with a difference model for the time-dependent Navier-Stokes equations have been reported by Schoenauer [10]. He concludes that the space mesh size must be inversely proportional to the Reynolds number. A coarse net produces a numerical "turbulence" which tends to the physical turbulence as the mesh size goes to zero. However, the existing computers are not fast enough for fluid flows which have Reynolds numbers in the turbulent regime.

Similar to Hotchkiss [5], D. Djurić and J. C. Thomas [11] apply a numerical model (following Harlow and Welch [1] and Deardorff [6]) to atmospheric boundary layer calculations, especially to transport and diffusion of gaseous air



pollutants in the vicinity of tall buildings. The equations used in this model follow those derived by Ogura and Phillips [12] in which the "anelastic" approximation is utilized. In these equations the basic density  $\rho$  is constant in the horizontal planes and varies only in height. The Coriolis term is not included because of the small scale of motion under consideration. Periodic boundary conditions were used except for pressure, which had a slight decrease in wind direction to provide a driving force which moves the air.

R. B. Lantz and K. H. Coats [13] use a quite different model for their three-dimensional calculation of spread and dilution of air pollutants. Their mathematical models are similar to the "Gaussian plume" models [14, 15, 16] and their extensions which can include topographic effects [17, 18]. A numerical solution of the three-dimensional material balances for pollutant flow and for the air stream is given. The pollutant material balance requires the solution of the three-dimensional convection-diffusion equation. Wind flow over uneven surfaces or around simple structures is calculated by numerically solving an equation for the velocity-potential which is modified such that it includes a variation of the horizontal velocity with height (logarithmic or power law). The numerical schemes used in the solution of the two balance equations are said to be efficient ones requiring minimal computer time. The mathematical description of individual

eddies downstream from obstacles is felt not essential to the pollutant dilution problem. The increased dispersion of the pollutant due to eddy formation is approximated by increasing the eddy diffusivity downstream of the obstacles.

There has long been a difference of opinion as to which of the possible forms of the equation of motion is the most suitable for numerical solutions. Some workers, as for example, Harlow and Welch [1], prefer to retain the velocities and pressure as dependent variables. Others, such as Aziz and Hellums [19] feel that it is advantageous to use instead the vorticity and stream function as dependent variables. Gosman, et al. [20], share the latter opinion. Their finite-difference model for steady two-dimensional flows, as described by elliptical partial differential equations, has proved to be very successful in a large number of problems to which it was applied. The model is capable of handling turbulent mean flows with variable fluid transport properties. Several turbulence models such as the Prandtl mixing length concept or a turbulence kinetic energy model using the Prandtl-Kolmogorov hypothesis have been employed. The computational procedure consists of solving the differential equations for the fundamental conservation laws of mass, momentum and energy which are complemented by auxiliary relations for the transport properties. Because of the established versatility of the model and because of the generality of its framework, the model shall be used in this investigation to study the turbulent flow with an

atmospheric velocity profile over a bluff surface obstruction.

An alternative approach, approximating atmospheric motions over surface obstructions has been carried out by Frost, et al. (1973) [21], in extending the concepts of boundary layer theory. Their method was applied to the specific geometry of a semi-elliptical cylinder. The characteristics of atmospheric shear flow over a rough terrain (disturbed boundary layer) are coupled with the turbulent boundary layer equations using Prandtl's mixing length hypotheses. Two approaches are presented to incorporate the pressure field and boundary conditions which exist within the large viscous region over the obstruction. The first considers a region in the immediate vicinity of the body in which the pressure distribution and outer boundary condition on the velocity are computed from potential theory for flow over the elliptical cylinder. The second approach considers a much larger region of influence, extending from the surface to the undisturbed flow at large heights above the obstruction and uses a vertical pressure decay function to blend into the undisturbed flow region.

The main conclusions drawn from the study were:

1. Localized maxima in wind speed occur at the top of the semi-elliptical obstruction.
2. An increase in the elliptical aspect ratio decreases the wind speed within the boundary layer at the top of the ellipse and returns it

to the logarithmic distribution characteristic of the undisturbed flow.

3. Increase in surface roughness affect the flow by decreasing the velocity in the boundary layer, with the most pronounced effect occurring near the surface of the smaller aspect ratio ellipse.
4. Reynolds number has a negligible effect on the overall flow for the range of Reynolds numbers considered.

To investigate the validity of the Prandtl mixing length theory for atmospheric flow in disturbed regions Frost and Harper [22] extended the above approach, still solving the boundary layer equations with equivalent boundary conditions, but using the conservation equation for turbulent kinetic energy (TKE) instead of Prandtl's mixing length (PML) to model the effect of turbulence. Comparing the respective flow fields predicted by the two models of PML and TKE it is found that there is only a small difference in the predicted velocity profiles, primarily in the regions of strong pressure gradients, caused through the diffusion and the convection of turbulence kinetic energy not accounted for in the PML concept. However, while the PML model does not provide any information about the turbulence structure of the flow field, the TKE model gives physically quite meaningful values of turbulence intensity levels which are presented and discussed in the study.

Although the method described has been used in both cases for the flow over semi-elliptical geometries only, it can generally be applied to any two-dimensional body shape. In the course of the following investigation it shall therefore be used for the calculation of the flow field over a bluff surface obstruction. Again the Prandtl mixing length concept will be employed in view of its reasonable results and its numerical efficiency. The potential model, however, used to compute the pressure gradient term and outer boundary condition for the flow over the semi-elliptical geometry, will be replaced by a more sophisticated model of inviscid shear flow over a bluff body.

This inviscid model, which in itself already represents an interesting analytical solution to the problem, is described in Chapter II. Its governing equations are developed and the required empirical input is discussed. The application of this model to atmospheric flow conditions is outlined and some typical results are presented.

Chapter III deals with the aforementioned boundary layer approach incorporating the pressure field input from the inviscid model of Chapter II. The governing turbulent boundary layer equations, their numerical solution procedure and the initial-and boundary-conditions are briefly reviewed. Solutions are given for selected parameters characterizing the undisturbed atmospheric velocity profile.

In Chapter IV the problem is then approached by solving the Navier-Stokes equations following the method of

Gosman, et al. [20]. Three different turbulence models are presented and compared--the PML concept, Prandtl-Kolmogorov's TKE model with a given turbulence length scale distribution and a TKE model with a simultaneous solution of a transport equation for the turbulence length scale. In contrast to the boundary-layer approach where the equations of motion are solved in terms of the primitive variables  $u$ ,  $w$  and  $p$ , the governing equations are written in terms of the vorticity  $\omega$  and the streamfunction  $\psi$  and the other physical properties involved. The equations are then expressed in a common form, differing only by a source term peculiar to the property which the equation represents. The transformation of the differential equations into difference equations which are solved by successive substitution, the incorporation of turbulence into the model as well as the respective boundary conditions used are explained. Finally, some results for different parameters of the approaching wind profile are presented and discussed in the remainder of the chapter.

## CHAPTER II

### INVISCID FLOW MODEL

#### I. INTRODUCTORY REMARKS

A suitable model for flow over a bluff body should at least include the occurrence of flow separation and a wake formation. For inviscid flow models this leads automatically to a free-streamline approach. However, the classical assumption of the free-streamline analysis [23] is that of a quiescent fluid on the inner side of the free streamline such that the free streamline remains one of constant pressure and velocity. This results in a constant pressure wake of infinite extent which is an inadequate representation of the actual case. The model yields a base pressure  $p_b$  which is equal to that at infinity, whereas it should really be  $p_b \ll p_\infty$ , thus leading to negative base pressure coefficients  $C_{p_b}$ . The conventional free-streamline theory therefore has to be applied with moderation.

A somewhat different free-streamline theory for an inviscid shear flow over a bluff body, featuring an upstream separation bubble and a closed downstream wake region with variable pressure, shall now be described.

Parkinson and Jandali [24] developed a simple theory for a two-dimensional incompressible uniform flow external to a bluff body and its wake. The desired flow separation

points are made the critical points of a conformal transformation to a region in which a surface source creates stagnation conditions at the critical points. The stagnation streamlines then transform to tangential separation streamlines in the physical plane (Figure 2.1). The position and the strength of the source is determined by the empirical requirements of the separation position and its pressure coefficient.

This model was then used by Kiya and Arie [25] and extended for their calculation to a separate flow past a bluff body attached to a wall on which the approaching turbulent boundary layer has been replaced by a hypothetical inviscid uniform shear flow (Figure 2.2). In addition, it utilizes a solution found by Fraenkel [26] to incorporate the formation of a corner eddy in front of the body. This model admits analytical solutions and automatically yields closed streamlines in front of the body which are geometrically very similar to those observed in practice. Like the Parkinson-Jandali model it includes a finite wake width and a pressure distribution on the separation streamline which decreases asymptotically towards the corresponding free stream value at infinity. The theory requires input of four empirical parameters which depend on the geometry of the body. These parameters are:

1. Location of the front face stagnation point.
2. Stagnation point pressure.
3. Location of the separation point.



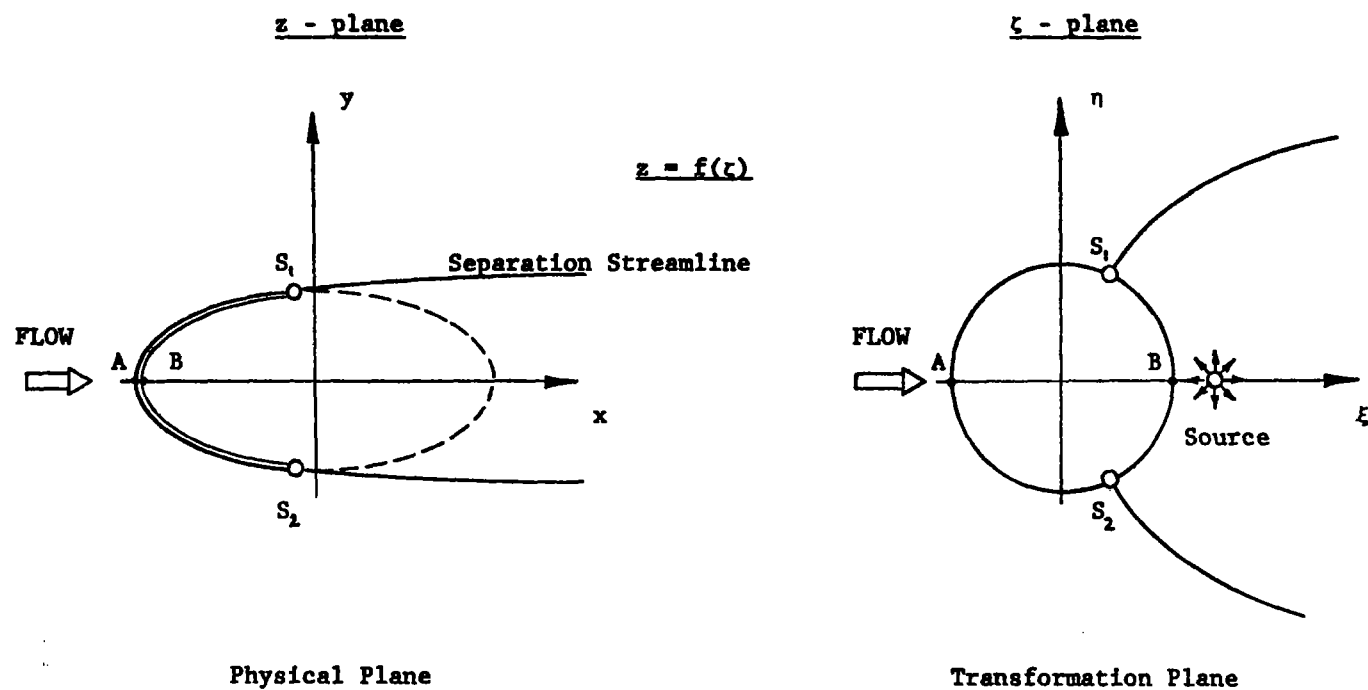


Figure 2.1. Physical- and basic transformation-planes with separation points  $S_1$  and  $S_2$  as critical points [24].

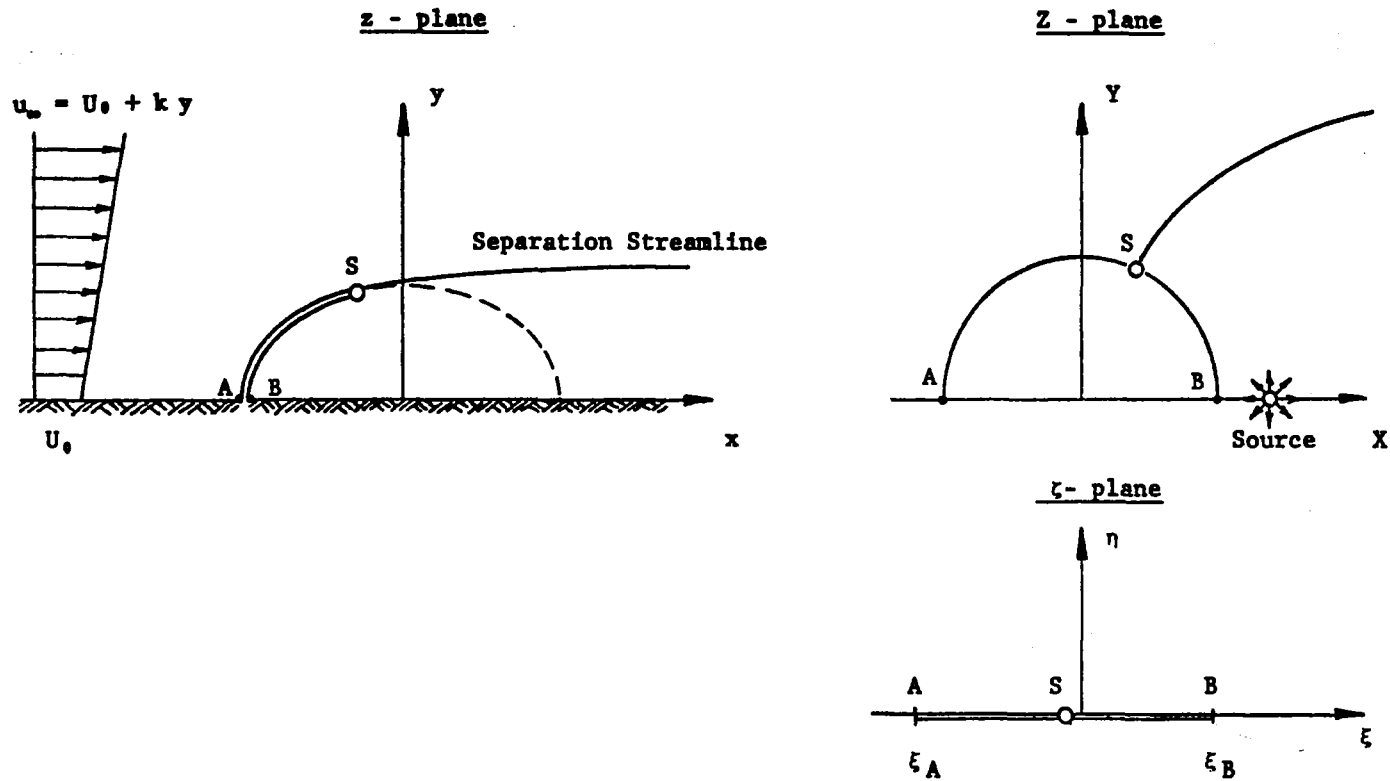


Figure 2.2. Physical- and transformation-planes for inviscid parallel shear flow over a bluff body attached to a wall [25].

#### 4. Separation point pressure.

In the present analysis the Kiya and Arie [25] model has been extended further. The original model yields a wake region which is finite in width, however, infinite in length. Through the addition of a sink equal in strength to the existing source, at a suitable downstream distance in the transformation plane it is possible to close the wake and thus eliminate the unrealistic feature of the original rear model region. This involves an additional empirical parameter, i.e., the location of the rear reattachment point.

## II. DEVELOPMENT OF GOVERNING EQUATIONS FOR INVISCID FLOW OVER A FENCE

The details of the inviscid flow model shall now be developed for the case of the flow over a fence.

We consider a two-dimensional incompressible, inviscid, steady uniform shear flow past a bluff body ASB as shown in Figure 2.3. The velocity profile at a large distance from the body shall be

$$u_{\infty}^* = U_0^* + k^* y^* \quad (2.1)$$

where  $U_0^*$  is the dimensional velocity at the wall and  $k^*$  the dimensional vorticity

$$k^* = \frac{\partial u^*}{\partial y^*} - \frac{\partial v^*}{\partial x^*} \quad (2.2)$$

which is constant throughout the flow field. Introducing a

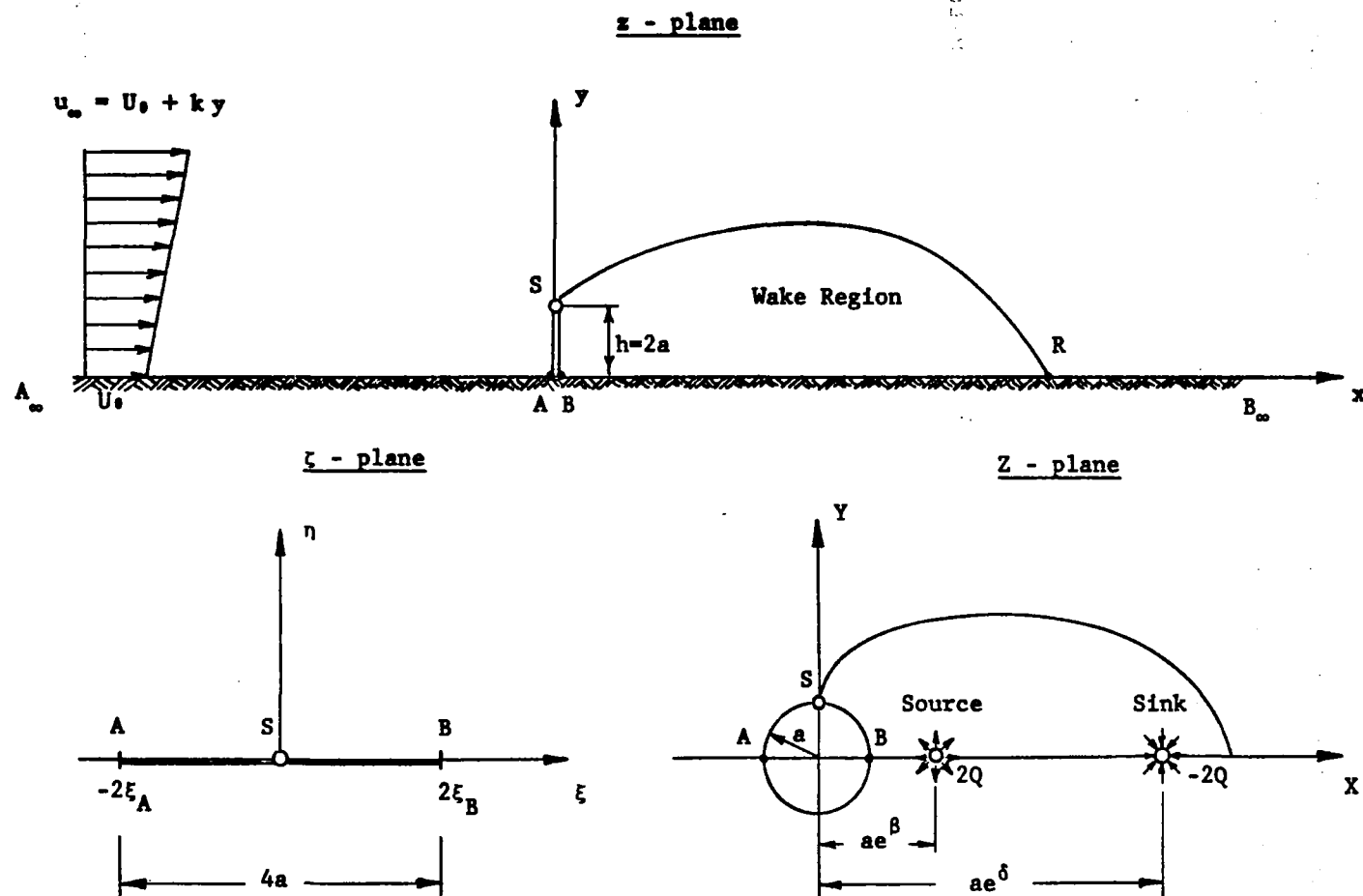


Figure 2.3. Physical- and transformation-planes for inviscid parallel shear flow over a fence.

stream function  $\psi^*$  by

$$u^* = \frac{\partial \psi^*}{\partial y^*}; \quad v^* = -\frac{\partial \psi^*}{\partial x^*} \quad (2.3)$$

where  $u^*$  and  $v^*$  are the velocity components of the velocity vector  $\vec{q}^*$  in the  $x^*$  and  $y^*$  direction respectively, i.e.,

$$\vec{q}^* = u^* \vec{i} + v^* \vec{j} \quad (2.4)$$

The continuity equation

$$\text{div } \vec{q}^* = 0$$

is then automatically satisfied. The vorticity vector  $\vec{\Omega}^*$  is given by

$$\vec{\Omega}^* = \text{curl } \vec{q}^*; \quad \frac{\partial v^*}{\partial x^*} - \frac{\partial u^*}{\partial y^*} = -\nabla^2 \psi^* \quad (2.5)$$

and from Equation 2.2

$$\nabla^2 \psi^* = k^* \quad (2.6)$$

We can nondimensionalize the coordinates by a reference length  $h^*$

$$x = \frac{x^*}{h^*}; \quad y = \frac{y^*}{h^*} \quad (2.7)$$

and the velocities by a reference value  $U_{\text{ref}}^*$

$$u = \frac{u^*}{U_{\text{ref}}^*}; \quad v = \frac{v^*}{U_{\text{ref}}^*}; \quad U_0 = \frac{U_0^*}{U_{\text{ref}}^*} \quad (2.8)$$

and thus rewrite Equations 2.1 and 2.2 as

$$u_{\infty} = U_0 + ky \quad (2.9)$$

and

$$k = \frac{\partial u}{\partial y} - \frac{\partial v}{\partial x} \quad (2.10)$$

Furthermore, Equation 2.6 becomes

$$\nabla^2 \psi = k \quad (2.11)$$

where

$$\psi = \frac{\psi^*}{U_{\text{ref}}^* \cdot h^*} \quad (2.12)$$

is the dimensionless stream function. It can easily be shown that Euler's equation of motion for steady flow

$$\nabla \frac{q^2}{2} - \vec{q} \times \text{curl } \vec{q} = -\text{grad } p \quad (2.13)$$

or

$$u \frac{\partial u}{\partial x} + v \frac{\partial u}{\partial y} = -\frac{\partial p}{\partial x}$$

$$u \frac{\partial v}{\partial x} + v \frac{\partial v}{\partial y} = -\frac{\partial p}{\partial y} \quad (2.14)$$

simply reduces to Equation 2.11 which is therefore the governing equation of our flow problem.

On the boundaries, we require the following conditions to be satisfied:

$$\psi = \text{const.} \quad (2.15)$$

on the wall and solid surface and

$$\frac{\partial \psi}{\partial y} \rightarrow U_0 + ky; \quad \frac{\partial \psi}{\partial x} \rightarrow 0 \quad (2.16)$$

at large distances away from the body, If we subdivide the stream function into two parts, i.e.,

$$\psi = \frac{1}{2} ky^2 + \Psi \quad (2.17)$$

then

$$\nabla^2 \psi = k + \nabla^2 \Psi \quad (2.18)$$

and from comparison with Equation 2.11 we get

$$\nabla^2 \Psi = 0 \quad (2.19)$$

as the new governing equation with the transformed boundary conditions

$$\Psi + \frac{1}{2} ky^2 = \text{const.} \quad (2.20)$$

on the wall and solid surface and

$$\frac{\partial \Psi}{\partial y} \rightarrow U_0; \quad \frac{\partial \Psi}{\partial x} \rightarrow 0 \quad (2.21)$$

at large distances away from the body.

Through the introduction of a function  $\phi$  which is related to  $\Psi$  by the Cauchy-Riemann relations

$$\frac{\partial \Phi}{\partial x} = \frac{\partial \Psi}{\partial y}; \quad \frac{\partial \Phi}{\partial y} = -\frac{\partial \Psi}{\partial x} \quad (2.22)$$

we can define a complex potential

$$W(z) = \Phi + i\Psi \quad (2.23)$$

where

$$z = x + iy \quad (2.24)$$

describes our physical  $z$ -plane. We can now transform the wall boundary  $A_\infty A$  and  $BB_\infty$  together with the fence contour  $ASB$  into the upper half of a new plane called the  $\zeta$ -plane (see Figure 2.3, page 17) where

$$\zeta = \xi + i\eta \quad (2.25)$$

and

$$-\xi_A = \xi_B = h = 2a \quad (2.26)$$

by using a suitable transformation

$$z = f(\zeta) \quad (2.27)$$

Under the assumption that this transformation behaves as

$$z \sim k_1 \zeta + k_2 \ln \zeta + k_3 + O(\zeta^{-1}) \quad (2.28)$$

for

$$|\zeta| \rightarrow \infty$$

Fraenkel [26] has found a solution to Equation 2.19 which



satisfies the boundary conditions for Equations 2.20 and 2.21, i.e.,

$$\Psi = \text{Im}(W_I + W_{II}) \quad (2.29)$$

where

$$W_I = U_0 \cdot k_1 \cdot \zeta \quad (2.30)$$

and

$$W_{II} = \frac{k}{2\pi} \int_{-2a}^{2a} \frac{y^2(\bar{\xi}, 0)}{\zeta - \bar{\xi}} d\bar{\xi} \quad (2.31)$$

In order to have a free streamline which originates from the separation point S, extends in the downstream direction and reattaches at R, we have to add to our stream function  $\Psi$  a combination of sinks and sources which are appropriately located. For this purpose a third complex plane, the Z-plane is introduced by the transformation

$$\zeta = Z + \frac{a^2}{Z} \quad (2.32)$$

Figure 2.3, page 17, shows this plane with its source-sink arrangement. In addition to the source at  $X = ae^\beta$  employed in Reference [25] a sink is placed downstream at the location  $X = ae^\delta$ .

The complex potential of the source-sink system in this plane is given by

$$W_{III} = \frac{Q}{\pi} [\ln(Z - ae^{\beta}) + \ln(Z - ae^{-\beta}) - \ln(Z - ae^{\delta}) - \ln(Z - ae^{-\delta}) + C] \quad (2.33)$$

If we add this to Equation 2.29 we get the stream function  $\psi$  of the resulting flow as

$$\psi = \frac{1}{2} ky^2 + \text{Im}(W_I + W_{II} + W_{III}) \quad (2.34)$$

The complex velocity

$$w = u - iv \quad (2.35)$$

can then be determined as

$$u - iv = ky + \frac{\partial \Psi}{\partial y} + i \frac{\partial \Psi}{\partial x} \quad (2.36)$$

or with the Cauchy-Riemann relations

$$u - iv = ky + \frac{dw}{dz} \quad (2.37)$$

which is

$$u - iv = ky + \left( \frac{dw_I}{d\zeta} + \frac{dw_{II}}{d\zeta} + \frac{dw_{III}}{d\zeta} \cdot \frac{dz}{d\zeta} \right) \bigg/ \frac{dz}{d\zeta} \quad (2.38)$$

Since the angle of intersection of the curve at S is not preserved in the z-plane the point S is the critical point of the transformation, i.e.,

$$\frac{dz}{d\zeta} = f'(0) = 0 \quad (2.39)$$

In order that the velocity at this point remains finite, we require from Equation 2.38 that

$$\left( \frac{dW_I}{d\zeta} + \frac{dW_{II}}{d\zeta} + \frac{dW_{III}}{d\zeta} \cdot \frac{dz}{d\zeta} \right)_{\zeta=0} = 0 \quad (2.40)$$

The three complex planes are related by

$$z = \zeta - \frac{a^2}{\zeta} \quad (2.41)$$

and

$$\zeta = z + \frac{a^2}{z} \quad (2.42)$$

To use Fraenkel's solution (Equation 2.19) one has to establish a relation between the  $z$ - and  $\zeta$ -plane from

Equations 2.41 and 2.42 and find the constants  $k_1$  and  $k_2$  in Equation 2.28. Kiya and Arie [25] have found  $W_I$  and  $W_{II}$  to be

$$W_I = U_0 \cdot \zeta = U_0 \cdot \left( z + \frac{a^2}{z} \right) \quad (2.43)$$

and

$$W_{II} = \frac{k}{2\pi} \left[ 4a\zeta + (\zeta^2 - 4a^2) \ln \frac{\zeta - 2a}{\zeta + 2a} \right] \quad (2.44)$$

However, to close the separation region,  $W_{III}$  had to be

determined differently as already given by Equation 2.33.

One can divide it into three parts

$$W_{III} = W_{III\beta} + W_{III\delta} + C \quad (2.45)$$

$$W_{III} = \frac{Q}{\pi} [F_{\beta}(Z) - F_{\delta}(Z)] + C \quad (2.46)$$

where

$$F_{\beta}(Z) = \ln(Z - ae^{\beta}) + \ln(Z - ae^{-\beta}) - \ln Z \quad (2.47)$$

$$F_{\delta}(Z) = \ln(Z - ae^{\delta}) + \ln(Z - ae^{-\delta}) - \ln Z \quad (2.48)$$

In terms of these three complex potentials, the complex velocity in the physical plane can be expressed by Equation 2.38, where from Equations 2.41 and 2.42

$$\frac{dz}{d\zeta} = \frac{Z^2}{Z^2 - a^2} \quad (2.49)$$

and

$$\frac{dz}{d\zeta} = \frac{Z^2 + a^2}{Z^2 - a^2} \quad (2.50)$$

Note, the latter expression has a simple zero at the separation point  $Z = ia$ .  $Q$  is now determined from Equation 2.40 as

$$Q = 2\pi a \left( U_0 + \frac{4ka}{\pi} \right) \frac{\cosh \beta \cdot \cosh \delta}{\cosh \delta - \cosh \beta} \quad (2.51)$$

Substituting the foregoing results into Equation 2.34 and rearranging source terms gives the following expression for the stream function  $\psi$ :

$$\psi = \frac{1}{2} ky^2 + \text{Im} \left[ \left( U_0 + \frac{2ka}{\pi} \right) \cdot \zeta + \frac{k}{2\pi} \left( z^2 - \ln \left( \frac{z-a}{z+a} \right)^2 \right) + \frac{Q}{\pi} [F_\beta(z) - F_\delta(z)] \right] + C \quad (2.52)$$

The complex velocity from Equation 2.38

$$u - iv = ky + \left( \frac{dw_I}{d\zeta} + \frac{dw_{II}}{d\zeta} + \frac{dw_{III}}{d\zeta} \cdot \frac{dz}{d\zeta} \right) \cdot \frac{d\zeta}{dz} \quad (2.53)$$

becomes

$$\begin{aligned} u - iv = ky + & \left[ \left( U_0 + \frac{4ka}{\pi} \right) + \frac{k}{\pi} \cdot \zeta \cdot \ln \left( \frac{\zeta - 2a}{\zeta + 2a} \right) \right. \\ & + \frac{Q}{\pi} \frac{z^2}{z^2 - a^2} \left( \frac{2(z - a \cosh \beta)}{z^2 - 2az \cosh \beta + a^2} \right. \\ & \left. \left. - \frac{2(z - a \cosh \delta)}{z^2 - 2az \cosh \beta + a^2} \right) \right] \frac{z^2 - a^2}{z^2 + a^2} \end{aligned} \quad (2.54)$$

Since the nondimensional vorticity  $k$  is constant throughout the flow field, Euler Equation 2.13 can be integrated to give Bernoulli's equation

$$\frac{q^2}{2} + p - k\psi = \text{const.} \quad (2.55)$$

or

$$\frac{u^2 + v^2}{2} + p - k\psi = \frac{u_\infty^2}{2} + p_\infty - k\psi_\infty \quad (2.56)$$

allowing the determination of the pressure coefficient

$$C_p = u_\infty^2 - (u^2 + v^2) - 2k(\psi_\infty - \psi) \quad (2.57)$$

which reduces on the body surface to

$$C_{p\text{surf}} = U_0^2 - v_{\text{surf}}^2 \quad (2.58)$$

Assuming that separation occurs at a given base pressure  $C_{pb}$ , assumed constant over the whole rear side of the fence, we can write

$$C_{pb} = U_0^2 - v_S^2 \quad (2.59)$$

As is required through Equation 2.40, that the separation velocity be finite,  $v_S$  is determined from Equation 2.54 by

$$\begin{aligned} iv_S &= -\lim(u - iv) \\ z &\rightarrow ia \\ y &\rightarrow iZa \\ \zeta &\rightarrow 0 \end{aligned} \quad (2.60)$$

By L'Hôpital's rule

$$v_S = \left( U_0 + \frac{4ka}{\pi} \right) \cdot \frac{\cosh \beta + \cosh \delta}{\cosh \beta \cdot \cosh \delta} \quad (2.61)$$

### III. REQUIRED EMPIRICAL INPUT

An inviscid shear flow model for the flow over a fence, yielding a realistic upstream separation bubble and a finite wake region has been formulated in the preceding section. The input of five empirical parameters is required to complete the model. These are:

1. The front face stagnation point location

$$z_{\max} = iy_{\max}$$

2. The front face stagnation point pressure

$$C_{p\max}$$

3. The separation point location

$$z_S = iy_S$$

4. The separation point pressure

$$C_{pS} = C_{pb}$$

5. The downstream reattachment point location

$$z_R = x_R$$

Using Equation 2.54 relationships between parameters 1, 3 and 5 respectively and Equation 2.58 for the remaining two parameters, one obtains five equations to solve for the five unknowns

$U_0$ ,  $k$ ,  $\beta$ ,  $\delta$  and  $v_S$

#### IV. DISCUSSION OF APPLICABILITY OF FENCE

##### MODEL TO RECTANGULAR BODIES

The flow over a rectangular block (see Figure 2.4) can be treated similarly to the one over a fence, since the external flow field is qualitatively the same as that for a fence provided reattachment does not occur on the roof. The upstream separation bubble is only insignificantly different and the downstream separation must occur at the sharp leading edge and thus at the same location as in the case of the fence. A different empirical input for the separation

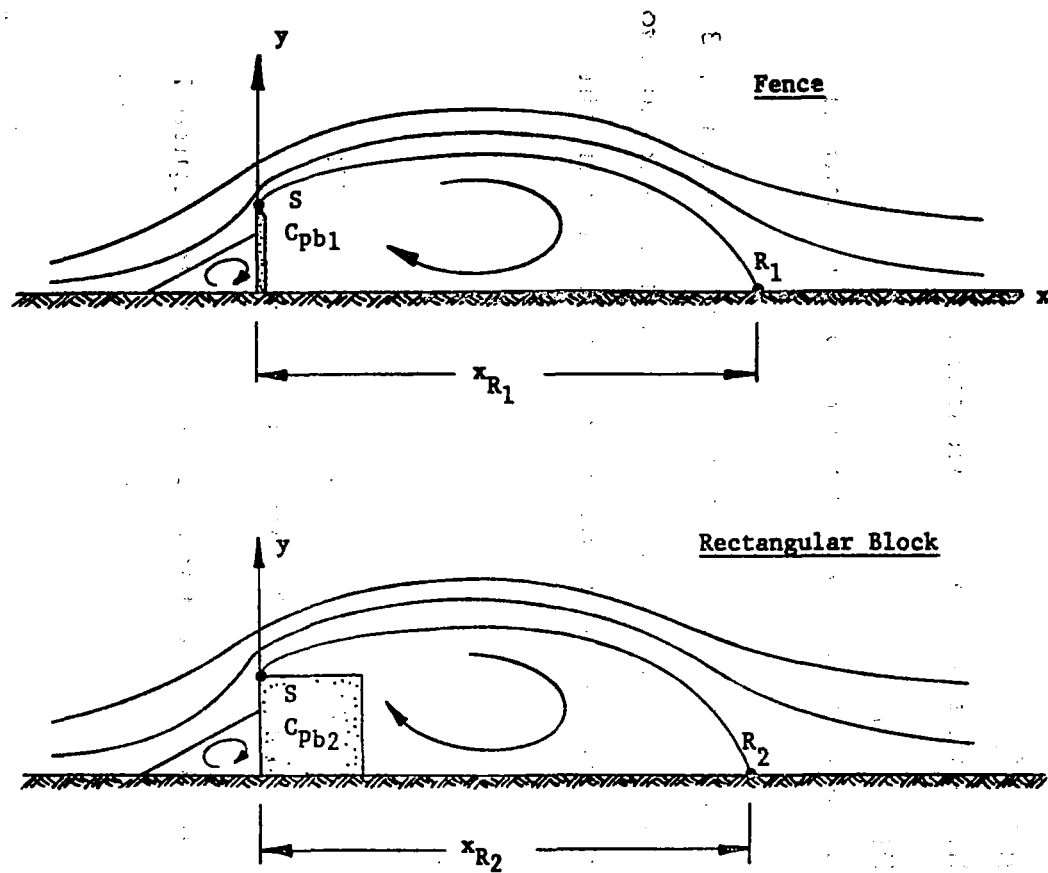


Figure 2.4. Implementation of different body geometries by using different empirical values  $C_{pb}$  and  $x_R$ .



base pressure and the downstream reattachment point would therefore account sufficiently for the new flow situation. Some typical base pressure coefficients for different building geometries are shown in Table 2.1. It is pointed out that the rectangular block buildings generally have higher  $C_{pb}$  values than that currently used for the case of the fence.

## V. RELATION TO ATMOSPHERIC FLOWS

Since the inviscid flow model is dependent on empirical inputs, it is reasonable to postulate that if these inputs are characteristic of bluff geometries in the atmospheric boundary layer, then the resulting solutions should reflect flow characteristics of the atmosphere.

One of the empirical input parameters discussed previously, which seems amenable to this approach, is the base pressure coefficient  $C_{pb}$ . According to experiments by Good and Joubert [27], pressures on the upstream face of a normal plate located in a smooth-wall-boundary layer are determined by a wall similarity law of the form:

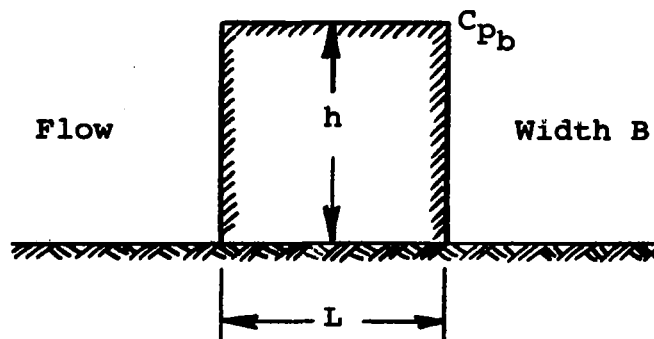
$$C_{pb} = - \left( \frac{u_*^*}{\bar{U}_{ref}^*} \right)^2 \left[ 152 \log \frac{h^* u_*^*}{v_*^*} - 147 + P \phi \left( \frac{h^*}{\delta^*} \right) \right] \quad (2.62)$$

Here  $P$  is constant for turbulent boundary layers with zero pressure gradient and  $\phi$  is a universal function of  $h^*/\delta^*$  which is tabulated in their paper. When  $h^*/\delta^*$  is less than

TABLE 2.1  
TYPICAL BASE PRESSURE COEFFICIENTS FOR  
DIFFERENT BUILDING GEOMETRIES

$h$	$L$	$B$	$C_{pb}$
1.0	0	$\infty$	-0.85
1.0	0.4	0.4	-0.6*
1.0	1.0	1.0	-0.5*
1.0	4.0	4.0	-0.3*

\*Source: Peter Sachs, Wind Forces in Engineering  
(New York: Pergamon Press, 1972).



0.5, as is the case for most atmospheric boundary layers,  $\phi(h^*/\delta^*)$  is negligibly small. Thus,

$$C_{pb} = - \left( \frac{u_*^*}{U_{ref}^*} \right)^2 \left( 152 \log \frac{h^* u_*^*}{\nu^*} - 147 \right) \quad (2.63)$$

Now  $C_{pb}$  obeys a wall similarity law in the sense that  $C_{pb} (U_{ref}^*/u_*^*)^2$  can be described as a function of  $h^* u_*^*/\nu^*$  only, for the case of the smooth wall.

Applying this to the case of the rough wall, where

$$\frac{h^* u_*^*}{\nu^*} \rightarrow \frac{h^*}{z_0^*} \quad (2.64)$$

the similarity law becomes:

$$C_{pb} = - \left( \frac{u_*^*}{U_{ref}^*} \right)^2 \left( 152 \log \frac{h^*}{z_0^*} - 147 \right) \quad (2.65)$$

Figure 2.5 shows a graphical representation of this equation for several dimensionless surface roughnesses. Extending the equation still further in order to relate to atmospheric flows and introducing a geostrophic drag coefficient

$$C_g = \frac{u_*^*}{G^*} \quad (2.66)$$

with  $G^*$  being the geostrophic wind, Equation 2.65 can be written as:

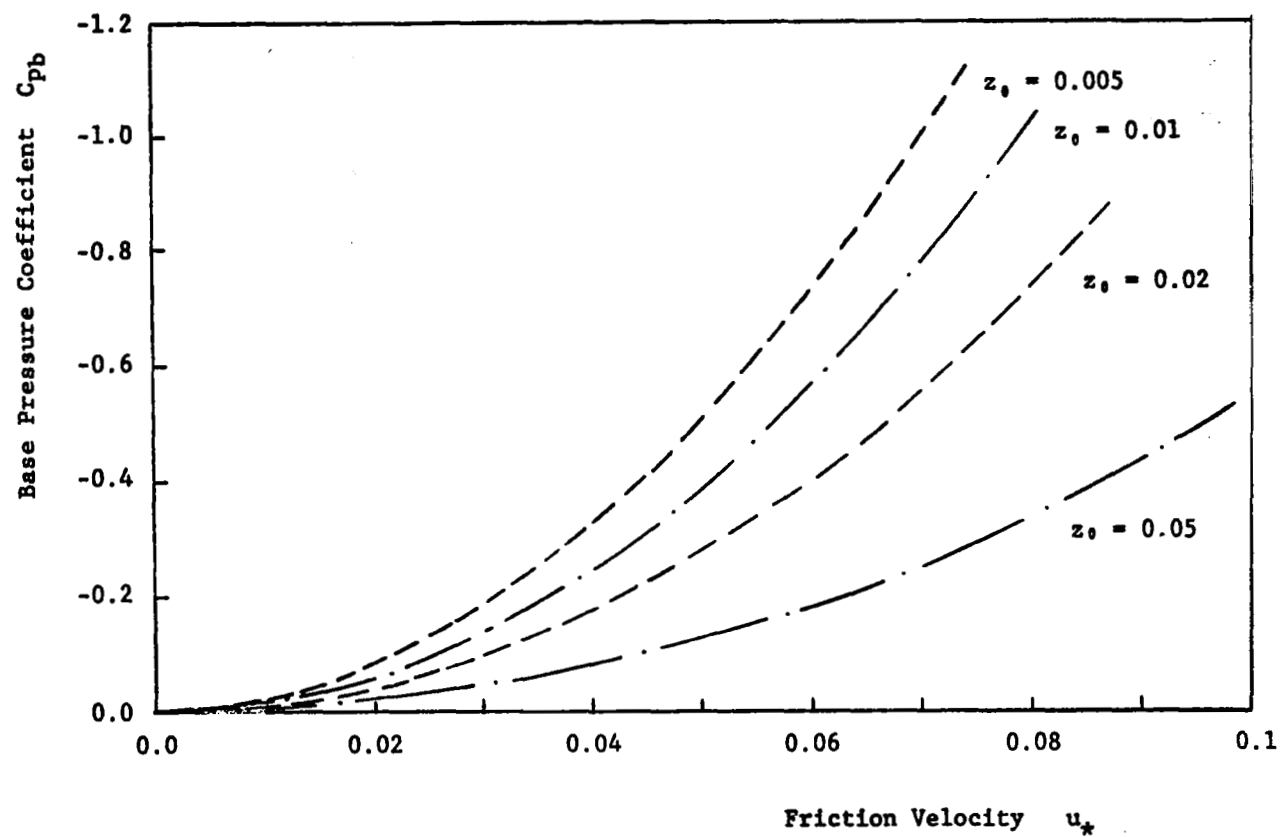


Figure 2.5. Graphical representation of Equation 2.65.

$$C_{pb} = - \left( \frac{G^*}{U_{ref}^*} \right)^2 C_g^2 \left( 152 \log \frac{h^*}{z_0^*} - 147 \right) \quad (2.67)$$

From Csanady [28], the geostrophic drag coefficient  $C_g$  is a function of the Rossby number  $Ro = \frac{f^* \cdot z_0^*}{G^*}$ , i.e.,

$$C_g^2 = f(Ro) \quad (2.69)$$

and hence one can rewrite Equation 2.65 as

$$C_{pb} = - \left( \frac{G^*}{U_{ref}^*} \right)^2 f(Ro) \left( 152 \log \frac{h^*}{z_0^*} - 147 \right) \quad (2.69)$$

It is proposed that the inviscid solution can thus be related to the prevailing atmospheric condition by using a  $C_{pb}$  value as an input, which is predicted from Equation 2.65 with known values of  $u_*^*$  and  $z_0^*$  or from Equation 2.69 with known values of  $G$ ,  $Ro$  and  $z_0^*$ .

## VI. RESULTS OF INVISCID MODEL

The aforementioned model was applied to the fence problem using the following empirical input-parameters

1. Front face stagnation point location

$$y_{max} = 0.6 \quad (2.70a)$$

2. Front face stagnation point pressure

$$C_{p_{max}} = 0.5 \quad (2.70b)$$

3. Separation point pressure

$$C_{p_S} = C_{p_b} = -0.85 \quad (2.70c)$$

#### 4. Downstream reattachment point location

$$x_R = 13.0 \quad (2.70d)$$

Conditions 1 and 4 were taken from Good and Joubert [27].

Condition 3 was determined from Equation 2.65 or Figure 2.5, page 33, for the values

$$u_* = \frac{u_*^*}{U_{ref}^*} = 0.0625$$

$$z_0 = \frac{z_0^*}{h^*} = 0.005 \quad (2.70e)$$

These four empirical input parameters  $y_{max}$ ,  $C_{pmax}$ ,  $C_{pb}$  and  $x_R$  lead to the following four calculated parameters:

$$U_0 = 0.7071$$

$$k = 1.0245$$

$$\cosh \beta = 1.3132$$

$$\cosh \delta = 10.725 \quad (2.71)$$

The streamline pattern computed on the basis of these values is shown in Figure 2.6 and an enlargement of the upstream separation region in Figure 2.7. As there are only limited experimental results available, especially from full scale studies, the quality of this flow field description cannot readily be determined. However, when compared with the small scale experimental results of [27] very good agreement is found, as can be seen in Figure 2.8.

Velocity profiles of the u-component for various x-stations are shown in Figure 2.9. Here the simplification

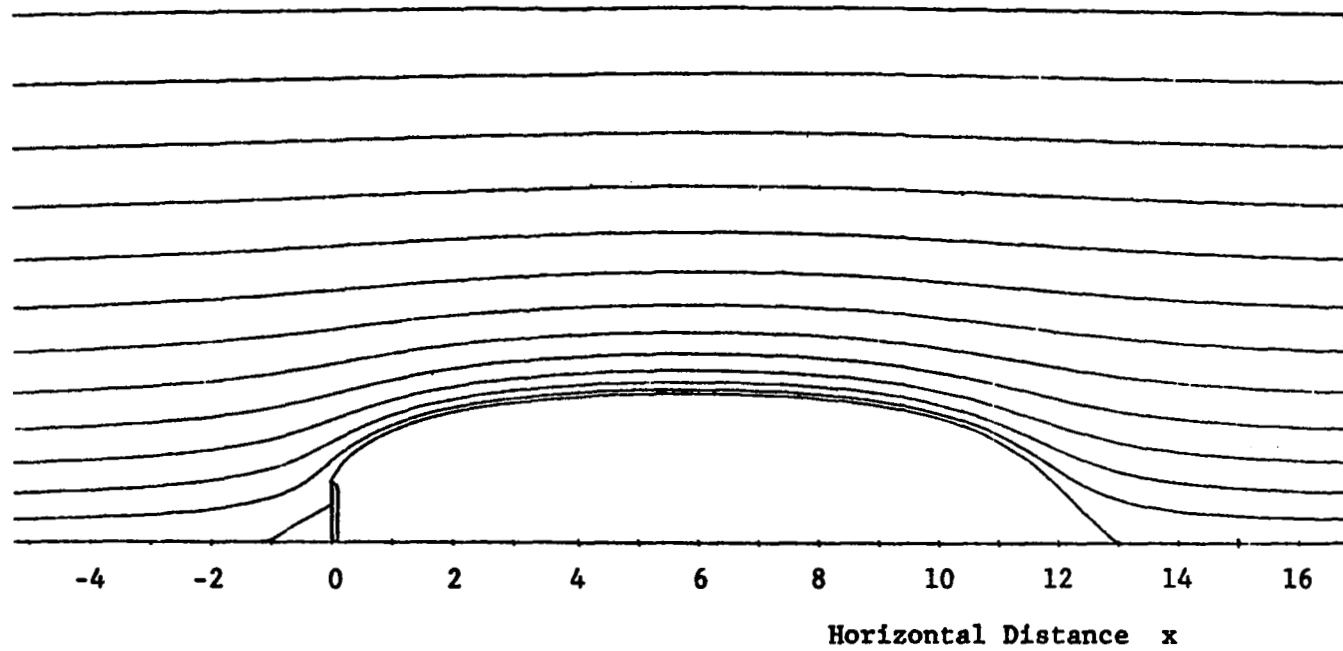


Figure 2.6. Streamlines for inviscid model.

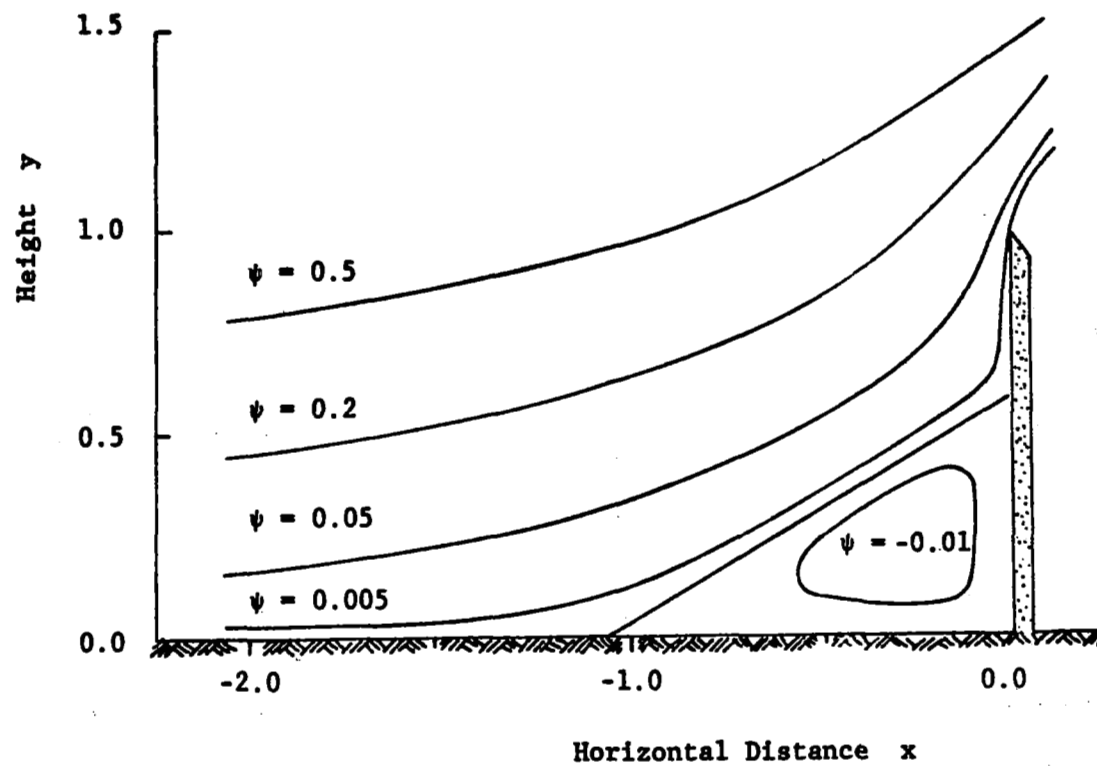


Figure 2.7. Streamline pattern in upstream fence region for inviscid model.



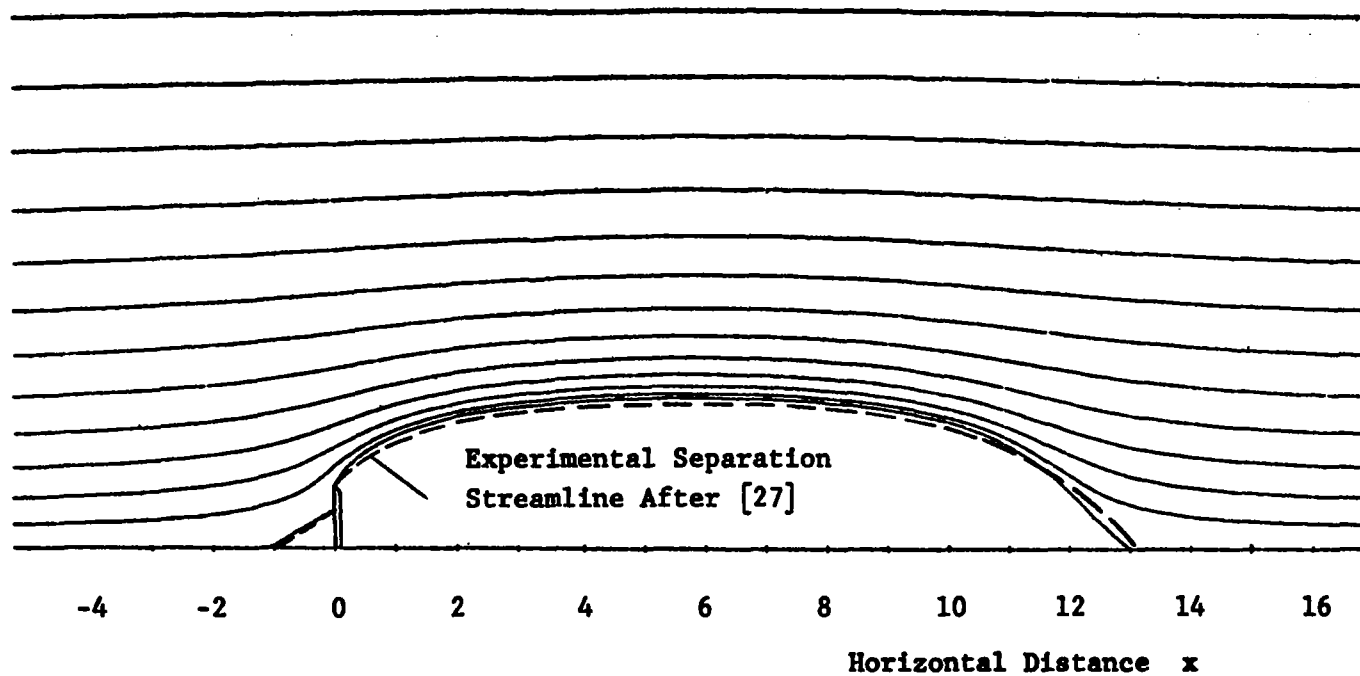


Figure 2.8. Comparison of analytically and experimentally determined separation streamline.

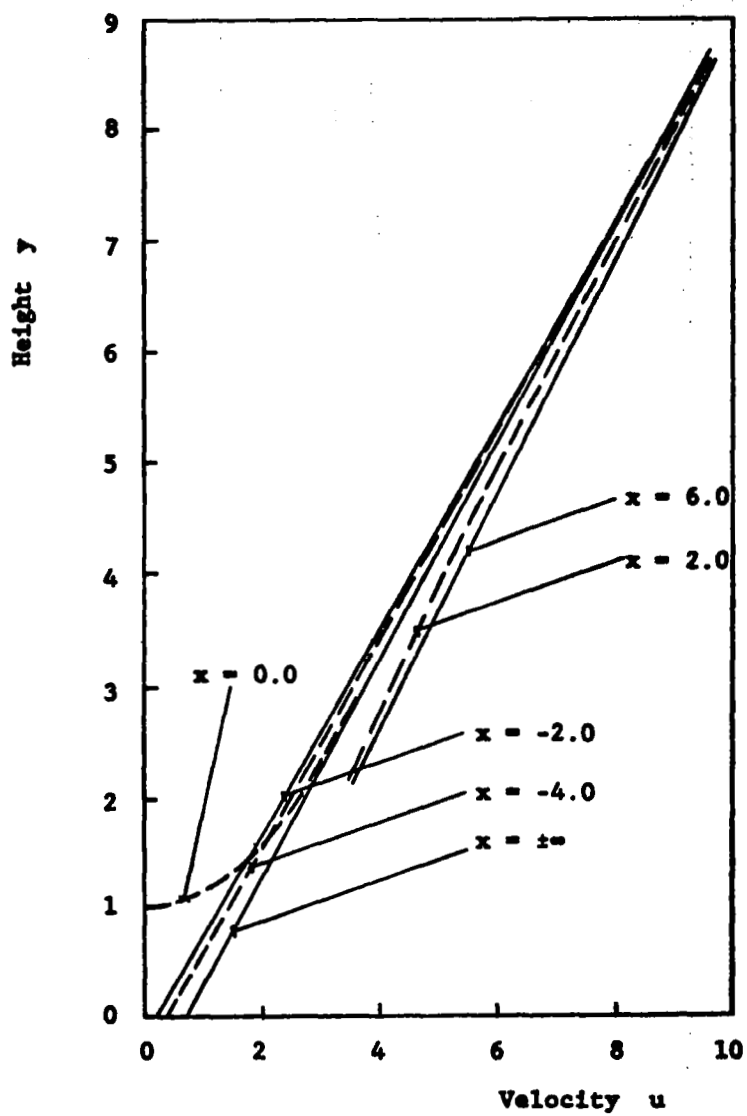


Figure 2.9. Velocity profiles for various x-stations.

of the model to a constant vorticity flow field becomes apparent in the almost linear velocity profiles. Nevertheless, the region of retarded flow upstream, the recirculating separation bubble in front of the fence and the accelerated flow region in the vicinity of the fence are qualitatively correct. This is also the case for the plot of the velocity gradient along various streamlines in Figure 2.10.

In turn, the computed pressure distribution is reasonable. The almost exact agreement of the pressure variation along the front face of the fence with experiments, which was already found for the infinite wake model [25], is maintained for the modified closed wake flow model. The pressure variation along given streamlines near the ground and along the separation streamline is shown in Figure 2.11. This pressure distribution will be used as the imposed pressure field in the viscous turbulent boundary layer approach to be described subsequently.

Relating the model to atmospheric flow conditions by varying the base pressure coefficient  $C_{pb}$  according to relation 2.65 but holding the remaining empirical input parameters constant, the results displayed in Figure 2.12 are achieved. It is found that the maximum height  $h_{\max}$  of the recirculation region behind the obstacle decreases with growing friction velocity  $u_*$  but increases for larger surface roughness  $z_0$ .

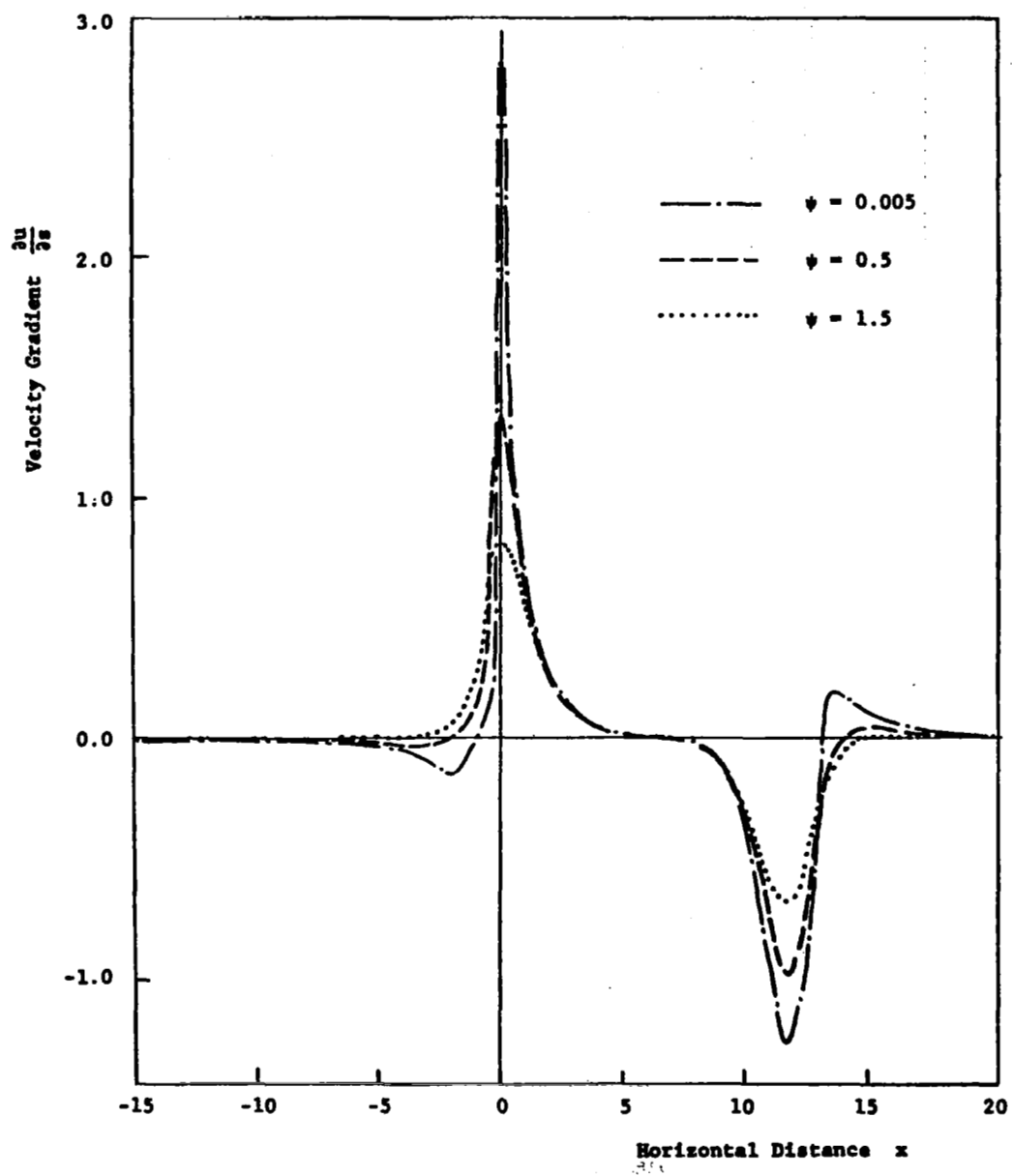


Figure 2.10. Velocity gradient along different streamlines.

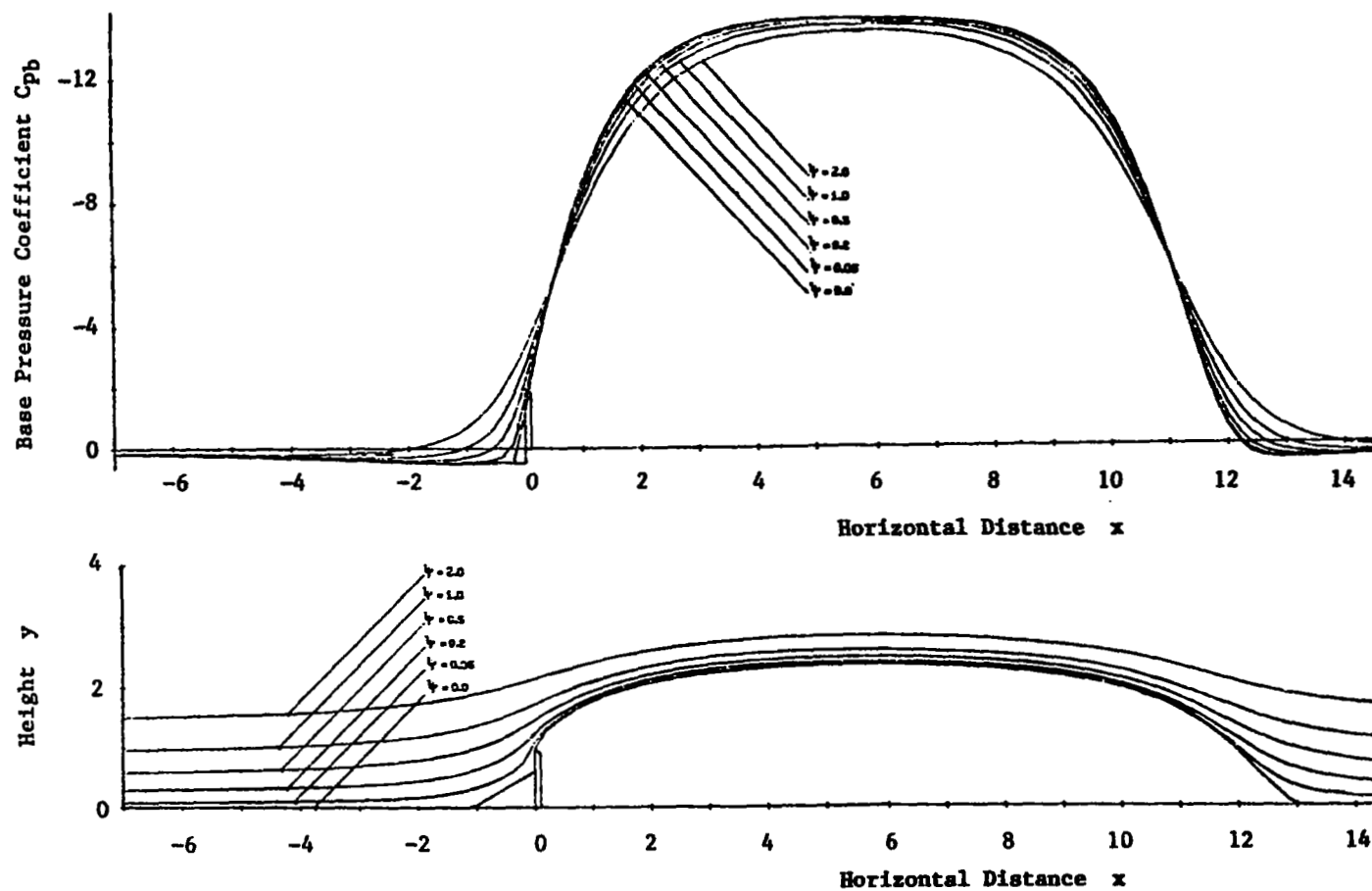


Figure 2.11.  $C_p$  distribution along various streamlines.

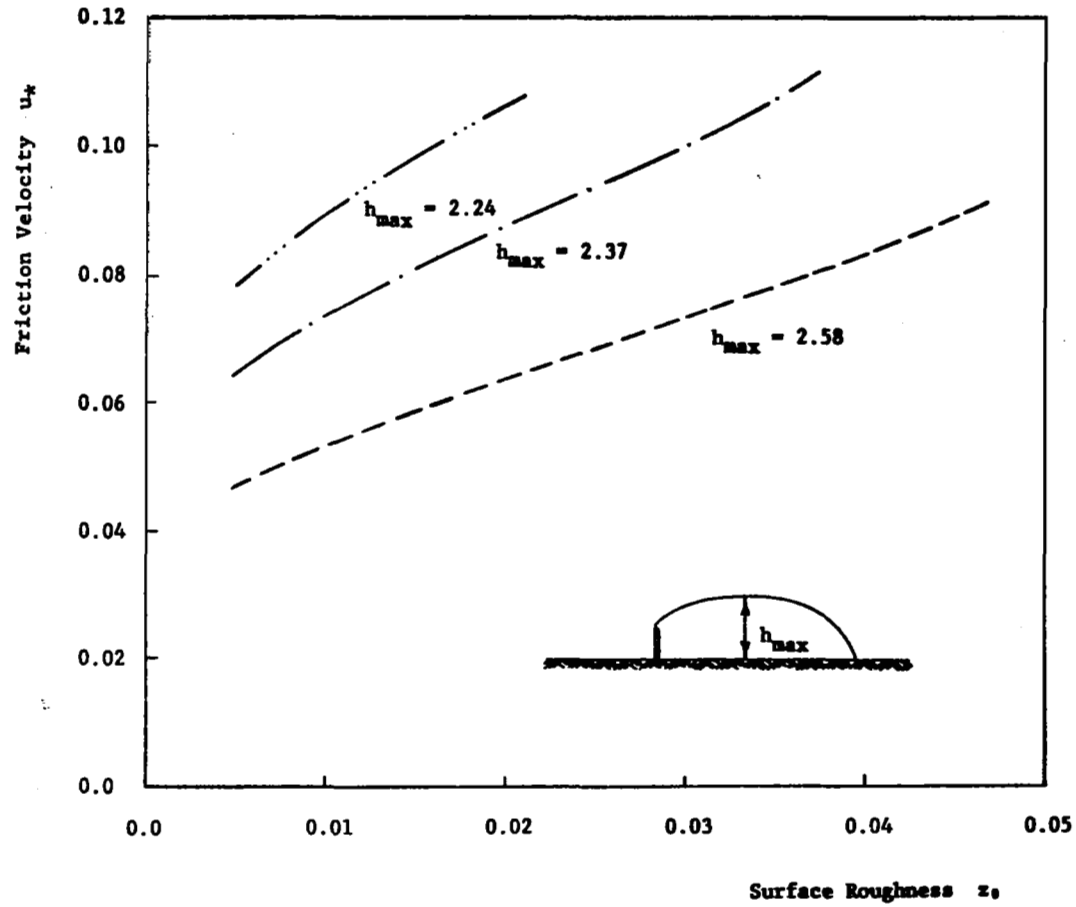


Figure 2.12. Maximum height of recirculation region in dependence of the parameters of the approaching wind.

Figure 2.13 shows the predicted velocity increase due to the presence of the obstruction calculated at an  $x$ -station of six obstacle heights downstream.  $U_{NF}$  represents the velocity profile which would exist at this particular location in the absence of the obstruction, i.e., the approach velocity profile as defined by Equation 2.1. The profiles for the velocity increase are given for various base pressure coefficients, which can be related to the atmospheric conditions with Equations 2.65 through 2.69.

In conclusion it can be said that this rotational inviscid model for the flow over a fence, featuring an upstream corner eddy and a finite wake region is in good agreement with experimental results in the vicinity of the obstruction. It describes quite realistically the size of the front separation bubble, predicts the pressure distribution along the front side of the fence and determines the downstream separation streamline enclosing the recirculating wake region. Through the simplification to a constant vorticity flow field, however, the far field representation which returns to the assumed linear velocity as  $y \rightarrow \infty$  is, with the exception of the streamline pattern, not realistic. One expects a logarithmic velocity profile in the atmosphere and hence both the upstream velocity profile and the velocity profile at  $y \rightarrow \infty$  should have this logarithmic form. To achieve more realistic far field velocity profiles a boundary layer approach which will give a better approximation to the flow in a turbulent natural atmosphere is

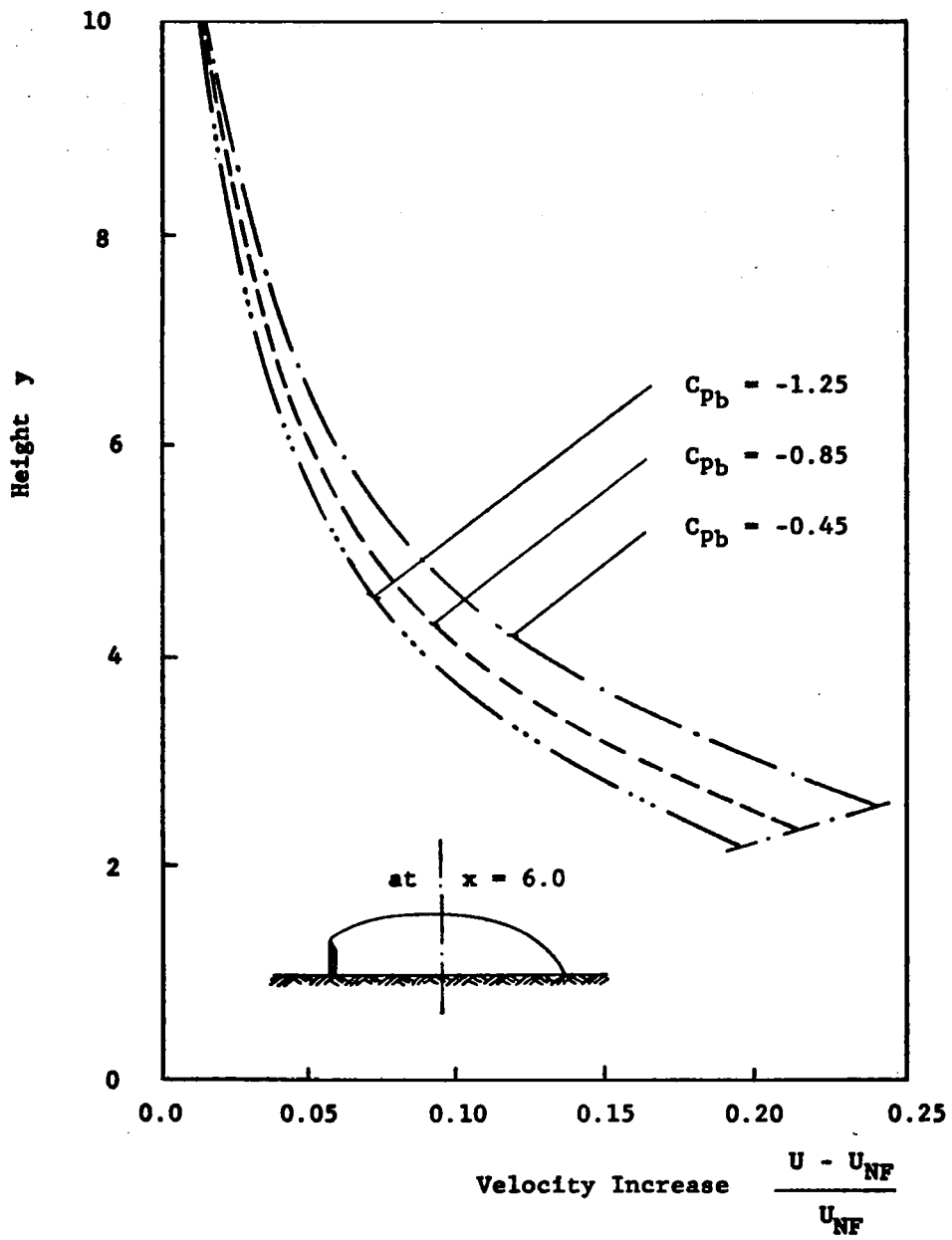


Figure 2.13. Velocity increase due to the presence of the fence.



developed in the following chapter. The results of the preceding analysis, however, become extremely useful in defining the imposed pressure distribution required in boundary layer analysis.

## CHAPTER III

### ANALYSIS OF ATMOSPHERIC FLOW OVER A BLUFF SURFACE OBSTRUCTION BY THE TURBULENT BOUNDARY LAYER APPROACH

To apply the concepts of boundary layer theory to two-dimensional atmospheric flow, consideration is given to a homogeneous terrain of infinite extent on which a bluff surface obstruction or fence of height  $h^*$  is located. The inviscid flow field around such a fence was established in the previous chapter. Far upstream of the obstruction the viscous turbulent atmospheric motion is described by the logarithmic velocity distribution

$$\bar{u}^* = \frac{u_*^*}{\kappa} \ln \left( \frac{z_0^* + z^*}{z_0} \right) \quad (3.1)$$

where  $u_*^*$  is the friction velocity defined in terms of the surface shear stress  $\tau_0^*$

$$u_*^{*2} = \frac{\tau_0^*}{\rho^*} \quad (3.2)$$

and  $\kappa$  the von Karman constant of value 0.35 to 0.4

#### I. GOVERNING EQUATIONS

The governing turbulent mean-flow boundary layer equations for steady flow within the atmospheric boundary

layer as derived in [21] are:

$$\frac{\partial \bar{u}^*}{\partial x^*} + \frac{\partial \bar{w}^*}{\partial z^*} = 0 \quad (3.3)$$

$$\bar{u}^* \frac{\partial \bar{u}^*}{\partial x^*} + \bar{w}^* \frac{\partial \bar{u}^*}{\partial z^*} = -\frac{1}{\rho_0^*} \frac{\partial \bar{p}^*}{\partial x^*} + \frac{\partial}{\partial z^*} \left( (\nu^* + \epsilon^*) \frac{\partial \bar{u}^*}{\partial z^*} \right) \quad (3.4)$$

$$\frac{\partial \bar{p}^*}{\partial z^*} = 0 \quad (3.5)$$

where overbar denotes an ensemble average and  $\rho_0^*$  is a constant density consistent with an adiabatic reference state. The pressure  $\bar{p}^*$  represents the difference between the total pressure and the hydrostatic pressure. It should be recalled that, in addition to the conventional boundary layer approximations, two other assumptions underlie the above equations:

1. The atmosphere is neutrally stable.
2. Coriolis effects are negligible, which is a reasonable assumption for the atmospheric boundary layer below 30 to 50 m, see for example Tverskoj [29].

The eddy viscosity,  $\epsilon^*$ , may be related to the mean flow through the Prandtl mixing length hypothesis in the following way:

$$\epsilon^* = \ell^{*2} \left| \frac{d\bar{u}^*}{dz^*} \right| \quad (3.6)$$

with the mixing length  $\ell^*$  as

$$\ell^* = (z_0^* + z^*)\kappa \quad (3.7)$$

It was already pointed out in Reference [21] that this assumption is not strictly correct in regions of large flow curvature, but it should suffice in view of further assumptions imposed later in this report on the curvature of the flow and the coordinate system used in the investigation.

## II. INCORPORATION OF THE INVISCID SOLUTION

When analyzing conventional boundary layer flow, the pressure gradient in Equation 3.4 is approximated by the pressure variation along the zero streamline determined from the inviscid flow solution for the respective body. This approximation is justified through Equation 3.5. Typical pressure changes for the inviscid flow over a fence are shown in Figure 2.11, page 42. When the pressure gradient along the zero streamline is introduced into the boundary layer equation for the bluff body, however, it may cause flow separation which cannot be handled with the boundary layer approximation. By successively introducing the pressure gradients of streamlines further away from the body, one can find the first streamline for which the corresponding pressure gradient does not yield an upstream separation. This streamline will be called the nonseparating streamline  $\psi_{ns}$ . The pressure gradient along this streamline is assumed to drive the flow in the present problem. This is believed to be a reasonable assumption in view of the fact that the

primary interest of this investigation is directed toward the solution farther away from the obstruction.

Another input from the inviscid solution into conventional boundary layer analysis is that a free-stream velocity at the outer edge of the boundary layer is prescribed. In the present approach however, the internal boundary layer produced by the surface obstruction has to merge with the undisturbed atmospheric boundary layer and its logarithmic velocity profile at a sufficiently high altitude. Letting the pressure gradient decay to zero in the vertical direction merges the velocity profile smoothly with the logarithmic one. Therefore, the form of the pressure distribution introduced into the boundary layer equations in previous approaches [21, 22] was given by

$$\frac{d\bar{p}^*(x^*, z^*)}{dx^*} = \left( \frac{d\bar{p}^*(x^*)}{dx^*} \right)_{\psi_{ns}} \cdot q(z^*) \quad (3.8)$$

where  $q(z^*)$  is the vertical decay function. An initial approximation of this function was given by the following second order quadratic decay function:

$$q(z^*) = \begin{cases} 1 & \text{for } \frac{z^*}{h^*} < 0.5 \\ \left( \frac{0.5}{z^*/h^*} \right)^2 & \text{for } \frac{z^*}{h^*} \geq 0.5 \end{cases} \quad (3.9)$$

In the current investigation this somewhat arbitrary approximation has been replaced by a pressure decay derived

from the inviscid model described in Chapter II. It must be noted, however, that the vertical pressure distribution based on a linear velocity profile will not behave the same in the far field as a logarithmic profile. Therefore, it is assumed that the respective vertical decay functions are proportional to their momentum flux, i.e.,

$$\frac{q(z^*)_{\log}}{U_{\log}^2(z^*)} = \frac{q(z^*)_{\text{lin}}}{U_{\text{lin}}^2(z^*)} \quad (3.10)$$

With the decay of the linear solution given as

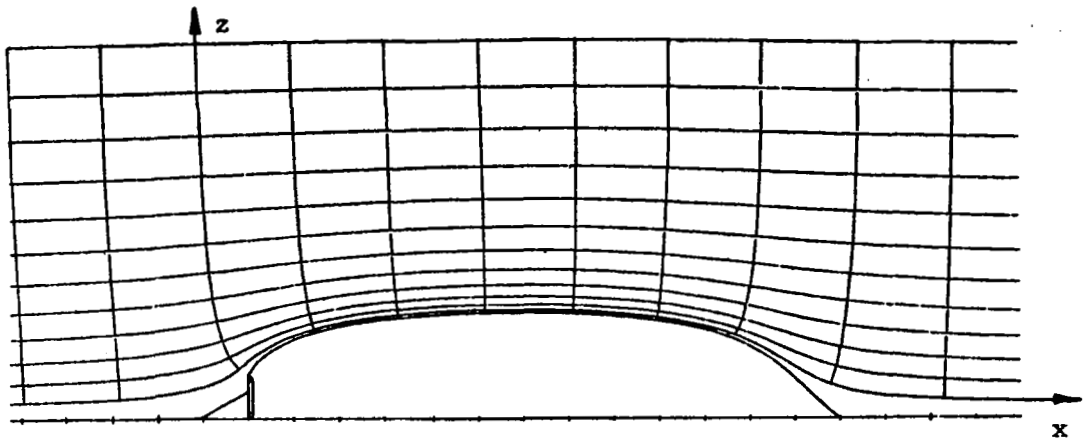
$$q(z^*)_{\text{lin}} = \frac{C_p(z^*) - C_{p_\infty}}{C_p(\psi_{\text{ns}}) - C_{p_\infty}} \quad (3.11)$$

the resulting pressure distribution finally becomes:

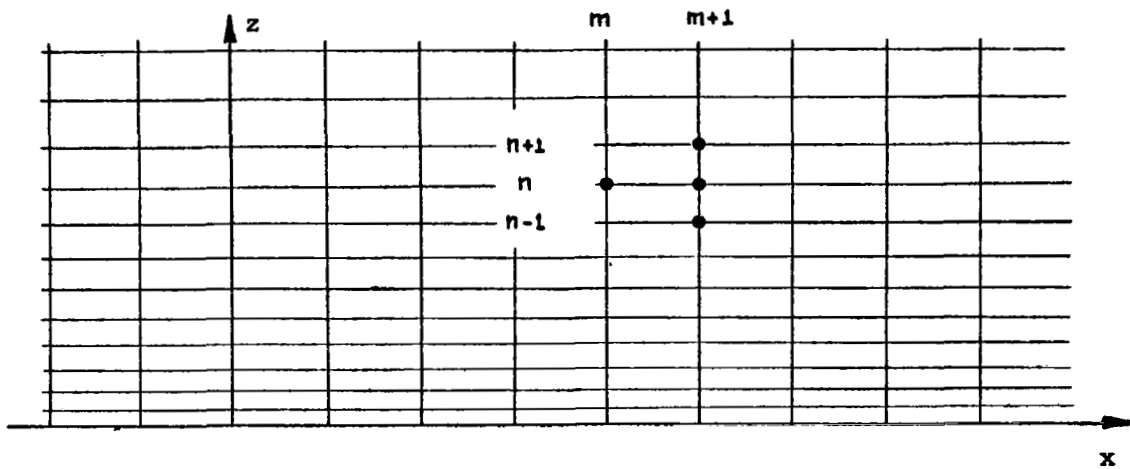
$$\frac{d\bar{p}^*(x^*, z^*)}{dx^*} = \left( \frac{d\bar{p}^*(x^*)}{dx^*} \right)_{\psi_{\text{ns}}} \cdot \frac{C_p(z^*) - C_{p_\infty}}{C_p(\psi_{\text{ns}}) - C_{p_\infty}} \cdot \left( \frac{U_{\log}}{U_{\text{lin}}} \right)^2 \quad (3.12)$$

### III. COORDINATE SYSTEM

Since the pressure force driving the boundary layer flow is determined along the inviscid streamlines over the fence, the coordinate system must also be oriented along these streamlines, resulting in the orthogonal system shown in Figure 3.1a. The curvature of this coordinate system is small throughout the flow regime, except in the vicinity of the upstream stagnation point and the downstream reattachment



(a) Physical Coordinates



(b) Assumed Numerical Coordinates

Figure 3.1. Coordinate system used in boundary layer approach for flow over a fence.

zone, where the slope of the zero streamline is discontinuous. It is argued, however, that at a location somewhat removed from the region of large curvature the flow will be driven by the pressure distribution along the non-separating streamline. This is in agreement with Hunt [30] as described later. Alternately one may look at the approximation as being an analysis of flow over a solid body defined by the nonseparating streamline which envelops the upstream and downstream separation regions. Since the primary interest in the present report is the flow field above the obstruction where aircraft operations occur, the boundary layer approximation as posed here is expected to provide meaningful results. Since the boundary layer concept is generally a first order approximation to viscous flow, neglecting the higher order effects produced by curvature, it is not expected that the present boundary layer analysis will provide accurate results in regions of strong curvature, as for example, in the upstream vicinity of the obstacle. On the other hand, there is little gain in transforming the boundary layer equations into curvi-linear coordinates thereby introducing additional complications. As a consequence the calculations have been carried out in the Cartesian coordinate system  $(x^*, z^*)$  shown in Figure 3.1b. The  $x^*$ -direction is measured along the inviscid streamline with the  $z^*$ -axis extending perpendicular to it at each  $x^*$ -station. The resulting velocity profiles calculated in this coordinate system are then assumed to exist perpendicular to



the zero streamline in the physical plane. This is believed to be a reasonable assumption for the following two reasons: first, the good geometrical agreement of the separation streamline of the inviscid solution with experimental results, as can be seen from Figure 2.8, page 38, and, second, that these geometrical effects of the recirculation region on the flow now enter the equations through the imposed pressure gradient.

Hunt [30] has shown that a first order analysis can be justified if

$$\frac{H^*}{L^*} \ll \frac{\ln(\delta_i^*/z_0^*)}{\ln(L^*/z_0^*)} \quad (3.13)$$

where  $H^*$  and  $L^*$  are the characteristic height and length of the disturbance and  $\delta_i^*$  the thickness of an internal boundary layer calculated from

$$\frac{\delta_i^*}{L^*} \cdot \ln \frac{\delta_i^*}{z_0^*} = 2\kappa^2 \quad (3.14)$$

In the present approach  $H^*$  and  $L^*$  would be chosen as shown in Figure 3.2, with  $H^*$  being the maximum height of the separation region  $h_{\max}^*$  as given in Figure 2.12, page 43, and  $L^*$  being the horizontal length of the combined upstream and downstream separation region, also specified by the inviscid solution. For a typical surface roughness of  $z_0^* = 0.005 h^*$  one would then get from the above condition Equation 3.13 with 3.14:

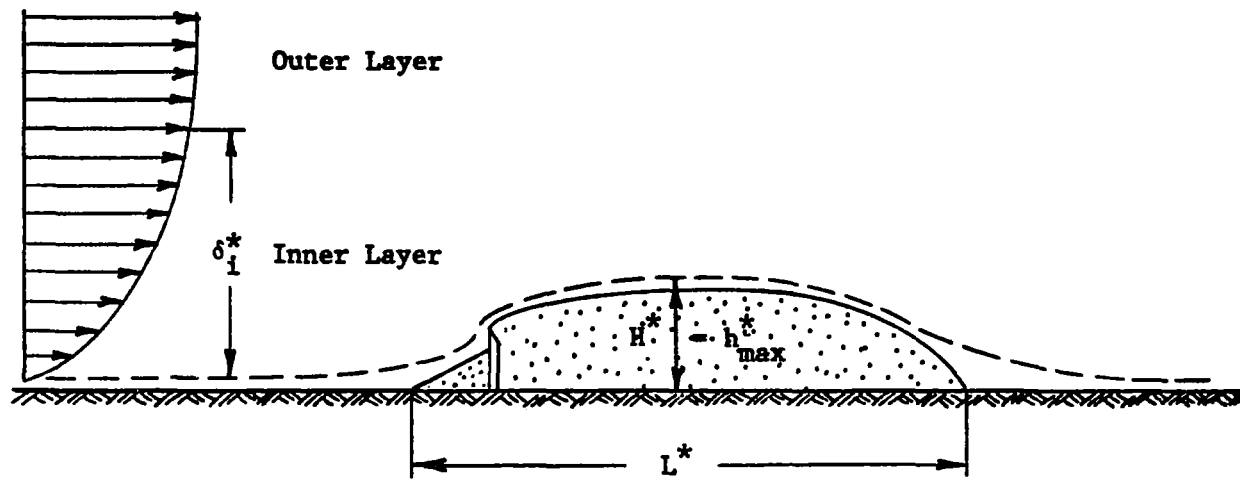


Figure 3.2. Justification of first order analysis after Hunt [30].

$$0.1693 \ll 0.6497$$

$$\text{or for } z_0^* = 0.05 h^*$$

$$0.1693 \ll 0.5858$$

which are reasonably satisfied.

The no-slip condition implied in the boundary layer solution at the lower boundary causes the calculated velocities to vanish along the zero streamline. This becomes physically unrealistic where the zero-streamline separates from the surface to become a free or dividing streamline. Therefore, the following model for calculating velocity profiles through the recirculating wake region behind the fence is proposed in form of an approximate solution using an integral technique under investigation by Kaul and Frost [31]. Figure 3.3 illustrates the flow regions considered and how they are matched with the present boundary layer profile.

A polynomial expression

$$\bar{u}^*(x^*, z^*) = A(x^*) + B(x^*)z^* + C(x^*)z^{*2} + D(x^*)z^{*3} \quad (3.15a)$$

is assumed with the following governing boundary conditions:

$$1. \quad \bar{u}^*(x^*, 0) = 0 \quad \text{at } z^* = z_0^* \quad (3.15b)$$

$$2. \quad \frac{\partial^2 \bar{u}^*}{\partial z^{*2}} = \frac{1}{v^* p_0^*} \frac{\partial p^*}{\partial x^*} \bigg|_{z^*=0} \quad \text{at } z^* = z_0^* \quad (3.15c)$$

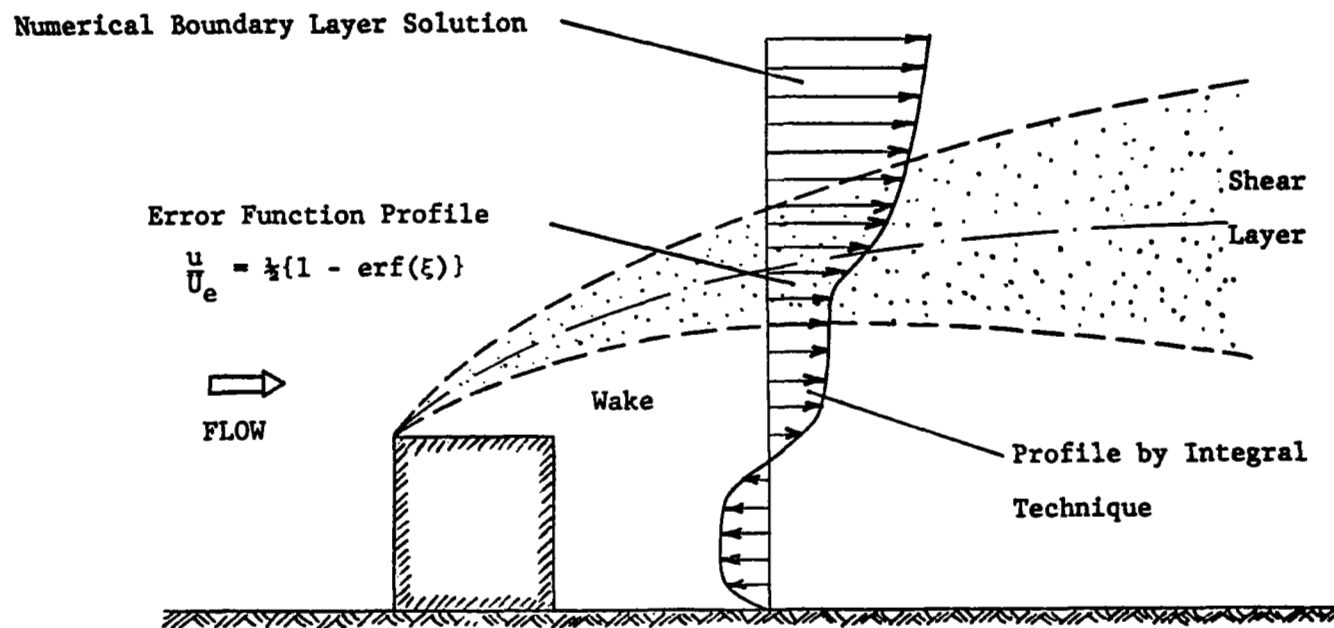


Figure 3.3. Matching of boundary-layer-velocity profile with shear layer- and wake-velocity profile [31].

$$3. \quad \frac{\partial \bar{u}^*}{\partial z^*} = \frac{\partial \bar{u}_{\text{erf}}^*}{\partial z^*} \quad \text{at } z^* = z_1^* \quad (3.15d)$$

$$4. \quad \bar{u}^*(x^*, z_1^*) = \bar{u}_{\text{erf}}^* \quad \text{at } z^* = z_1^* \quad (3.15e)$$

$$5. \quad \int_0^{z_1^*} \bar{u}^*(z^*) dz^* = 0 \quad (3.15f)$$

Thus there are five equations for the five unknowns  $z_1$ ,  $A$ ,  $B$ ,  $C$  and  $D$ . Condition 1 implies the no-slip condition at the wall. Condition 2 assumes that the pressure distribution along the surface is sufficiently well known that an empirical correlation can be found to obtain  $\partial p^*/\partial x^*|_{z^*=0}$ . Conditions 3 and 4 state matching of the shear layer flow, expressed as an error function velocity profile

$$\bar{u}^* = \frac{1}{2} U_e^* [1 - \text{erf}(\xi^*)] \quad (3.16)$$

with the wake flow at the edge of the separated flow. Condition 5 states conservation of mass in the recirculation region, if the zero streamline is assumed to encompass the rear separation bubble.

Further details and results of the incorporation of this wake flow model into the boundary layer approach can be found in Reference [31] and shall therefore not be reported here. The primary interest of this investigation is to study the flow through which landing and ascending aircraft would pass, i.e., the region somewhat above  $\psi_{\text{ns}}$  where the

boundary layer analysis described in the preceding is expected to provide meaningful results.

#### IV. NUMERICAL SOLUTION

The governing equations (3.3 through 3.5) were non-dimensionalized by adopting some characteristic length  $L^*$  and velocity  $U_\infty^*$  from the flow field over the fence. The height,  $h^*$ , of the obstruction was chosen to be the characteristic length for this case. The characteristic velocity is somewhat arbitrary and is assigned a value equal to that of the undisturbed logarithmic velocity profile evaluated at three obstacle heights above the ground. The resulting equations in nondimensionalized form are then given by:

$$\frac{\partial \bar{u}}{\partial x} + \frac{\partial \bar{w}}{\partial z} = 0 \quad (3.17)$$

$$\bar{u} \frac{\partial \bar{u}}{\partial x} + \bar{w} \frac{\partial \bar{u}}{\partial z} = -\frac{\partial \bar{p}}{\partial x} + \frac{1}{Re} \frac{\partial}{\partial z} \left[ (1 + \epsilon) \frac{\partial \bar{u}}{\partial z} \right] \quad (3.18)$$

where

$$x = \frac{x^*}{h^*}; \quad z = \frac{z^*}{h^*} \quad (3.19)$$

$$\bar{u} = \frac{\bar{u}^*}{U_\infty^*}; \quad \bar{w} = \frac{\bar{w}^*}{U_\infty^*} \quad (3.20)$$

$$\bar{p} = \frac{\bar{p}^*}{\rho_0^* U_\infty^{*2}}; \quad \bar{\epsilon} = \frac{\epsilon^*}{\nu^*} \quad (3.21)$$

and  $Re$  denotes the Reynolds number

$$Re = \frac{U_{\infty}^* h^*}{\nu^*} \quad (3.22)$$

Expanding Equation 3.18, the equations to be solved are given by:

$$\frac{\partial \bar{u}}{\partial x} + \frac{\partial \bar{w}}{\partial z} = 0 \quad (3.23)$$

$$\bar{u} \frac{\partial \bar{u}}{\partial x} + \bar{w} \frac{\partial \bar{u}}{\partial z} = -\frac{\partial \bar{p}}{\partial x} + \frac{1}{Re} \left( \frac{\partial^2 \bar{u}}{\partial z^2} (1 + \epsilon) + \frac{\partial \bar{u}}{\partial z} \frac{\partial \epsilon}{\partial z} \right) \quad (3.24)$$

with the eddy viscosity model relating the turbulent motion to the mean flow variables:

$$\epsilon = (z_0 + z)^2 \kappa^2 \left| \frac{d\bar{u}}{dz} \right| \quad (3.25)$$

These three equations together with the boundary and initial conditions form a closed set of nonlinear, parabolic, partial differential equations. They were approximated by an implicit finite difference scheme. After linearization of the inertia terms, the resulting tridiagonal matrix was solved by an elimination routine. A detailed description is given in Frost, et al. [21].

The lower boundary condition imposed a no-slip mean velocity at the wall. In addition surface roughness effects were incorporated into the numerical procedure by applying the logarithmic velocity distribution to the two points closest to the lower boundary, thereby implying a wall layer of height-in-variant shear stress and friction velocity  $u_*$ .

It was assumed that the value of  $u_*$  is given by:

$$u_* = \frac{\kappa \bar{u}(3)}{\ln\left(\frac{3\Delta z + z_0}{z_0}\right)} \quad (3.26)$$

where  $\bar{u}(3)$  is the velocity at the grid point  $z = 3\Delta z$ . The velocity at grid point 2 can be calculated by the logarithmic law as:

$$\bar{u}(2) = \frac{u_*}{\kappa} \ln\left(\frac{2\Delta z + z_0}{z_0}\right) \quad (3.27)$$

and  $\bar{u}(1)$  will remain zero.

The upper boundary condition specifies the velocity to be equal to the initial logarithmic profile at 10 fence heights above the obstruction. Thus the velocity profile, which merges with that of the logarithmic profile due to the decaying pressure gradient, is matched with the undisturbed flow at the outer boundary.

The velocity  $\bar{w}$  in the vertical direction was obtained by integrating the continuity equation (3.23) using the above calculated velocity profile of  $\bar{u}$ .

The choice of mesh size for the problem considered was dictated primarily by the truncation error of the difference equations and, in some cases, by the stability criteria. A balance between the accuracy required in the solution and the computing time necessary to meet these conditions had to be achieved. For these reasons plus some numerical experimentation the following mesh sizes were



chosen. A constant grid size in the marching (x) direction of 0.1 the fence height  $h$  and a variable mesh size in the vertical (z) direction incorporated through a parabolic stretching function. Typical grid sizes ranged from 0.01 near the wall to 0.35 of the obstacle height at the upper boundary. Computing times for a  $20.0 \times 10.0$  flow region were approximately four minutes on an IBM-360-65 computer.

## V. RESULTS AND DISCUSSION

Numerical solutions of the turbulent boundary layer equations have been carried out to assess the influence of a number of different parameters on the solution. The following parametric effects are discussed in corresponding order: (1) the influence on the solution of the pressure variations taken along different nonseparating streamlines  $\psi_{ns}$ , (2) the effect of the quadratic pressure decay function as compared to a more natural pressure decay based on the inviscid model of Chapter II, and (3) the change of the resulting flow field due to parametric variation of the approaching logarithmic wind profile.

As to the first effect, calculations using the decay function given in Equation 3.9 were carried out for the three streamlines

$$\psi_{ns} = 0.05; 0.1; 0.2$$

respectively. Their physical location as calculated from the inviscid model and the resulting pressure distribution

can be seen in Figure 2.11, page 42. Only small changes occur in the computed velocity profiles for the different solutions. It should be noted that the profiles presented here and in the following are as obtained in the assumed numerical coordinate system shown earlier in Figure 3.1b, page 52, i.e., the profiles of various x-stations are plotted relative to the same origin ( $\psi_{ns}$ ) and are not shifted according to their actual location in the physical coordinate system. Comparing Figures 3.4 and 3.5 one finds that at the location of maximum velocity overshoot, at  $x = 6.0$  there is only a 1.2% difference in velocity between the  $\psi_{ns} = 0.05$  and the  $\psi_{ns} = 0.2$  solution, with the velocity increasing toward the latter. It is apparent that the solutions are relatively insensitive to the choice of streamline which lends credence to the assumption that the far flow field is driven by the pressure gradient along the first streamline for which separation does not occur.

The effect of the pressure decay based on the inviscid model (Equation 3.12) as compared to the quadratic pressure decay (Equations 3.8 and 3.9) was investigated among others for the  $\psi_{ns} = 0.05$  streamline. The results are shown in Figures 3.5 and 3.6. It can be seen that the quadratic decay function dampens the overshoot and merges the velocity profile somewhat faster into the undisturbed logarithmic profile than the inviscid decay function. The slower decay of the inviscid model seems more realistic as it distributes the disturbance better in the vertical

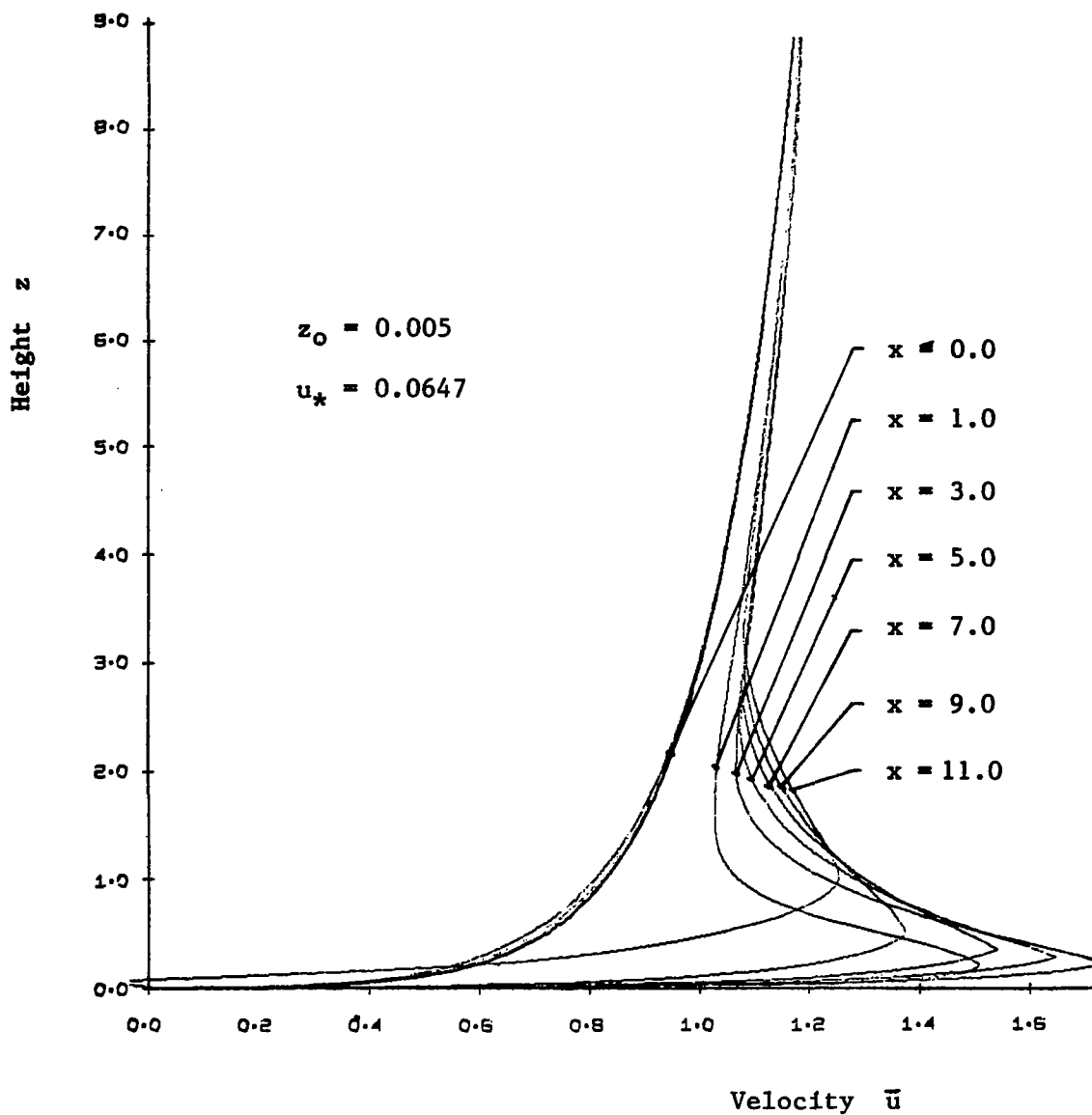


Figure 3.4. Velocity profiles for  $\psi_{ns} = 0.2$  and quadratic pressure decay function.

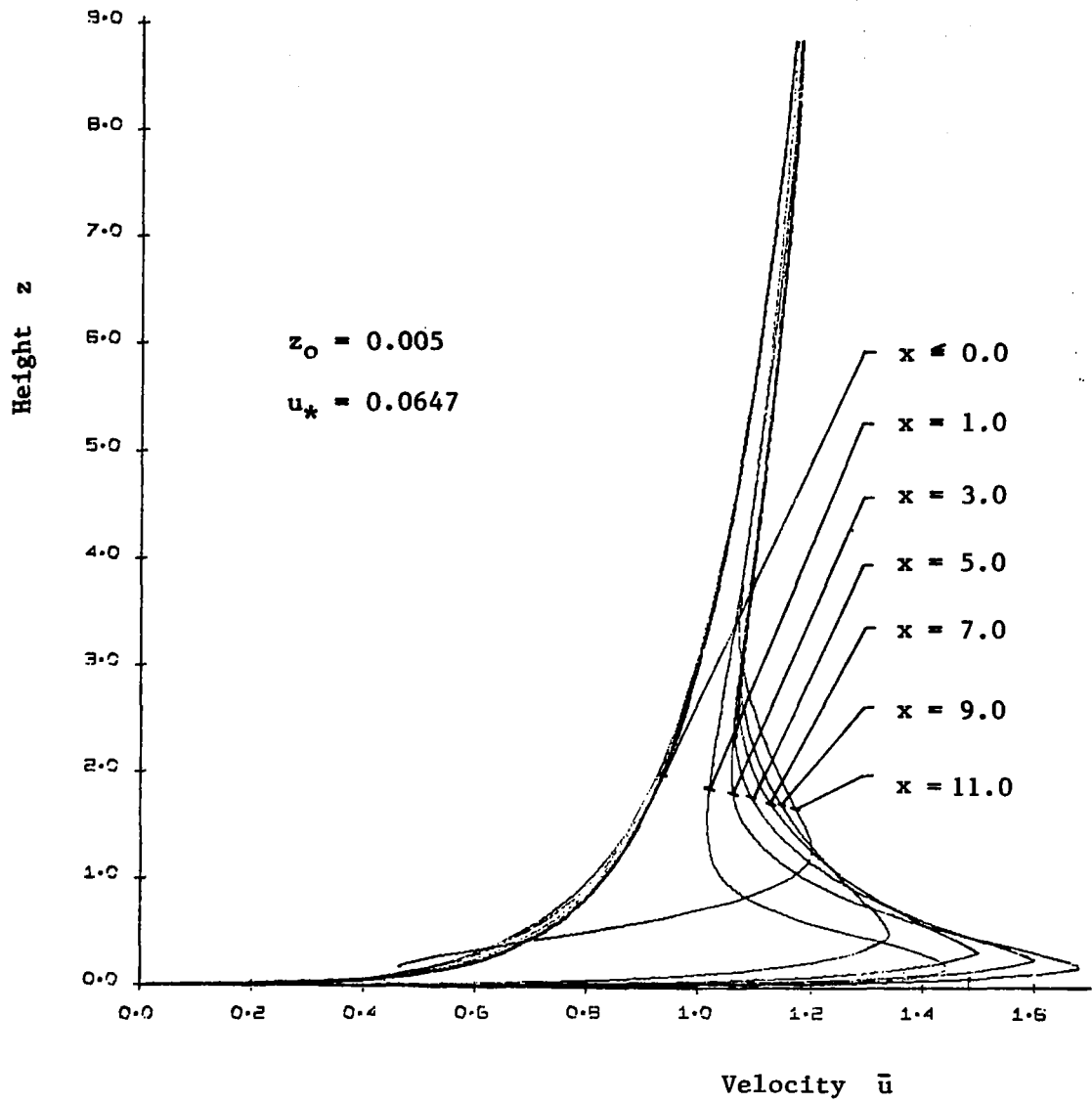


Figure 3.5. Velocity profiles for  $\psi_{ns} = 0.05$  and quadratic pressure decay function.

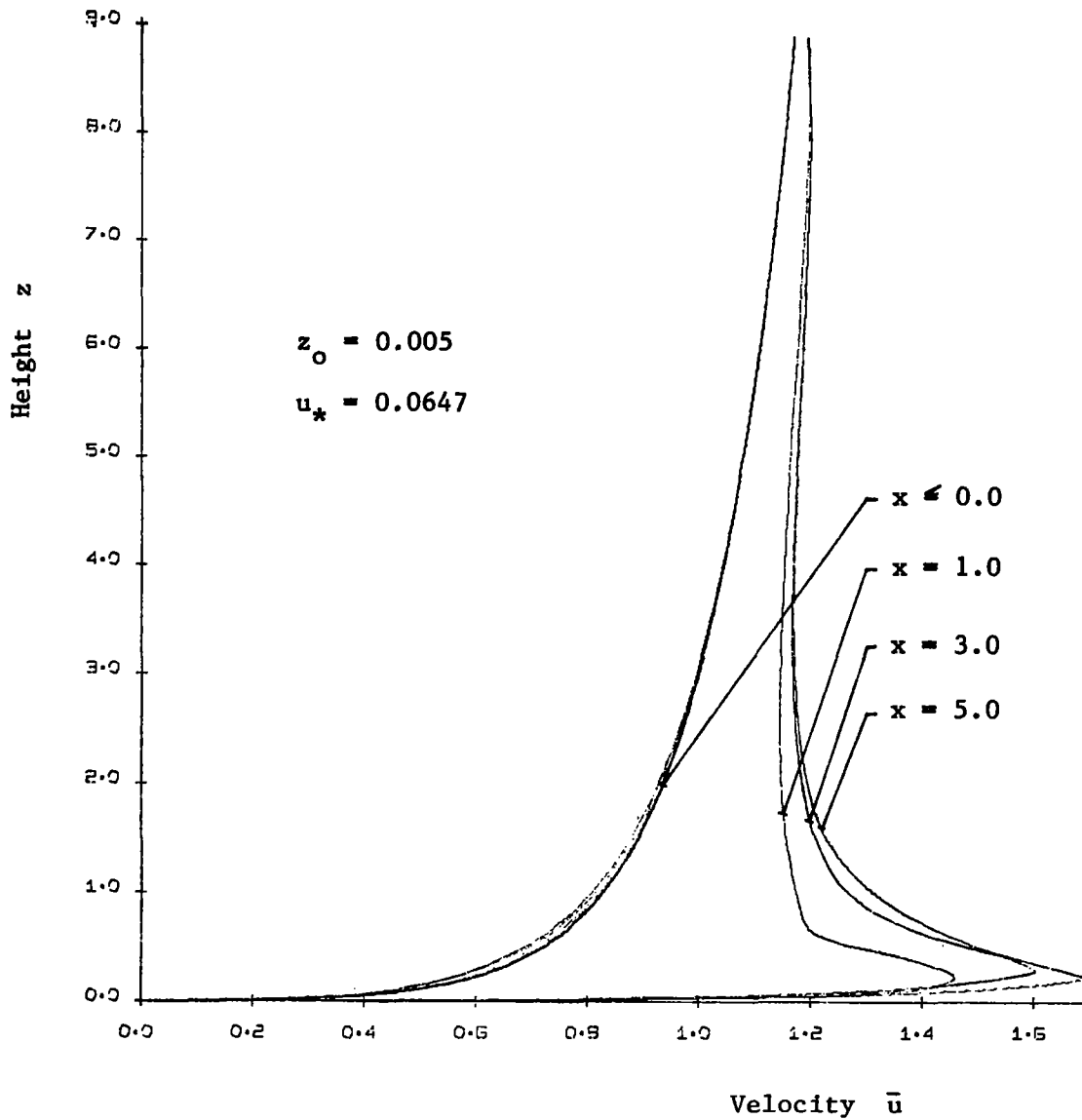


Figure 3.6. Velocity profiles for  $\psi_{ns} = 0.05$  and inviscid pressure decay function.

direction. However, the difference between the two is small and only a comparison with experimental data can show which is the better decay function.

The combinations of parameters investigated in the third group to ascertain the influence of the approaching wind on the solution are tabulated in Table 3.1 and graphically presented in Figure 3.7, which is similar to the previously discussed Figure 2.5, page 33. The respective data points (Cases 1-4) were selected in the following way: four different surface roughness parameters  $z_0$  ranging from  $z_0 = 0.005$  to  $z_0 = 0.05$  were chosen. With Equation 3.26 and the earlier assumption that the reference velocity is that at three obstacle heights above level terrain one can determine the corresponding dimensionless friction velocities  $u_*$  from:

$$u_* = \frac{u_*^*}{U_\infty^*} = \frac{K}{\ln\left(\frac{3.0 + z_0}{z_0}\right)} \quad (3.28)$$

The resulting input parameters  $C_{pb}$  introduced into the inviscid model, determining the respective pressure variation, is then found from Equation 2.65. Table 3.2 gives a complete list of the various empirical input parameters for the inviscid model and the corresponding calculation parameters. It should be noted, that  $y_m$ ,  $C_{p_{max}}$  and  $x_R$  were kept constant in all four cases. The final results are given in Figures 3.8 through 3.11. Comparing the various

TABLE 3.1  
PARAMETERS FOR THE DIFFERENT DATA POINTS INVESTIGATED

Case	$z_0$	$u_*$	$C_{pb}$
Boundary Layer Approach			
1	0.005	0.0625	-0.7920
2	0.010	0.0700	-0.7693
3	0.020	0.0792	-0.6978
4	0.050	0.0973	-0.4805
Inviscid Test Case			
Set 2	0.005	0.0647	-0.8500

Equation 3.28:

$$\left( \frac{u_*^*}{U_{ref}^*} \right) = \frac{0.4}{\ln \left( \frac{3.0 + z_0}{z_0} \right)}$$

Equation 2.65:

$$C_{pb} = - \left( \frac{u_*^*}{U_{ref}^*} \right)^2 \left( 152 \log \left( \frac{1}{z_0} \right) - 147 \right)$$

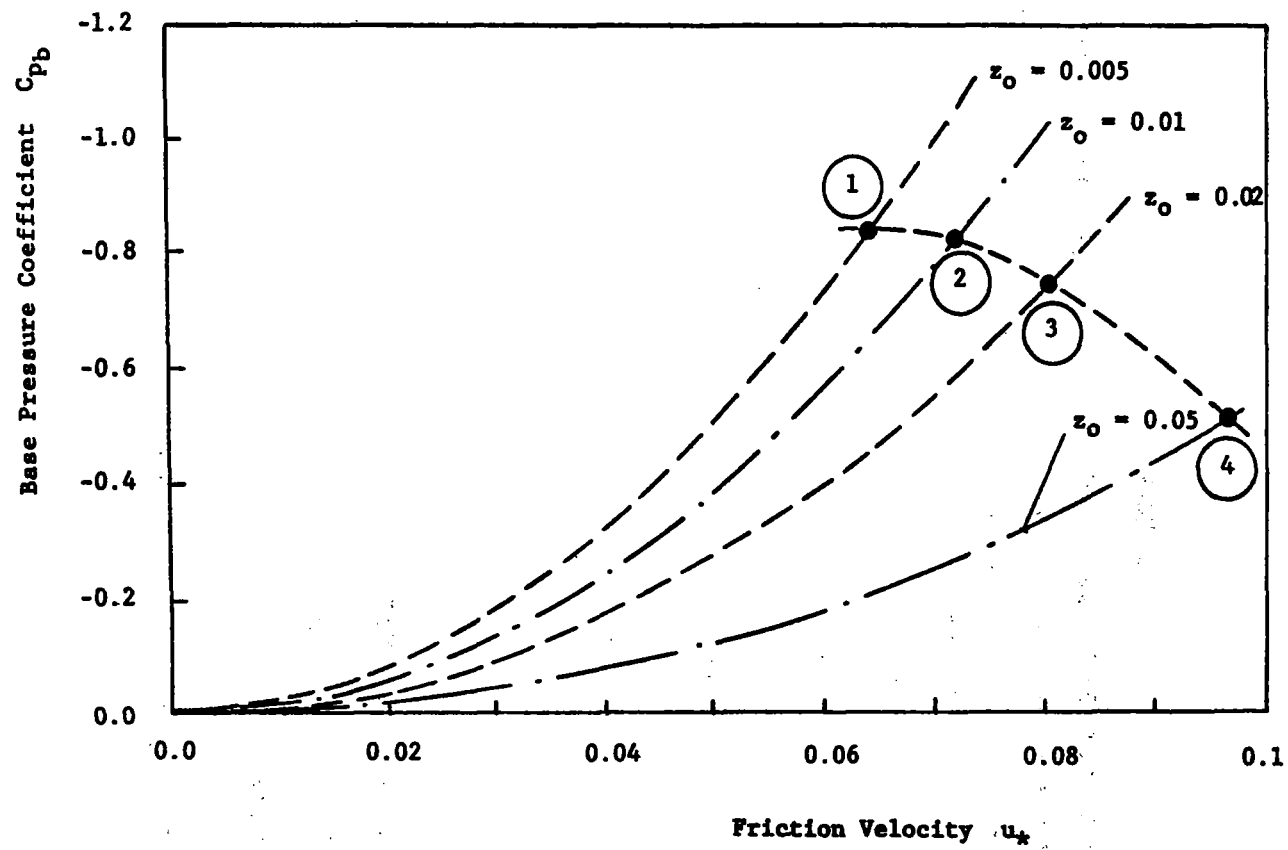


Figure 3.7. Graphical representation of investigated data points.



TABLE 3.2

EMPIRICAL INPUT AND RESULTING CALCULATION PARAMETERS FOR  
RESPECTIVE DATA POINTS

Case	$C_{pb}$	$U_0$	$\cosh \beta$	$\cosh \delta$	$k$
1	-0.7920	0.70711	1.3348	10.705	1.00830
2	-0.7693	0.70711	1.3436	10.697	1.00170
3	-0.6978	0.70711	1.3733	10.669	0.98091
4	-0.4805	0.70711	1.4827	10.566	0.91163

$$y_{\max} = 0.6, C_{p\max} = 0.5, x_R = 13.0$$

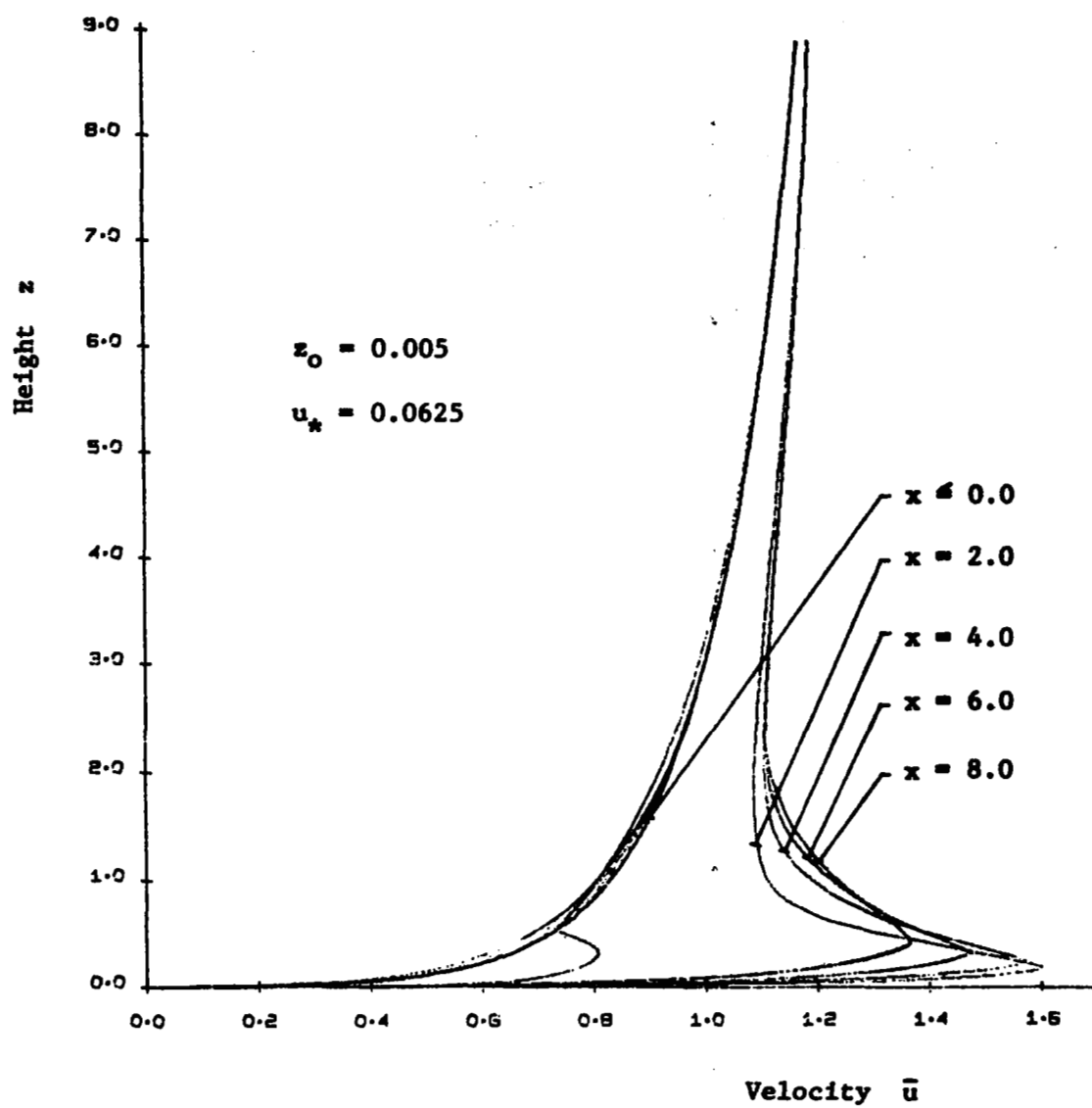


Figure 3.8. Velocity profiles for case 1.

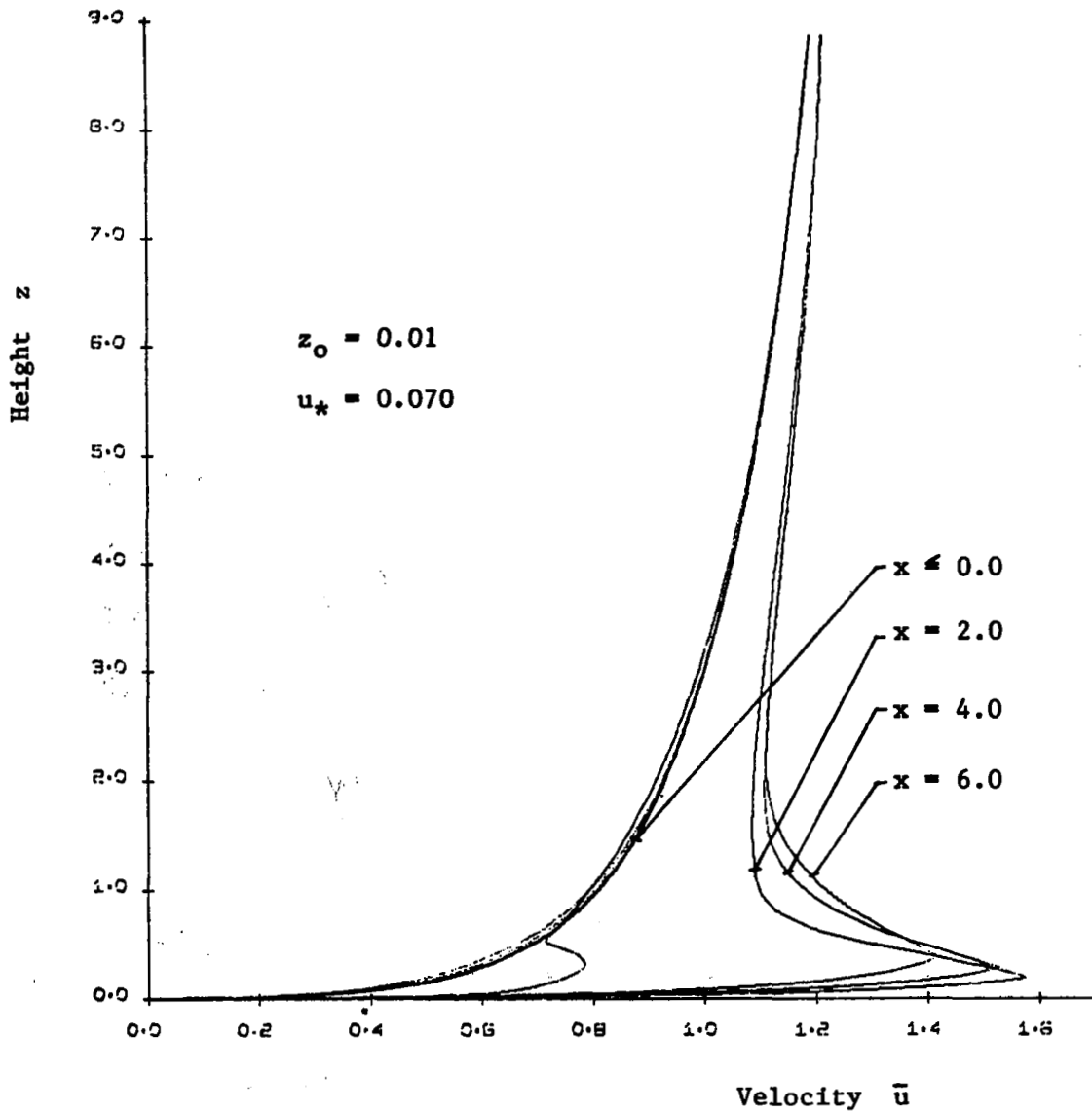


Figure 3.9. Velocity profiles for case 2.

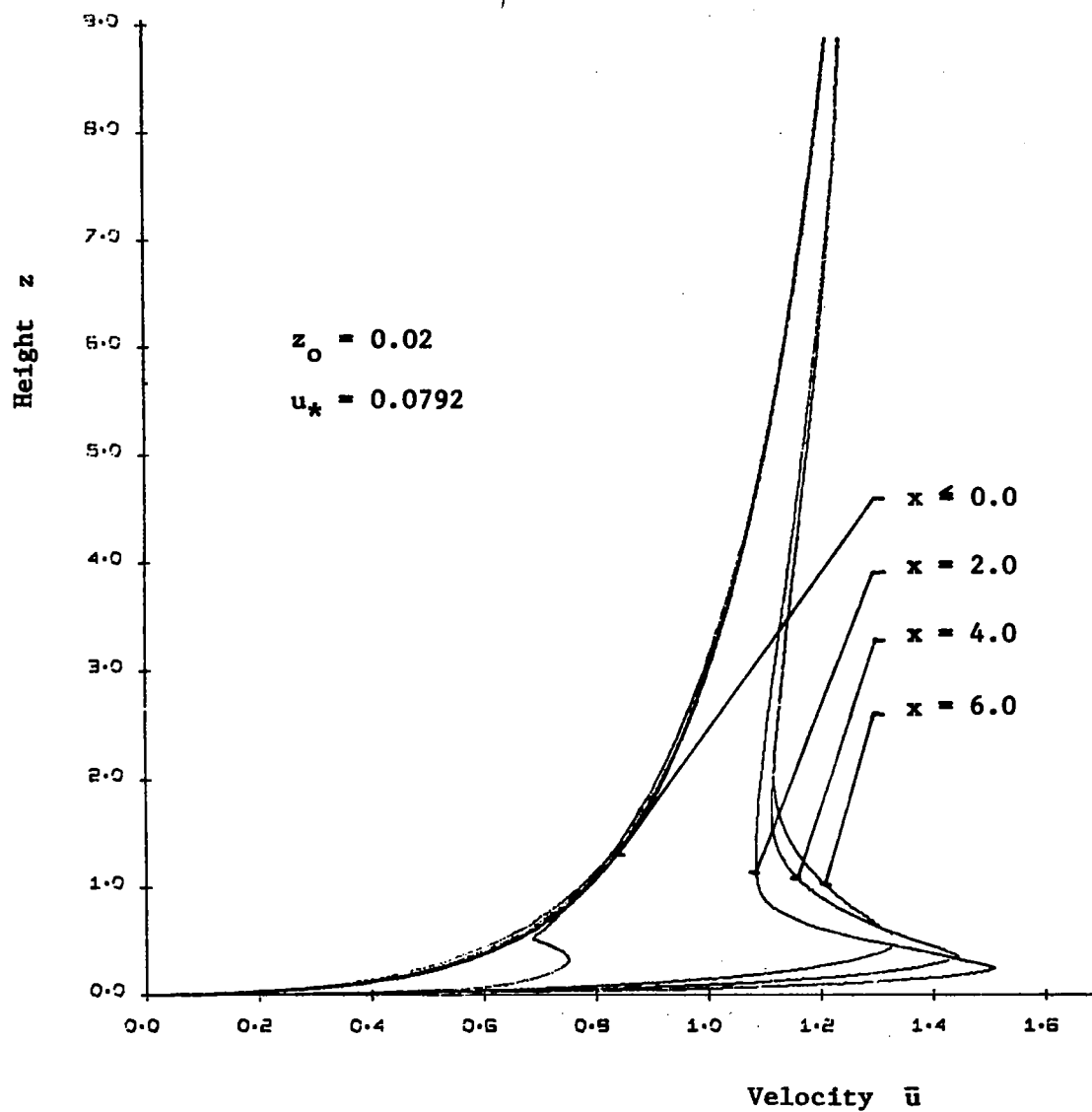


Figure 3.10. Velocity profiles for case 3.

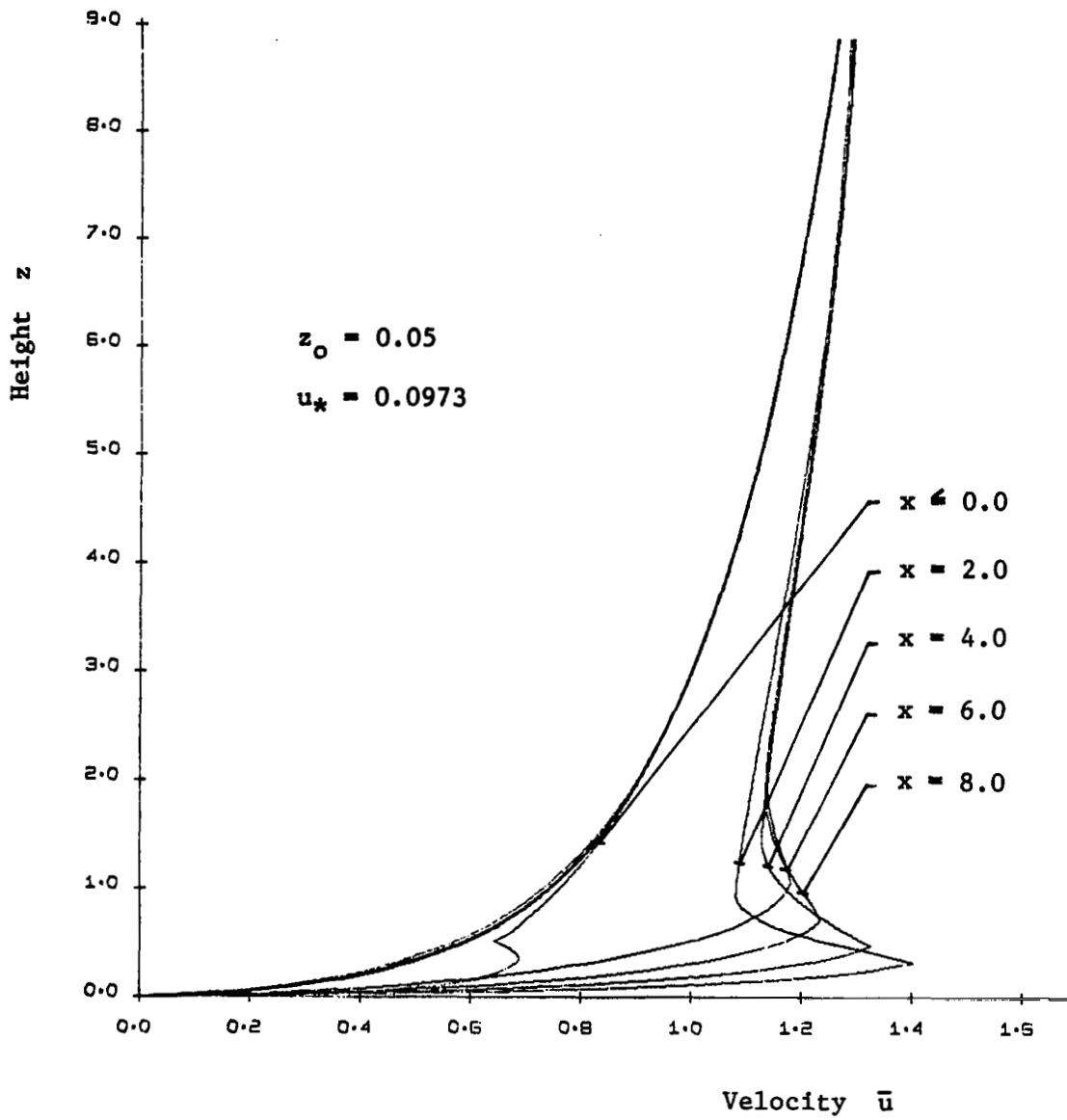


Figure 3.11. Velocity profiles for case 4.

velocity profiles for the two extreme cases 1 and 4, one finds that for increasing surface roughness  $z_0$  and friction velocity  $u_*$  there is a decrease of velocity overshoot of about 7% at almost all  $x$ -stations over the recirculation region downstream of the obstruction. Whereas the roughness effect, i.e., decreasing velocity for increasing roughness is dominant in the inner flow region, the influence of the friction velocity, i.e., increasing velocity for increasing  $u_*$  dominates in the outer flow field. This tendency appears realistic as the fuller approach velocity profile with smaller  $z_0$ , which carries more mass and higher momentum near the wall can be expected to have the larger overshoot.

Plotting the profile of the velocity increase due to the presence of the obstacle near the highest point of the recirculating region, i.e., at  $x \approx 6.0$  shown in Figure 3.12 one observes the same trend: Case 1, with the fattest initial profile due to its lowest surface roughness, shows the largest velocity increase.

This suggests that a high rise building, for example, located in a downtown area of large buildings, i.e., high surface roughness, will not experience as significant an overshoot as the same building in a resort or residential area surrounded by natural terrain or small houses having low surface roughness.

With regard to the overshoot in the velocity profiles, one would generally expect it to be somewhat smaller in magnitude and to be distributed over a wider vertical

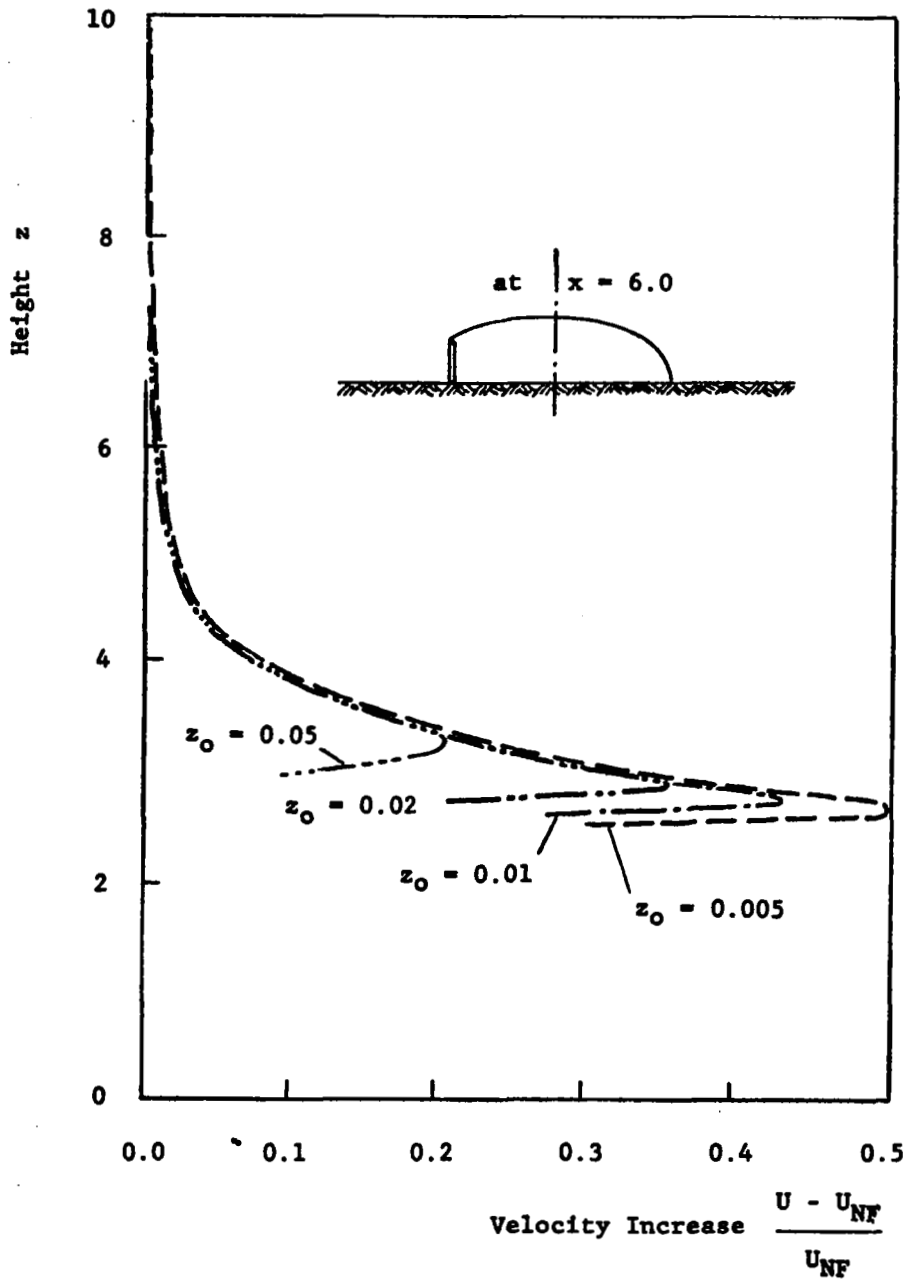


Figure 3.12. Velocity increase due to the presence of the fence for various upstream conditions.

range, as the full scale experimental data of Frost, et al. [32] and partially the wind tunnel data of Good and Joubert [27] indicate. A comparison with these experiments is given in Figures 3.13 and 3.14. It should be pointed out that the former tests were conducted for a rectangular block building, whereas, the latter were for a fence. In order to make the respective velocity distributions independent of the specific parameters of the approach velocity and to facilitate a comparison, all profiles are referenced to their undisturbed upstream profile. In Figure 3.13 the boundary layer profiles of the previous Figure 3.5 (quadratic decay), page 65, and Figure 3.6 (inviscid decay), page 66, are plotted together with a typical profile obtained by Reference [32] in an atmospheric boundary layer flowing over a block building. The horizontal location of these profiles is one obstacle height downstream of the obstruction face. The stronger and more confined overshoot region predicted by the boundary layer model probably results from the fact that the wake is treated as a solid body. Because it is intended to match the present boundary layer model with the proposed integral technique for the recirculation region later, this was believed to be a reasonable temporary assumption. It implied, however, that not only the velocity decays to zero but also that the mixing length reduces to  $l = \kappa \cdot z_0$  along the separating streamline, leading to a relatively small eddy viscosity and low shear in this region, not at all representing the highly turbulent free shear



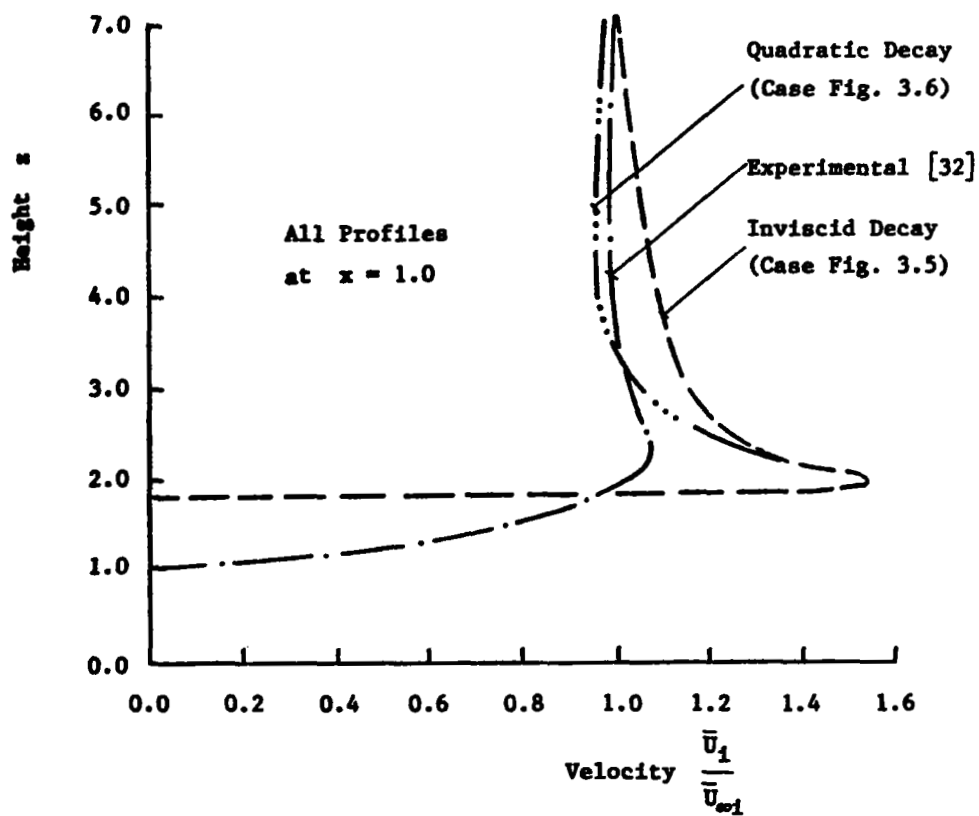


Figure 3.13. Comparison of velocity profiles at  $x = 1.0$  obtained from boundary layer model and full scale experiments [32].

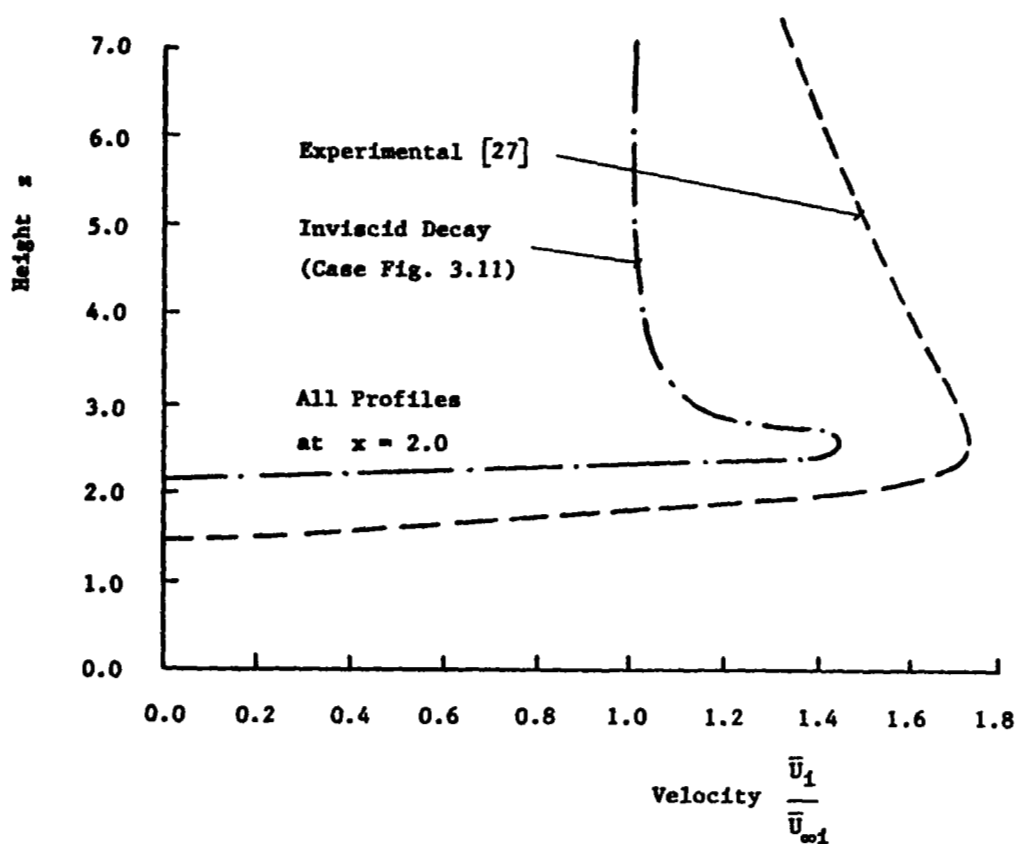


Figure 3.14. Comparison of velocity profiles at  $x = 2.0$  obtained from boundary layer model and wind tunnel experiments [27].

layer. The result is the larger virtually laminar overshoot in the vicinity of the separating streamline. High shear would not only reduce the overshoot in magnitude but also spread it out further in the vertical direction. The mass and momentum diffusion from the shear layer along the separating streamline into the recirculation region cannot be taken adequately into account through the solid surface assumption and thus lead to the increased overshoot.

On the other hand, comparison with the small scale tests of [27] in Figure 3.14 shows a measured overshoot which is even larger than that predicted by the theoretical model, however, less rapidly decaying in the vertical direction.

It should be noted here that the two experiments differ in an important parameter. While the first tests [32] were conducted in an atmospheric boundary layer where the ratio of obstacle height  $h^*$  to boundary layer thickness  $\delta^*$  is very small, i.e.,

$$\frac{h^*}{\delta^*} \ll 1$$

the latter tests were conducted in a smooth flat plate type boundary layer with

$$\frac{h^*}{\delta^*} \approx 2.5$$

and hence should, because of the increased mass displacement near the obstruction, produce a larger overshoot. Taking

this into consideration, the predicted velocity profiles for atmospheric flows should tend towards the first experiments. If, in addition, it is realized that these tests are not strictly two-dimensional because of the finite width of the block building, but have three-dimensional character allowing flow around the sides, thereby diminishing the overshoot over the top of the building, the comparison with the calculated velocity profiles may look more reasonable.

Concluding this chapter, one might say that because of the solid body wake assumption and the related simplifications, e.g., in the mixing length prescription, the boundary layer analysis yields results which show overshoot regions in the velocity profiles that are somewhat higher than expected. As there are not sufficient experimental data available for direct comparison, only qualitative conclusions can be drawn, following the trends pointed out in the foregoing discussion.

## CHAPTER IV

### ANALYSIS OF ATMOSPHERIC FLOW OVER A BLUFF SURFACE OBSTRUCTION BY THE TURBULENT NAVIER-STOKES EQUATIONS

The complete two-dimensional equations of motion are applied to an atmospheric flow over a forward facing step, as shown in Figure 4.1. Analogous to the previous approach the atmospheric motion far upstream of the obstruction is described by the logarithmic profile given in Equations 3.1 and 3.2. Again the atmosphere is assumed to be neutrally stable and Coriolis effects are assumed negligible due to the small scale of motion under consideration.

#### I. GOVERNING EQUATIONS

With the above assumptions the governing turbulent mean-flow equations for steady incompressible flow can be written as follows.

Momentum equation in  $x^*$ -direction

$$\begin{aligned} \bar{u}^* \frac{\partial \bar{u}^*}{\partial x^*} + \bar{w}^* \frac{\partial \bar{u}^*}{\partial z^*} = & -\frac{1}{\rho_0^*} \frac{\partial \bar{p}^*}{\partial x^*} + \frac{\partial}{\partial x^*} \left[ \frac{\mu_{eff}^*}{\rho_0^*} \left( 2 \frac{\partial \bar{u}^*}{\partial x^*} \right) \right] \\ & + \frac{\partial}{\partial z^*} \left[ \frac{\mu_{eff}^*}{\rho_0^*} \left( \frac{\partial \bar{u}^*}{\partial z^*} + \frac{\partial \bar{w}^*}{\partial x^*} \right) \right] \end{aligned} \quad (4.1)$$

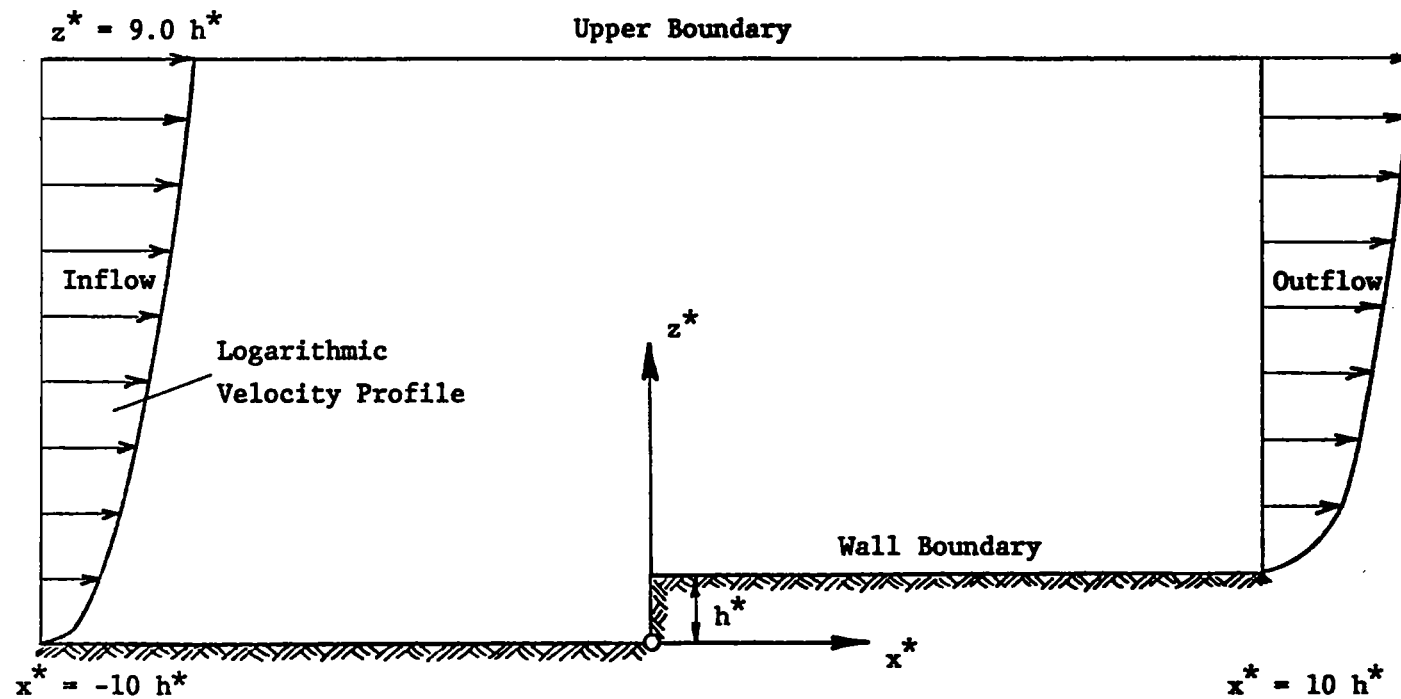


Figure 4.1. Description of flow region considered.

momentum equation in  $z^*$ -direction

$$\begin{aligned} \bar{u}^* \frac{\partial \bar{w}^*}{\partial x^*} + \bar{w}^* \frac{\partial \bar{w}^*}{\partial z^*} = & -\frac{1}{\rho_0^*} \frac{\partial \bar{p}^*}{\partial z^*} + \frac{\partial}{\partial z^*} \left( \frac{\mu_{\text{eff}}^*}{\rho_0^*} \left( 2 \frac{\partial \bar{w}^*}{\partial z^*} \right) \right) \\ & + \frac{\partial}{\partial x^*} \left( \frac{\mu_{\text{eff}}^*}{\rho_0^*} \left( \frac{\partial \bar{u}^*}{\partial z^*} + \frac{\partial \bar{w}^*}{\partial x^*} \right) \right) \end{aligned} \quad (4.2)$$

and the continuity equation

$$\frac{\partial \bar{u}^*}{\partial x^*} + \frac{\partial \bar{w}^*}{\partial z^*} = 0 \quad (4.3)$$

where overbars again denote the ensemble average. Analogous to the turbulent boundary layer concept, turbulence is incorporated through an "effective viscosity"

$$\mu_{\text{eff}}^* = \mu^* + \mu_t^* \quad (4.4)$$

which is composed of the molecular viscosity  $\mu^*$  and a turbulent viscosity  $\mu_t^*$ . Unlike  $\mu^*$ , the turbulent viscosity  $\mu_t^*$  is not a property of the fluid. Its value will vary from point to point in the flow, being largely determined by the structure of the turbulence at the respective location. Several methods, discussed in detail in the next paragraph, are used to express the turbulent viscosity in terms of known or calculable flow quantities. To eliminate the pressure from the governing equations (4.1 and 4.2) the stream function  $\psi^*$  is introduced

$$\bar{u}^* = \frac{1}{\rho^*} \frac{\partial \psi^*}{\partial z^*} \quad (4.5)$$

$$\bar{w}^* = -\frac{1}{\rho^*} \frac{\partial \psi^*}{\partial x^*} \quad (4.6)$$

together with the vorticity  $\omega^*$

$$\omega^* = \frac{\partial \bar{w}^*}{\partial x^*} - \frac{\partial \bar{u}^*}{\partial z^*} \quad (4.7)$$

Differentiating the  $x^*$ -momentum equation with respect to  $z^*$ , the  $z^*$ -momentum equation with respect to  $x^*$  and subtracting one from the other, one obtains after some rearrangements

$$\begin{aligned} \frac{\partial}{\partial x^*} \left( \omega^* \frac{\partial \psi^*}{\partial z^*} \right) - \frac{\partial}{\partial z^*} \left( \omega^* \frac{\partial \psi^*}{\partial x^*} \right) - \frac{\partial^2}{\partial x^{*2}} (\mu_{\text{eff}}^* \omega^*) \\ - \frac{\partial^2}{\partial z^{*2}} (\mu_{\text{eff}}^* \omega^*) - S_{\omega}^* = 0 \end{aligned} \quad (4.8)$$

where

$$\begin{aligned} S_{\omega}^* = 2 \left[ -\frac{\partial}{\partial x^* \partial z^*} \left( \mu_{\text{eff}}^* \left( \frac{\partial \bar{u}^*}{\partial x^*} - \frac{\partial \bar{w}^*}{\partial z^*} \right) \right) + \frac{\partial^2}{\partial x^{*2}} \left( \mu_{\text{eff}}^* \frac{\partial \bar{u}^*}{\partial z^*} \right) \right. \\ \left. - \frac{\partial^2}{\partial z^{*2}} \left( \mu_{\text{eff}}^* \frac{\partial \bar{w}^*}{\partial x^*} \right) \right] \end{aligned} \quad (4.9)$$

Equation 4.8 is generally known as the vorticity transport equation. It reduces the two momentum equations (4.1 and 4.2) in the three variables  $\bar{u}^*$ ,  $\bar{w}^*$ ,  $\bar{p}^*$ , to one equation in the two variables  $\omega^*$  and  $\psi^*$ .

A second equation can be derived from Equation 4.7 with Equation 4.6

$$\nabla^2 \psi^* = -\rho^* \omega^* \quad (4.10)$$



known as the stream function equation. Gosman, et al. [20] have shown that these new governing equations (4.8 and 4.10) can be expressed in the common form of an elliptical partial differential equation, suitable for simultaneous numerical integration, i.e.,

$$a \left[ \frac{\partial}{\partial x^*} \left( \phi \frac{\partial \psi^*}{\partial z^*} \right) - \frac{\partial}{\partial z^*} \left( \phi \frac{\partial \psi^*}{\partial x^*} \right) \right] - \frac{\partial}{\partial x^*} \left( b \frac{\partial}{\partial x^*} [c\phi] \right) - \frac{\partial}{\partial z^*} \left( b \frac{\partial}{\partial z^*} [c\phi] \right) + d = 0 \quad (4.11)$$

Here  $\phi$  is the respective dependent variable  $\psi^*$  or  $\omega^*$  and  $a$ ,  $b$ ,  $c$  and  $d$  are functions depending on the variable under consideration.

After rearranging some terms, Equation 4.11 can be rewritten, using tensor notation, as

$$a\rho^*\bar{u}_i^* \frac{\partial \phi}{\partial x_i^*} = \frac{\partial}{\partial x_j^*} \left( b \frac{\partial}{\partial x_j^*} (c\phi) \right) - d \quad (4.12)$$

Table 4.1 lists what the functions "a" through "d" must be.

TABLE 4.1  
COEFFICIENT FUNCTIONS OF EQUATION 4.11 OR 4.12

$\phi$	a	b	c	d
$\omega^*$	1	1	$\mu_{eff}^*$	$-S_{\omega}^*$
$\psi^*$	0	$1/\rho^*$	1	$-\omega^*$

Gosman, et al. [20] developed an algorithm for solving Equation 4.11 which is used in this study.

## II. TURBULENCE MODELS

Following the turbulent viscosity concept, there remains the task of formulating  $\mu_t^*$ , that is relating it to some known quantities of the mean flow. These resulting auxiliary relationships can either be simple algebraic expressions or more sophisticated differential equations. Together with the governing equations (4.8 and 4.10) and appropriate boundary conditions they form a closed set of equations describing the flow for the problem of interest.

### Mixing Length Model

Among the models which employ algebraic relations for  $\mu_t^*$  is Prandtl's mixing-length hypothesis (PML), already known from the boundary layer approach. The hypothesis is that the turbulent viscosity is equal to the local product of the density, the magnitude of the mean rate of strain and the square of a characteristic length scale of the turbulent motion, i.e., the mixing length  $\ell^*$ .

$$\mu_t^* = \rho^* \ell^{*2} \left[ \left( \frac{\partial \bar{u}^*}{\partial z^*} \right)^2 + \left( \frac{\partial \bar{w}^*}{\partial x^*} \right)^2 \right]^{1/2} \quad (4.13)$$

The mixing length must be prescribed algebraically for the whole flow field. In the present investigation its distribution is made dependent on the shortest distance from the

wall as indicated in Figure 4.2.

$$\ell^*(x^*, z^*) = \begin{cases} \kappa(z^* + z_0^*) & \text{for } x^* < 0; \\ & z^* < |x^*| \\ \kappa(|x^*| + z_0^*) & \text{for } x^* < 0; \\ & |x^*| \leq z^* \leq |x^*| + h^* \\ \kappa(z^* - h^* + z_0^*) & \text{for all } x^*; \\ & z^* > |x^*| \end{cases} \quad (4.14)$$

### Turbulence Kinetic Energy Model

We now turn to a model of turbulence where the determination of  $\mu_t^*$  requires the solution of a differential equation for one property of turbulence. The model was first suggested by Kolmogorov [33] and Prandtl [34] and differs from the previous mixing length model by the assumption that  $\mu_t^*$  is dependent on the level of turbulence of the fluid and a length scale. The level of turbulence is characterized by the mean kinetic energy of the velocity fluctuations, defined as

$$k^* = \frac{1}{2}(\overline{u^{*'^2}} + \overline{v^{*'^2}} + \overline{w^{*'^2}}) \quad (4.15)$$

where  $u^{*'} , v^{*'} , w^{*'}$  are the fluctuating parts of the velocity components. The quantity  $k^*$  is called the turbulence kinetic energy (TKE). It is related to the effective viscosity by

$$\mu_{\text{eff}}^* = \rho^* \cdot k^{*1/2} \cdot \ell^* \cdot C_\mu \quad (4.16)$$

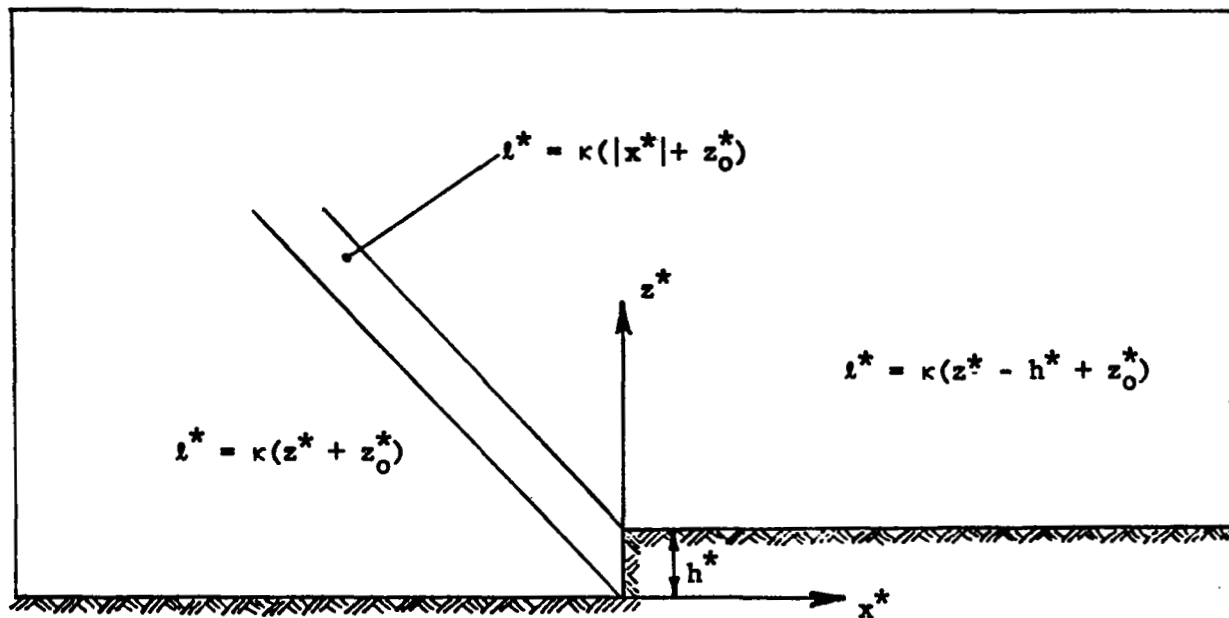


Figure 4.2. Assumed mixing length distribution.

where  $C_\mu$  is an empirical constant or function to be discussed later.  $k^*$  is determined from a differential equation of the same form as Equation 4.12, containing convection, diffusion and source terms. It may be shown after some lengthy algebra that such an equation can be derived from Equations 4.1 through 4.3. For a detailed derivation see Wolfshtein [35]. This transport equation for the turbulence kinetic energy is

$$\rho^* \bar{u}_j^* \frac{\partial k^*}{\partial x_j^*} = \frac{\partial}{\partial x_j^*} \left( \Gamma_{k,eff}^* \frac{\partial k^*}{\partial x_j^*} \right) + S_k^* \quad (4.17)$$

where  $\Gamma_{k,eff}^*$  is an exchange coefficient for the turbulence kinetic energy defined in terms of a Schmidt number based on the effective viscosity

$$\Gamma_{k,eff}^* = \frac{\mu_{eff}^*}{\sigma_{k,eff}} \quad (4.18)$$

The last term in Equation 4.17 represents "sources" and "sinks" of turbulence; it consists basically of two parts, one accounting for the rate of generation of turbulent kinetic energy by the turbulent shear stress and another representing the energy dissipation by viscous action, deducible from dimensional analysis

$$S_k^* = \mu_t^* \left( \frac{\partial \bar{u}_i^*}{\partial x_j^*} + \frac{\partial \bar{u}_j^*}{\partial x_i^*} \right) \frac{\partial \bar{u}_i^*}{\partial x_j^*} - C_D \rho^* \frac{k^{*3/2}}{\ell^*} \quad (4.19)$$

$C_D$  is another function to be determined empirically.

In this model the length scale  $\ell^*$  is still prescribed algebraically and is assumed to be equal to the mixing length distribution of Equation 4.14.

The determination of the functions  $C_\mu$  and  $C_D$  still poses some problems especially in cases where there are no experimental results available. In terms of a turbulent Reynolds number

$$R_t = \frac{\rho^* \cdot k^{*1/2} \cdot \ell^*}{\mu^*} \quad (4.20)$$

one can express the functions as

$$\begin{aligned} C_\mu &= C_{\mu 0} + \frac{1}{R_t} \\ C_D &= C_{D 0} + \frac{1}{R_t} \end{aligned} \quad (4.21)$$

i.e., when  $R_t$  is large we can expect the molecular viscosity to have negligible effect on the transport process and the functions take on constant values. However, when  $R_t$  is very small and turbulence effects are negligible, the functions tend to  $\frac{1}{R_t}$ .

The "universality" of the constants  $C_{\mu 0}$  and  $C_{D 0}$ , for which many users of the model had hoped, could not be achieved; the values were found to be quite different depending on the experiment under consideration. Wolfshtein [35], modeling a jet impinging normally on a wall, uses

$$C_{\mu_0} = 0.22; \quad C_{D_0} = 0.416$$

Ng and Spalding [36] use

$$C_{\mu_0} = 1.0; \quad C_{D_0} = 0.1$$

for their calculations of boundary layers near walls, as do Rodi and Spalding [37] in their modeling of free turbulent flows. Launder, et al. [44], however, employ

$$C_{\mu_0} = 0.09; \quad C_{D_0} = 1.0$$

in their numerical solution for free turbulent shear flows.

In view of the fact that there is only insufficient experimental data available for the present investigation, no attempt shall be made to propose new values for the two constants in question. Instead, the influence of their variation on the flow field shall be studied.

### Two-Equation Model of Turbulence

The next logical step from the turbulence kinetic energy model described in the previous paragraph is to remove the uncertainty from the length scale distribution especially in recirculating flow regions and to calculate  $l^*$  rather than to prescribe it algebraically. Rotta [38] was the first to propose a differential equation for the length scale, deriving it from the Navier-Stokes equations. Gosman, et al. [20] reformulated the equation into the common form of their transport equation, thus, together with

the  $k^*$  equation they arrived at a two-equation model of turbulence. The equation for  $\ell^*$  is

$$\rho^* \bar{u}_j^* \frac{\partial \ell^*}{\partial x_j^*} = \frac{\partial}{\partial x_j^*} \left( \Gamma_{\ell, \text{eff}} \frac{\partial \ell^*}{\partial x_j^*} \right) + S_{\ell}^* \quad (4.22)$$

with

$$S_{\ell}^* = -\mu_t^* \left( \frac{\partial \bar{u}_i^*}{\partial x_j^*} + \frac{\partial \bar{u}_j^*}{\partial x_i^*} \right) \frac{\partial \bar{u}_i^*}{\partial x_j^*} \frac{\ell^*}{k^*} \cdot C_B + \rho^* k^{*1/2} \cdot C_S \quad (4.23)$$

being the "source" term of the turbulent length scale. It consists of a positive contribution representing the rate of growth of  $\ell^*$  as a result of the dissipation of energy, especially from smaller eddies and a negative contribution accounting for the tendency of the shear stress to reduce  $\ell^*$  by rupturing the large eddies.  $C_B$  and  $C_S$  are again functions of  $R_t$  having similar behavior as  $C_{\mu}$  and  $C_D$  in Equation 4.21, i.e.,

$$C_B = C_{B_0} + \frac{1}{R_t}$$

$$C_S = C_{S_0} + \frac{1}{R_t} \quad (4.24)$$

$C_{B_0}$  and  $C_{D_0}$  are constants to be determined empirically.



### III. NUMERICAL SOLUTION

#### Numerical Procedure

The mathematical problem posed in the previous chapter has been solved by utilizing and extending the numerical procedure of Gosman, et al. [20]. For a detailed description the reader is referred to this reference. Only a brief outline is given here.

The governing differential equations (4.8, 4.10, 4.17, 4.22 or 4.12 in general) are replaced by algebraic finite difference equations which are obtained by integration over finite areas rather than Taylor series expansion, assuring a broader range of applicability especially in non-rectangular coordinate systems. The integration of the convection terms employs "upwind differencing," a one-sided, rather than centered space differencing, where the scheme is backward when the velocity is positive and forward when it is negative. This formulation of the first order terms gives greater numerical stability than can be obtained with central differences. The remaining diffusion and source terms, however, are expressed in a weighted central difference form.

Because of the nonlinear character of the resulting finite difference equations they are solved by an iterative, successive substitution technique.

### Physical and Numerical Coordinate System

The physical coordinate system was chosen such that the origin was located at the lower step corner, with the positive  $x^*$ -axis pointing in downstream direction parallel to the wall and the  $z^*$ -axis directed normally to it aligned with the front face of the step. (See Figure 4.1, page 83.) In this coordinate system the flow regime considered extends ten step heights in the upstream and downstream directions and nine step heights in the vertical direction. The origin of the numerical coordinates was situated at the lower left corner of the flow field (Figure 4.3) with I indexing in the  $x^*$ -direction and J indexing in the  $z^*$ -direction. In the iteration process the field was swept from left to right beginning at the wall and proceeding in the increasing J-direction.

The distribution of the grid points is shown in Figure 4.4. As indicated, a variable mesh was used which gradually decreased in size near the wall and in the vicinity of the step.

### Boundary Conditions

Depending on the turbulence model under consideration the number of differential equations to be solved ranges from two equations in  $\omega^*$  and  $\psi^*$  to four equations in  $\omega^*$ ,  $\psi^*$ ,  $k^*$  and  $\ell^*$ . The number of boundary conditions required for the respective case then changes accordingly. Due to the elliptical nature of the flow problem, these

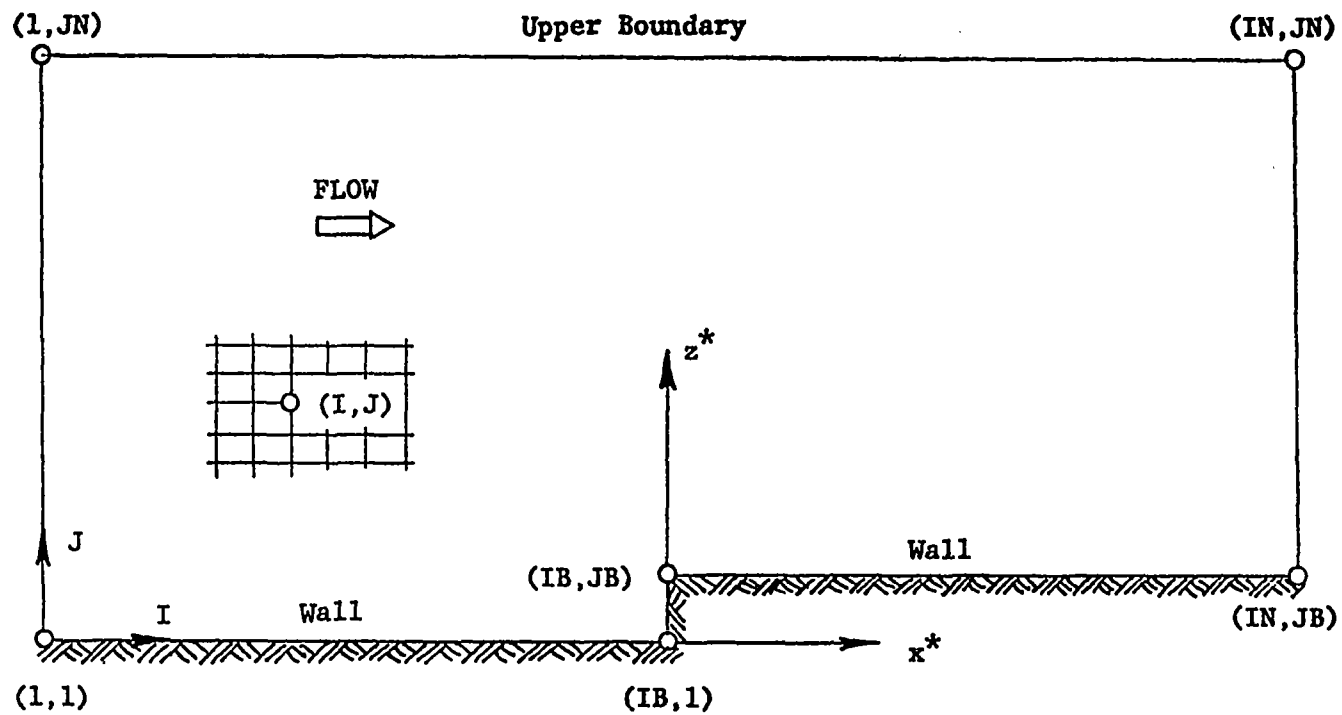


Figure 4.3. Description of physical  $(x^*, z^*)$  and numerical  $(I, J)$  coordinate system used.

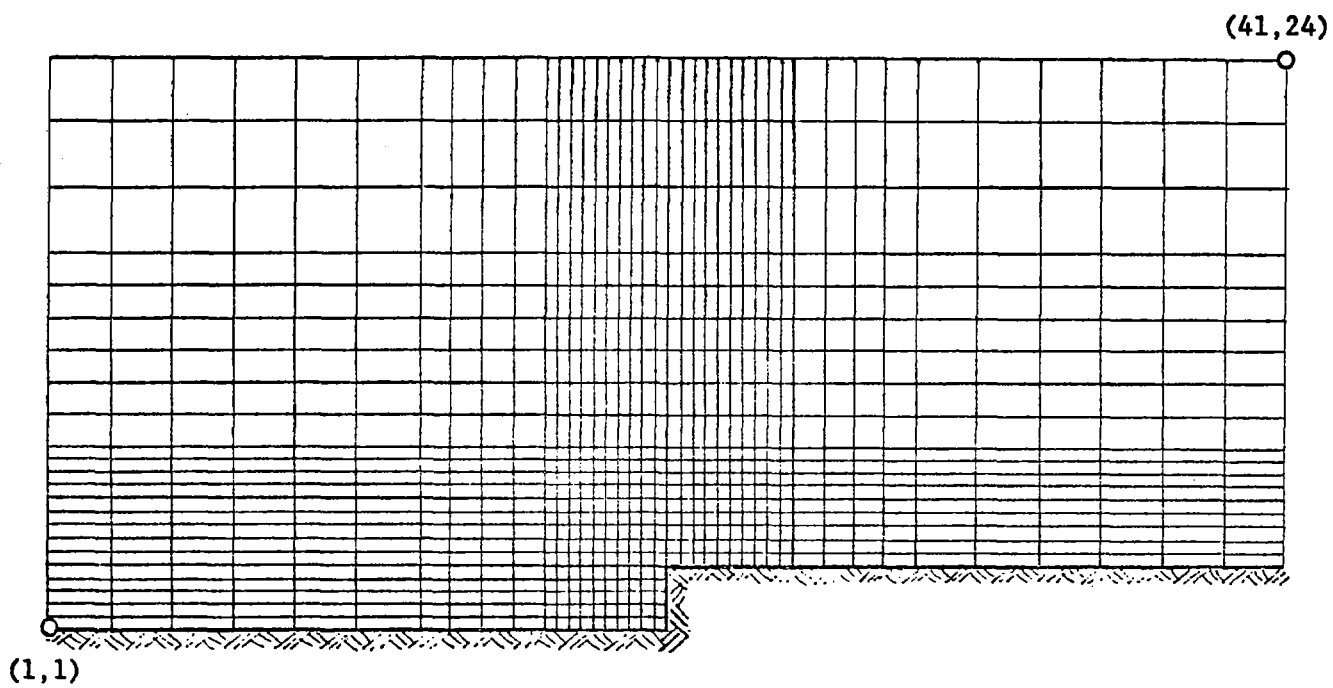


Figure 4.4. Actual grid distribution.

boundary conditions are prescribed along the entire boundary of the flow regime, i.e., following Figure 4.1, page 83, along the inlet, the outlet, the upper and lower boundaries (wall). All conditions are either of Dirichlet or Neumann type.

Inflow. At the inflow a logarithmic velocity profile of the form

$$u^* = \frac{u_*^*}{\kappa} \ln \frac{z^* + z_0^*}{z_0^*} \quad (4.25)$$

is assumed. The  $\psi^*$  boundary condition can then be determined by integrating the velocity profile over the inlet height

$$\psi^*(z^*) = \rho^* \frac{u_*^*}{\kappa} \int_0^{z^*} \ln \frac{z^* + z_0^*}{z_0^*} dz^* \quad (4.26)$$

which yields

$$\psi^*(z^*) = \rho^* \frac{u_*^*}{\kappa} \left[ (z^* + z_0^*) \ln \frac{z^* + z_0^*}{z_0^*} - (z^* + z_0^*) \right] + C \quad (4.27)$$

where C can be determined such that  $\psi^* = 0$  at the wall.

Then

$$\psi^*(z^*) = \rho^* \frac{u_*^*}{\kappa} \left[ (z^* + z_0^*) \left( \ln \frac{z^* + z_0^*}{z_0^*} - 1 \right) + z_0^* \right] \quad (4.28)$$

The condition for the vorticity  $\omega^*$  is

$$\omega^*(z^*) = \frac{\partial \bar{w}^*}{\partial x^*} - \frac{\partial \bar{u}^*}{\partial z^*} \quad (4.29)$$

where the last term can be calculated from the  $\psi^*$ -distribution as

$$\frac{\partial \bar{u}^*}{\partial z^*} = \frac{1}{\rho^*} \frac{\partial^2 \psi^*}{\partial z^{*2}} = \frac{u_*^*}{\kappa} \frac{1}{z^* + z_0^*} \quad (4.30)$$

The remaining term of the inflow vorticity was allowed to develop as part of the solution by approximating

$$\frac{\partial^2 \bar{w}^*}{\partial x^{*2}} = 0 \quad (4.31)$$

and setting

$$\left. \frac{\partial \bar{w}^*}{\partial x^*} \right|_{1,J} = \left. \frac{\partial \bar{w}^*}{\partial x^*} \right|_{2,J} = -\frac{1}{\rho^*} \left. \frac{\partial^2 \psi^*}{\partial x^{*2}} \right|_{2,J} \quad (4.32)$$

The employed boundary condition for the turbulent kinetic energy  $k^*$  was derived from the constant shear assumption underlying the derivation of the logarithmic law of the wall.

$$\tau_t^*(z^*) = \rho^* u_*^{*2} = \text{const.} \quad (4.33)$$

In terms of the Prandtl-Kolmogorov formulation (Equation 4.16) one can write

$$\tau_t^*(z^*) = \rho^* k^{*1/2} \kappa^* C_{\mu 0} \frac{\partial \bar{u}^*}{\partial z^*} \quad (4.34)$$

Equating the two and substituting  $\ell^*$  from Equation 4.14 and

the velocity gradient from Equation 4.30 one obtains the boundary conditions for  $k^*$  at the inlet as

$$k^* = \left( \frac{u_*^*}{C_{\mu 0}} \right)^2 \quad (4.35)$$

The corresponding condition on the turbulence length scale is then

$$l^* = \kappa (z^* + z_0^*) \quad (4.36)$$

Outflow. Two sets of outlet boundary conditions were used. The first one assumes that the outlet location is sufficiently far downstream of the step that an undisturbed logarithmic velocity profile has developed again.

$$u^* = \frac{u_{*out}^*}{\kappa} \ln \frac{z^* + z_0^* - h^*}{z_0^*} \quad (4.37)$$

$\psi^*$  can then again be determined by integrating  $u^*$

$$\psi^*(z^*) = \rho^* \frac{u_{*out}^*}{\kappa} \left[ (z^* + z_0^* - h^*) \left( \ln \frac{z^* + z_0^* - h^*}{z_0^*} - 1 \right) + z_0^* \right] \quad (4.38)$$

where  $u_{*out}^*$  is calculated from the conservation of mass through inlet and outlet, as no mass will be assumed to cross the other boundaries,

$$\dot{V}_{in}^* = \dot{V}_{out}^* \quad (4.39)$$

with

$$\dot{V}_{in}^* = \int_0^{H^*} \bar{u}^* dz^*$$

$$\dot{V}_{in}^* = \frac{u_{in}^*}{\kappa} \left[ (H^* + z_0^*) \ln \frac{H^* + z_0^*}{z_0^*} - H^* \right] \quad (4.40)$$

and

$$\dot{V}_{out}^* = \frac{u_{out}^*}{\kappa} \left[ (H^* + z_0^* - h^*) \ln \frac{H^* + z_0^* - h^*}{z_0^*} - (H^* - h^*) \right] \quad (4.41)$$

the friction velocity at the outlet is

$$u_{out}^* = \frac{\dot{V}_{in}^* \kappa}{(H^* + z_0^* - h^*) \ln \left( \frac{H^* + z_0^* - h^*}{z_0^*} \right) - (H^* - h^*)} \quad (4.42)$$

Analogue to the inlet, the first term of the vorticity boundary condition is determined from the  $\psi^*$  distribution by

$$\frac{\partial \bar{u}^*}{\partial z^*} = \frac{1}{\rho^*} \frac{\partial^2 \psi^*}{\partial z^{*2}} \quad (4.43)$$

while the other  $\omega^*$ -term is calculated with the aforementioned assumption

$$\frac{\partial^2 \bar{w}^*}{\partial x^{*2}} = 0 \quad (4.44)$$

i.e.,

$$\left. \frac{\partial \bar{w}^*}{\partial x^*} \right|_{IN,J} = \left. \frac{\partial \bar{w}^*}{\partial x^*} \right|_{IN-1,J} = -\frac{1}{\rho^*} \frac{\partial^2 \psi^*}{\partial x^{*2}} \quad (4.45)$$



The remaining conditions on  $k^*$  and  $l^*$  were similar to Equations 4.35 and 4.36

$$k^* = \left( \frac{u_{*out}}{C_{\mu_0}} \right)^2 \quad (4.46)$$

and

$$l^* = \kappa (z^* + z_0^* - h^*) \quad (4.47)$$

The second set of outlet boundary conditions consisted of less restrictive formulations for  $\omega^*$  and  $\psi^*$ .

The assumption for  $\psi^*$  was that

$$\frac{\partial^2 \bar{w}^*}{\partial x^{*2}} = 0 \quad (4.48)$$

or

$$\left. \frac{\partial^2 \psi^*}{\partial x^{*2}} \right|_{IN,J} = \left. \frac{\partial^2 \psi^*}{\partial x^{*2}} \right|_{IN-1,J} = \left. \frac{\psi_{IN}^* - 2\psi_{IN-1}^* + \psi_{IN-2}^*}{(\Delta x^*)^2} \right|_J$$

which yields

$$\psi_{IN,J}^* = 2\psi_{IN-1}^* - \psi_{IN-2}^* \quad (4.49)$$

For the vorticity it is assumed that its gradient in the flow direction vanishes

$$\frac{\partial \omega^*}{\partial x^*} = 0 \quad (4.50)$$

The turbulent kinetic energy  $k$  was allowed to decay to the

initial free stream turbulence level

$$k^* = \left( \frac{u_*^*}{C_{\mu_0}} \right)^2 \quad (4.51)$$

Upper boundary. The location of the upper boundary was assumed far enough out that velocity deflections caused by the step were negligibly small. Consequently the stream-line condition is

$$\psi^* = \text{const.} \quad (4.52)$$

i.e., no flow is crossing the upper boundary.

The vorticity condition imposed was that of a vanishing gradient

$$\frac{\partial \omega^*}{\partial z^*} = 0 \quad (4.53)$$

which was also required for the turbulence kinetic energy, however, in the horizontal or  $x^*$ -direction

$$\frac{\partial k^*}{\partial x^*} = 0 \text{ or } k^* = \text{const.} \quad (4.54)$$

The length scale was prescribed as given by Equation 4.14.

Wall boundary. As the flow is parallel to the wall the condition for the stream function must be

$$\psi^* = \text{const.} \quad (4.55)$$

along the entire wall boundary.

The vorticity boundary condition is more problematic, as it essentially drives the flow. It can be derived from a Taylor-series expansion of the stream function around a near wall point (NP),  $\Delta n$  away from the wall, in terms of the wall point (P) conditions

$$\psi_{NP}^* = \psi_P^* + \left. \frac{\partial \psi^*}{\partial n^*} \right|_P \Delta n^* + \frac{1}{2} \left. \frac{\partial^2 \psi^*}{\partial n^{*2}} \right|_P (\Delta n^*)^2 + \frac{1}{6} \left. \frac{\partial^3 \psi^*}{\partial n^{*3}} \right|_P (\Delta n^*)^3 + \text{H.O.T.} \quad (4.56)$$

By the no-slip condition:

$$\left. \frac{\partial \psi^*}{\partial n^*} \right|_P = 0 \quad (4.57)$$

$$\left. \frac{\partial^2 \psi^*}{\partial n^{*2}} \right|_P = -\rho^* \omega^* \quad (4.58)$$

Combining the last two expressions, one gets

$$\left. \frac{\partial^3 \psi^*}{\partial n^{*3}} \right|_P = \frac{\partial}{\partial n^*} \left( \left. \frac{\partial^2 \psi^*}{\partial n^{*2}} \right|_P \right) = -\rho^* \left. \frac{\partial \omega^*}{\partial n^*} \right|_P \quad (4.59)$$

Substituting these into Equation 4.56 and solving for  $\omega_P^*$

$$\omega_P^* = -\frac{2(\psi_{NP}^* - \psi_P^*)}{(\Delta n^*)^2 \cdot \rho^*} - \left( \left. \frac{\partial \omega^*}{\partial n^*} \right|_P \right) \frac{\Delta n^*}{3} \quad (4.60)$$

The vorticity gradient at the wall was approximated by

$$\left( \left. \frac{\partial \omega^*}{\partial n^*} \right|_P \right) = \frac{\omega_{NP}^* - \omega_P^*}{\Delta n^*} \quad (4.61)$$

yielding the second order vorticity formulation

$$\omega_P^* = -\frac{3(\psi_{NP}^* - \psi_P^*)}{(\Delta n^*)^2 \cdot \rho^*} - \frac{1}{2} \omega_{NP}^* \quad (4.62)$$

The turbulence kinetic energy specification along the wall poses some problems.  $k^* = 0$  is incompatible with the inlet and outlet conditions of

$$k_{in}^* = \left( \frac{u_{*}^*}{C_{\mu 0}} \right)^2 \quad (4.63)$$

and

$$k_{out}^* = \left( \frac{u_{*out}^*}{C_{\mu 0}} \right)^2 \quad (4.64)$$

It was therefore assumed that  $k^*$  obeyed Equation 4.63 also along the wall, however, with  $u_{*}^*$  varying as

$$u_{*}^*|_{wall} = \ell^* \left. \frac{\partial \bar{u}^*}{\partial z^*} \right|_{wall} \quad (4.65)$$

implying a logarithmic velocity profile from the wall to the first interior node. Furthermore, at the wall,

$$u_{*}^*|_{wall} = \kappa \cdot z_0^* \cdot (-\omega^*) \quad (4.66)$$

or

$$k_{wall}^* = \left( \frac{\kappa \cdot z_0^* \cdot \omega^*}{C_{\mu 0}} \right)^2 \quad (4.67)$$

The length scale was prescribed by

$$\ell^* = \kappa \cdot z_0^* \quad (4.68)$$

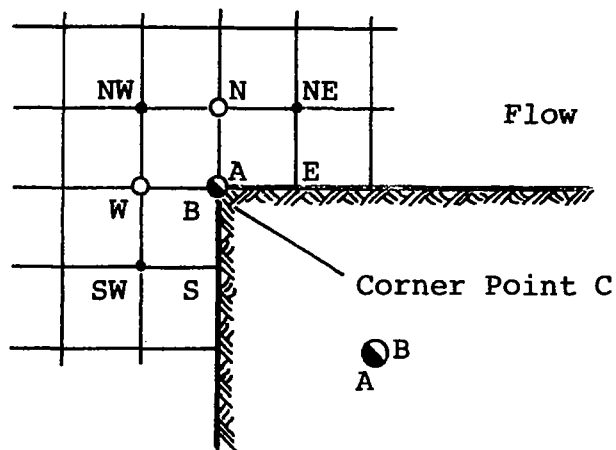
Special treatment at step corner. The stream function at the upper corner presents no problem. Like the rest of the wall  $\psi_C^* = 0$ . Similarly,  $k_C^*$  and  $\ell_C^*$  are uniquely prescribed by the lower boundary condition. But there are several alternatives for the evaluation of  $\omega_C^*$ . Referring to Figure 4.5 one can apply Equation 4.62 either to the upstream side (face) of the step or to the downstream wall obtaining respectively:

$$\omega_C^* = \omega_B^* = -\frac{3\psi_W^*}{\rho^* (\Delta x^*)^2} - \frac{1}{2} \omega_W^* \quad (4.69)$$

and

$$\omega_C^* = \omega_A^* = -\frac{3\psi_N^*}{\rho^* (\Delta z^*)^2} - \frac{1}{2} \omega_N^* \quad (4.70)$$

There are also other possibilities. Seven different methods are given in Roache [39], and most of these are investigated in the present study; they are listed in Figure 4.5. Method (1) represents an attempt to force separation at the corner, assuming that the vorticity vanishes at a separation point. Method (2) is based on the idea that, since separation occurs tangentially to the upstream wall, upstream wall evaluation should be used. Method (3) is an attempt to average out both values, while method (4) is derived from adding both values in a first order formulation. Method (5)



$$\omega_A^* = -\frac{3(\psi_N^* - \psi_C^*)}{\Delta n^{*2} \cdot \rho^*} - \frac{1}{2} \omega_N^*$$

$$\omega_B^* = -\frac{3(\psi_W^* - \psi_C^*)}{\Delta n^{*2} \cdot \rho^*} - \frac{1}{2} \omega_W^*$$

#### Vorticity Boundary Conditions for C

(1)  $\omega_C^* = 0$

(4)  $\omega_C^* = -2(\psi_W^* + \psi_N^*)/\Delta n^{*2} \cdot \rho^*$

(2)  $\omega_C^* = \omega_B^*$

(5) Discontinuous Value

$$\omega_{C1}^* = \omega_B^* \quad \omega_{C2}^* = \omega_A^*$$

(3)  $\omega_C^* = (\omega_A^* + \omega_B^*)/2$

or  $\omega_{C2}^* = 0$

Figure 4.5. Investigated boundary conditions for upper step corner point.

arises from the argument that no continuity of  $\omega^*$  can be expected for the geometric singularity of the corner.

When applied to the laminar flow case, obtained by setting the turbulent viscosity equal to zero, all methods functioned well and enforced separation from the corner. The second formulation, however, was the most effective in producing a well developed realistic separation region. For this reason it was used in all subsequent calculations.

#### Accuracy, Convergence and Economy

Carrying out the numerical solution to the above set of differential equations, a balance is required between the convergence and accuracy and the amount of computing time necessary to meet these conditions. One of the most important factors affecting this balance is the grid spacing. Therefore, the following sections will discuss the effects of grid dimensions on accuracy and convergence.

Influence of grid size on accuracy. Accuracy is the deviation of the numerical solution from the exact solution. Unfortunately, this exact solution is unknown in most cases, thus the accuracy is not easily determined. One possibility to overcome this difficulty is to test the numerical procedure with a simple problem for which the exact solution is known. This allows an estimate of the general accuracy of the procedure. The optimum grid size, however, cannot be transferred to another problem, as it strongly depends on

the physical case under consideration, i.e., the size and location of the occurring gradients.

Another way is to investigate the dependence of the respective solution on increment size and find the grid size for which a further decrease brings no further or at most minor improvements in the solution. The grid size for the present analysis was essentially determined by this approach with some additional compromise toward economy. The following discussion shall compare some results obtained from the grid size actually used for all subsequent calculations with results obtained from a grid with twice as fine a mesh. Such a grid increases the computing time by a factor of four. All calculations were carried out for a surface roughness  $z_0^* = 0.45$  [m] and a friction velocity of  $u_*^* = 0.75$  [m/sec]. Figures 4.6 through 4.11 show the vertical vorticity and stream function distributions at three  $x^*$ -stations for the two different grid systems. In the first four figures for the  $x^* = 6.0 h^*$  and  $x^* = 0.0$  locations there are almost no differences in the respective  $\omega^*$ - and  $\psi^*$ -distributions and consequently no improvement through the finer mesh. The situation is slightly different a short distance behind the step corner at  $x^* = 0.8 h^*$ . The stream function, the better behaved function of the two, is again almost identical in both cases. The vorticity-distribution, however, shows differences. Even the finer mesh does not quite predict the wall vorticity correctly, although it shows the correct trend, indicated by the dotted line in



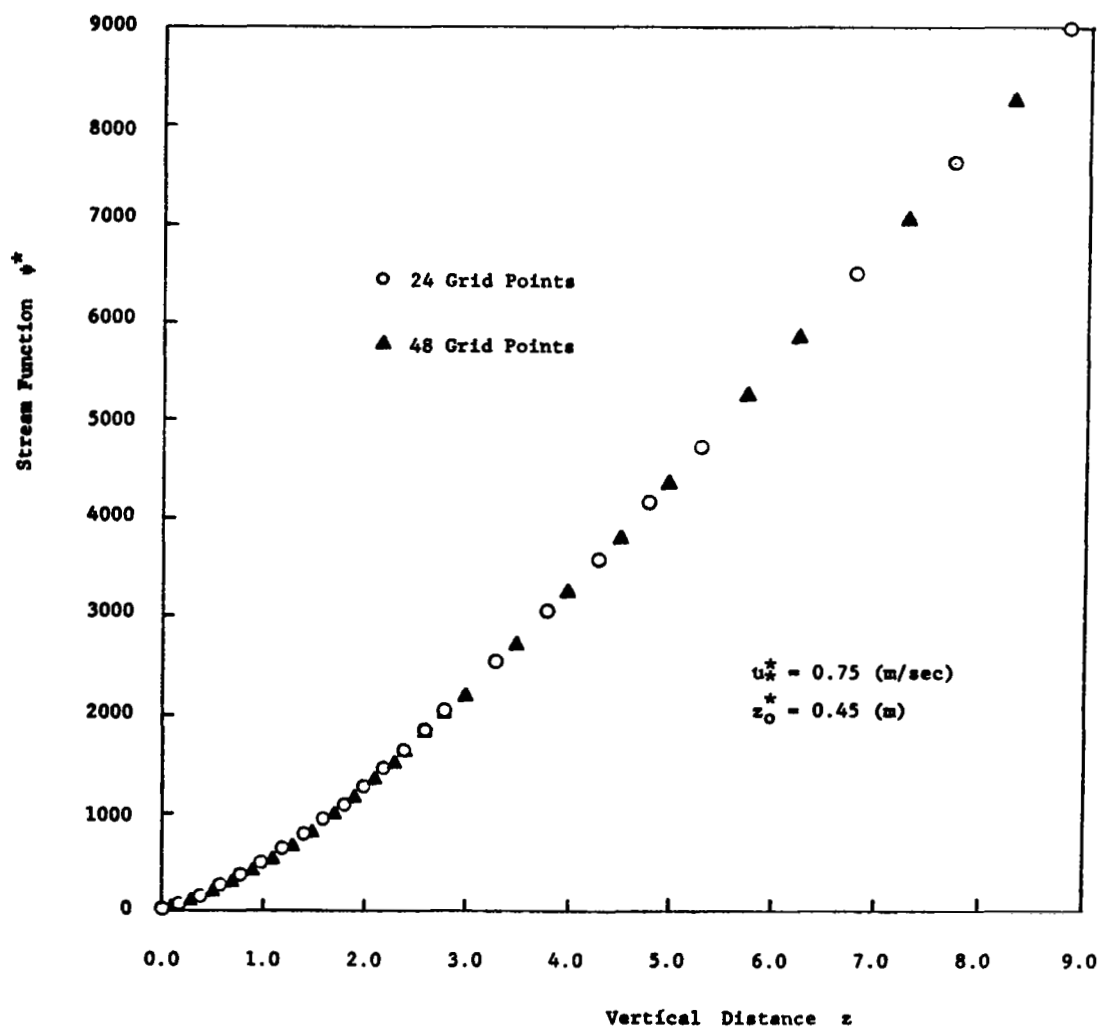


Figure 4.6. Stream function distribution at  $x = -6.0$  for different grid sizes.

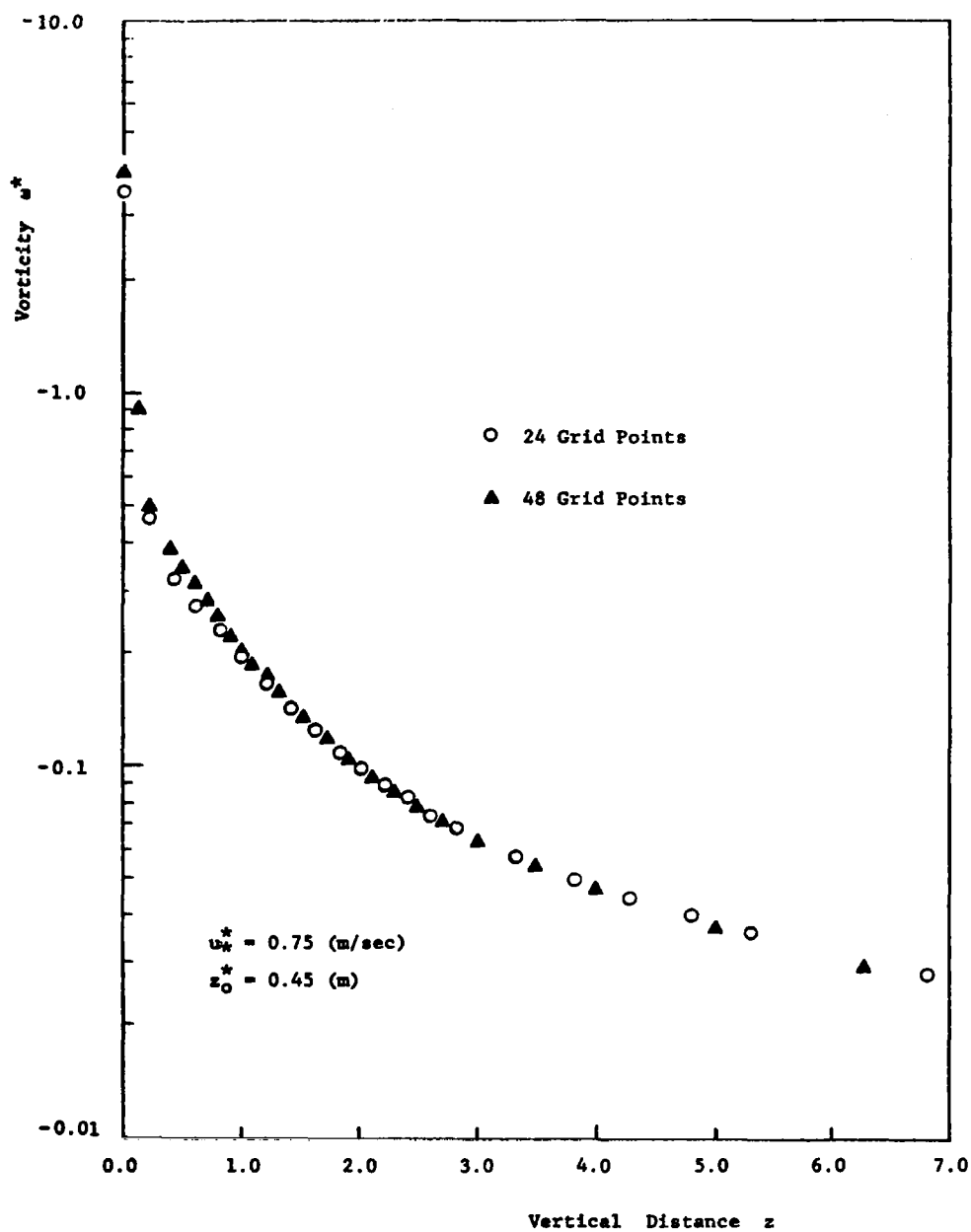


Figure 4.7. Vorticity distribution at  $x = -6.0$  for different grid sizes.

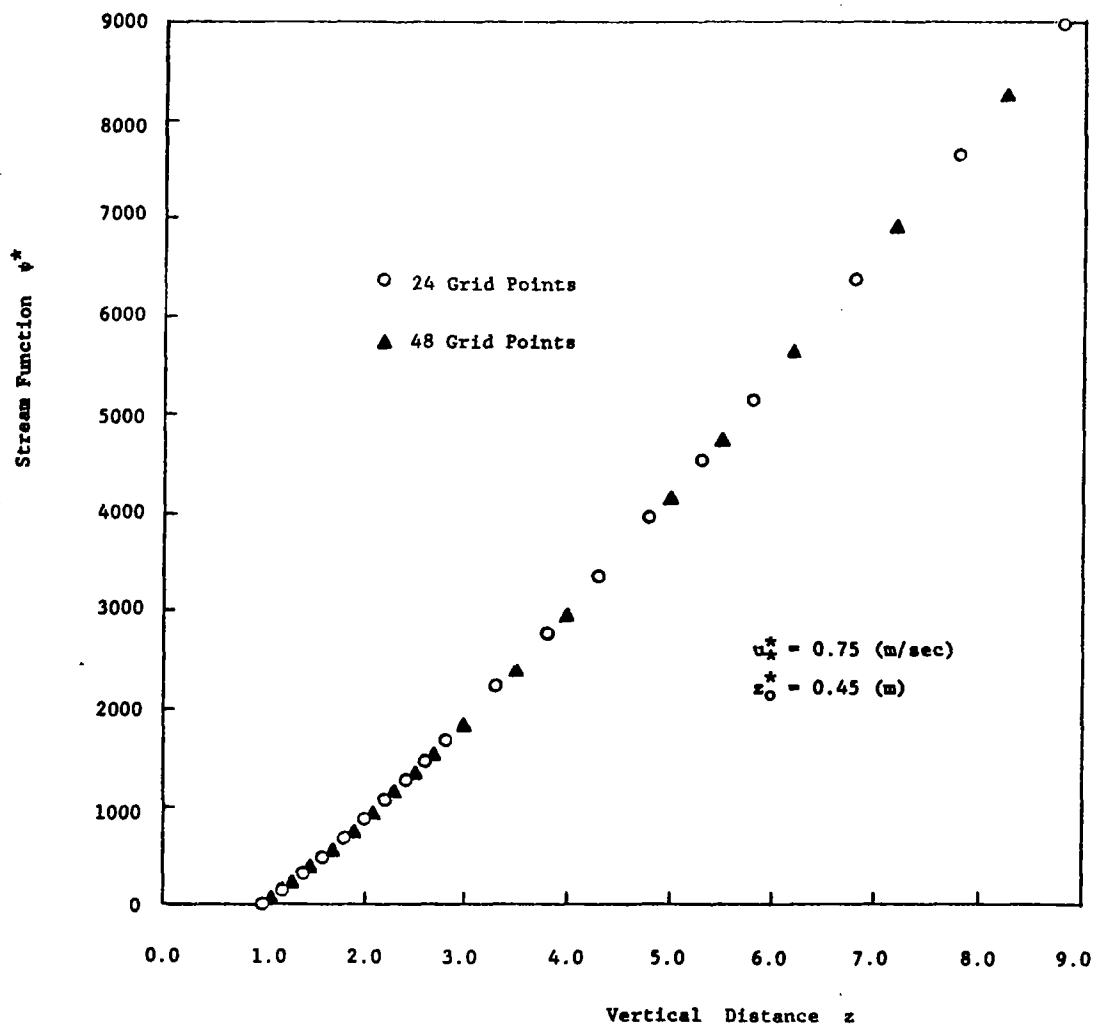


Figure 4.8. Stream function distribution at  $x = 0.0$  for different grid sizes.

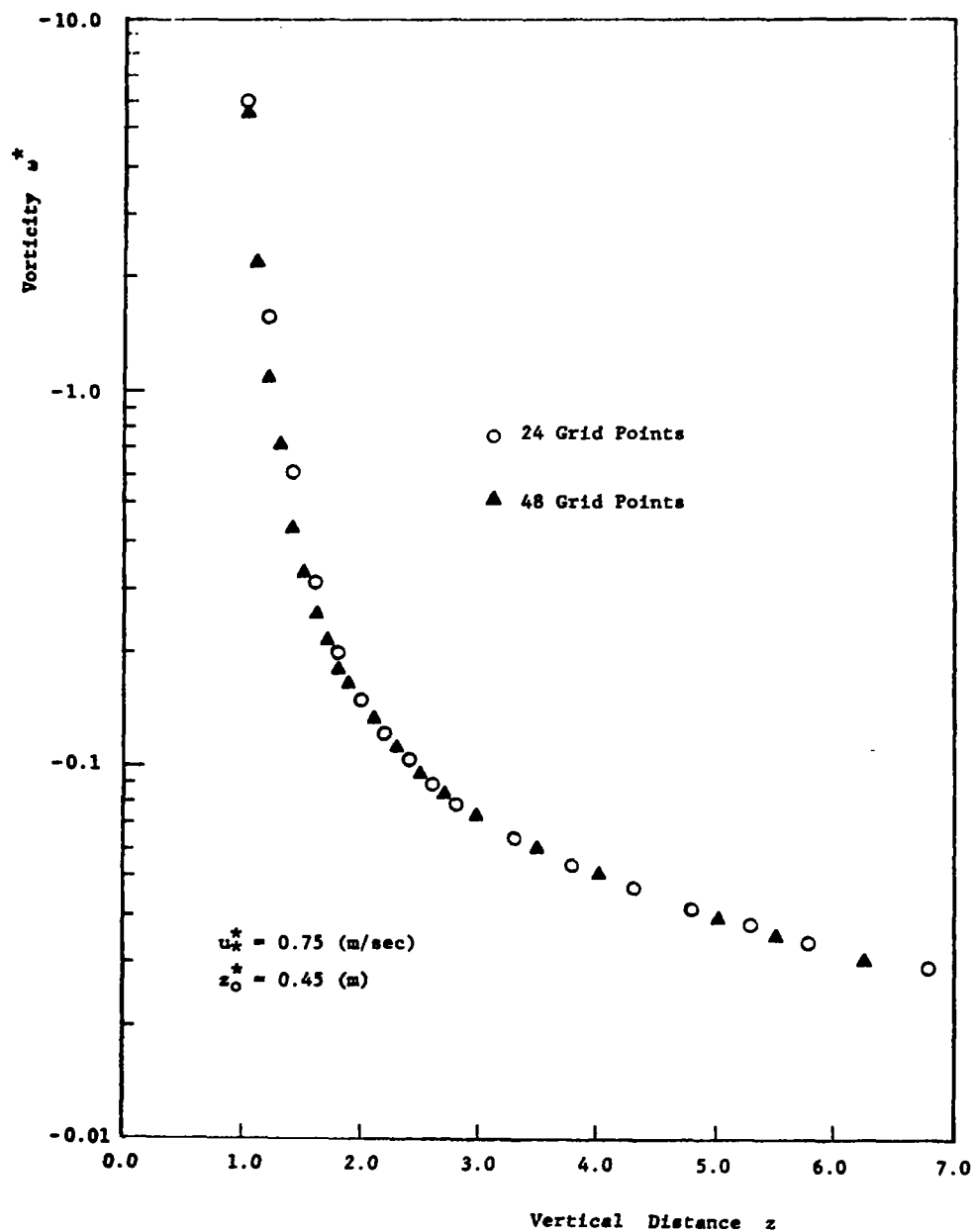


Figure 4.9. Vorticity distribution at  $x = 0.0$  for different grid sizes.

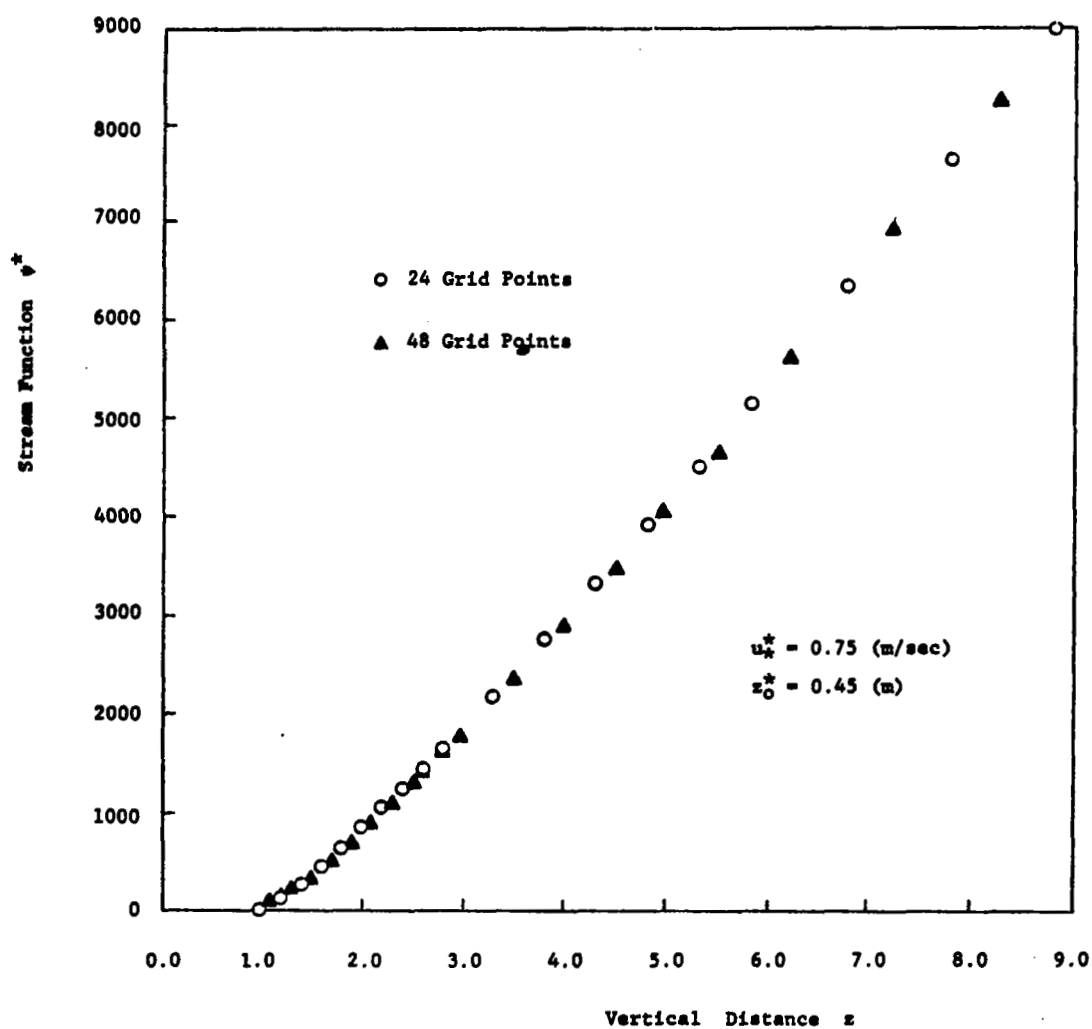


Figure 4.10. Stream function distribution at  $x = 0.8$  for different grid sizes.

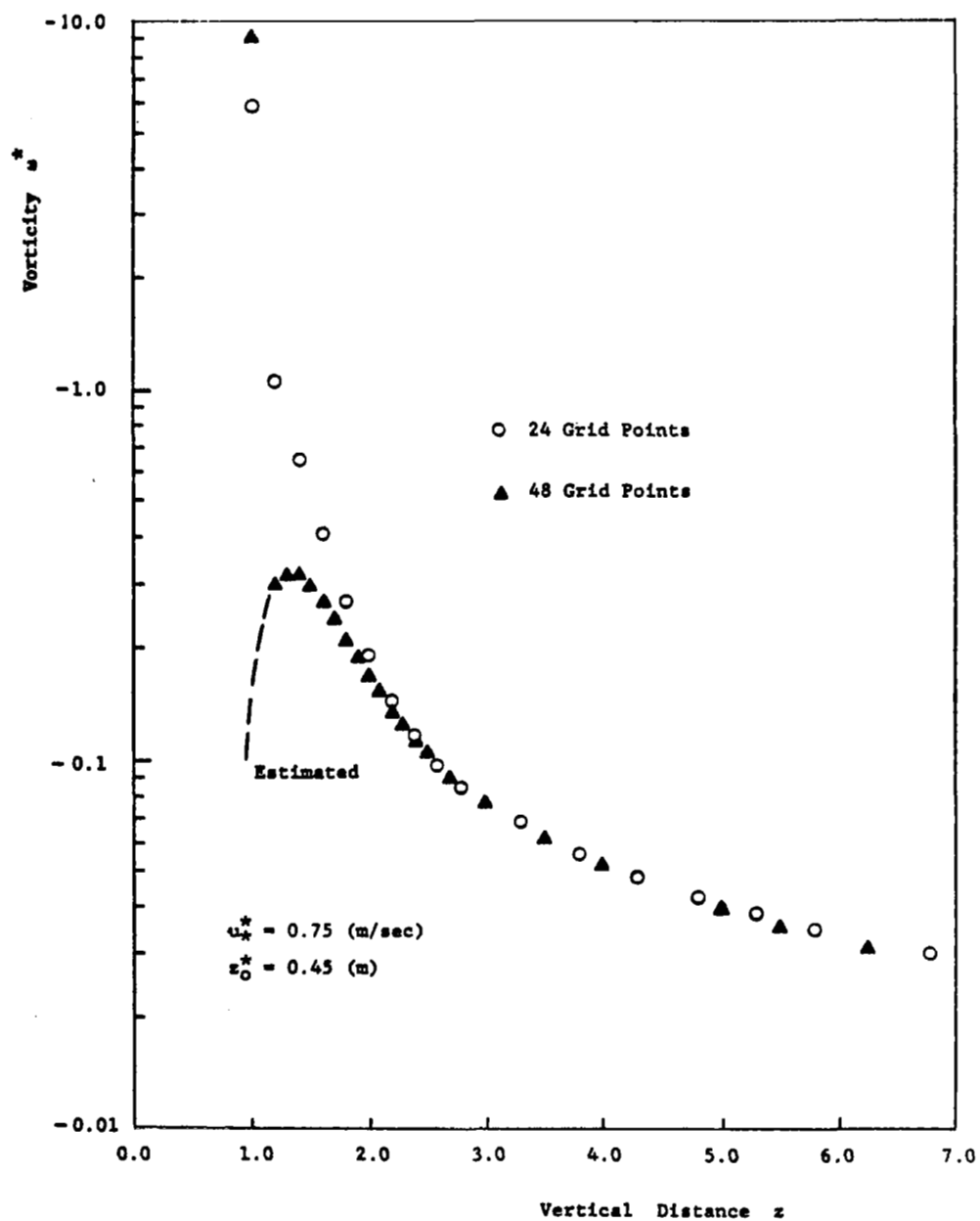


Figure 4.11. Vorticity distribution at  $x = 0.8$  for different grid sizes.

Figure 4.11. Because of the expected flow separation at the top step corner and the resulting recirculation region behind it, the vorticity should reverse its sign in the vicinity of the wall as one approaches the wall in the vertical direction from the inside of the flow field. This can best be demonstrated by looking at some results from a laminar flow case obtained by setting the turbulent viscosity to zero. Here the separation region is bigger and thus more grid points fall into this region. Looking at stream function distributions for two different  $x^*$ -stations downstream of the step corner in Figures 4.12 and 4.14, and a vorticity distribution in Figure 4.13 corresponding to the first  $x^*$ -station, it is seen that at  $x^* = 1.6 h^*$  the coarser grid does not give negative streamline values near the wall, which one would expect because of the separation from the corner. The finer grid, on the other hand, produces the expected negative  $\psi^*$ -values. At  $x^* = 3.0 h^*$  the separation region is large enough that even with the coarse grid negative  $\psi^*$ -values can be obtained near the wall. Consequently the stream-function plots for the two grids look as shown in Figure 4.15, where (a) is the plot for the coarse and (b) the plot for the fine grid. The two vorticity distributions for the  $x^* = 1.6 h^*$  stations are shown in Figure 4.13. They demonstrate how inside the separation region the vorticity changes sign in the vicinity of the wall even for the coarse grid. Because of the stronger developed separation region in the laminar case, i.e., its

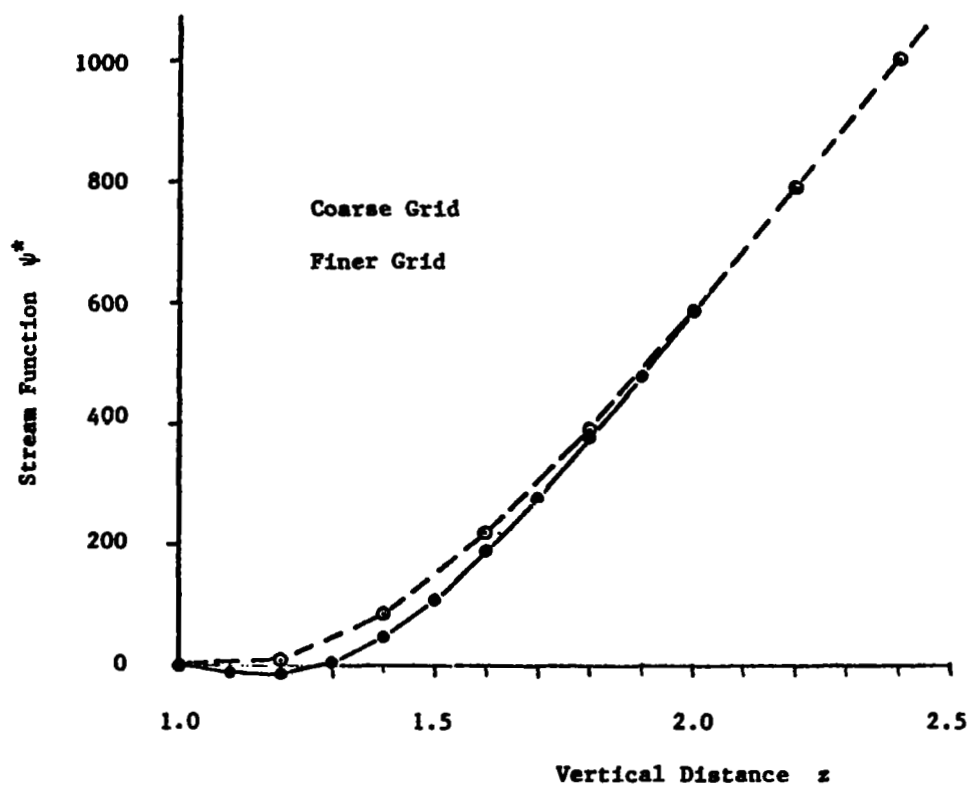


Figure 4.12. Near wall stream function distribution for laminar flow at  $x = 1.6$ .



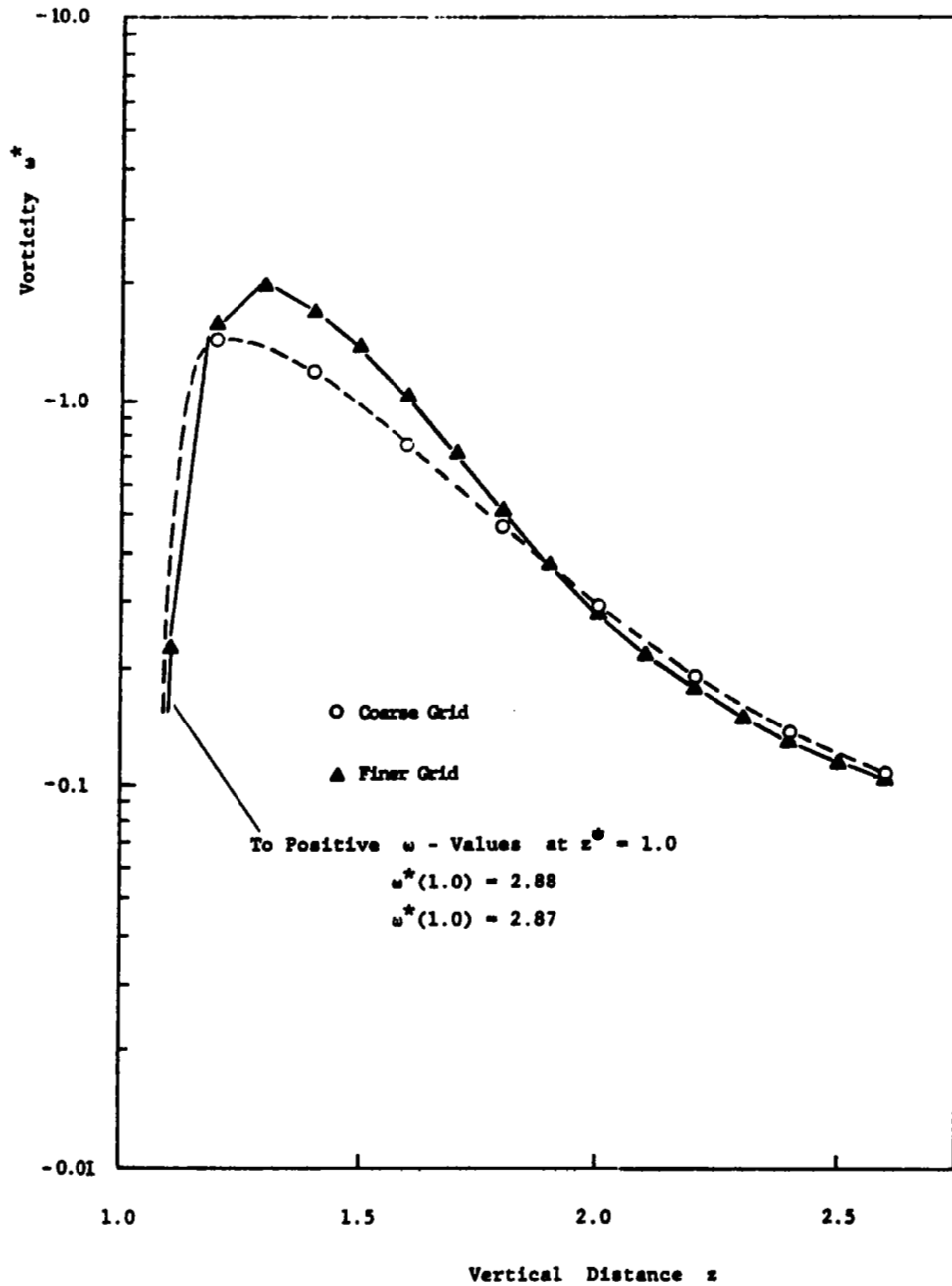


Figure 4.13. Near wall vorticity distribution for laminar flow at  $x = 1.6$ .

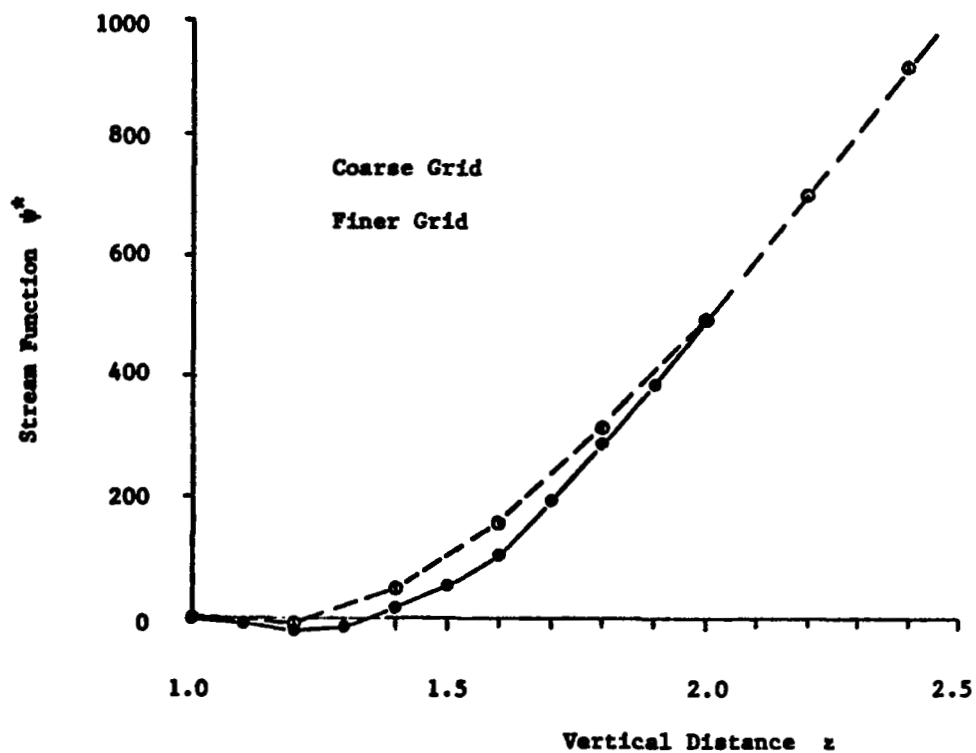
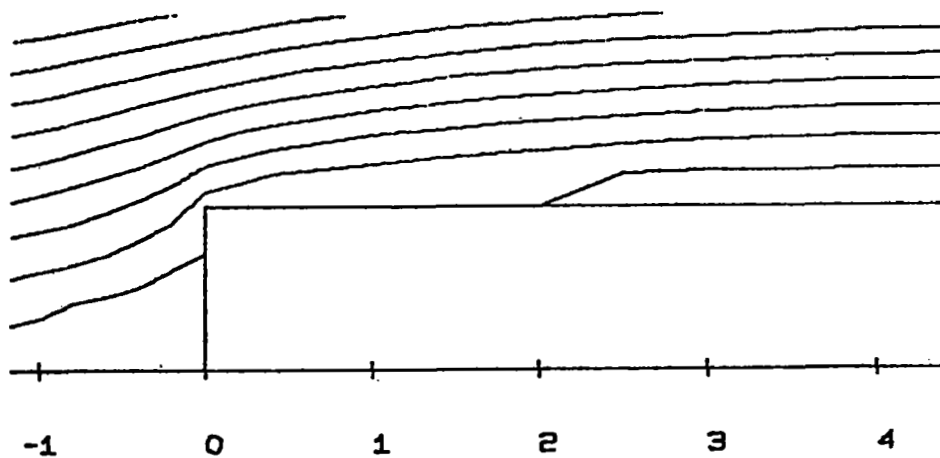
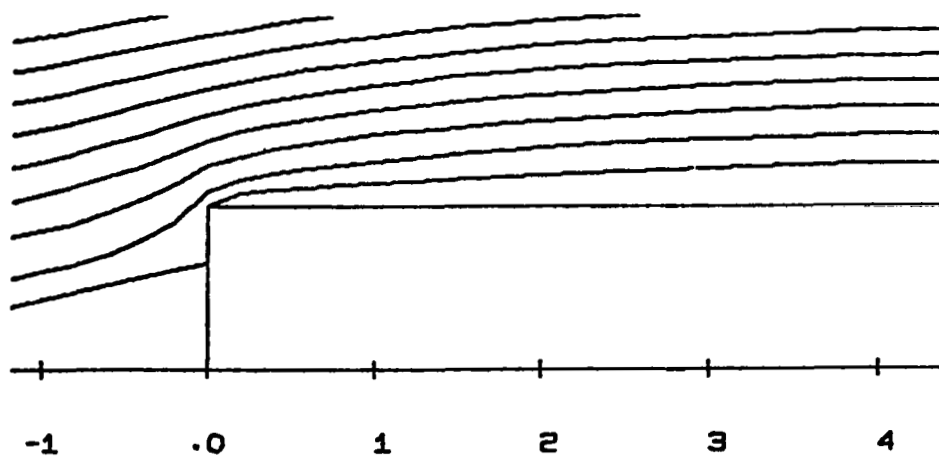


Figure 4.14. Near wall stream function distribution for laminar flow at  $x = 3.0$ .



(a)



(b)

Figure 4.15. Streamline plots for laminar flow; (a) coarse grid, (b) finer grid.

greater physical extent, vorticity wall predictions are better than in the turbulent case where the separation region is considerably smaller.

The above fine grid calculations were obtained from solving a small flow regime behind the step with fixed boundary conditions, interpolated from coarse grid calculations, except for the vorticity boundary condition at the wall, which was allowed to develop as a new solution.

It should be pointed out that the  $\omega^*$ -boundary condition (Equation 4.62) is based on the linear vorticity distribution. However, as can be seen from previous figures, the vorticity is linear only in the very close proximity of the wall. When a fine enough mesh is used, the point near the wall is in this linear vorticity region and the wall vorticity predictions are good. In either case, the vorticity away from the wall is not very sensitive to mesh size and is hardly influenced by the local inaccuracies at the wall inside the turbulent separation region.

To summarize the findings of the foregoing investigation, one might say that except for a small region in the immediate vicinity of the wall at a short downstream section behind the step corner the coarse grid produces reasonable results, which can only be modestly improved by the fine grid calculations requiring four times as much computing time. The calculations show further that inaccuracies in the vorticity wall predictions inside the turbulent separation region on top of the step, do not propagate far

inside the flow field but remain limited to a small area near the wall. The external flow field remains largely unaffected.

If one wishes to improve the predictions in the near wall separation region, however, one can choose from several possibilities. The first has already been mentioned during the discussion, i.e., decrease of the grid size near the wall until the variation of all computed quantities changes approximately linearly between adjacent mesh points. Unfortunately, this is not always easily accomplished. Besides sizeable increases in computing time, convergence problems can easily occur when unsuitable grid distributions are used. More information on this subject is contained in the next section dealing with convergence.

A second possibility is to leave the grid unaltered, but abandon the assumption of linear variation of properties near the wall, putting in its place some information about the way in which the properties actually vary in the interval in question. The relations containing this information are commonly referred to as "wall functions." Suitable formulae for turbulent flows near smooth walls with zero pressure gradient were derived from Couette flows by Patankar and Spalding [40, 41] and Wolfshtein [35]. While the former base their functions on the Prandtl mixing-length concept, the latter makes use of the Prandtl-Kolmogorov hypothesis. In both cases, some of the important constants and functions needed for the completion of the system of

equations were deduced by reference to experimental data.

For rough walls, no wall functions have been derived yet. A paper by P. A. Taylor and Y. Delage [42] is a first approach in this direction. For their computation of atmospheric boundary layers with zero pressure gradient over rough terrain they assume a constant flux wall layer having a logarithmic velocity profile for the calculation of the first interior grid point. The formulation of the wall boundary condition for the turbulence kinetic energy (Equation 4.67) is based on this assumption.

The provision of a comprehensive set of wall functions valid for most situations of practical interest is one of the prime tasks of current research in computational fluid dynamics dealing with turbulence.

A third alternative, much less sophisticated, follows the basic wall function concept to account for the nonlinear behavior near the wall. Taking advantage of the fact that in the present problem  $\omega^*$  and  $\psi^*$  are fairly independent of grid size inside the flow field it determines the location of the separating streamline, i.e., the second zero of  $\psi^*$ , by extrapolation from the interior of the flow field. Figure 4.16(b) shows a typical turbulent flow  $\psi^*$ -distribution through the separation region as obtained with the coarser grid. With the assumption of linear variation the distribution between grid points follows the solid line. This is a good approximation except for the small region near the wall, where the estimated correct distribution is

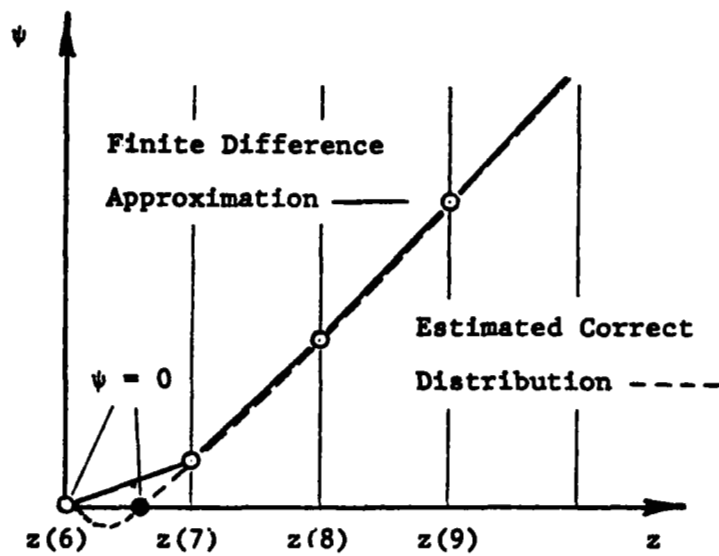
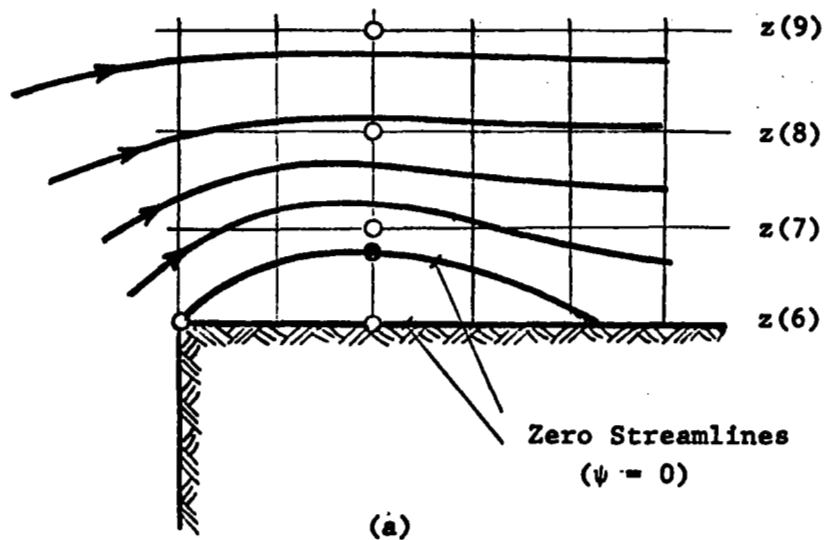


Figure 4.16. Explanation of extrapolation of second zero of stream function value.

represented by the dotted line. The second zero of  $\psi^*$ , the separation streamline, will always be neglected by the linear approximation if it falls between the first two grid-points. Because of the almost linear, slightly parabolic behavior of the stream function closer to the wall, as seen in Figures 4.6, 4.8, and 4.10, pages 110, 112, and 114, a parabolic extrapolation was used for the location of the second zero of the stream function, starting from the first two interior  $\psi$  values towards the wall. A typical result is presented in Figure 4.17 which shows streamline plots for the same flow case with (4.17(b)) and without (4.17(a)) extrapolation of the separating streamline.

Factors affecting convergence. While accuracy greatly depends on mesh size, the convergence of the iterative solution procedure heavily depends on the mesh size variation. Recommendations from an accuracy viewpoint, e.g., variable grid size near walls, have to be applied with caution when laying out a suitable mesh. It has been experienced by Gosman, et al. [20] and also in this study that near walls nonuniform grid spacing between grid lines parallel to the wall may cause divergence due to the coupling of the vorticity and the stream function equation through the vorticity boundary condition (Equation 4.62). The suggested [20] remedies listed below have been found quite effective.

1. Near the wall the ratio of consecutive intervals



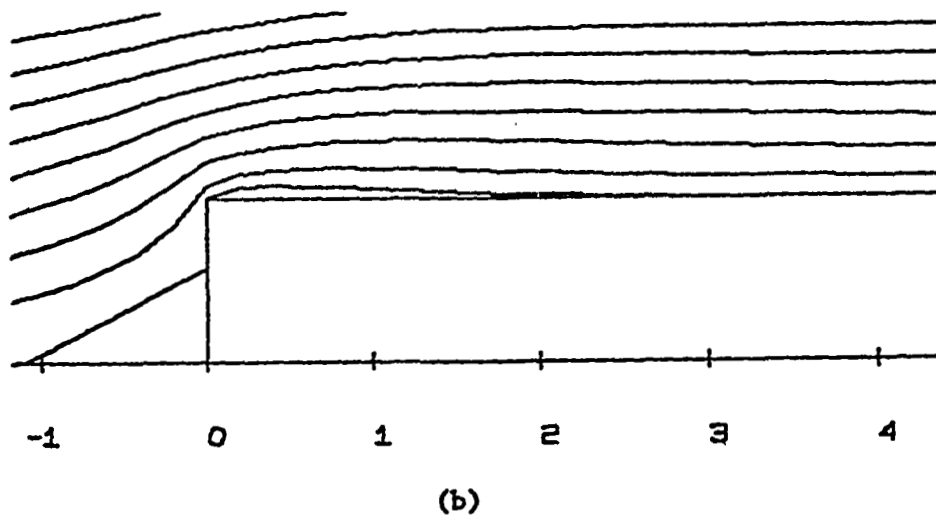
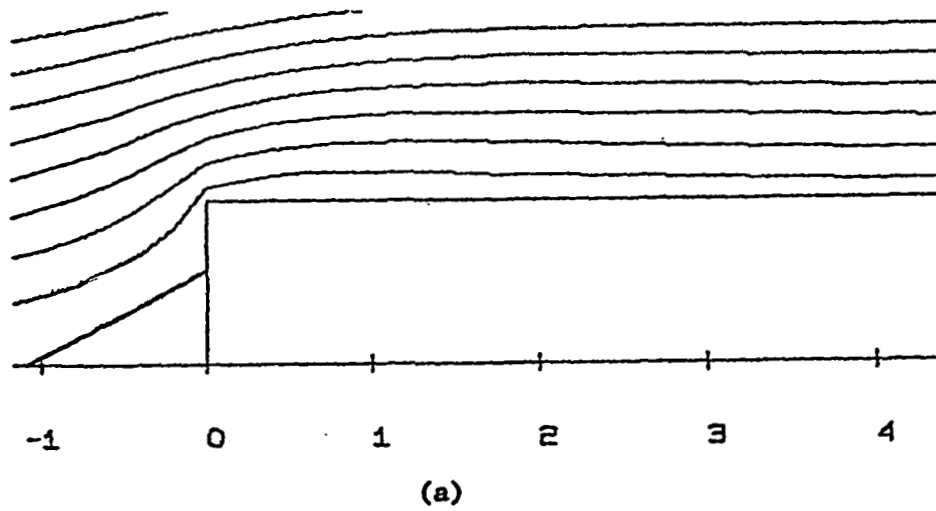


Figure 4.17. Streamline plots using (a) normal linear interpolation, and (b) parabolic extrapolation of the separating streamline.

between the nodes normal to the wall should be kept as close to unity (i.e., uniform) as possible or otherwise below 1.5.

2. The vorticity boundary condition (Equation 4.62) should not be used explicitly at the wall, but be incorporated into the general substitution formula for the iterative solution (implicit formulation for vorticity).

In the present investigation this last condition was not necessary to assure convergence.

Another source of divergence is that even inside the flow field large variations of the coefficients in the substitution formula may occur. This is true especially in the turbulent kinetic energy solution cycle for the source term  $S_k^*$  (Equation 4.19). As shown by [20], the substitution formula can in this case be rearranged through simple algebraic manipulations such that variations in a modified source term stay small. It was found in the present study that this approach may also be used for the substitution formula of the turbulent length scale if its source term  $S_\lambda^*$  (Equation 4.23) should cause divergence.

A more commonly employed remedy against divergence of the iteration process, although more time consuming, is known as under-relaxation. Compared to the method just discussed, it is more easily applied in the various cases, but has the disadvantage of slowing down the iteration process, thus increasing the computing time, depending on the

degree of under-relaxation. For the present problem there was no need for under-relaxation. On the contrary, the stream function, related to the vorticity by a Poisson type equation (Equation 4.10), could be over-relaxed to speed up the solution.

Termination of computation. The computation was assumed to have converged to a sufficiently exact solution if the difference of the dependent variable  $\phi$  at point P between successive iterations became small, i.e.,

$$\left| \frac{\phi_P^N - \phi_P^{N-1}}{\phi_P^N} \right|_{\max} \leq \epsilon = 0.01 - 0.05 \quad (4.71)$$

The superscript N denotes the nth iteration.  $\phi_P$  rather than  $\phi_{\max}$  was chosen in the denominator as a scaling factor in order to assure relatively good convergence also in areas of small  $\phi_P$  values. For the average solution using the Two-Equation model of turbulence with a  $41 \times 24$  grid system (Figure 4.4, page 97) this was normally achieved after about 50 iterations, taking about 7-1/2 minutes on an IBM-360-65 computer.

#### IV. RESULTS AND DISCUSSION

The results obtained in the present study include a laminar flow solution and three turbulent flow solutions, the first of which uses the mixing length model, the second,

the turbulent energy hypothesis with a prescribed mixing length distribution, and the third, the Two-Equation model (all described in Section II of this chapter). For the latter turbulence model a parametric study of two parameters of the approach wind profile,  $u_*^*$  and  $z_0^*$ , was carried out. Before these results will be discussed, some light shall be shed on factors influencing the solution and affecting the accuracy from a different viewpoint than that discussed in the previous sections. It is referred to the empiricism involved in the solution procedure entering not only through a "proper" choice of coefficients  $C_{\mu_0}$ ,  $C_{D_0}$ ,  $C_{B_0}$  and  $C_{S_0}$  in Equations 4.16, 4.19 and 4.23, but also through the selection of "suitable" boundary conditions whose dominating effects are not always recognized.

### Factors Influencing the Solution

Boundary conditions. In many cases it is quite easy to conjure up some kind of plausible boundary conditions, but attempts to determine boundary conditions which are equally realistic, accurate and stable can be highly frustrating and often their selection ends with the compromise that the first condition is neglected in favor of the last two.

This is even more the case when conditions cannot properly be formulated because the necessary empirical information is not available. Unfortunately, the only way around this problem is to extend the computations far enough

upstream or downstream that either realistic assumptions can be made (vanishing gradients) or the influence from the boundary conditions becomes negligibly small for the region of interest in the flow field.

This problem arises not so much with the formulation of the more familiar boundary conditions for vorticity and stream function, which, with the exceptions discussed earlier, are believed to be rather unequivocal, partially because one can draw heavily from wind tunnel tests or flow visualization experiments.

The problem appears, however, with the more unknown variables  $k^*$  and  $\epsilon^*$ , with the formulation of the outflow boundary condition being the most controversial. Should the turbulence kinetic energy, for example, be allowed to decay back to the original free stream value (Equation 4.52) or should it exceed this value in dependence on the higher local friction velocity (Equation 4.46)? Should it be constant in the  $z^*$ -direction or should its streamwise variation be zero? Fortunately, none of the above conditions posed any convergence problems so they could all be investigated. The results are shown in Figures 4.18 and 4.19. It should be mentioned that the stream function as well as the vorticity pattern were hardly affected by the above changes in the  $k^*$ -boundary condition and are therefore omitted. A comparison between the turbulence kinetic energy distributions of the first two cases shows that the influence of the outflow boundary conditions

(a)

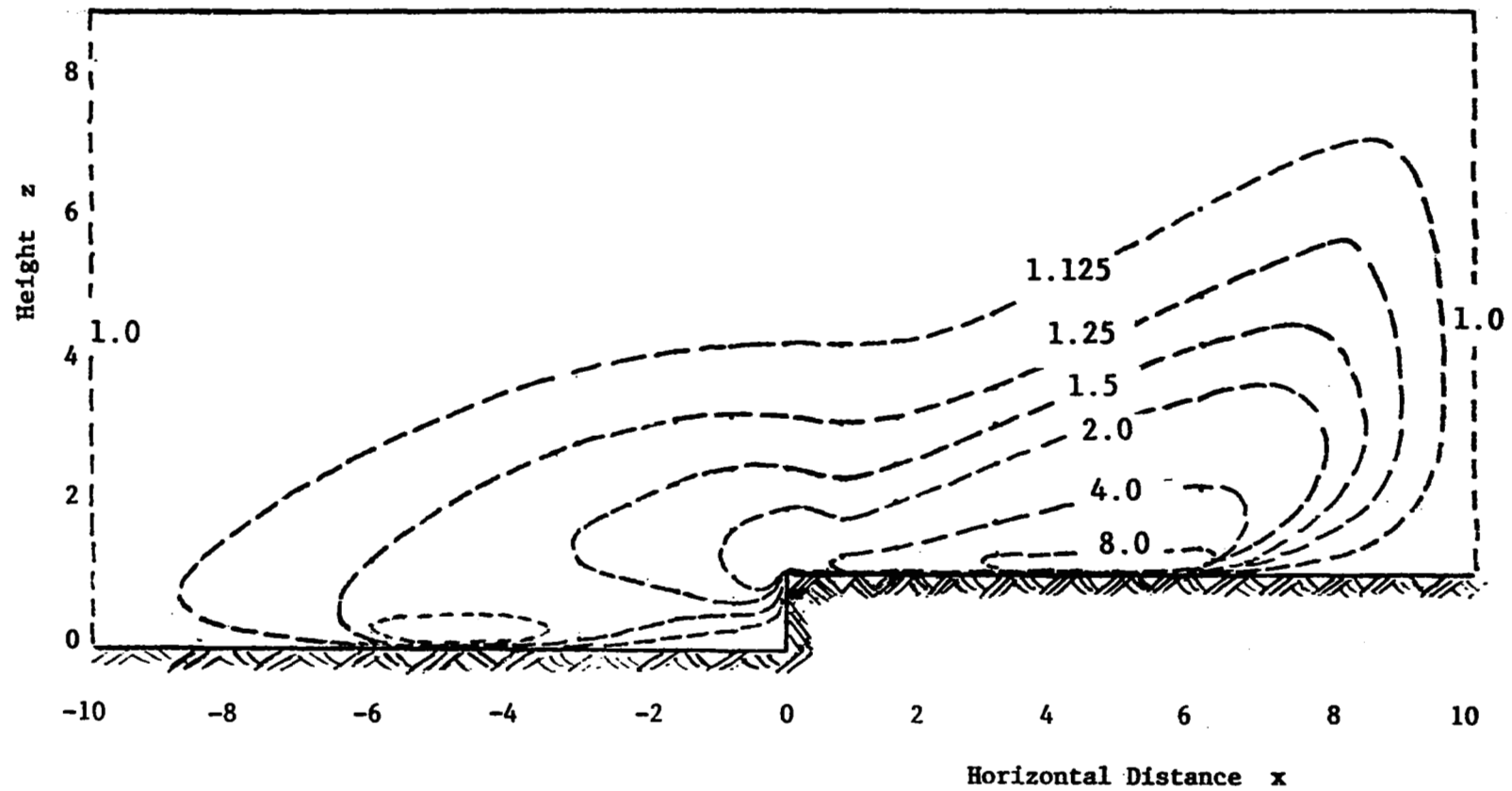


Figure 4.18. Influence of outflow boundary condition on k-solution;  
(a)  $k^* = (u_*^*/C_{\mu_0})^2$  and (b)  $(\partial k^*/\partial x^*) = 0$ .

(b)

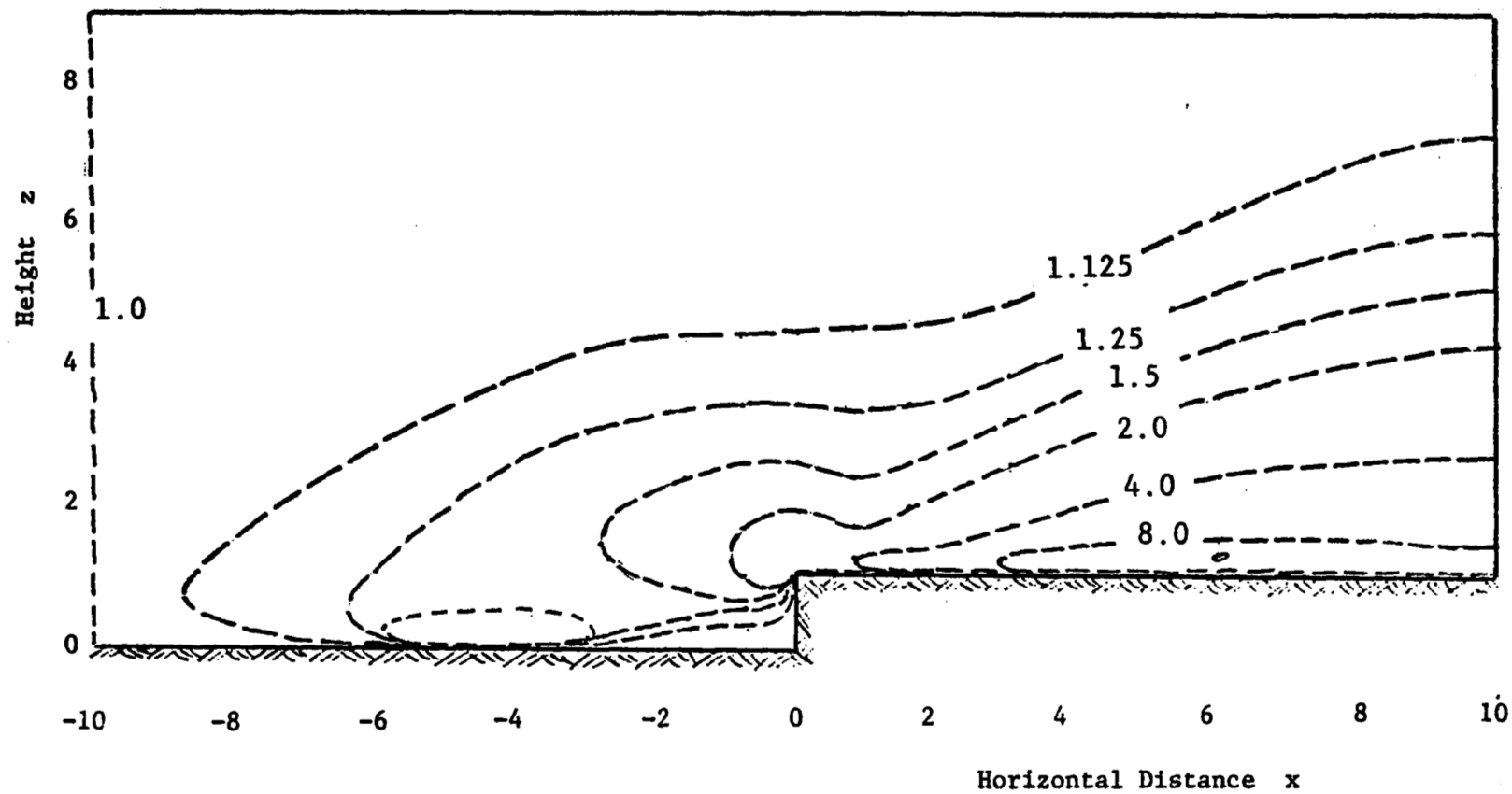


Figure 4.18. (continued)

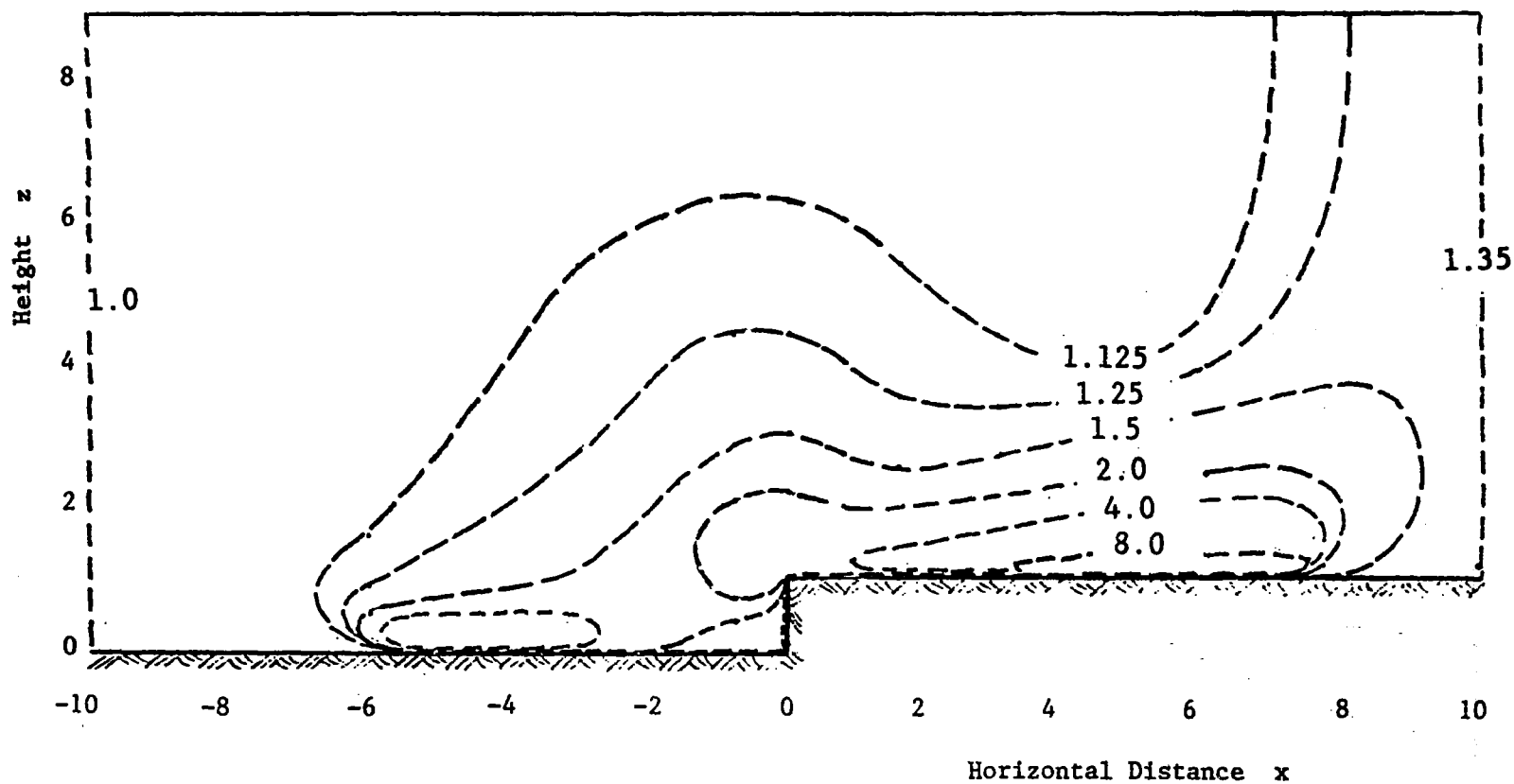


Figure 4.19. Influence of outflow boundary condition on k-solution,  
 $k^* = (u_{*out}^*/C_{\mu_0})^2$ .



(a)

$$k^* = \left( \frac{u_{*}^*}{C_{\mu_0}} \right)^2 \quad (4.52)$$

and (b)

$$\frac{\partial k^*}{\partial x^*} = 0$$

is limited to a far downstream region about seven step heights behind the step. Apart from this region the two solutions are the same and, therefore, independent of their particular boundary condition. The third case with

$$k^* = \left( \frac{u_{*out}^*}{C_{\mu_0}} \right)^2 \quad (4.46)$$

shows a somewhat different picture. The changes brought about by this condition seem bigger and reach farther into the flow field than in the previous case. While with the first two conditions the  $k^*$ -decay in  $z^*$ -direction is faster before the step than it is behind it, the reverse is true here. This behavior is partially a result of the upper boundary condition  $\partial k^* / \partial z^* = 0$ . More realistically this boundary condition should be  $\partial k^* / \partial x^* = 0$  which is equivalent to  $k^* = \text{const.}$  Substituting this boundary condition into the case presented in Figure 4.18(a), one obtains the distribution shown in Figure 4.20. Comparing the two one finds hardly any or little changes.

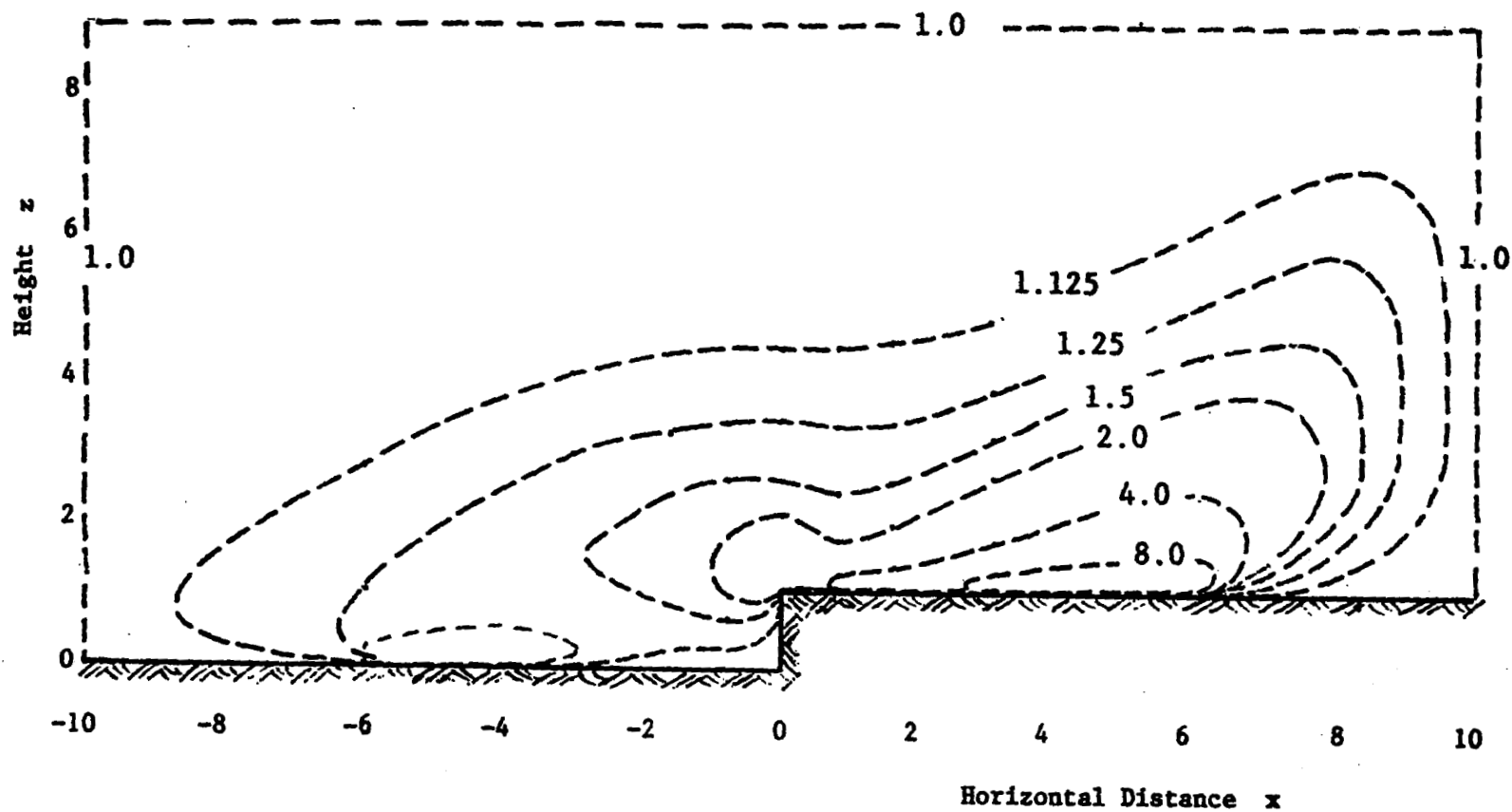


Figure 4.20. Influence of upper boundary condition on  $k$ -solution,  
 $(\partial k^*/\partial x^*) = 0$ .

In conclusion, it can be said that in the present study, except for the conditions chosen in Figure 4.19, page 133, the upper and outflow boundary conditions for  $k^*$  do not significantly influence the solution. The question if (a) or (b), i.e.,  $k^* = \text{const.}$  or  $k^* = f(z^*)$ , is the more realistic boundary condition becomes superfluous, because apart from the immediate vicinity of the boundary they gave the same results. For this reason and the fact that prescribed boundary values give generally better convergence than normal gradient type conditions, the  $k^*$ -boundary conditions of Figure 4.20 were mainly used in the following computations. Similar arguments hold for the boundary conditions of the turbulence length scale  $\ell^*$ .

Empirical coefficients. It was already pointed out earlier that the empirical constants appearing in Equations 4.19 and 4.23 are no universal constants, but depend on the particular flow case under consideration. It is common practice to determine these constants in a preliminary evaluation by applying the governing equations to simple flow situations such as Couette flows [35], flows with homogeneous turbulence behind a grid [36] or turbulent boundary layers in local equilibrium where the generation of turbulence at any point in the flow field is balanced by the local dissipation [36]. To achieve closure, the relations found this way will then have to be supplemented with information gained from experimental data. However, if

experimental results are not available, there is little hope for an exact determination of the constants and the above path has to be abandoned.

Instead, we shall proceed in a different fashion and shall look at the individual constants and examine how their variation effects the solution. Also, a trial set of "universal" constants deduced from an early proposal of Spalding [43] for a Two Equation model actually using length scale as the second turbulent transport equation will be tested. Finally, a set of preliminary constants will be selected as a result of the foregoing investigation.

Table 4.2 gives a summary of the individual sets of constants reviewed. Case 1 is the reference solution. Cases 2 through 6 represent attempts to assess the respective influence of variations in the effective viscosity ( $\Delta C_{\mu_0}$ ), in the turbulence kinetic energy dissipation rate ( $\Delta C_{D_0}$ ), in the effects of length scale stretching ( $\Delta C_{S_0}$ ) and of the length scale breaking ( $\Delta C_{B_0}$ ) on the solution. The investigation included the survey of the respective  $\psi^*$ ,  $k^*$  and  $\lambda^*$  distributions.

The results are shown in Figures 4.21 through 4.28. The turbulence kinetic energy distributions have been non-dimensionalized with the turbulence kinetic energy of the undisturbed approach flow and for easier comparison the turbulence length scale variations for the different cases are presented in a single figure (4.28) where only the respective lines of constant  $\lambda^*$  passing through one and the

TABLE 4.2

SET OF EMPIRICAL CONSTANTS USED IN TRIAL CALCULATIONS

Case	$C_{\mu_0}$	$C_{D_0}$	$C_{S_0}$	$C_{B_0}$
1	1.0	1.0	1.0	1.0
2	0.1	1.0	1.0	1.0
3	1.0	0.1	1.0	1.0
4	1.0	1.0	0.1	1.0
5	1.0	1.0	1.0	0.1
6	2.0	1.0	1.0	1.0
7	1.74	1.18	0.27	0.14
8	1.0	0.1	0.27	0.14

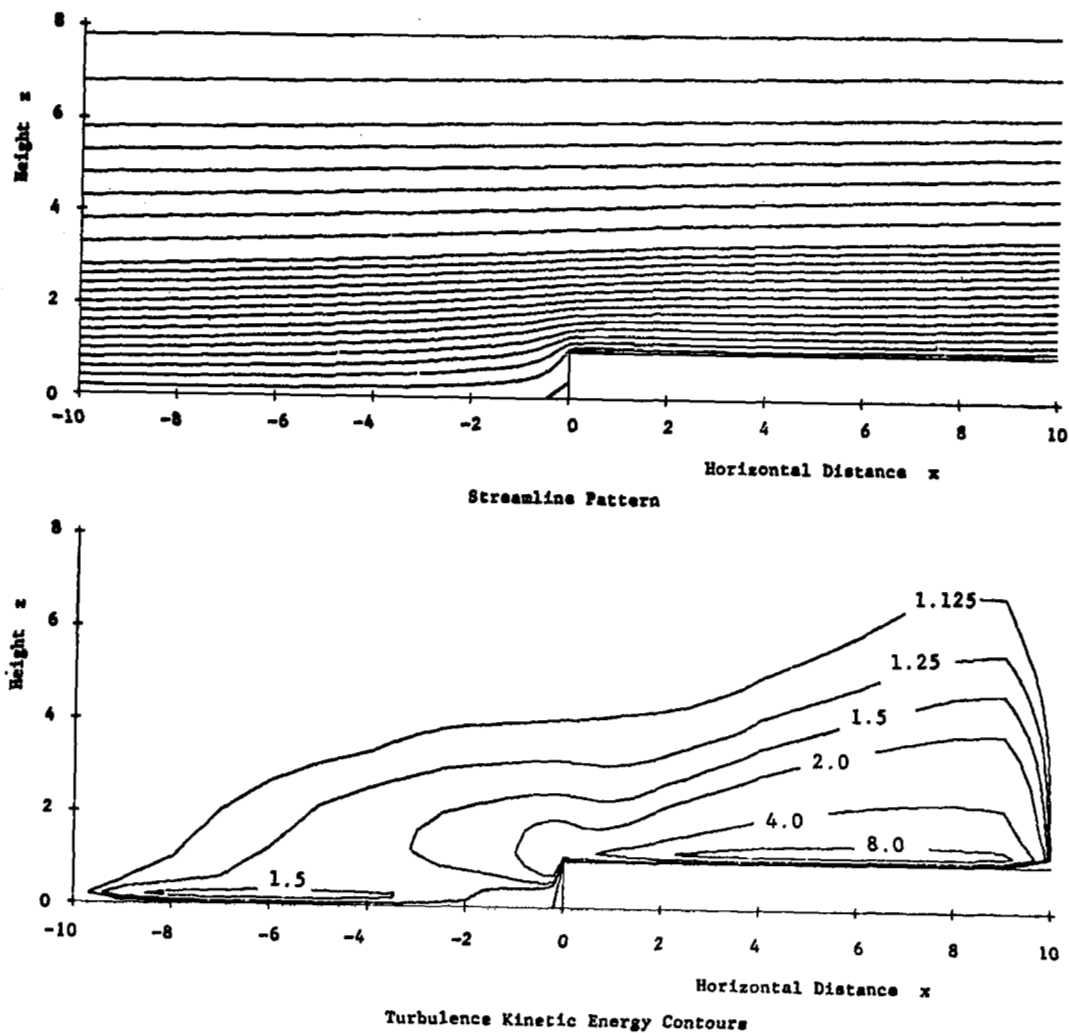


Figure 4.21. Streamline pattern and turbulence kinetic energy contours for case 1 ( $C_{\mu 0} = 1.0$ ,  $C_{D0} = 1.0$ ,  $C_{S0} = 1.0$ ,  $C_{B0} = 1.0$ ).

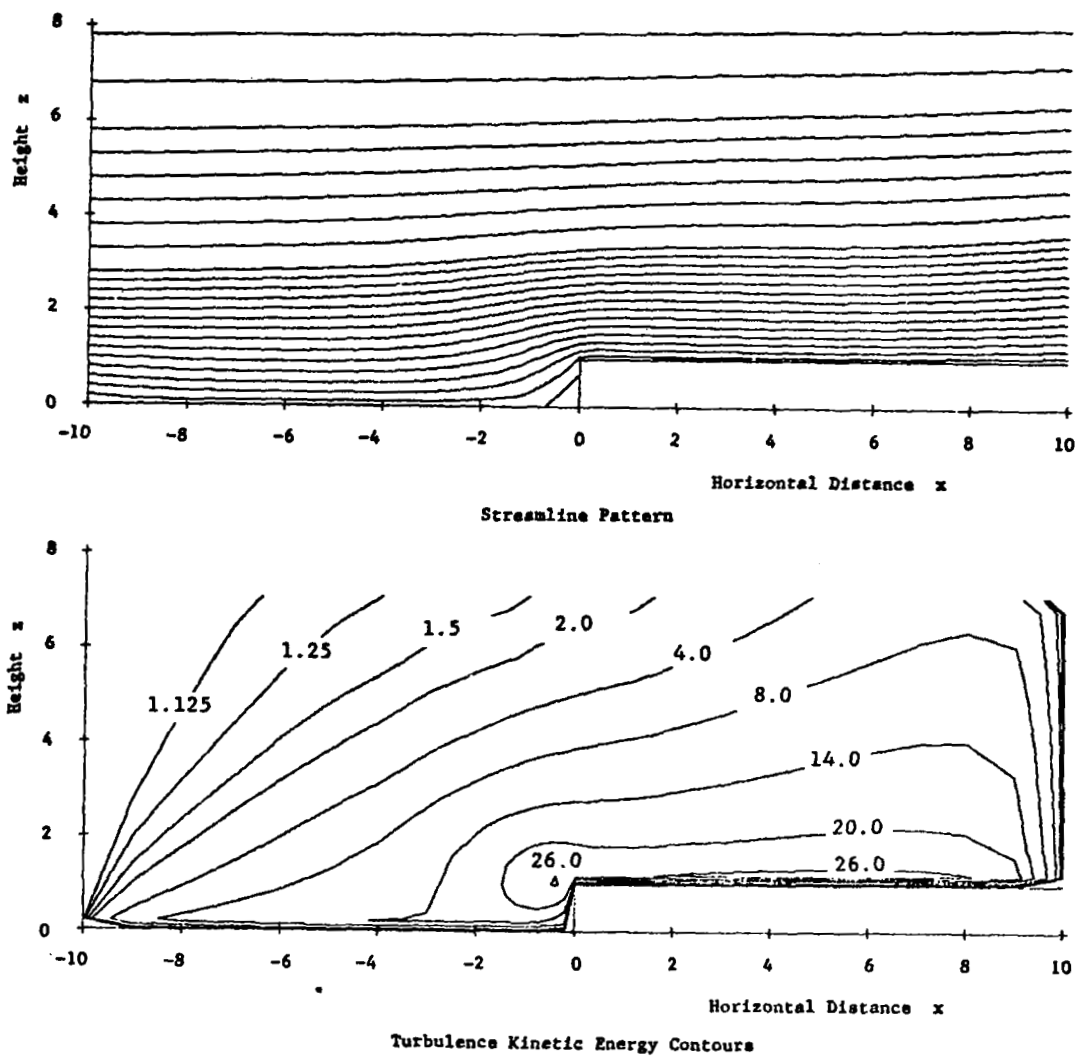


Figure 4.22. Streamline pattern and turbulence kinetic energy contours for case 3 ( $C_{\mu 0} = 1.0$ ,  $C_{D0} = 0.1$ ,  $C_{S0} = 1.0$ ,  $C_{B0} = 1.0$ ).

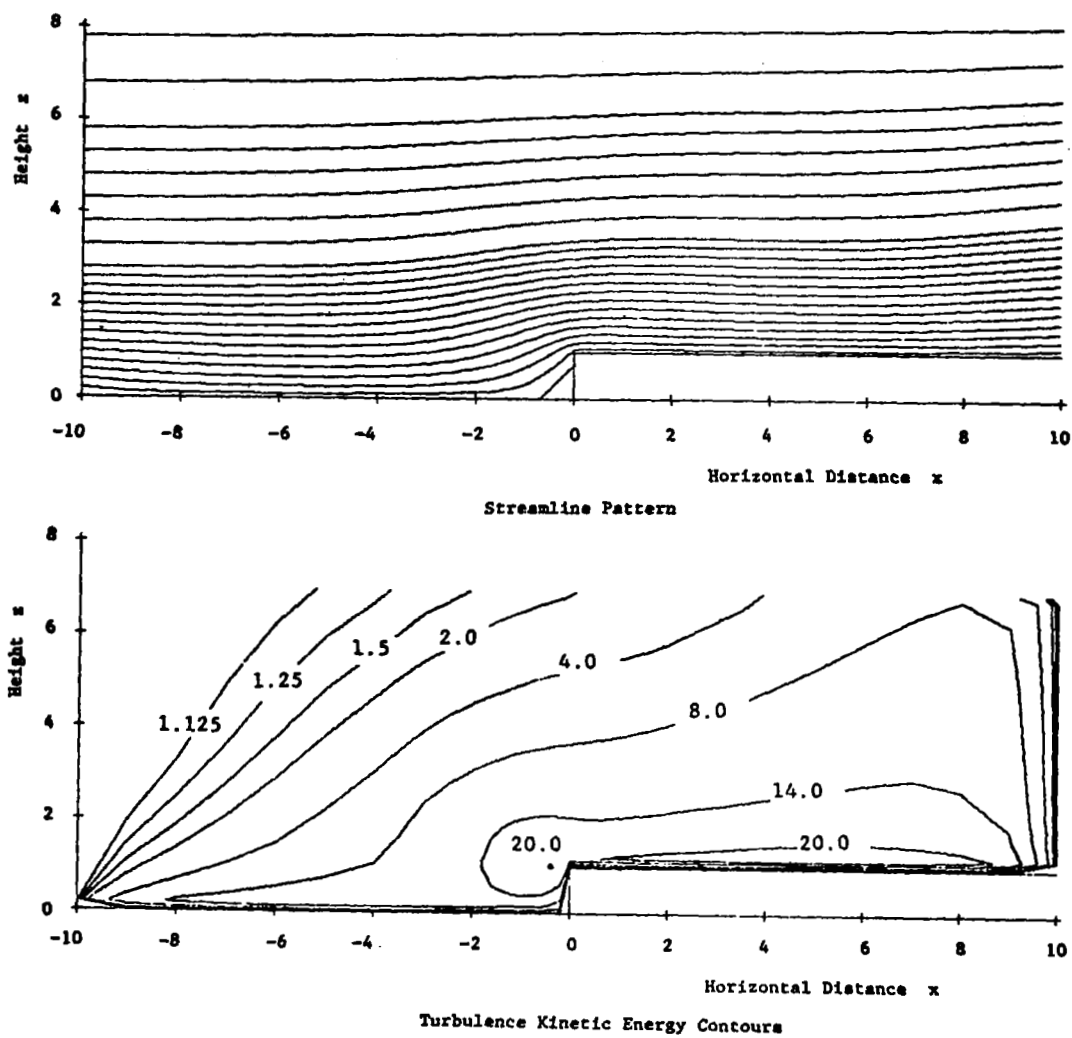


Figure 4.23. Streamline pattern and turbulence kinetic energy contours for case 5 ( $C_{\mu 0} = 1.0$ ,  $C_{D0} = 1.0$ ,  $C_{S0} = 1.0$ ,  $C_{B0} = 0.1$ ).



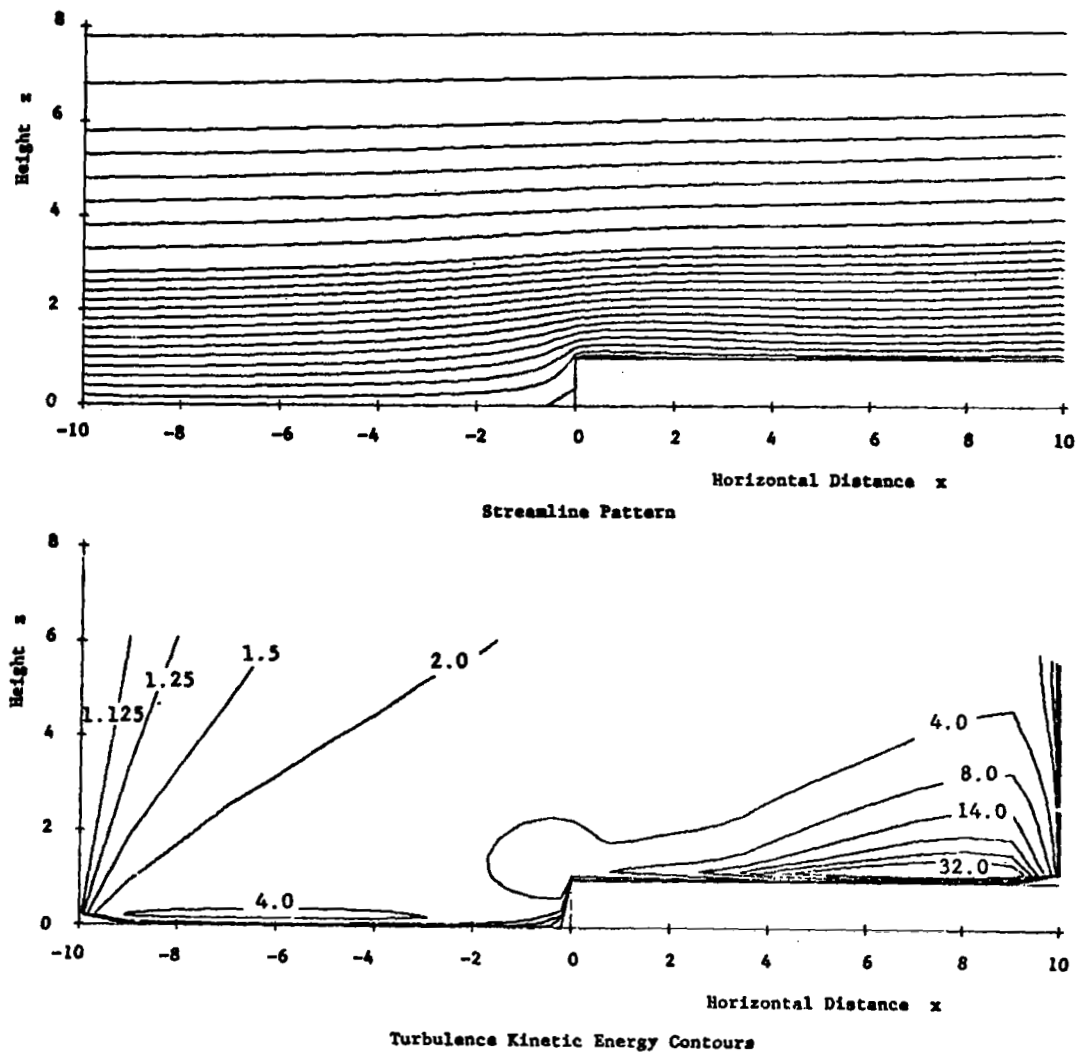


Figure 4.24. Streamline pattern and turbulence kinetic energy contours for case 6 ( $C_{\mu 0} = 2.0$ ,  $C_{D0} = 1.0$ ,  $C_{S0} = 1.0$ ,  $C_{B0} = 1.0$ ).

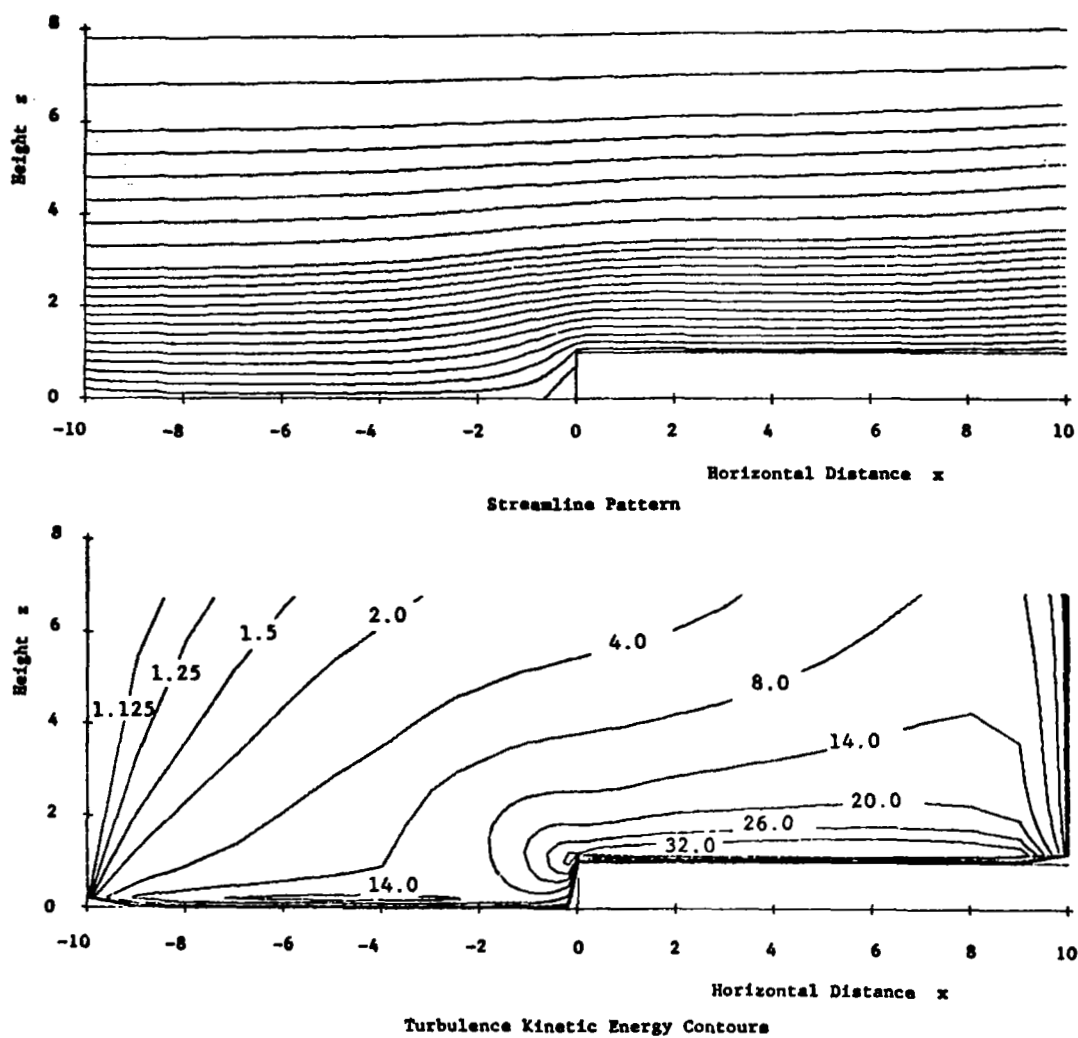


Figure 4.25. Streamline pattern and turbulence kinetic energy contours for case 7 ( $C_{\mu 0} = 1.74$ ,  $C_{D0} = 1.18$ ,  $C_{S0} = 0.27$ ,  $C_{B0} = 0.14$ ).

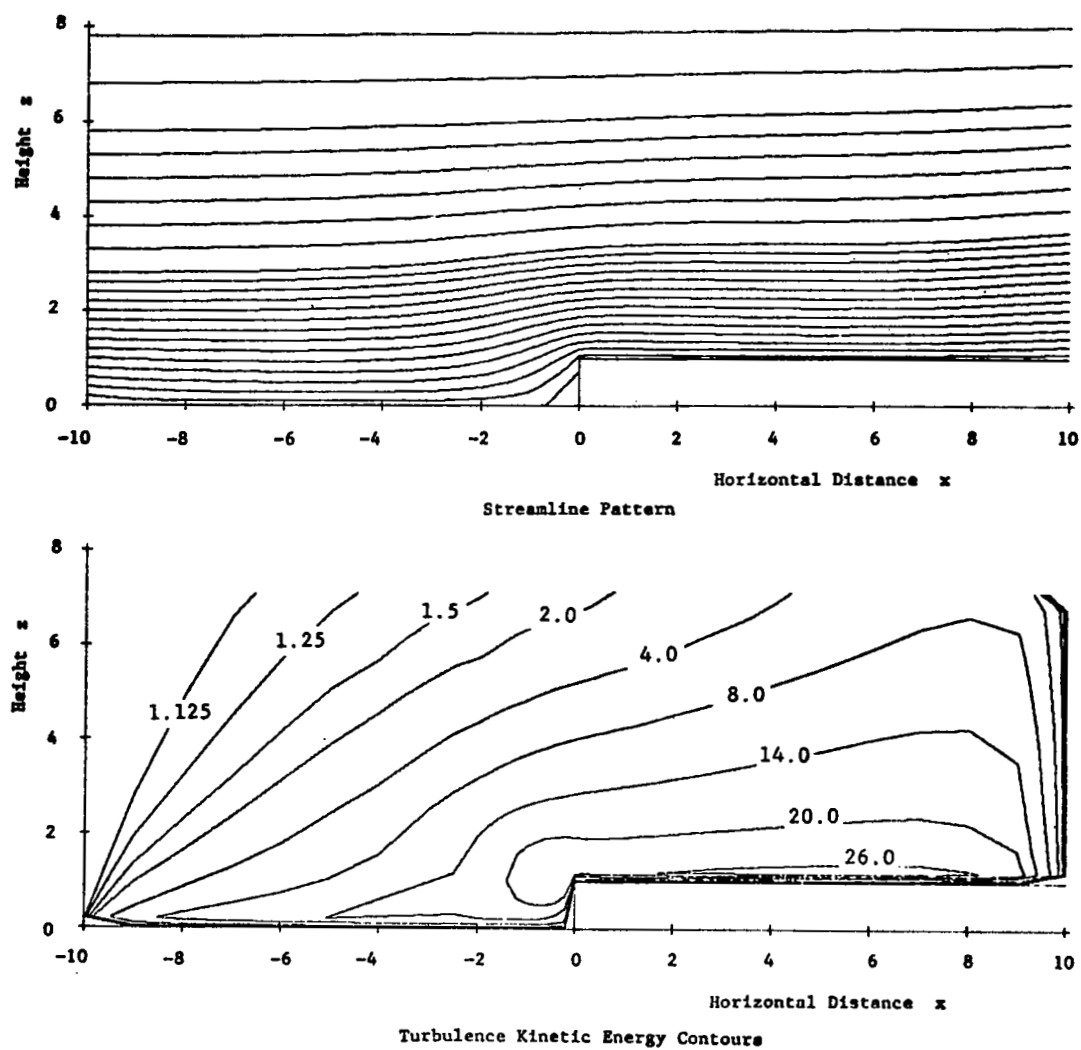


Figure 4.26. Streamline pattern and turbulence kinetic energy contours for case 8 ( $C_{\mu 0} = 1.0$ ,  $C_{D0} = 0.1$ ,  $C_{S0} = 0.27$ ,  $C_{B0} = 0.08$ ).

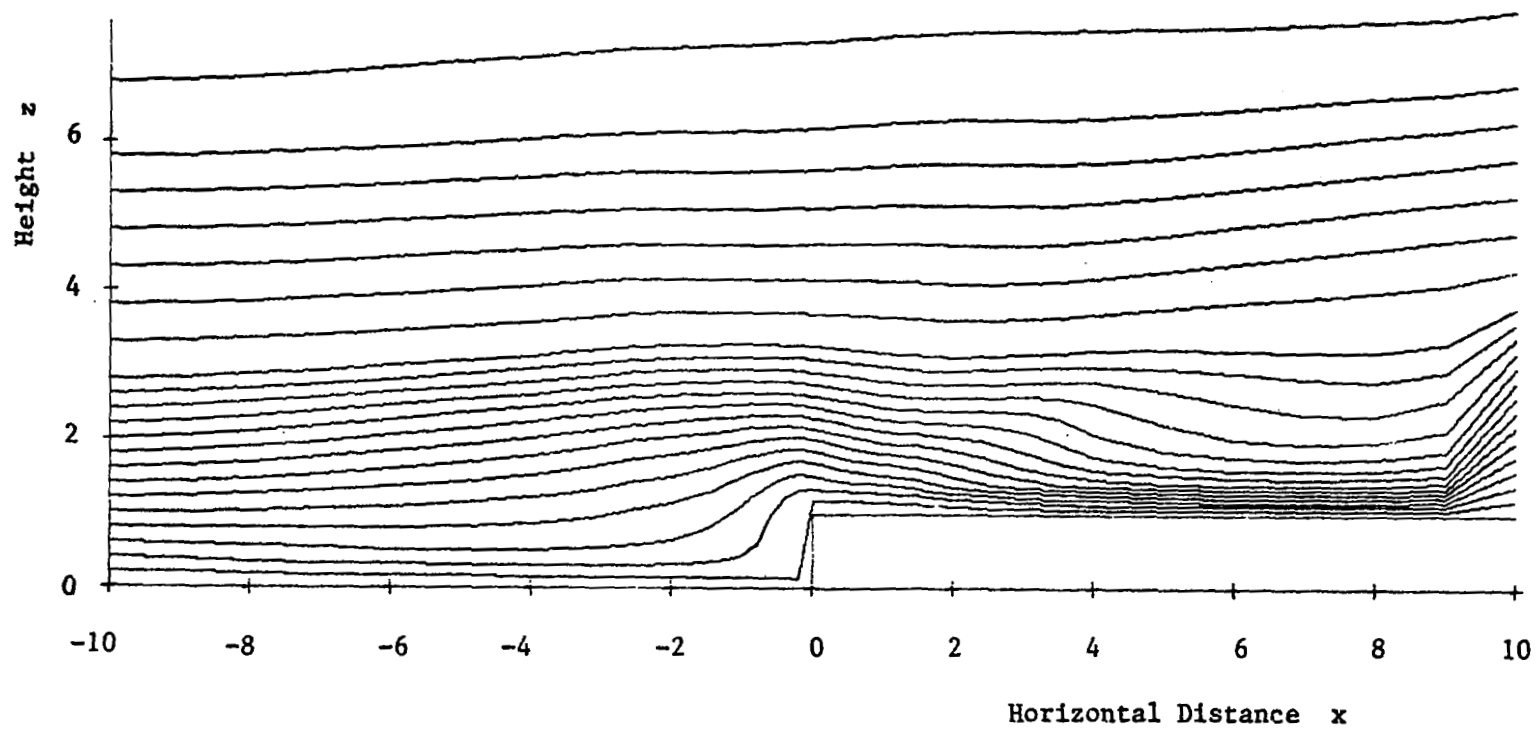


Figure 4.27. Length scale distribution for case 1 (lines of constant  $l^*$ ).

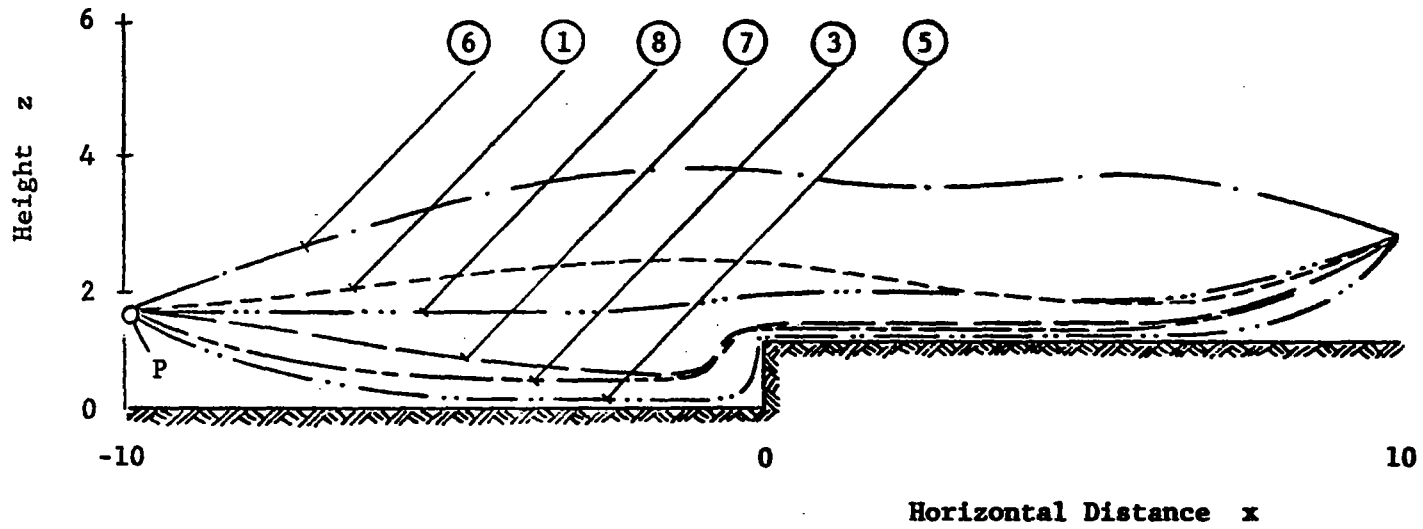


Figure 4.28. Lines of constant length scale passing through point P for the different cases.

same upstream point P are plotted. Case 1, the reference solution, with all constants set equal to unity shall not be further discussed at the moment. We shall return to this solution later.

In case 2 with  $C_{\mu_0} = 0.1$  for which no figure is shown, it was intended in view of Equation 4.16 and the first term on the right side of Equation 4.19 to cut down the turbulence kinetic energy production. This was easily achieved, however, the amount of reduction was too large. Everywhere in the flow field  $k^*$  was smaller than the approach condition of unity, implying that the step would reduce turbulence. A reasonable reduction should be obtained for a value of  $C_{\mu_0}$  only slightly smaller than one.

An increase in  $k^*$  was obtained in case 6 (Figure 4.24) with  $C_{\mu_0} = 2.0$ . Compared with the reference solution, a doubling of  $C_{\mu_0}$  produced a maximum  $k^*$  about four times as large.

The turbulence kinetic energy levels should also increase if the dissipation rate is diminished, thereby increasing the net-production (Equation 4.19). This was done in case 3 by setting  $C_{D_0} = 0.1$ . The resulting  $k^*$ -distribution (Figure 4.22) has a maximum of about 3-1/4 times that of the reference case, which like case 6 is unrealistically high.

The attempt to decrease the length scale stretching contribution (Equation 4.23) by reducing  $C_{S_0}$  to 0.1 in case 4 failed, because the numerical procedure diverged.

However, decreasing the length scale breaking contribution with  $C_{B_0} = 0.1$ , thus increasing the net  $\ell^*$ -production and the  $k^*$ -generation (case 5) had a similar effect to decreasing the dissipation in case 3. The  $k^*$ -levels rose in the maximum to about 3-1/2 times the reference values.

Thus, there are four effective means to increase the turbulence kinetic energy levels:

1. Increase  $C_{\mu_0}$ .
2. Increase  $C_{S_0}$ .
3. Decrease  $C_{D_0}$ .
4. Decrease  $C_{B_0}$ .

Reducing the turbulence kinetic energy requires opposite measures but from the experience with cases 2 and 4 we know that these have to be applied with greater moderation.

In the above trials only one of the respective constants was changed at a time to test the individual effect, but due to the coupling of the governing equations, changes of several parameters at a time can have quite different effects than can be estimated from the individual behavior and a more systematic investigation is required.

However, we shall restrict ourselves in the current study to the above cases and will only, out of curiosity, try Spaldings [43] coefficients (case 7). The resulting  $k^*$ -distribution is as high as some of the previous cases ( $C_{\mu_0} = 2.0$ ). This is probably a result of the relatively large value for  $C_{\mu_0}$ .

Other researchers from the same group of Gosman, et al. [20] at the Imperial College [36, 37] later used much lower values for the constants in the  $k^*$ -equation and these values were also tried, case 8. The constants for the  $\ell^*$ -equation from [43], i.e.,  $C_{S_0} = 0.27$  and  $C_{B_0} = 0.08 C_{\mu_0}$  were still retained, however. Figure 4.26, page 144, shows the corresponding  $k^*$ -distribution, which surprisingly enough is almost identical to the one in case 3 where  $C_{\mu_0}$  and  $C_{D_0}$  had the same values, though different coefficients for the  $\ell^*$ -equation were used. It seems that the influence of  $C_{\mu_0}$  and  $C_{D_0}$  dominates the influence of the coefficients in the length scale equation.

Until this point we have only looked at the turbulence kinetic energy distributions, but the goodness or physical reality of a solution is probably better recognized from the stream function distribution or even the length scale plot.

It is interesting to note that in the respective stream function plots there are hardly remarkable changes, except for the cases 1 and 6 which are the only ones producing a noticeable separation from the corner.

It is, therefore, not without reason that the length scale distributions in Figure 4.28, page 146, for these two cases are different from those of the remaining cases. They are not only different, but more important physically more meaningful. This insofar as it seems quite correct that  $\ell^*$  decreases as one approaches the step parallel to the wall,



due to the acceleration in the flow field, stretching the vortices or due to the breaking of the larger eddies by the increasing shear.

It can be seen in Figure 4.27, page 145, that closer to the wall the reverse is true. Here the increase of  $\ell^*$  along a line of constant height represents the dissipation of energy from smaller eddies and the formation of larger eddies due to the deceleration of the flow which finally results in the formation of the front separation region.

A similar phenomenon should occur near the upper separation region in those cases where separation occurs (cases 1 and 6). It seems realistic that after the region of decreasing  $\ell^*$  in front of the step a region of growth of  $\ell^*$  should develop because it is essential for the top separation or recirculation region to form that energy is dissipated from the smaller eddies into this region of larger  $\ell^*$ .

This estimated correct behavior in the  $\ell^*$ -distribution is predicted only in cases 1 and 6, which from this viewpoint seem to be the most realistic. They are also the only ones to create a top separation region in the  $\psi^*$ -plot which is experimentally known. In case 6, however, the turbulence kinetic energy distribution was very high, and not as realistic as for the reference case.

For these reasons it is believed that case 1, where all "empirical" constants are set equal to unity, presents a physically meaningful description of the flow problem under

investigation. Therefore, it is recommended that until suitable experimental results are available to redefine the values of the individual constants, reasonable realistic predictions can be expected with values of unity for these constants, which were used throughout all subsequent calculations.

### Comparison of Different Models

Before looking at the results of the three turbulence models we shall take a brief look at some results of a "laminar" solution, which were obtained in the early stages of the program checkout, when the computer code for turbulent flow with the appropriate boundary conditions was tested with the turbulent viscosity  $\mu_t$  set equal to zero, to save computing time.

Laminar solution. As already indicated above we are not dealing with a truly laminar solution because of two reasons: First, the inflow and outflow boundary conditions for the stream function and the vorticity were based on the same logarithmic approach velocity profile used in the subsequent turbulent cases. A parabolic power law profile would have been a more suitable condition. Second, the occurring Reynolds number based on the step height

$$Re_n = \frac{u_n^* h^*}{\nu} \quad (4.72)$$

where

$$u_n^* = \frac{u_*^*}{\kappa} \ln \frac{h^* + z_0^*}{z_0^*} \quad (4.73)$$

of  $3.93 \times 10^6$  lies certainly outside the laminar flow regime. Therefore the "laminar" solution would probably better be called "quasi-laminar," in the sense that only the laminar or molecular viscosity is used for the calculation of a flow field which should actually be turbulent. Although one may question the validity of the solution under these circumstances, it exhibits some interesting features and shows typical laminar behavior when compared to some of the later turbulent solutions.

Figures 4.29 and 4.30 show the streamline distribution and a plot of the velocity profiles in the vicinity of the step. The laminar character of the flow can best be recognized by taking a short look at one of the subsequent turbulent solutions, for example Figure 4.31, and comparing the two solutions. We know from experience that laminar flow favors separation, while turbulence tends to suppress it, or leads to fast reattachment of the flow. The same trend can be observed here. In the laminar solution the flow ahead of the step separates earlier than in the turbulent case. In general, the disturbance caused by the step, recognized by the deflection of the streamlines, is felt much further upstream by the laminar flow than it is by the turbulent flow. While separation from the upper step corner is strong in the laminar case with the separation region extending far downstream, reattachment occurs already a

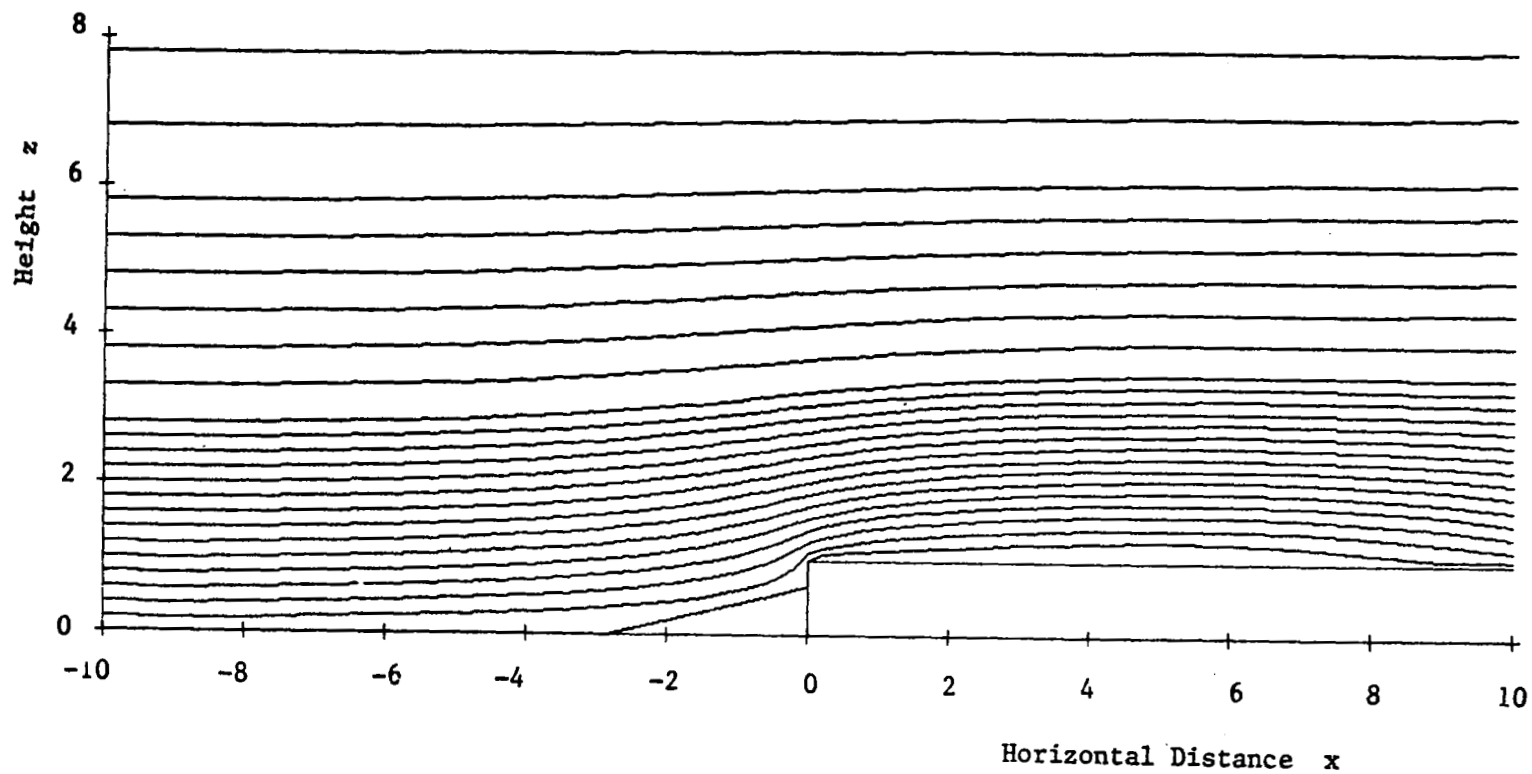


Figure 4.29. Streamline pattern for laminar flow solution ( $Re_n = 3.9 \times 10^6$ ).

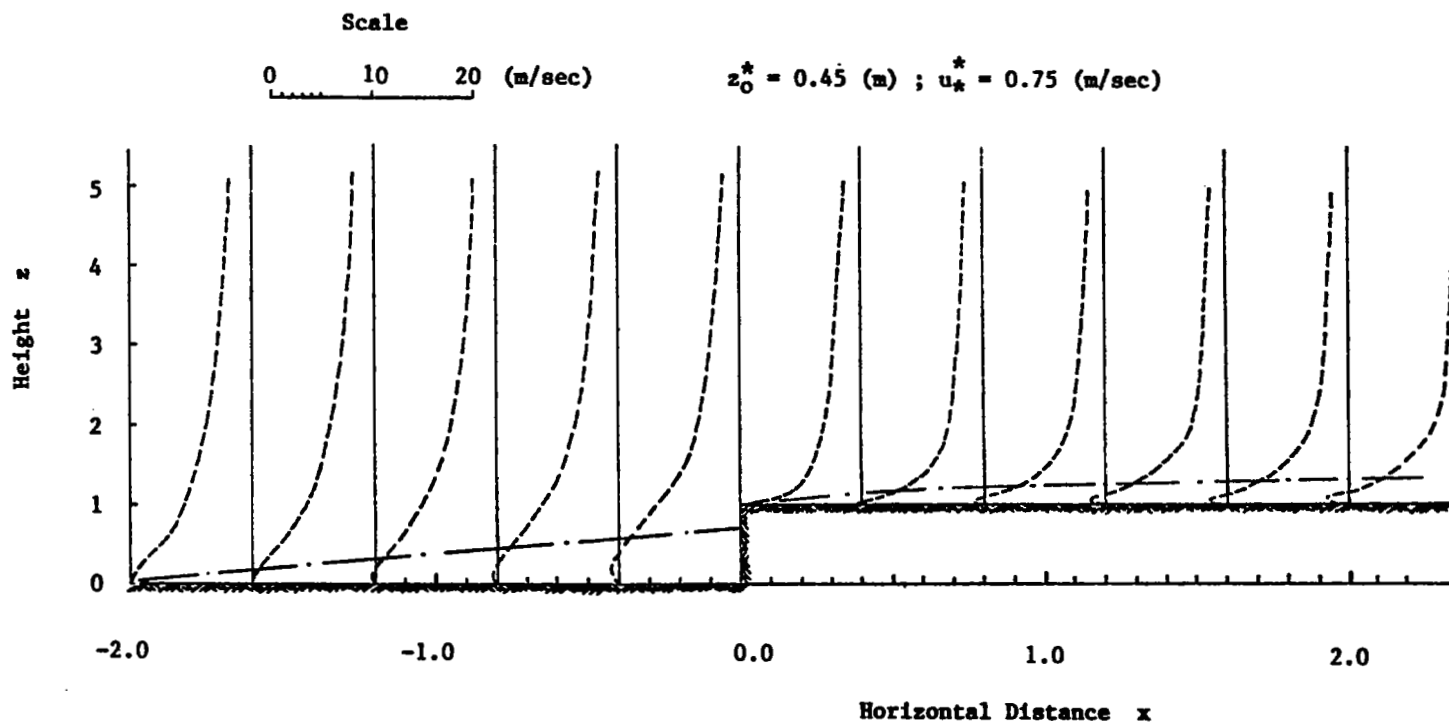


Figure 4.30. Velocity profiles for laminar flow solution.

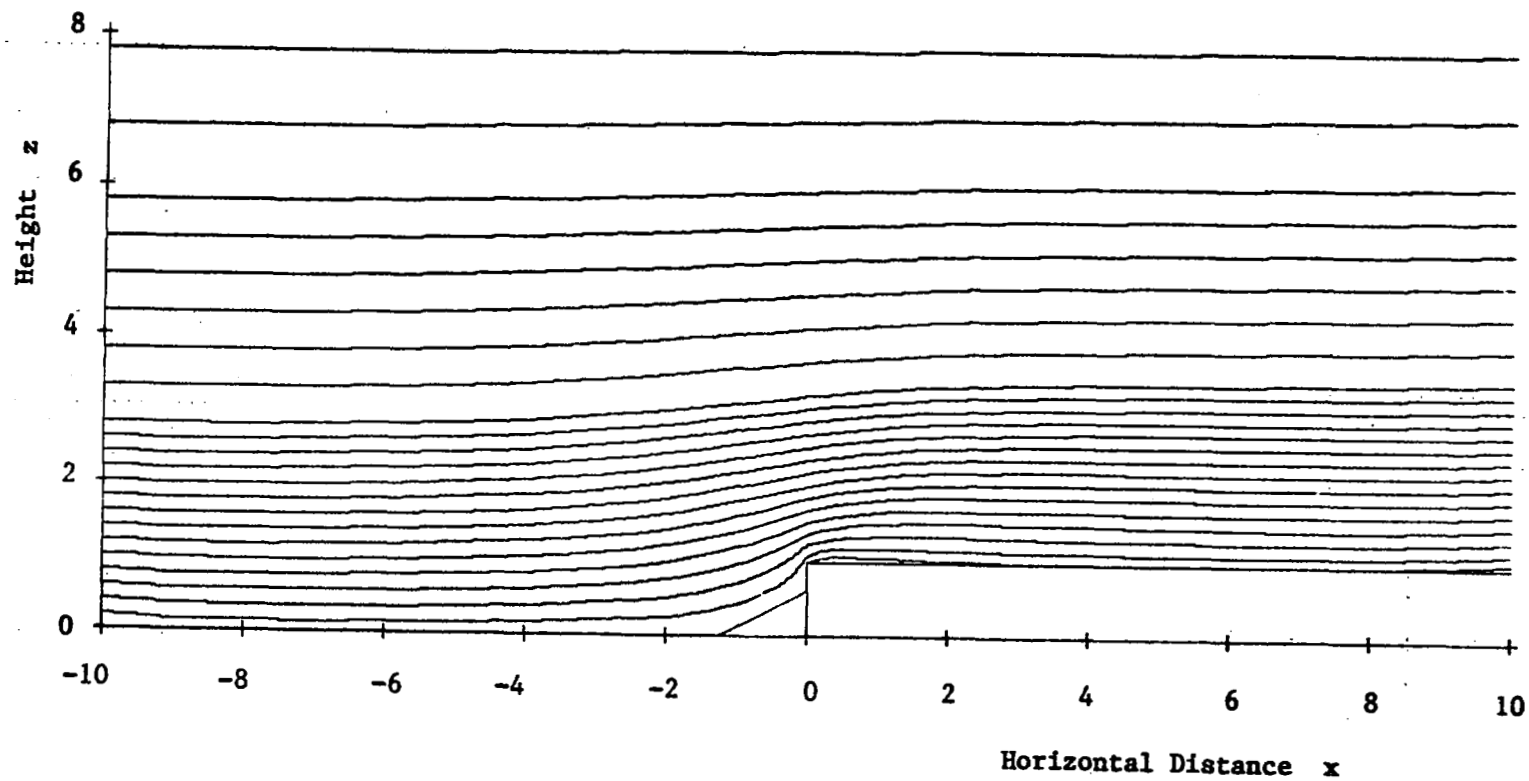


Figure 4.31. Streamline pattern for turbulent flow solution using the Prandtl-mixing-length concept ( $Re_n = 3.9 \times 10^6$ ).

short distance behind the upper step corner in the turbulent case.

Comparison of different turbulent solutions. Results for the three different turbulence models employed are shown in Figures 4.31 through 4.36. A streamline pattern for the PML model, a streamline distribution and the turbulence kinetic energy contours for the TKE model and finally a streamline pattern with turbulence kinetic energy and length scale distributions for the Two-Equation model.

From the respective streamline distributions it seems at first glance that all three solutions give approximately the same answers. However, this is deceiving as inspection of the remaining figures indicates and it is therefore appropriate to mention that the streamline pattern is not really a sensitive indicator of the correctness of the turbulence model. It is thus more informative to look at the turbulent quantities like turbulence kinetic energy, shear stress or effective viscosity, where the last two can readily be compared in all three solutions.

In Figures 4.37 and 4.38 we see the individual effective viscosity predictions along the upper step wall for the near wall nodes as well as for the surface itself. Although measurements of shear stress near reattachment are not completely reliable, it is fairly well known that the surface shear stress

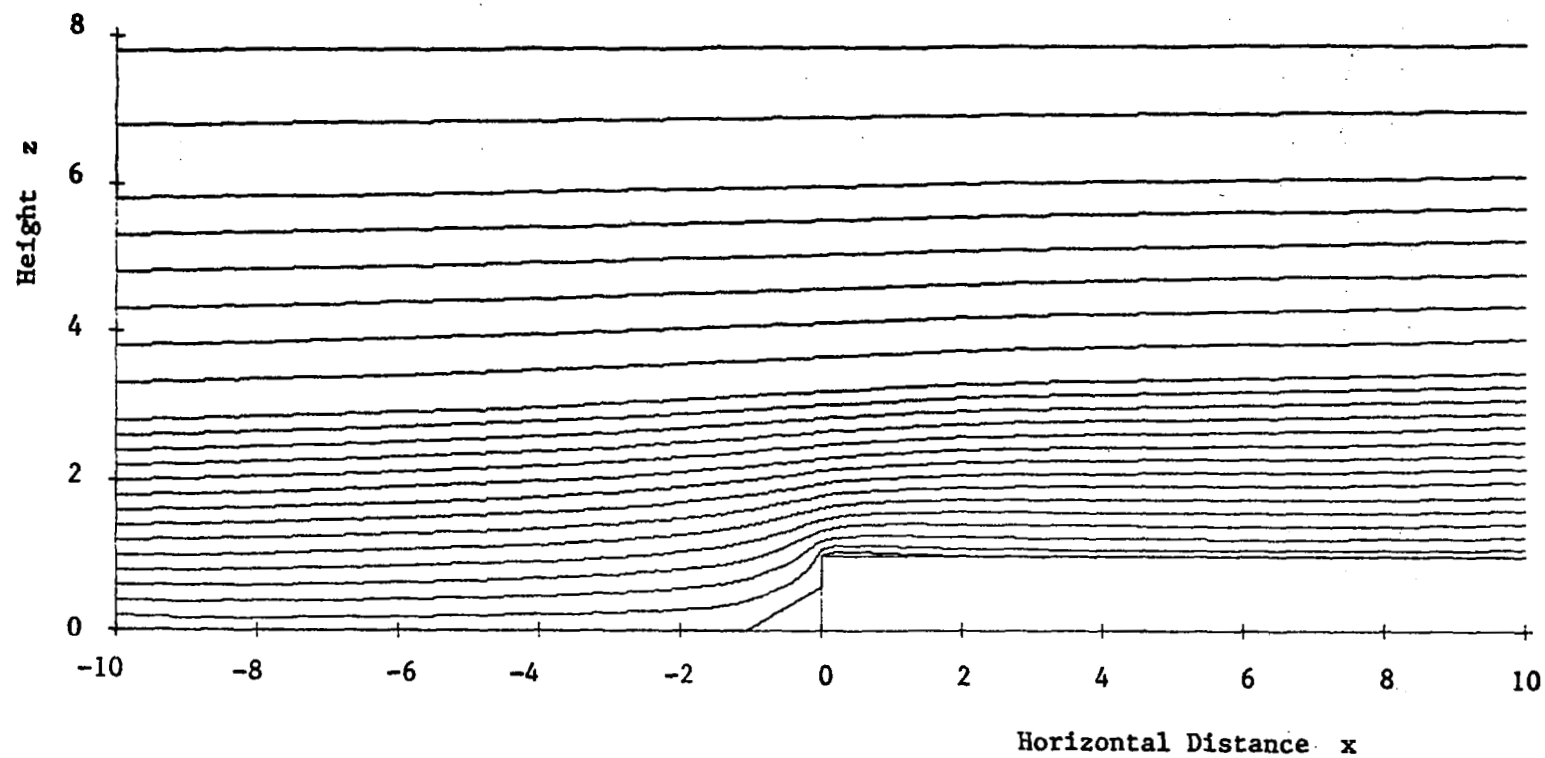


Figure 4.32. Streamline pattern for turbulent flow solution using the turbulence kinetic energy concept with prescribed length scale; One-Equation model ( $Re_n = 3.9 \times 10^6$ ).



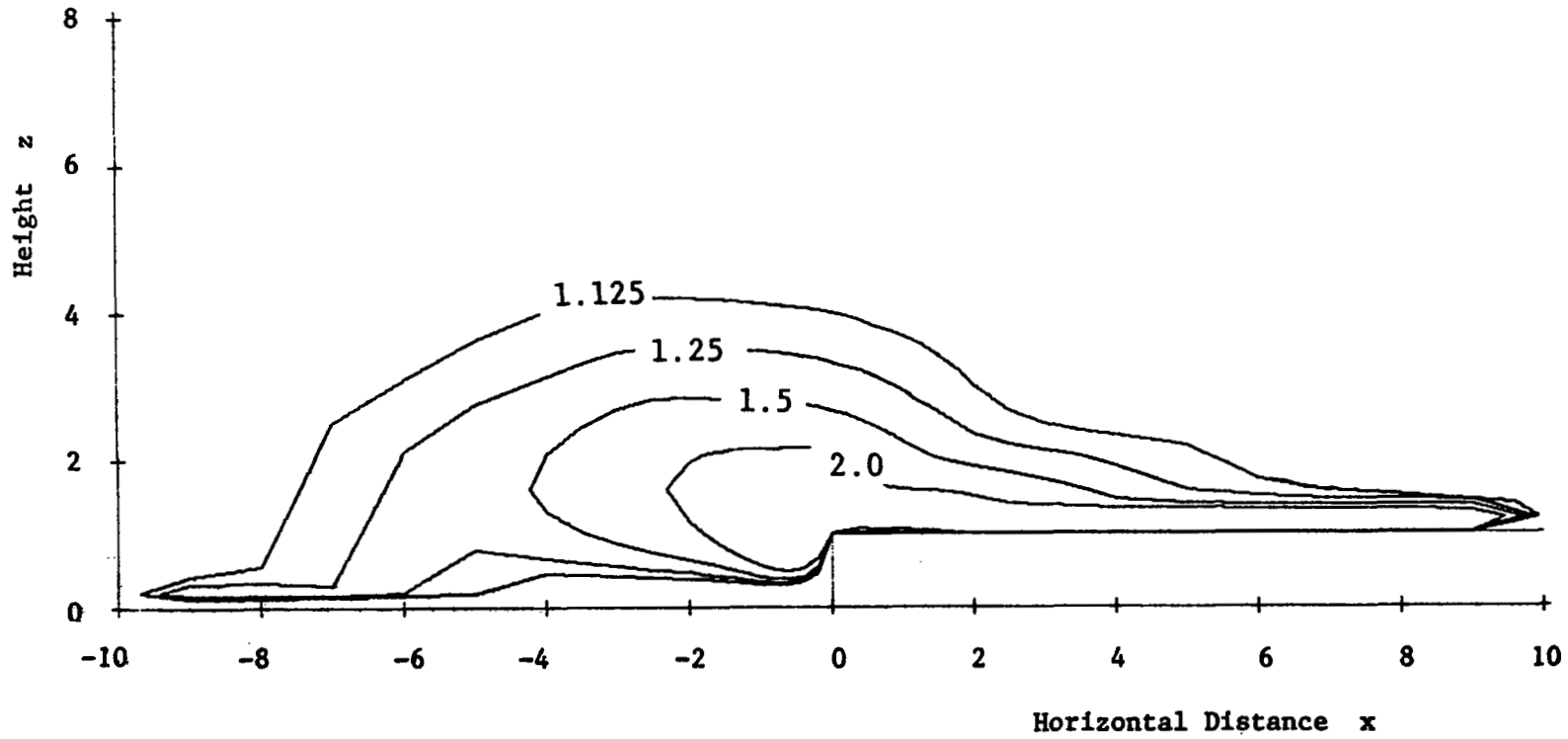


Figure 4.33. Turbulence kinetic energy contours for One-Equation model.

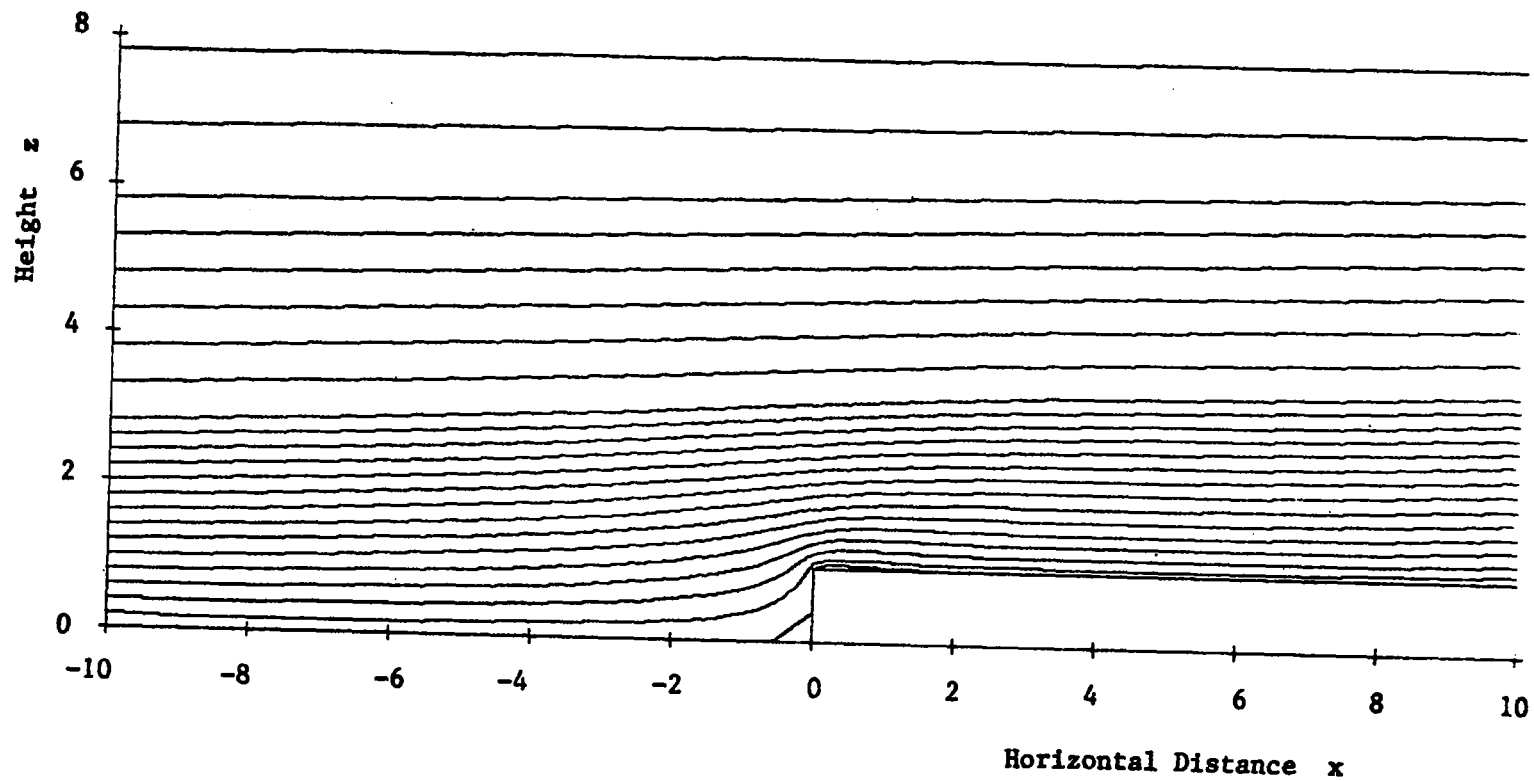


Figure 4.34. Streamline pattern for turbulent flow solution using the turbulence kinetic energy concept with calculated length scale; Two-Equation model ( $Re_n = 3.9 \times 10^6$ ).

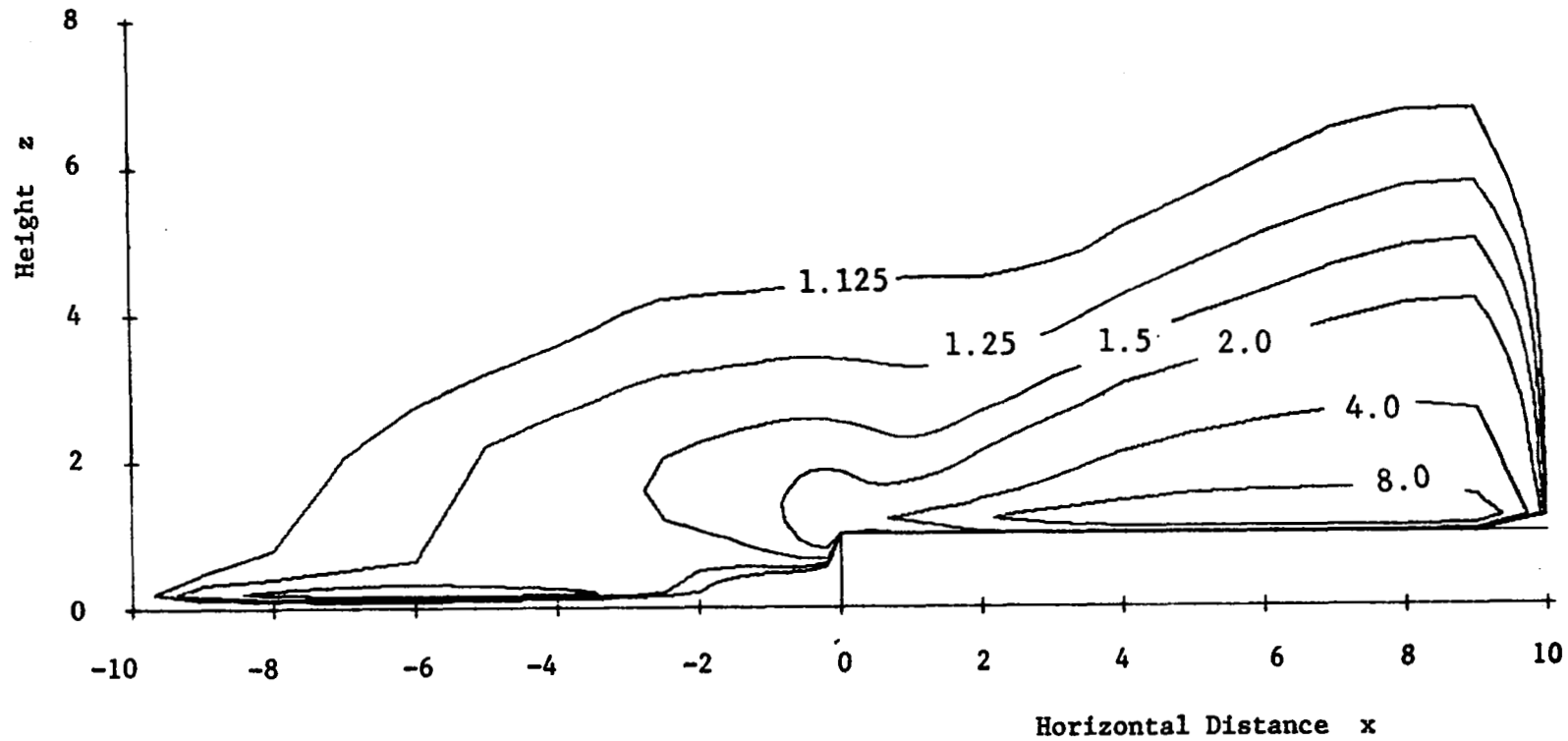


Figure 4.35. Turbulence kinetic energy contours for Two-Equation model.

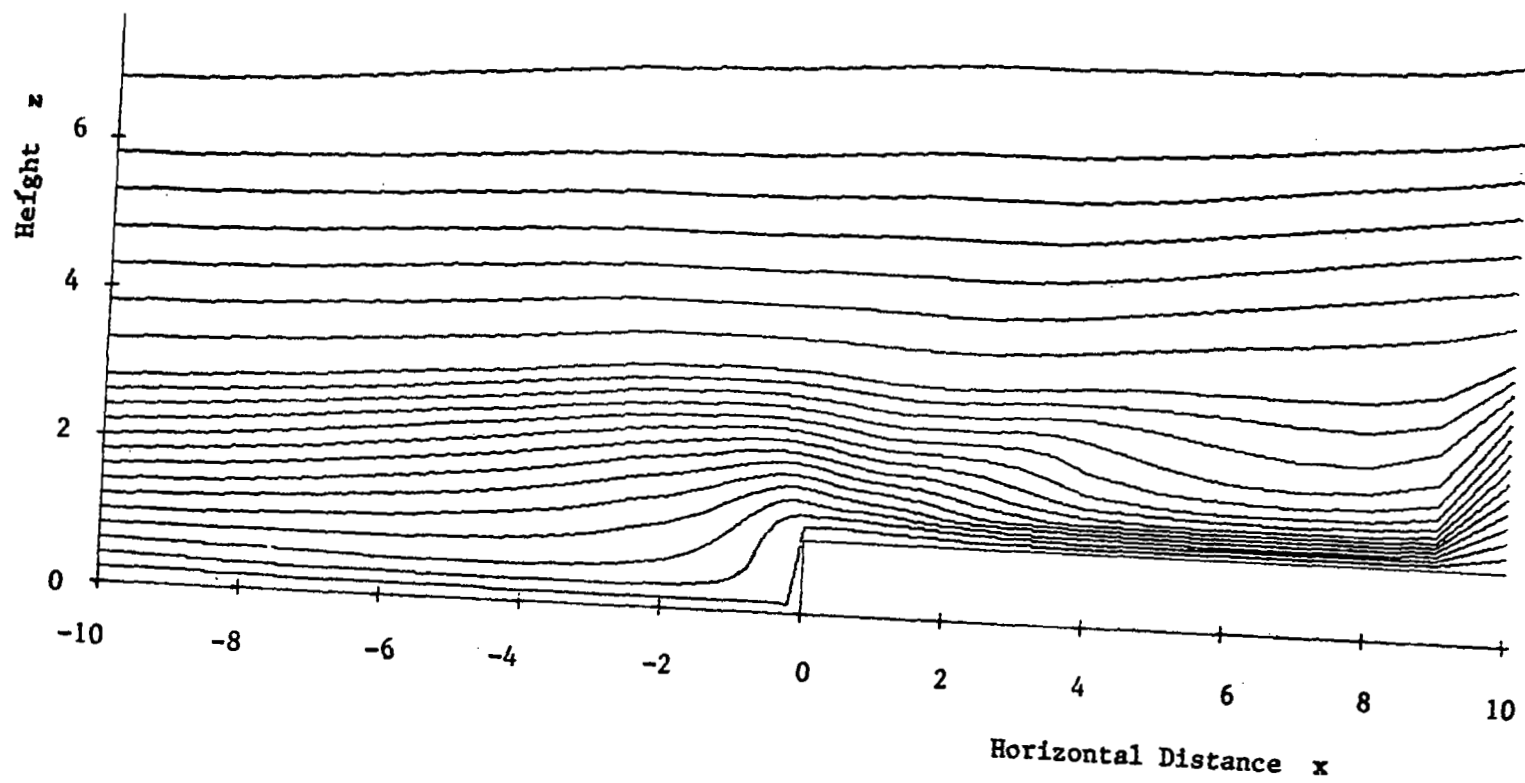


Figure 4.36. Length scale distribution for Two-Equation model (lines of constant  $\ell^*$ ).

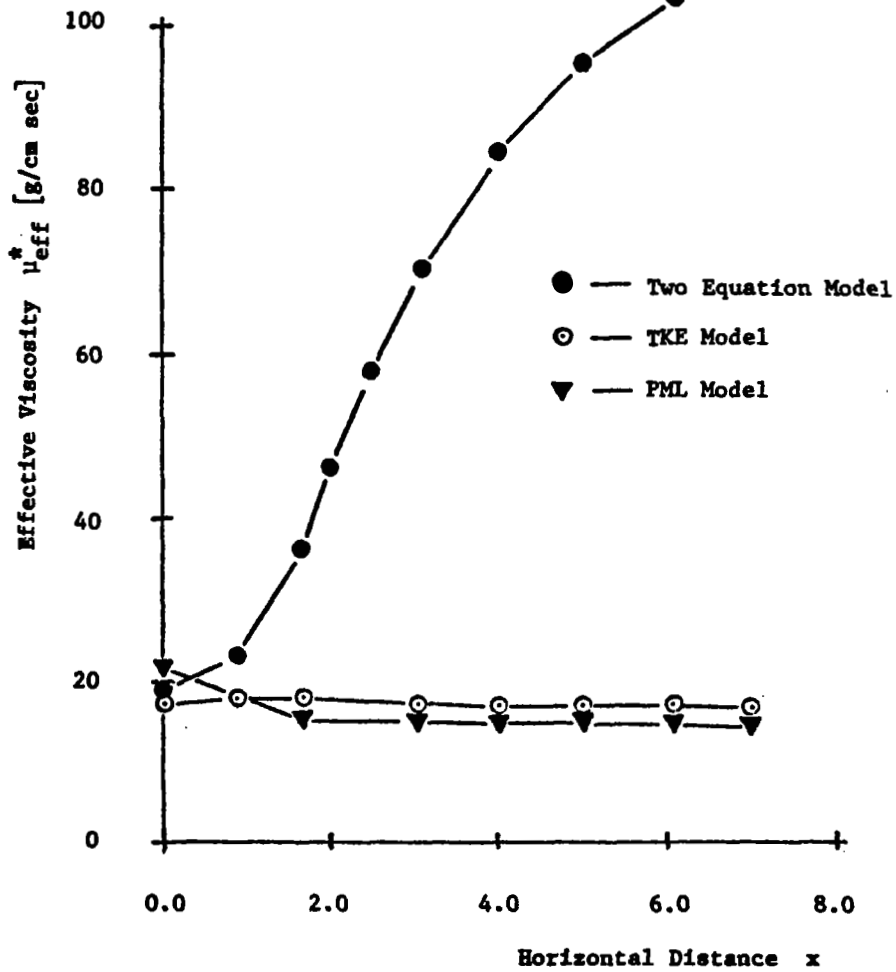


Figure 4.37. Effective viscosity variation along near wall nodes on the top of the step for the different turbulence models.

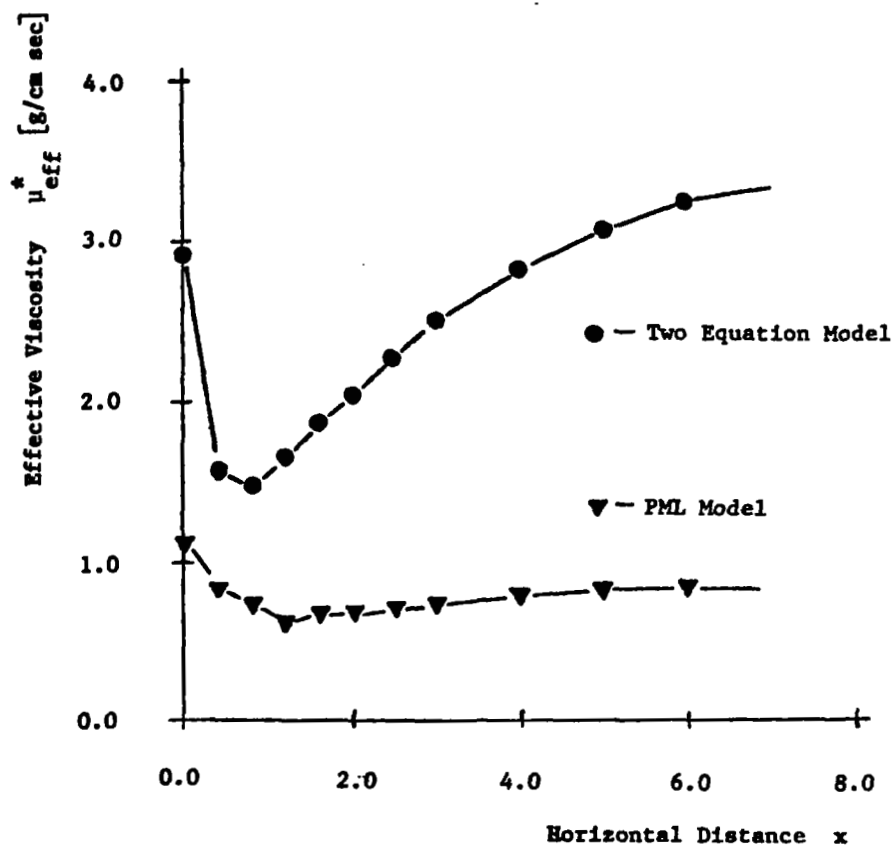


Figure 4.38. Effective viscosity variation along the wall on the top of the step for different turbulence models.

$$\tau_{\text{wall}}^* = \mu_{\text{eff}}^* \left. \frac{\partial u^*}{\partial z^*} \right|_{\text{wall}}$$

and thus with it the effective viscosity rises rapidly after reattachment. However, as near the reattachment point the mean velocity gradients are low, the PML model with Equation 4.13 likewise predicts low values for  $\mu_{\text{eff}}^*$  or  $\mu_t^*$ . Surprisingly enough, the results of the TKE model are little better and only the Two-Equation model follows the expected trend.

The weakness of the PML model with Equation 4.13 lies not only in the incorrect implication that  $\mu_t^*$  vanishes whenever the mean velocity gradients are zero, but more generally in the fact that  $\mu_t^*$  is assumed to depend only on local flow properties. We know, however, from experience that the local level of velocity fluctuations is determined not only by the events of the point in question, but also by influences which have originated some distance upstream. For instance, the high level of velocity fluctuations at the above reattachment point originates from a highly turbulent shear layer issuing from the upper step corner. It is important that this nonlocal character of turbulence is taken into account.

The fact that the TKE model incorporates an additional transport equation for  $k^*$  permits account to be taken of the influence of neighboring regions on the local turbulence energy. However, as seen in Figure 4.37 and also

reported by [44], a TKE model without a length scale transport equation produces results that for wall boundary layers are only insignificantly better than those obtained with PML models. To show how difficult it is to make an accurate guess for the length scale distribution entering the TKE model, reference is made to an  $\ell^*$ -distribution actually calculated with the Two-Equation model in Figure 4.36, page 161. It is the convective transport of  $\ell^*$  which plays an important role in the determination of the flow properties and which results in more physically correct predictions with the Two-Equation model.

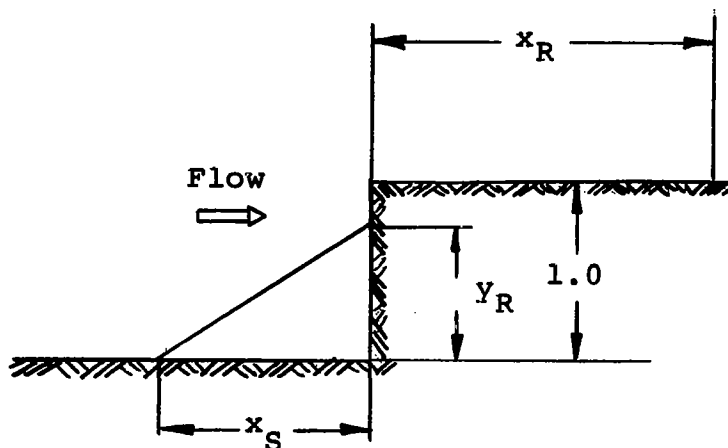
Taking a second look at the respective stream function plots one notices a difference in the geometry of the upstream and downstream separation bubbles for the different models. The predicted dimensions decrease from PML to TKE to Two-Equation model. Table 4.3 gives the approximate values for the individual cases. This decrease certainly is associated with the higher turbulence levels of the respective models.

Generally the top separation region seems somewhat smaller in its vertical extent than one would expect. Besides this possibly being the result of the problem mentioned in Section III of this chapter, it also seems logical that in an atmospheric boundary layer where the ratio of the step height to boundary layer thickness, i.e.,  $h^*/\delta^*$  is small, smaller separation regions should occur than those reported for most wind tunnel experiments where  $h^*/\delta^*$  is



TABLE 4.3  
GEOMETRIES OF SEPARATION REGIONS FOR DIFFERENT  
TURBULENCE MODELS

Model	$x_S$	$y_R$	$x_R$
PML	1.2	0.6	2.2
TKE	1.0	0.6	1.4
Two-Equation	0.6	0.4	1.2



usually large. More on this topic will be found in the parametric study given in the next section.

Let us now turn to a closer examination of the turbulence kinetic energy contours for the TKE and Two-Equation model in Figures 4.33 and 4.35, pages 158 and 160. These can readily be related to the more commonly used turbulence intensities

$$\hat{u}^* = \left[ \frac{1}{3} (\overline{u^{*2}} + \overline{v^{*2}} + \overline{w^{*2}}) \right]^{1/2} / u_*^* \quad (4.74)$$

by

$$\hat{u}^* = \left[ \frac{2}{3} k^* \right]^{1/2} / u_*^* \quad (4.75)$$

In the Two-Equation model the energy contours reveal quite realistically that the shear layer, which grows from the corner of the step, generates high energy levels. These are carried downstream giving rise to comparatively high turbulence intensities in the downstream region of the reattachment point. This downstream convection of energy together with the increase in the level of length scale (Figure 4.36, page 161) conspire to produce particularly high turbulent viscosity in the region behind reattachment.

This phenomenon is also visible in the TKE model  $k^*$ -contours. However, the intensities in the downstream reattachment region are considerably smaller because of the inadequate prescription of the length scale, thus resulting

in the low  $\mu_t^*$  predictions there, as already seen in Figure 4.37, page 162.

Another yet more eye-catching difference is the diffusion of  $k^*$  in the TKE model as compared to the Two-Equation model, especially in the downstream flow region. Experience tells us that turbulent shear layers usually spread at a rate  $x^m$  with  $m$  depending on the type of flow. Likewise should the shear layer originating from the step corner spread out and with it the turbulence kinetic energy or turbulence intensity. Again this behavior is only in the Two-Equation model described correctly.

In the flow region ahead of the step the turbulent intensities do not differ that greatly for the two models. Qualitatively the predictions seem to agree quite well with the experimental findings of Taulbee and Robertson [45, 46] who report that the turbulent intensities increase strongly toward the front separation point. Primarily there is a spreading of the zone over which the higher intensities extend rather than a significant increase in magnitude. The peak intensities occur appreciably outside the dividing streamline, which defines the outer edge of the front separation bubble. Outside this peak the turbulence decreases with  $z^*$  as it does in any boundary layer. Inside the separation bubble the turbulence decreases with distance to an essentially small constant value. The authors point out, however, that the peak intensities and shear levels reached here are still considerably less than values typical of

those in fully developed jets or free shear layers, like the one originating from the step corner (compare with Figure 4.35, page 160).

Finally, to complete the presentation of the dependent variables involved in the calculation, a vorticity contour plot determined from the Two-Equation model is given in Figure 4.39. It shows very clearly the downstream influence of the step on the vorticity pattern, the creation of a highly disturbed region with steep vorticity gradients not only normally to the wall but also in the flow direction. The outer edge of this disturbance or wake region can be approximated as indicated by the dotted line, which, for this particular flow case, is roughly of the form  $z^* = (x^*/h^*)^{0.6}$ .

It is also interesting to note that apart from this region and the immediate upstream vicinity of the step, the constant vorticity lines follow quite closely the streamline pattern so that the application of the "Frozen Vorticity Theory" of Taulbee and Robertson [45, 46] to the current flow problem seems to be a reasonable assumption in this flow region. "Frozen Vorticity" assumes that for certain flow situations where boundary changes and effects occur so suddenly that viscosity or turbulent mixing do not have any time to act on the flow, the diffusion of vorticity can be neglected. The vorticity is then fluid bound, i.e., "frozen" to the stream function and its distribution fixed as given by the approach flow. The governing stream

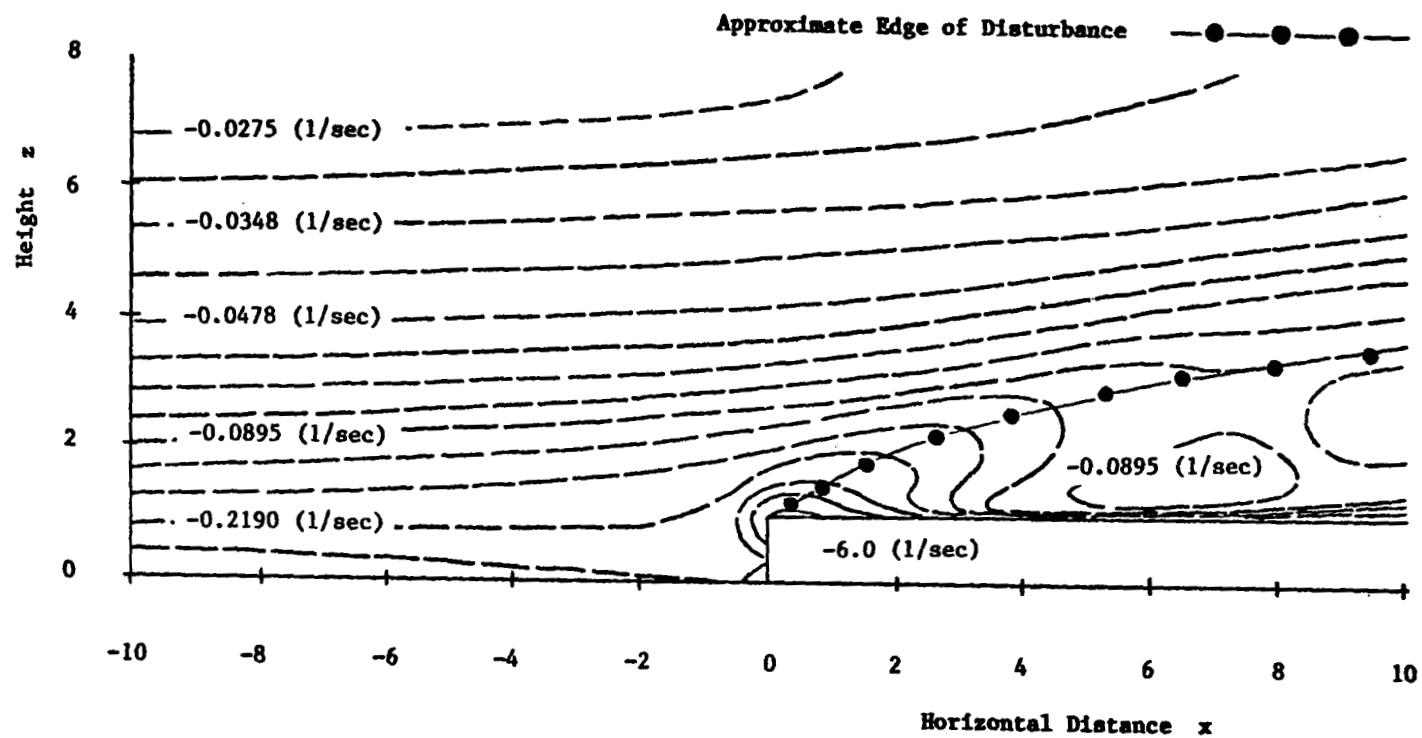


Figure 4.39. Vorticity distribution for Two-Equation model.

function equation (4.10) would reduce under these circumstances to

$$\nabla^2 \psi^* = -\rho^* \omega^* (\psi^*) \quad (4.76)$$

To summarize the key results of this paragraph, one might say that all three turbulence models, PML, TKE, and the Two-Equation model, yield quite realistic streamline patterns and velocity distributions. In the prediction of turbulent flow properties like  $k^*$  and  $\tau^*$  the Two-Equation model was found to be superior. The inadequacies of the PML and TKE model are that they either neglect (PML) or do not adequately account for (TKE) the convective transport of turbulence quantities which in the current flow problem is especially important as the step strongly influences the downstream flow region.

#### Effect of Variation of the Parameters of the Approaching Wind

A parametric study was conducted utilizing the Two-Equation model to assess the influence of the parameters of the approaching wind profile,  $u_*^*$  and  $z_0^*$ , as well as the step height  $h^*$  on the solution.

Before proceeding to the calculation and discussion of selected flow solutions it is useful to study the dimensionless aspects of the flow problem.

A nondimensional form of the governing equations was obtained by adopting the step height  $h^*$  as the characteristic

length and the friction velocity  $u_*^*$  as the characteristic velocity.

Introducing

$$\begin{aligned}
 \omega &= \frac{\omega^* h^*}{u_*^*} ; & \psi &= \frac{\psi^*}{\rho^* u_*^* h^*} \\
 k &= \frac{k^*}{u_*^{*2}} ; & \ell &= \frac{\ell^*}{h^*} \\
 x &= \frac{x^*}{h^*} ; & z &= \frac{z^*}{h^*} \\
 z_0 &= \frac{z_0^*}{h^*} ; & Re_* &= \frac{\rho^* u_*^* h^*}{\mu^*}
 \end{aligned} \tag{4.77}$$

The effective viscosity can then be nondimensionalized as

$$\mu_{\text{eff}}^* = \frac{\mu_{\text{eff}}^*}{\rho^* u_*^* h^*} = \frac{1}{Re_*} + \frac{\mu_t^*}{\rho^* u_*^* h^*} \tag{4.78}$$

which yields for the Prandtl-Kolmogorov formulation of the turbulent viscosity

$$\mu_{\text{eff}}^* = \frac{1}{Re_*} + C_{\mu_0} k^{1/2} \ell \tag{4.79}$$

The resulting nondimensional form of the governing equations then is:

Stream function equation (continuity)

$$\frac{\partial^2 \psi}{\partial x^2} + \frac{\partial^2 \psi}{\partial z^2} = -\omega \tag{4.80}$$

Vorticity transport equation (momentum)

$$\bar{u} \frac{\partial \omega}{\partial x} + \bar{w} \frac{\partial \omega}{\partial z} = \frac{\partial}{\partial x} \left( \frac{\partial}{\partial x} (\mu_{\text{eff}} \omega) \right) + \frac{\partial}{\partial z} \left( \frac{\partial}{\partial z} (\mu_{\text{eff}} \omega) \right) + S_{\omega} \quad (4.81a)$$

with

$$S_{\omega} = 2 \left[ -\frac{\partial^2}{\partial x \partial z} \left( \mu_{\text{eff}} \left( \frac{\partial \bar{u}}{\partial x} - \frac{\partial \bar{w}}{\partial z} \right) \right) + \frac{\partial^2}{\partial x^2} \left( \mu_{\text{eff}} \frac{\partial \bar{u}}{\partial z} \right) - \frac{\partial^2}{\partial z^2} \left( \mu_{\text{eff}} \frac{\partial \bar{w}}{\partial x} \right) \right] \quad (4.81b)$$

Turbulence kinetic energy transport

$$\bar{u} \frac{\partial k}{\partial x} + \bar{w} \frac{\partial k}{\partial z} = \frac{\partial}{\partial x} \left( \frac{\mu_{\text{eff}}}{\sigma_{k,\text{eff}}} \frac{\partial k}{\partial x} \right) + \frac{\partial}{\partial z} \left( \frac{\mu_{\text{eff}}}{\sigma_{k,\text{eff}}} \frac{\partial k}{\partial z} \right) + S_k \quad (4.82a)$$

with

$$S_k = 2\mu_t \left[ \left( \frac{\partial \bar{u}}{\partial x} \right)^2 + \left( \frac{\partial \bar{w}}{\partial z} \right)^2 \right] + \left( \frac{\partial \bar{u}}{\partial z} + \frac{\partial \bar{w}}{\partial x} \right)^2 - C_D \frac{k^{3/2}}{\ell} \quad (4.82b)$$

and the transport equation for the turbulence length scale

$$\bar{u} \frac{\partial \ell}{\partial x} + \bar{w} \frac{\partial \ell}{\partial z} = \frac{\partial}{\partial x} \left( \frac{\mu_{\text{eff}}}{\sigma_{\ell,\text{eff}}} \frac{\partial \ell}{\partial x} \right) + \frac{\partial}{\partial z} \left( \frac{\mu_{\text{eff}}}{\sigma_{\ell,\text{eff}}} \frac{\partial \ell}{\partial z} \right) + S_{\ell} \quad (4.83a)$$

with

$$S_{\ell} = k^{1/2} C_S - 2\mu_t \left[ \left( \frac{\partial \bar{u}}{\partial x} \right)^2 + \left( \frac{\partial \bar{w}}{\partial z} \right)^2 \right] + \left( \frac{\partial \bar{u}}{\partial z} + \frac{\partial \bar{w}}{\partial x} \right)^2 \quad (4.83b)$$

After nondimensionalizing also the boundary conditions, e.g., the inlet conditions in the four variables  $\psi$ ,  $\omega$ ,  $k$  and  $\ell$ :



$$\psi = \frac{1}{\kappa} \left[ (z + z_0) \left( \ln \frac{z + z_0}{z_0} - 1 \right) + z_0 \right]$$

$$\omega = -\frac{1}{\kappa(z + z_0)} - \frac{\partial^2 \psi}{\partial x^2}$$

$$k = 1$$

$$l = \kappa(z + z_0) \quad (4.84)$$

one finds that the problem reduces from the three dimensional parameters  $u_*^*$ ,  $z_0^*$  and  $h^*$  to the two dimensionless groups  $z_0$  and  $Re_*$ .

However, in view of Equation 4.72 and the high Reynolds number usually occurring in atmospheric flows, where

$$\frac{1}{Re_*} \ll \mu_t \quad (4.85)$$

the flow problem becomes essentially independent of Reynolds number. Thus, the only remaining significant parameter is  $z_0$ .

In the subsequent study calculations were carried out for the following five values of  $z_0$ .

$$(1) \ z_0 = 0.005$$

$$(2) \ z_0 = 0.020$$

$$(3) \ z_0 = 0.045$$

$$(4) \ z_0 = 0.075$$

$$(5) \ z_0 = 0.100$$

The resulting  $\psi$ -,  $k$ - and  $l$ -distributions for the cases 1, 3 and 5 are shown in Figures 4.40 through 4.42.

(a)

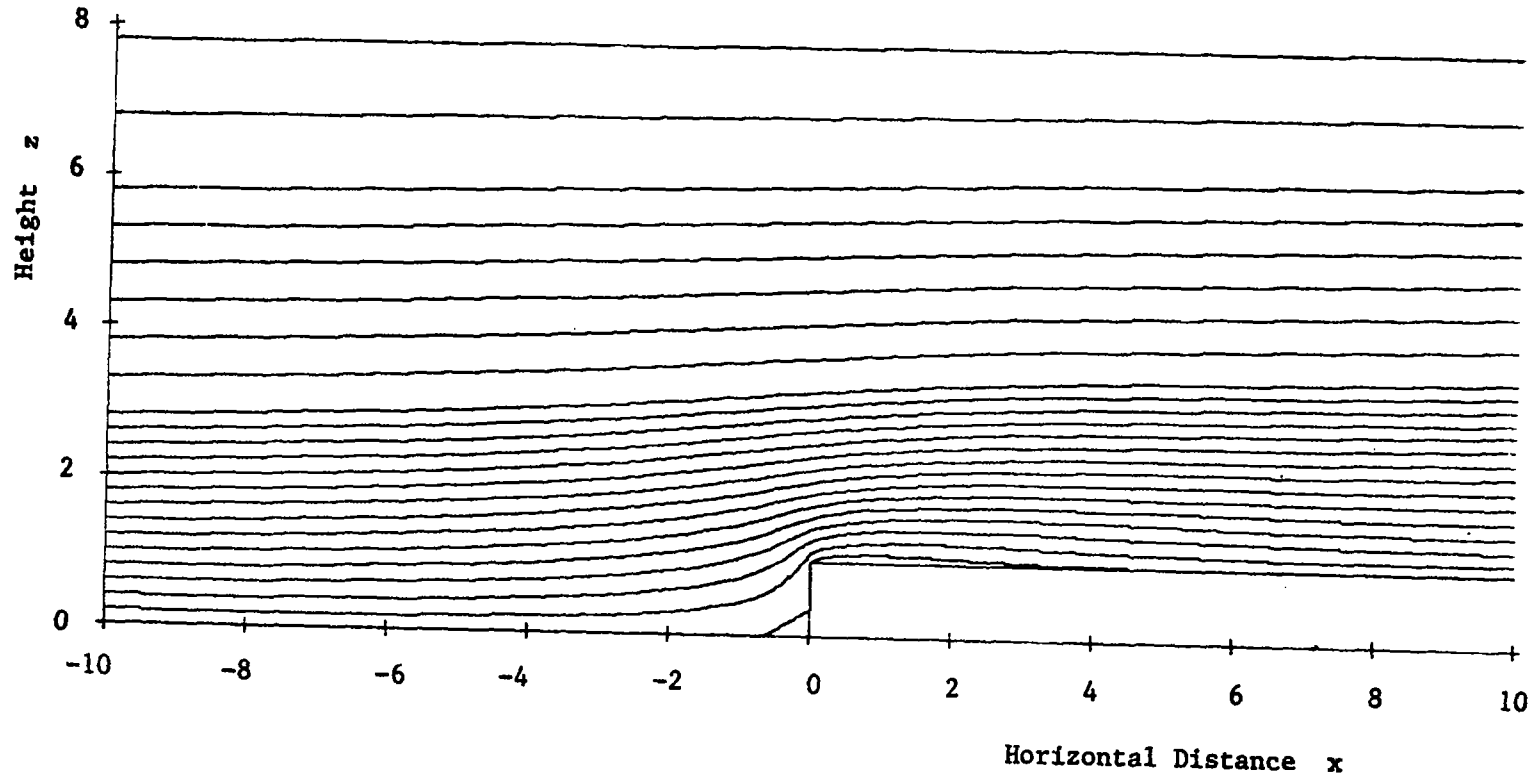


Figure 4.40. Stream function pattern for (a)  $z_0 = 0.005$ , (b)  $z_0 = 0.045$ ,  
(c)  $z_0 = 0.1$ .

(b)

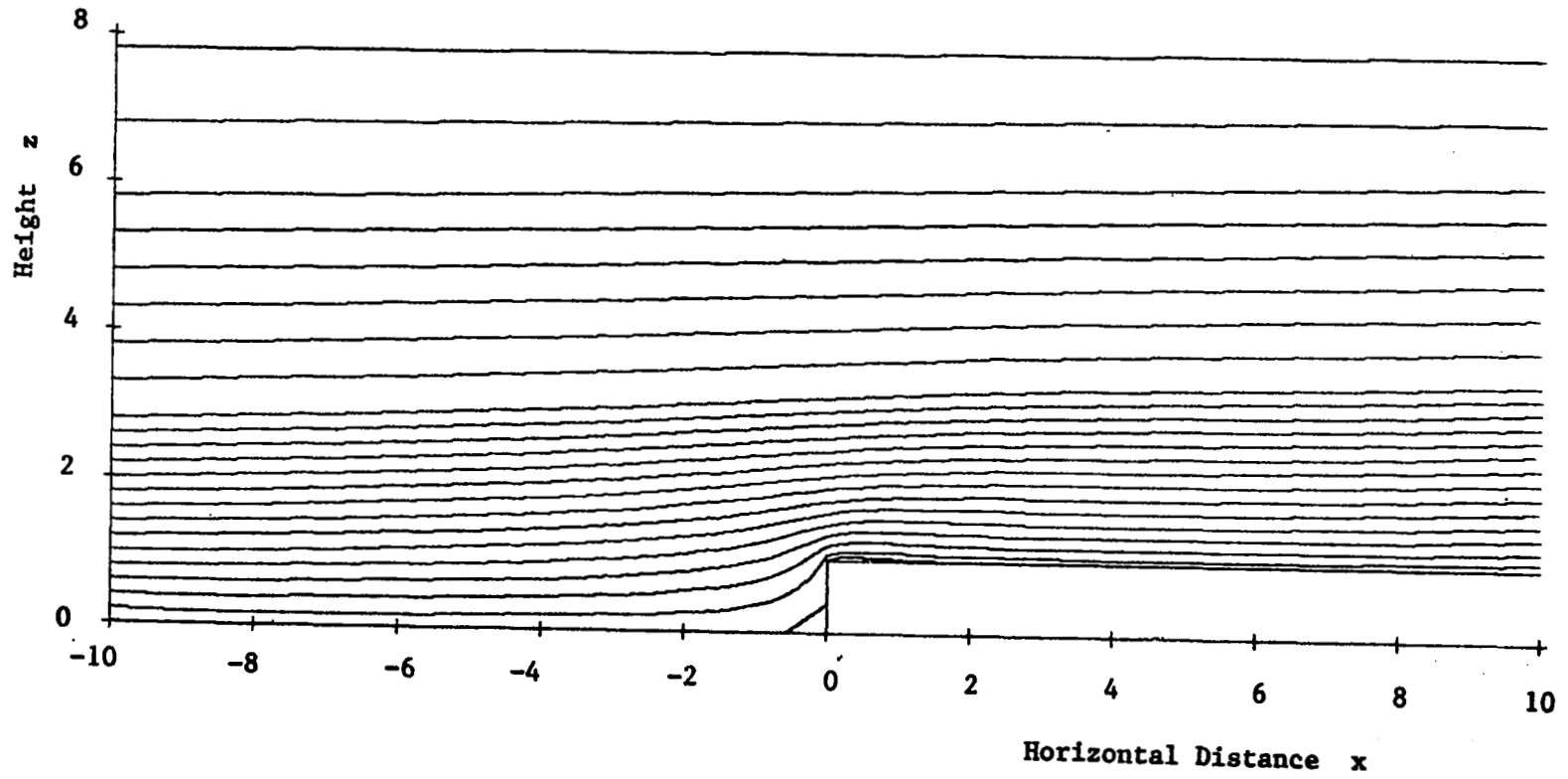


Figure 4.40. (continued)

(c)

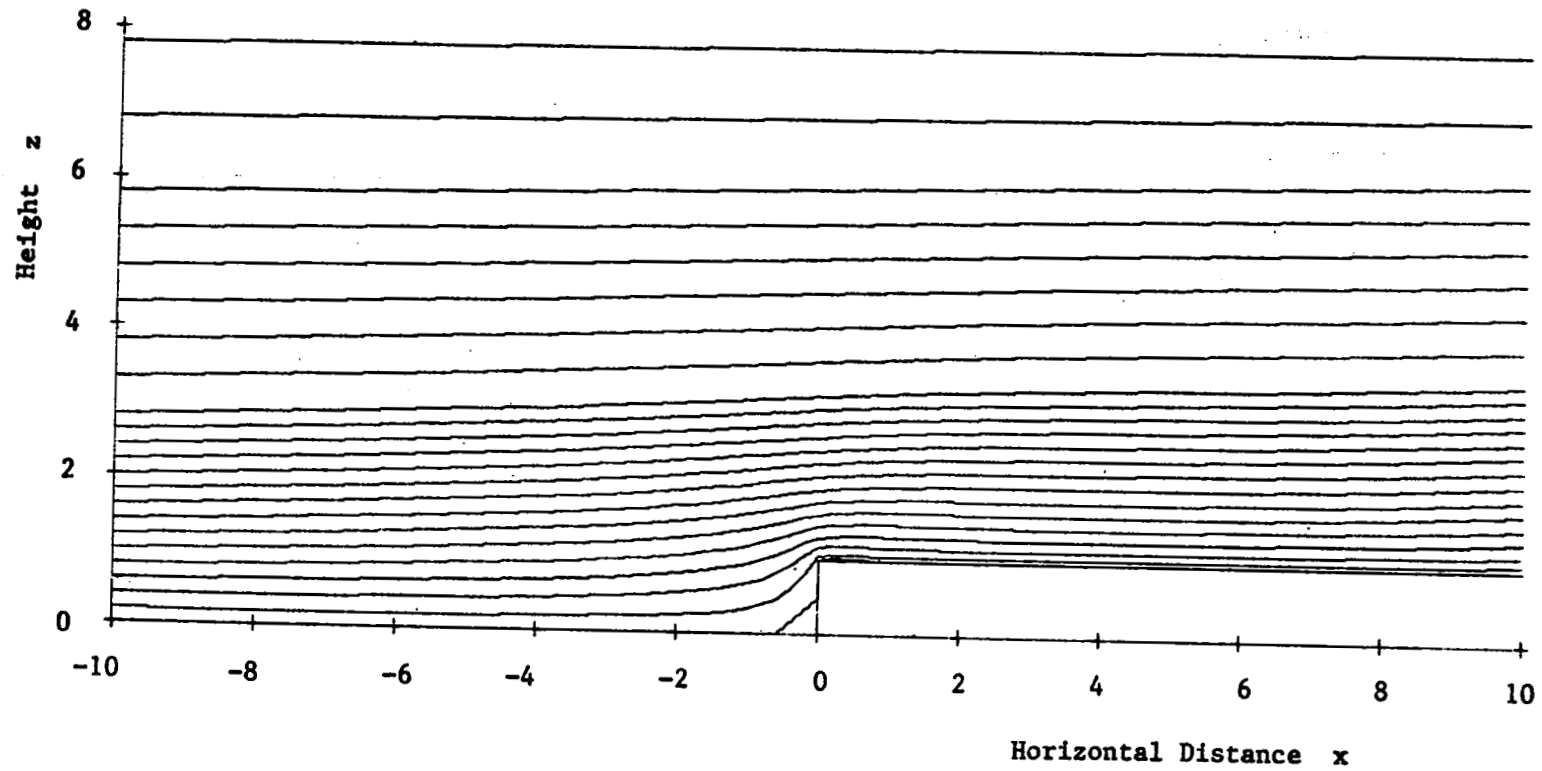


Figure 4.40. (continued)

(a)

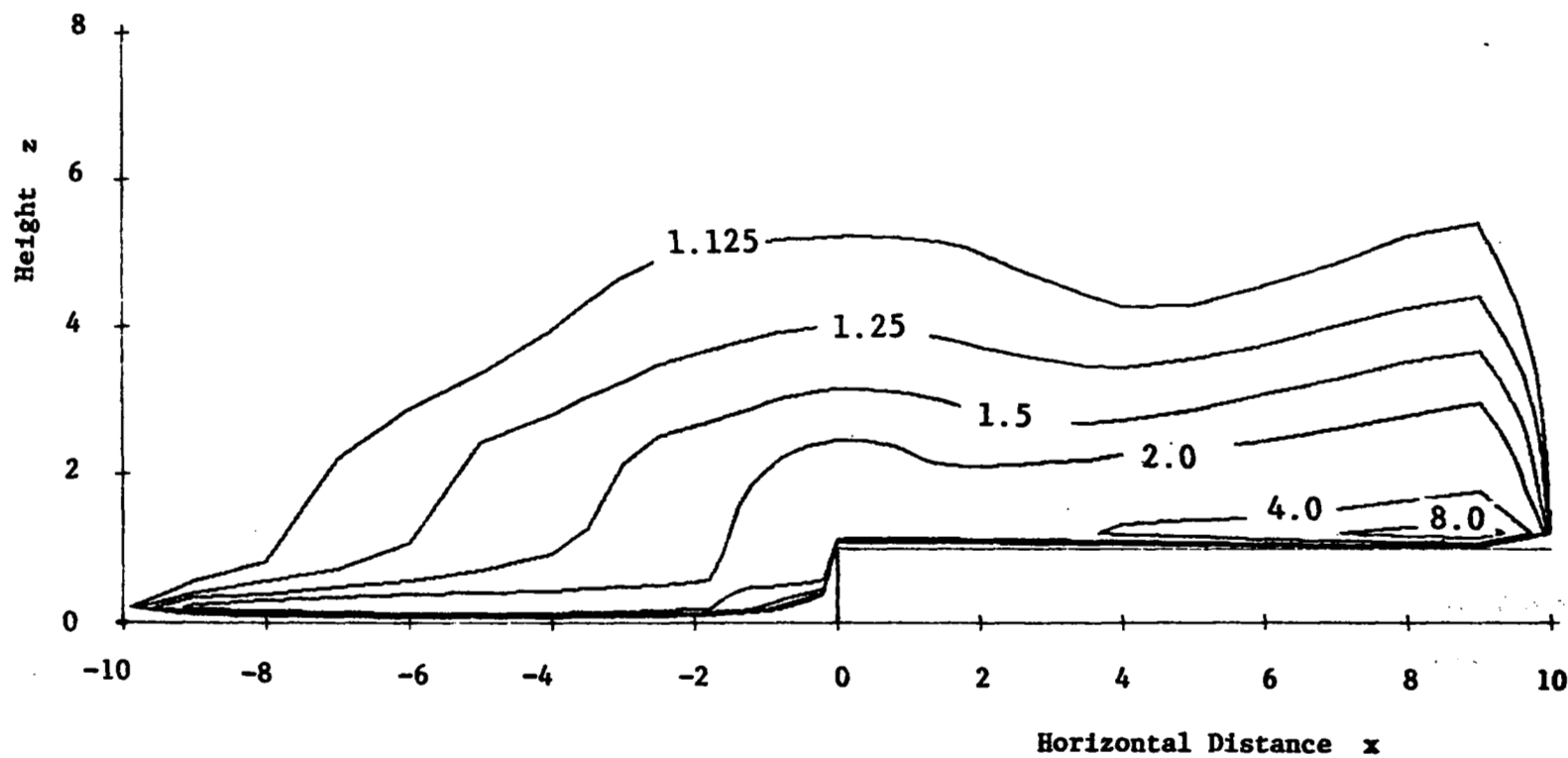


Figure 4.41. Turbulence kinetic energy contours for (a)  $z_0 = 0.005$ ,  
(b)  $z_0 = 0.045$ , (c)  $z_0 = 0.1$ .

(b)

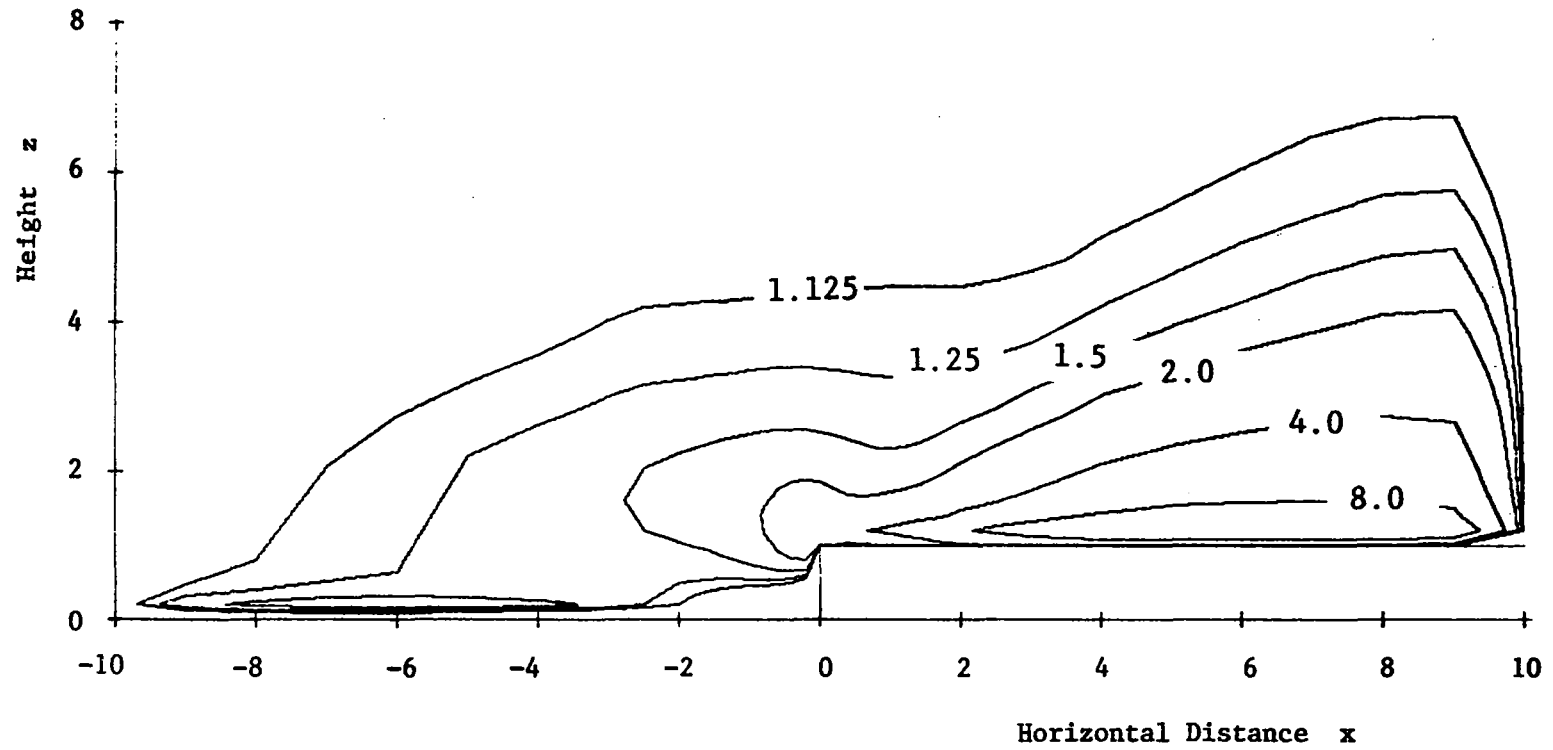


Figure 4.41. (continued)

(c)

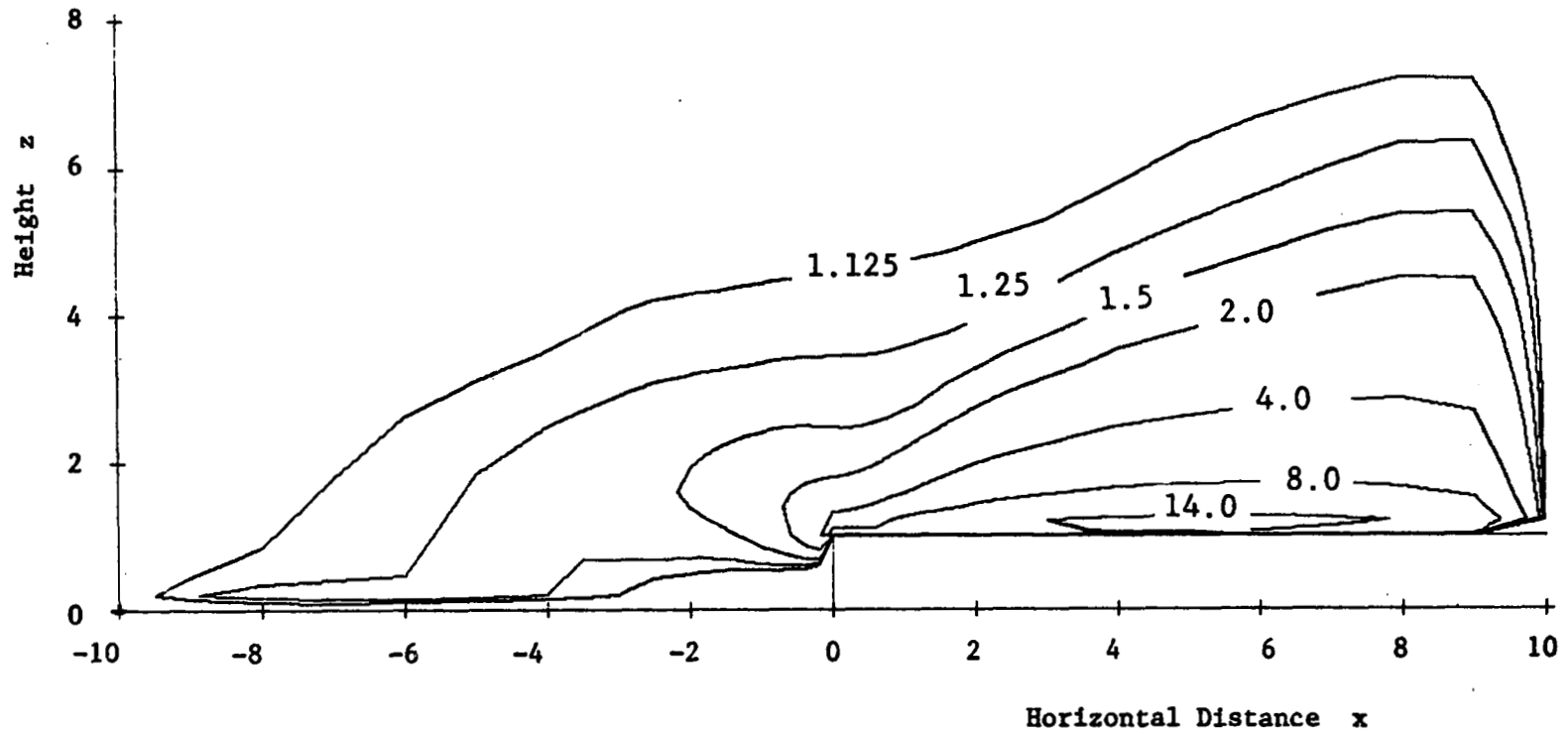


Figure 4.41. (continued)

(a)

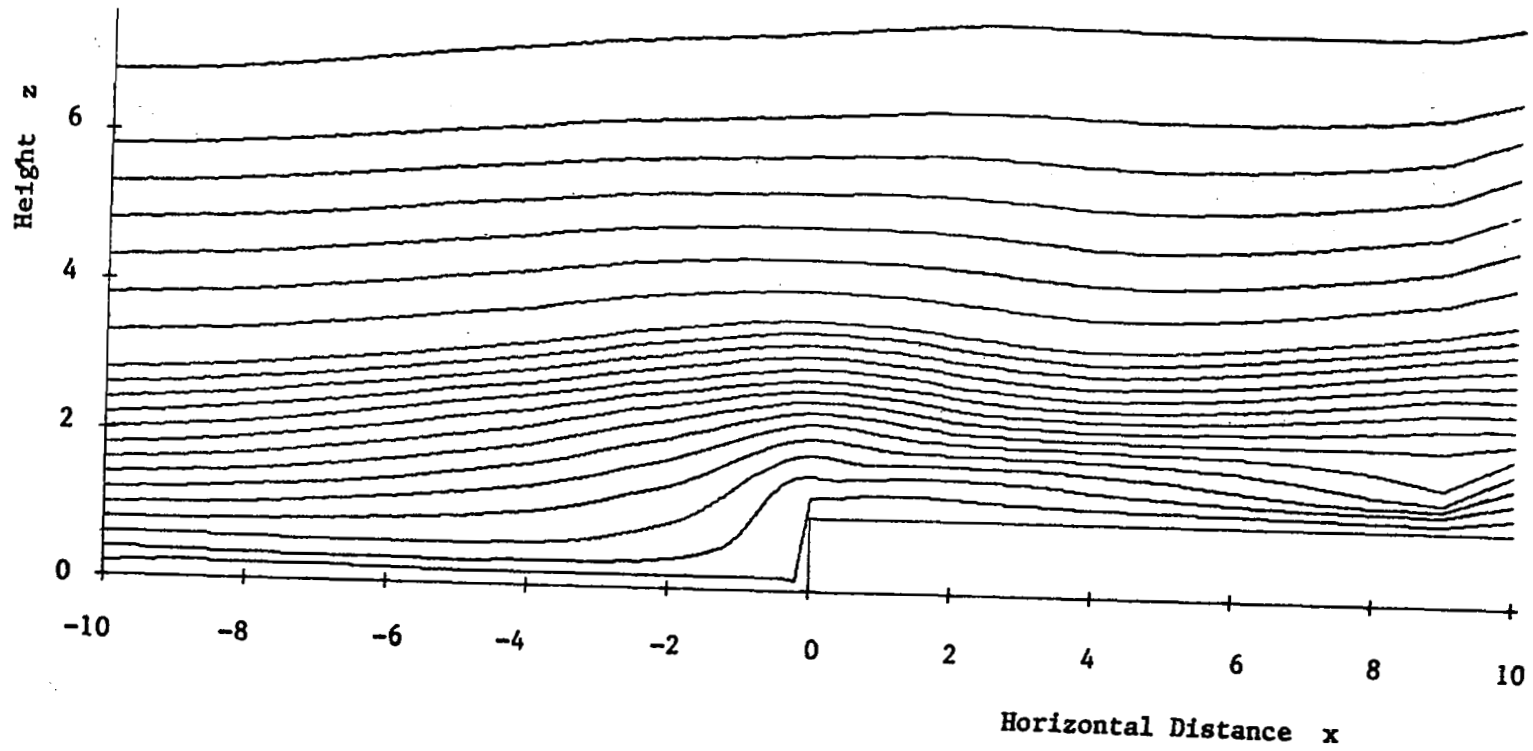


Figure 4.42. Lines of constant turbulence length scale for (a)  $z_0 = 0.005$ , (b)  $z_0 = 0.045$ , (c)  $z_0 = 0.1$ .



(b)

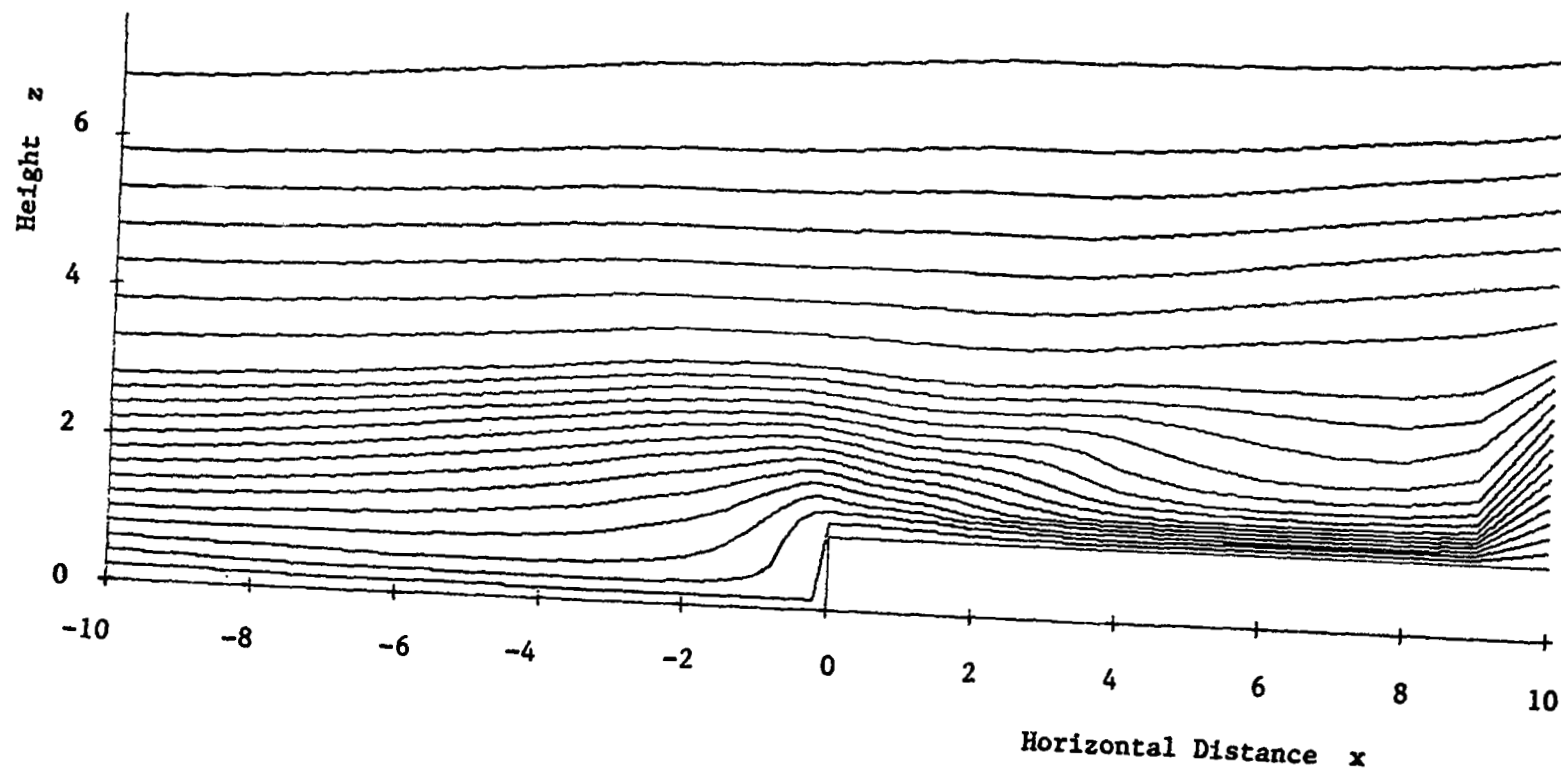


Figure 4.42. (continued)

(c)

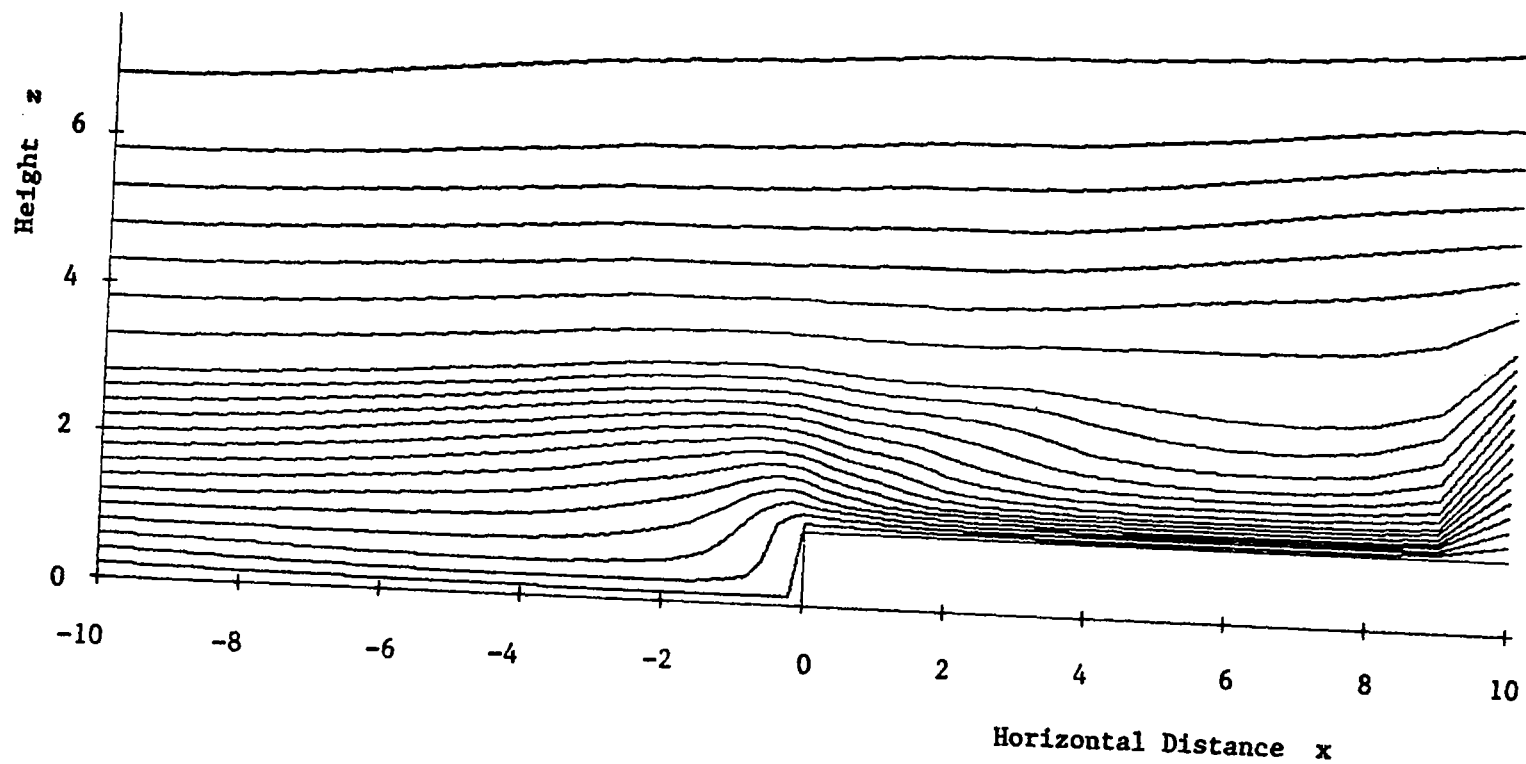


Figure 4.42. (continued)

Comparing the various streamline patterns one notices that the shapes of the upstream and downstream separation regions vary with  $z_0$ . While the top reattachment length  $x_R$  changes substantially, the front separation distance  $x_S$  varies only slightly. Figures 4.43 and 4.44 reveal the geometry of the separations and reattachments as characterized by the distances  $x_S$ ,  $y_R$  and  $x_R$ .

The reattachment length  $x_R$  was found to increase with decreasing  $z_0$ , indicating that a smoother surface or larger step height would delay reattachment of the flow on top of the step. The reason for this is readily understood by looking at the respective TKE- and  $\ell$ -contour plots in Figures 4.41 and 4.42. For smaller  $z_0$  the turbulence intensities and length scale are seen to decrease in the upstream and downstream vicinity of the upper step corner. This is a result of the higher flow acceleration created by the displacement of a fuller approach velocity profile containing higher momentum near the wall (see also Figure 4.45(b)). Acceleration in the flow is generally known to diminish turbulence production and to reduce the turbulence length scale or typical eddy size by means of vortex stretching. These lower turbulence intensities together with the reduced length scale lead to a lower effective viscosity or shear on top of the step, delaying reattachment and causing  $x_R$  to increase.

For the forward separation region the situation is somewhat different. Except for a small region in the lower

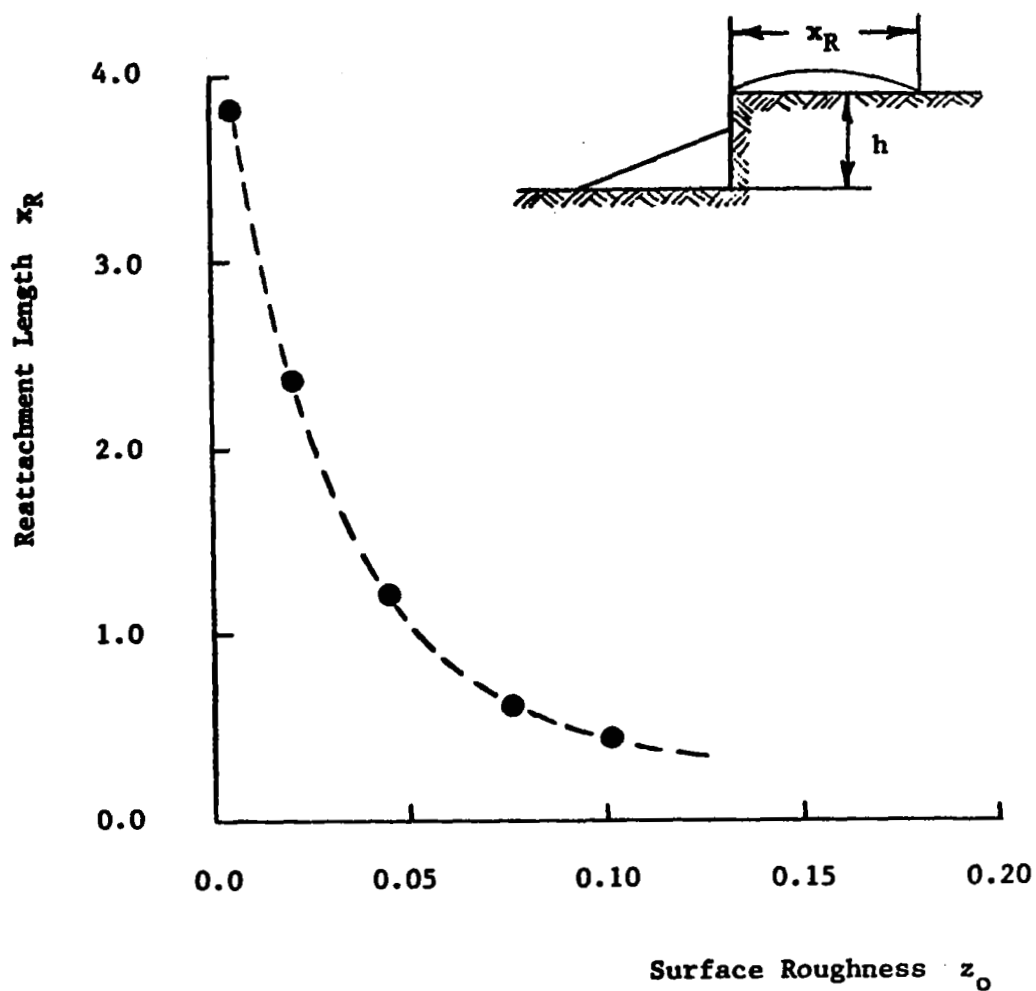
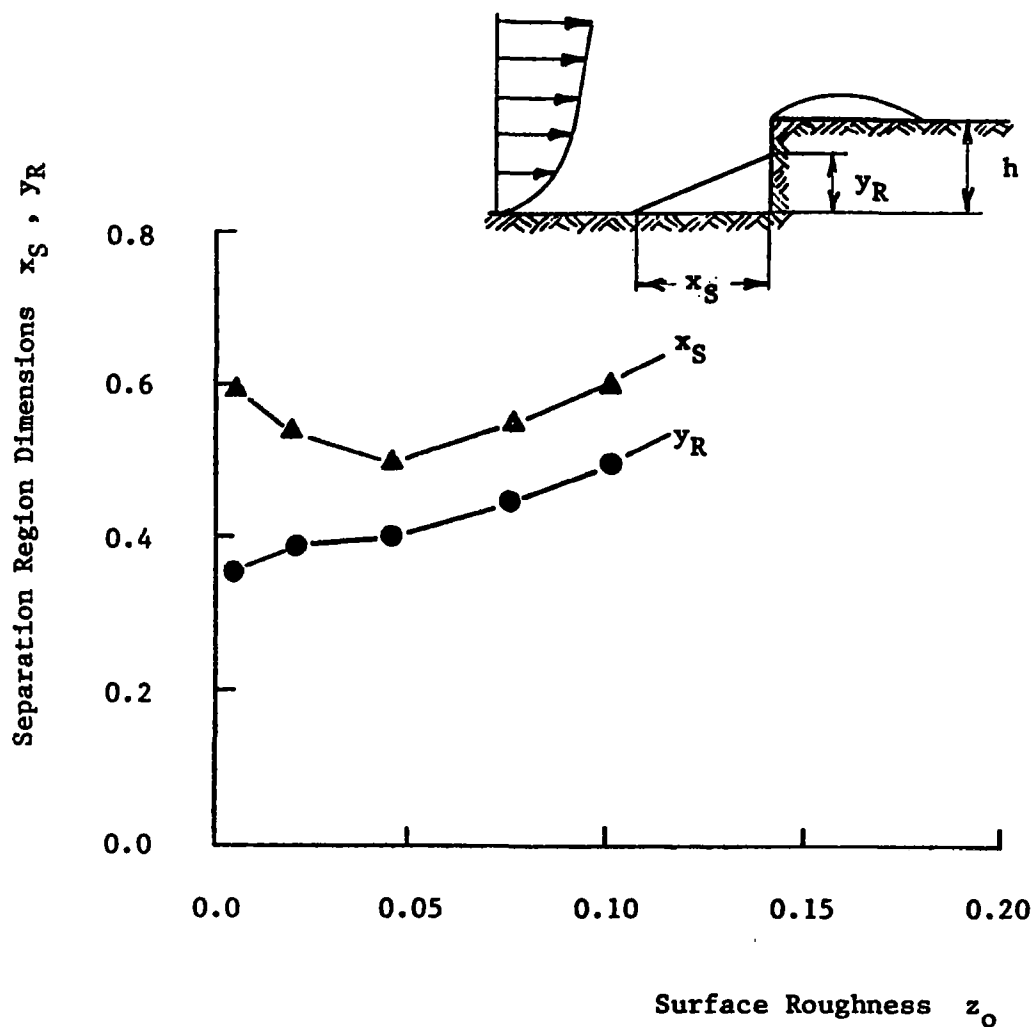
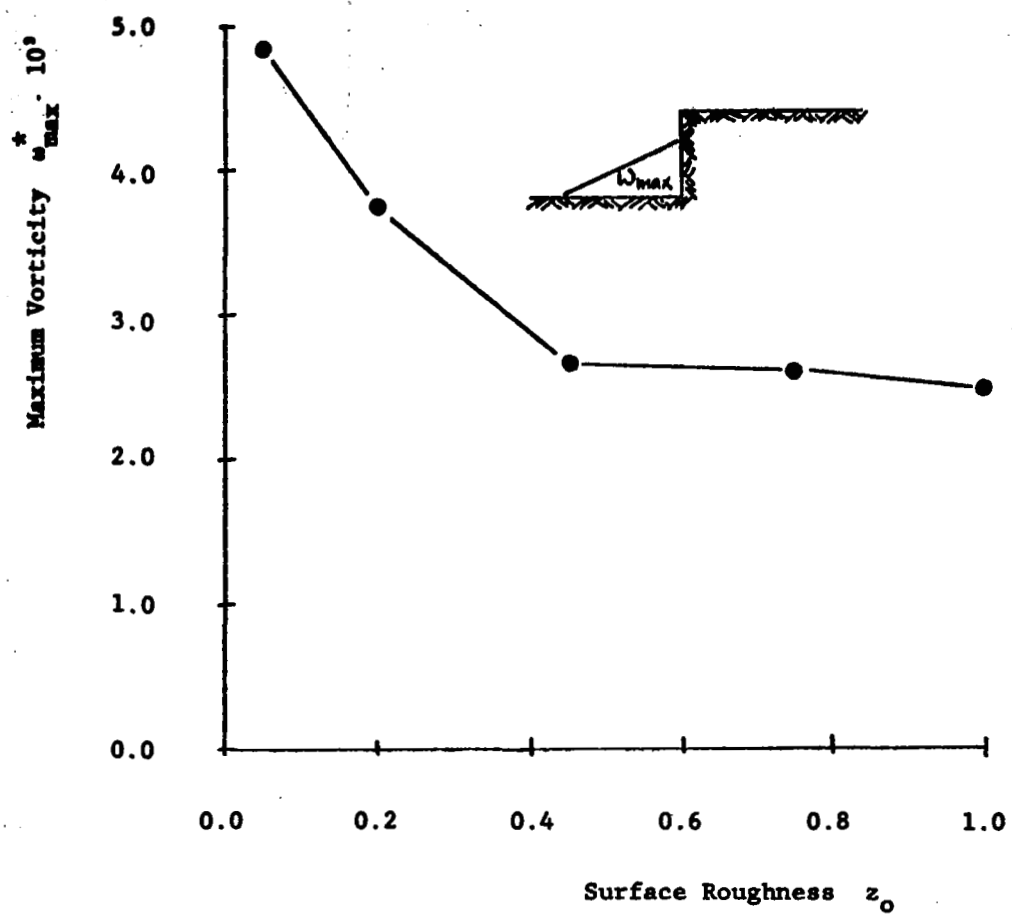


Figure 4.43. Reattachment length of top separation region in dependence of  $z_0$ .



(a)

Figure 4.44. Forward separation region; (a) geometry in dependence of  $z_0$ , (b) maximum vorticity in dependence of  $z_0$ .



(b)

Figure 4.44. (continued)

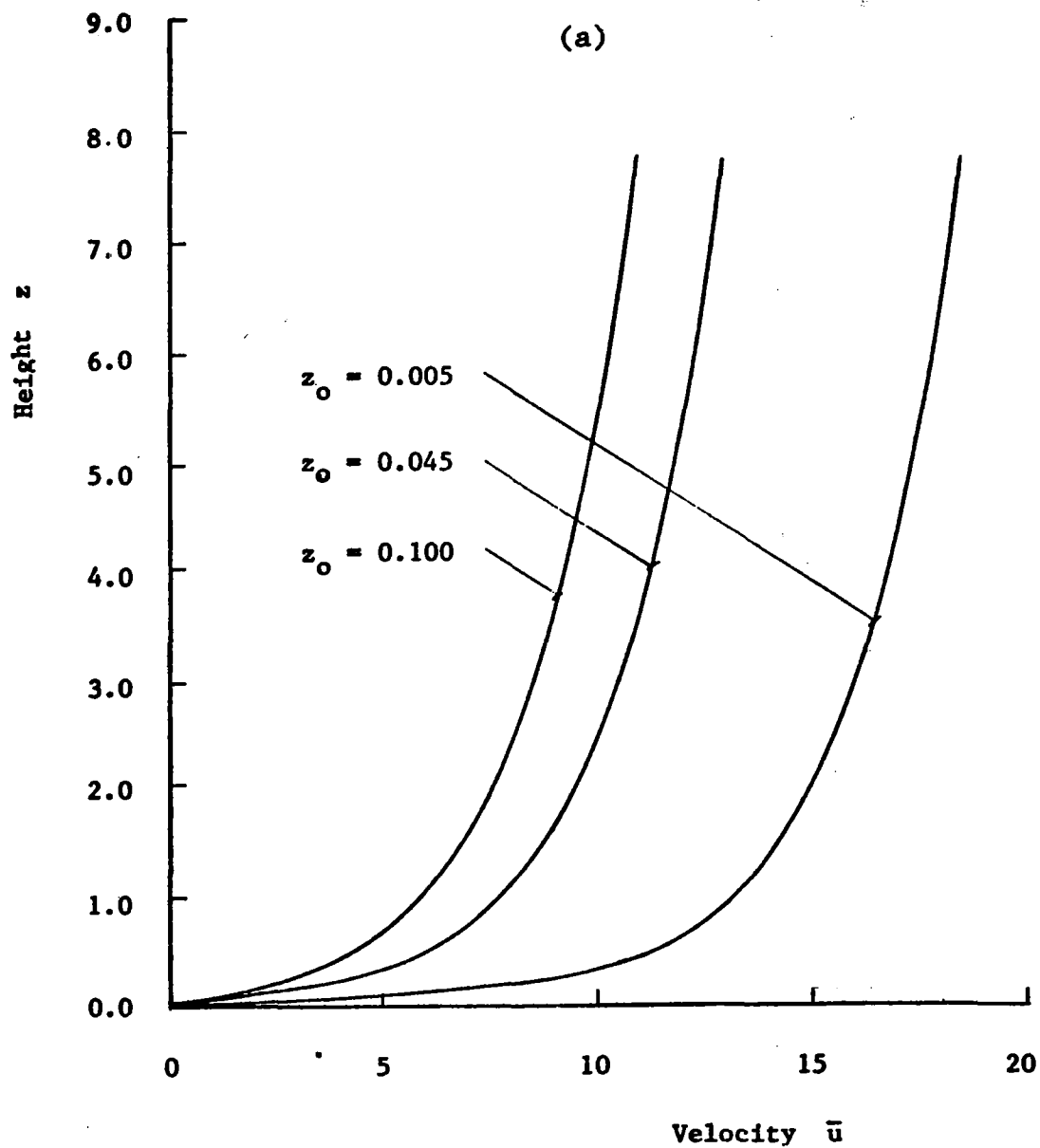


Figure 4.45. Velocity profiles for various  $z_0$ ; (a) approach velocities, (b) velocity overshoot at  $x = 0$  due to the step for different  $z_0$ .

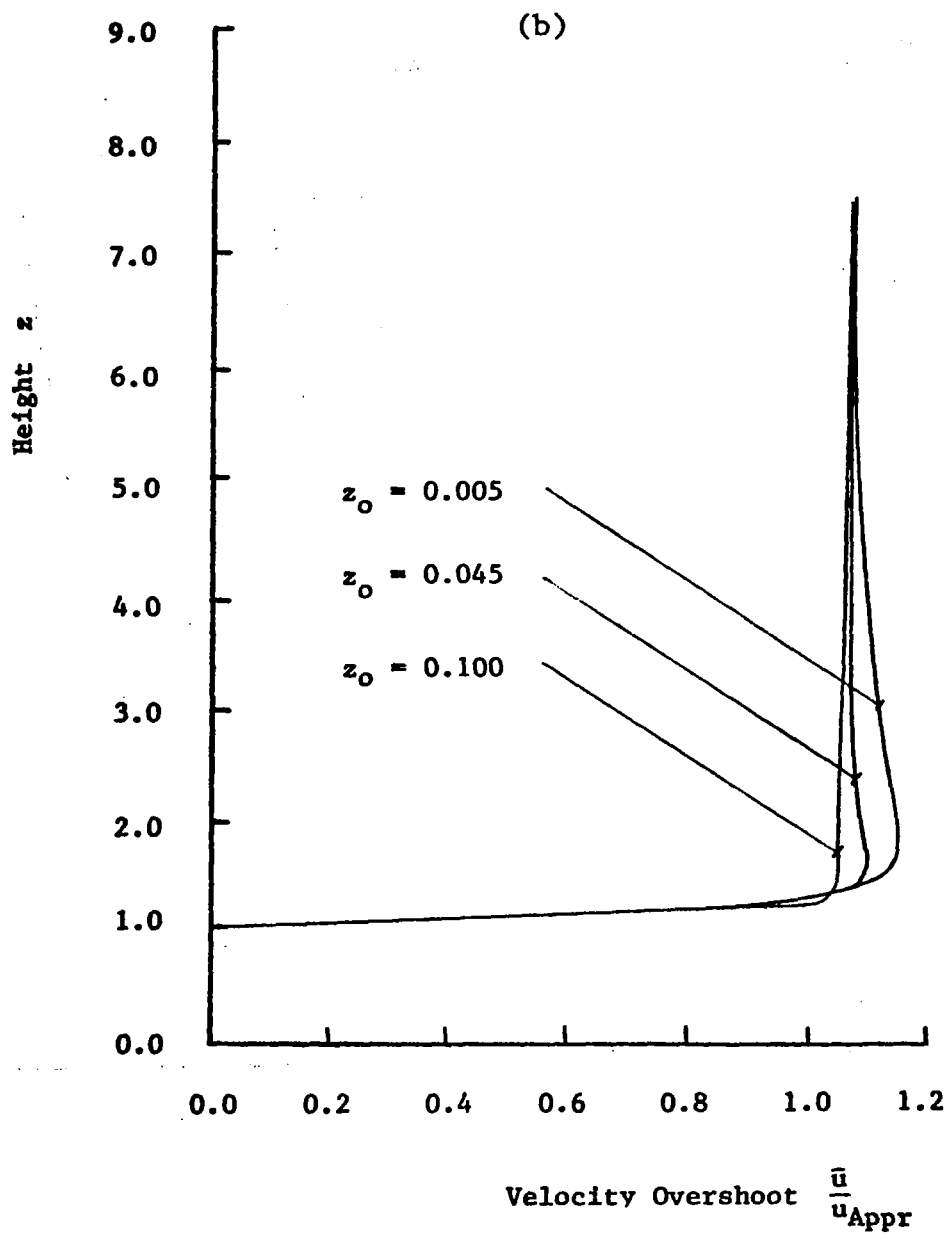


Figure 4.45. (continued)



$z_0$  range, the bubble is found to grow in size with increasing surface roughness parameter, even though the maximum vorticity occurring inside the bubble decreases, as shown in Figure 4.44(b). In the  $z_0$ -range under consideration where the vorticity decreases only slightly the growth of the bubble seems to be influenced largely by the growth of the turbulence length scale. In the lower  $z_0$ -range mentioned above, however, the steep decline of vorticity seems to be more influential than the growth of the length scale resulting in a partial reduction of bubble size.

Taulbee and Robertson [46] presented the results of their investigation for smooth walls in dependence of the ratio of step height to boundary layer thickness  $h^*/\delta^*$ . This ratio is small for most atmospheric boundary layer flows and changes only little; however, it is similar to the ratio  $h^*/z_0^*$  used here, in the sense that both parameters  $\delta^*$  and  $z_0^*$  characterize the nature of the approaching velocity profile in relation to the height of the obstruction. Although a direct comparison with the above results is not possible because the functional relation between  $\delta^*$  and  $z_0^*$  is unknown, one can nevertheless compare common trends. Taulbee and Robertson's results predict for

$$\frac{h^*}{\delta^*} = 1.8 \rightarrow x_R = 3.8$$

and for a step height a fourth of the above:

$$\frac{h^*/4}{\delta^*} = 0.45 \rightarrow x_R = 2.3$$

For the present study the surface roughness of  $z_0 = 0.005$  predicts the same reattachment length as  $h^*/\delta^* = 1.8$ , i.e.,

$$\frac{z_0^*}{h^*} = 0.005 \rightarrow x_R = 3.8$$

and for a fourth of the step height we get

$$\frac{z_0^*/4}{h^*} = 0.02 \rightarrow x_R = 2.35$$

Carrying on the comparison in this fashion for several other step heights, one finds the predictions for the reattachment length  $x_R$  in almost exact agreement with the results of [46]. Proceeding the same way with dimensions  $x_S$  and  $y_R$  of the front separation bubble, however, agreement is not as good, with the predictions of the Two-Equation model being consistently lower than Taulbee and Robertson's results. As already noted during the comparison of the three turbulence models (see Table 4.2, page 138) this is possibly a consequence of the higher turbulence and turbulent viscosity in the  $k$ - $\ell$ -model and could be adjusted by a redetermination of the empirical constants.

More information is contained in the gradients of the stream function, i.e., the velocity distributions. Figure 4.45, page 188, indicates how the presence of the step affects the horizontal velocity profile at  $x = 0.0$  for the different roughness parameters. The profile with the

strongest velocity gradient at the wall and the highest momentum near the surface produces the largest velocity overshoot. This is easily perceived because for the smaller  $z_0$ , the flow carries more mass near the wall, which is suddenly displaced by the step, creating a locally accelerated flow region. This result was also obtained in the boundary layer analysis. The overshoot is in accordance with the lower shear predictions and longer reattachment lengths for the smaller  $z_0$ .

For completeness, Figure 4.46 shows a set of velocity profiles over the entire flow region for case 1 with  $z_0 = 0.005$ .

The turbulence kinetic energy contours reveal that for increasing  $z_0$ , the turbulence energy levels in the shear layer growing from the step corner rise accordingly. Likewise, the turbulent viscosity and with it the turbulent shear stress increases in unison. The same trend becomes apparent by looking at Figure 4.47 which, for easier comparison, shows the individual turbulence profiles together at the  $x = 3.0$  downstream location. Once more this gives the reason, why for smaller surface roughnesses bigger overshoot and larger downstream separation regions are expected.

The following Figure 4.48 gives again a complete set of turbulence intensity profiles over the whole flow field for case 1 with  $z_0 = 0.005$ . As already pointed out in the

(a)

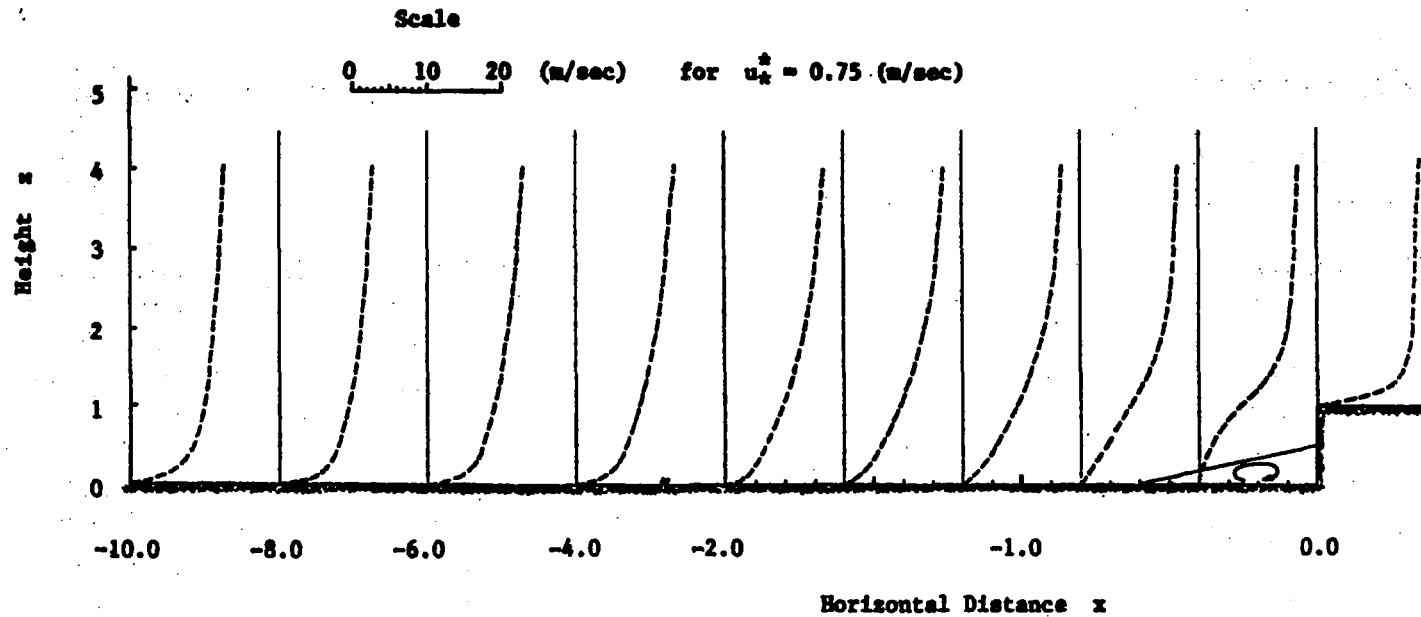


Figure 4.46. Velocity distribution for  $z_0 = 0.005$ ;  
(a) ahead of the step, (b) in the vicinity of  
the step.

(b)

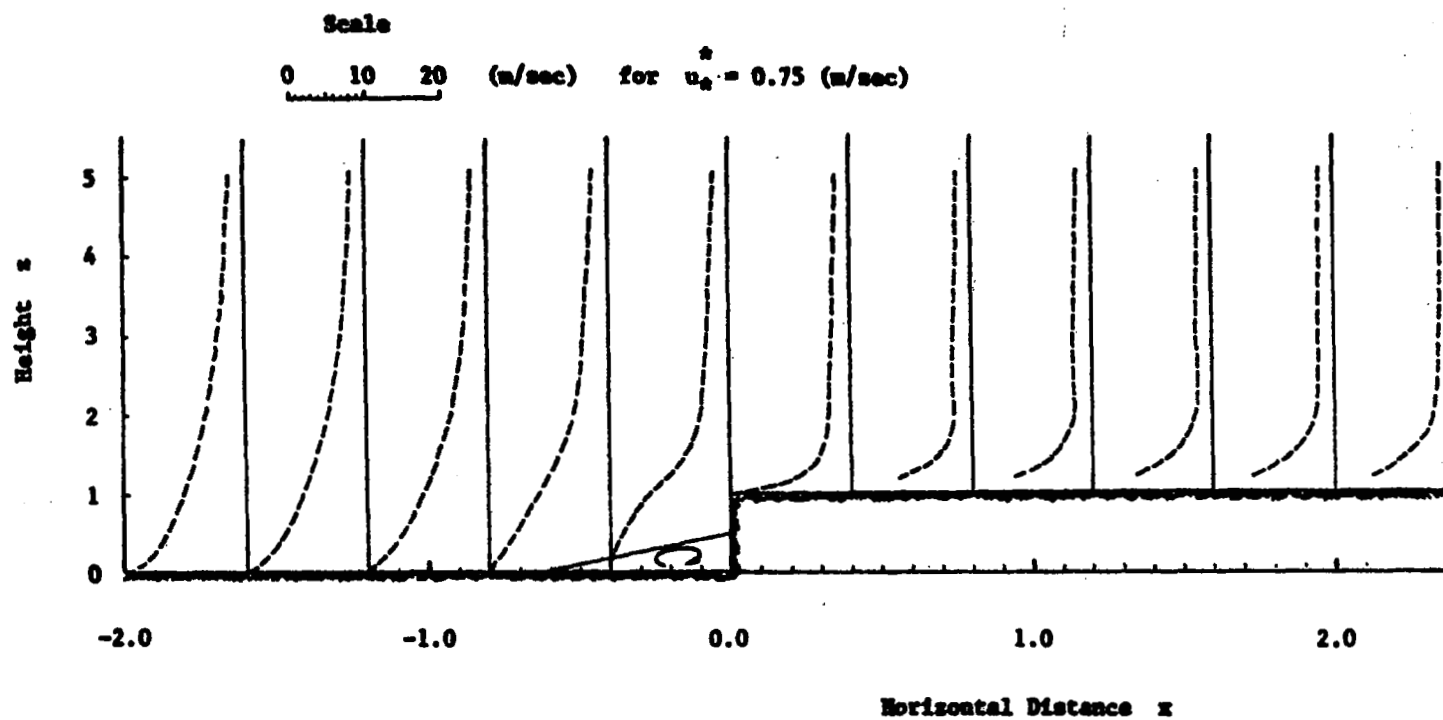


Figure 4.46. (continued)

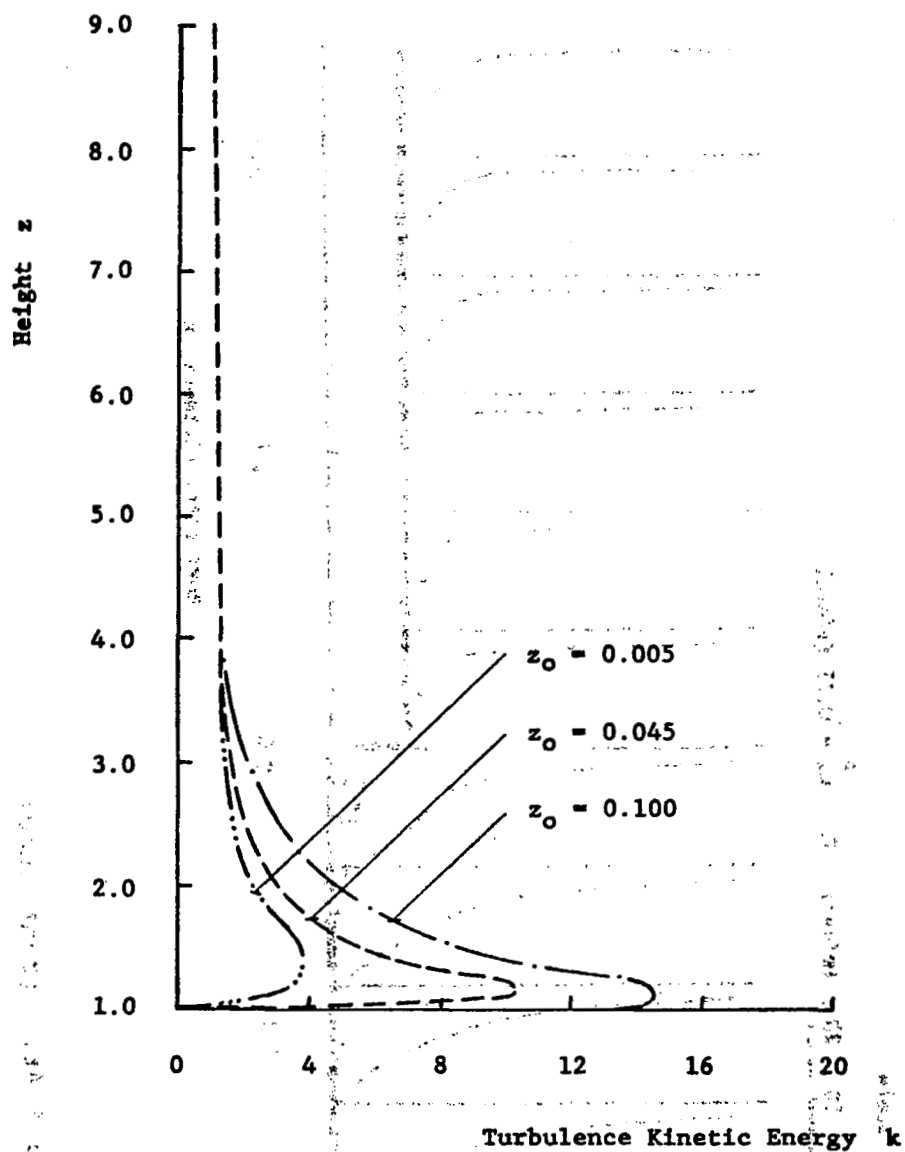


Figure 4.47. Turbulence kinetic energy profiles at  $x = 3.0$  for different  $z_0$ .

(a)

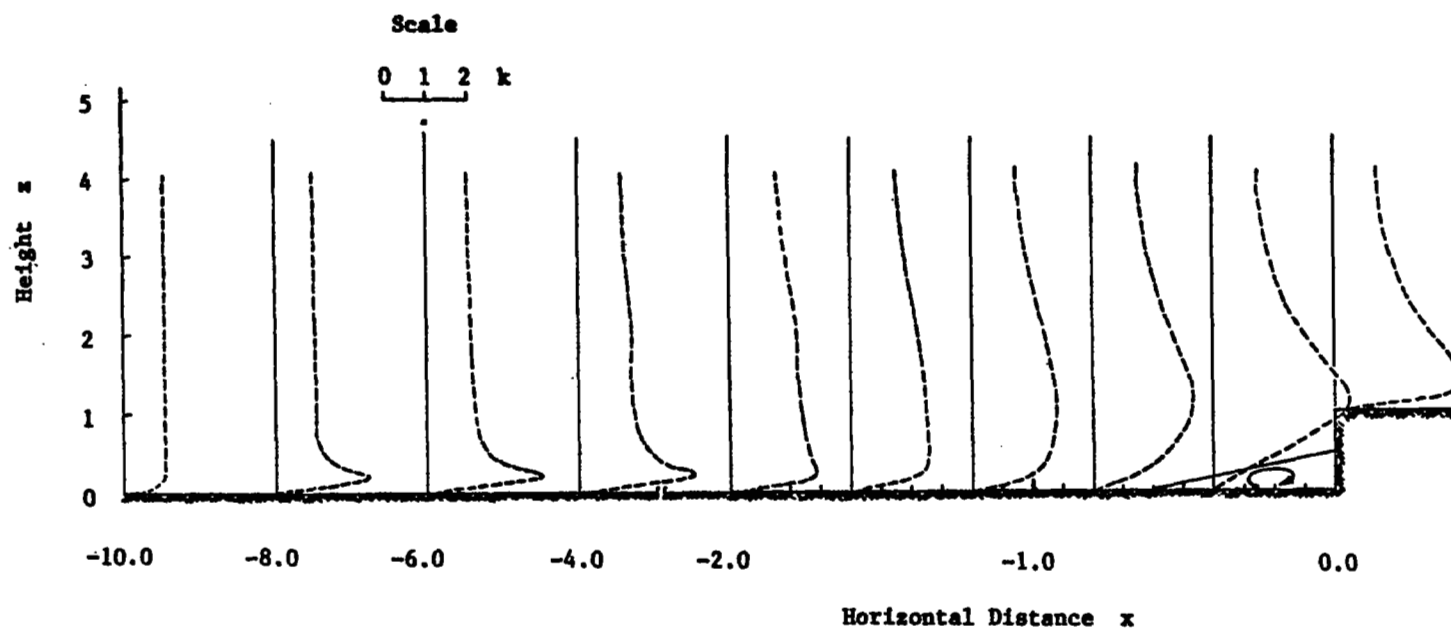


Figure 4.48. Turbulence kinetic energy distribution for  $z_0 = 0.005$ ;  
 (a) ahead of the step, (b) in the vicinity of the step.

(b)

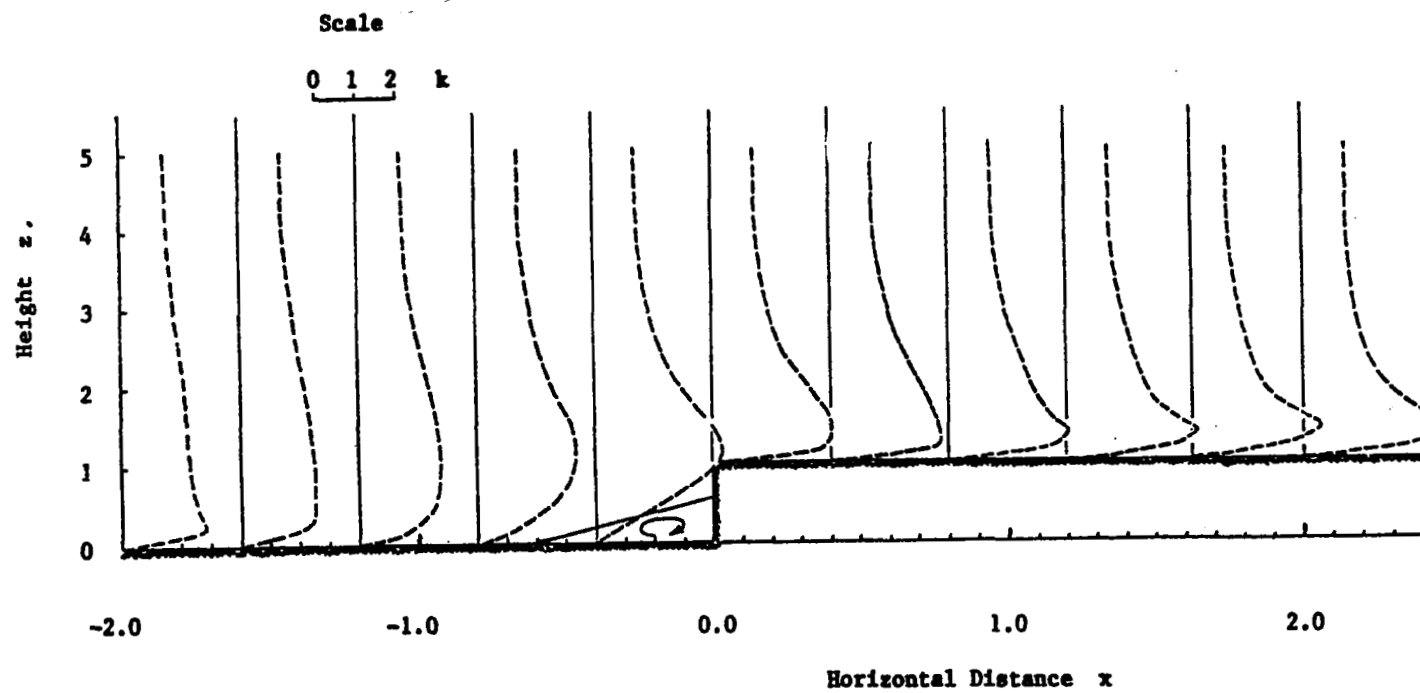


Figure 4.48. (continued)



previous sections, these profiles essentially agree with the findings of Taulbee and Robertson [46].

The turbulence length scale plots expose how different the  $\ell$ -distributions actually can become from the linear variation originally assumed in Equations 4.36 and 4.47. The downstream influence of the step on the turbulence structure is recognized by the growth in  $\ell$  indicating an increase of typical eddy size in the spreading shear layer. To facilitate a comparison between the various roughness parameters and their effects on the turbulence structure, Figure 4.49 shows the  $\ell$ -profiles at  $x = 3.0$  for the different  $z_0$ . The profiles have been nondimensionalized with Equation 4.47 to allow easy comparison with the linear distribution. In accordance with earlier results the rougher surfaces produce shear layers with sizeable increases in the typical eddy size, which through Equation 4.16 augment the turbulent viscosity and tend to shorten the upper separation regions. For small  $z_0$ , however, the  $\ell$  predictions are below those given in Equation 4.47, hence leading to higher overshoot and delayed reattachment.

From the four variables  $\omega$ ,  $\psi$ ,  $k$  and  $\ell$ , the vorticity and the  $z_0$ -influence on it has not yet been discussed. Recall, Figure 4.39, page 170, showed the vorticity contours for  $z_0 = 0.045$ . It was pointed out that a disturbance region with locally high streamwise vorticity gradients is formed and spreads downstream parabolically. Figure 4.50 shows how a surface roughness change affects the extent of

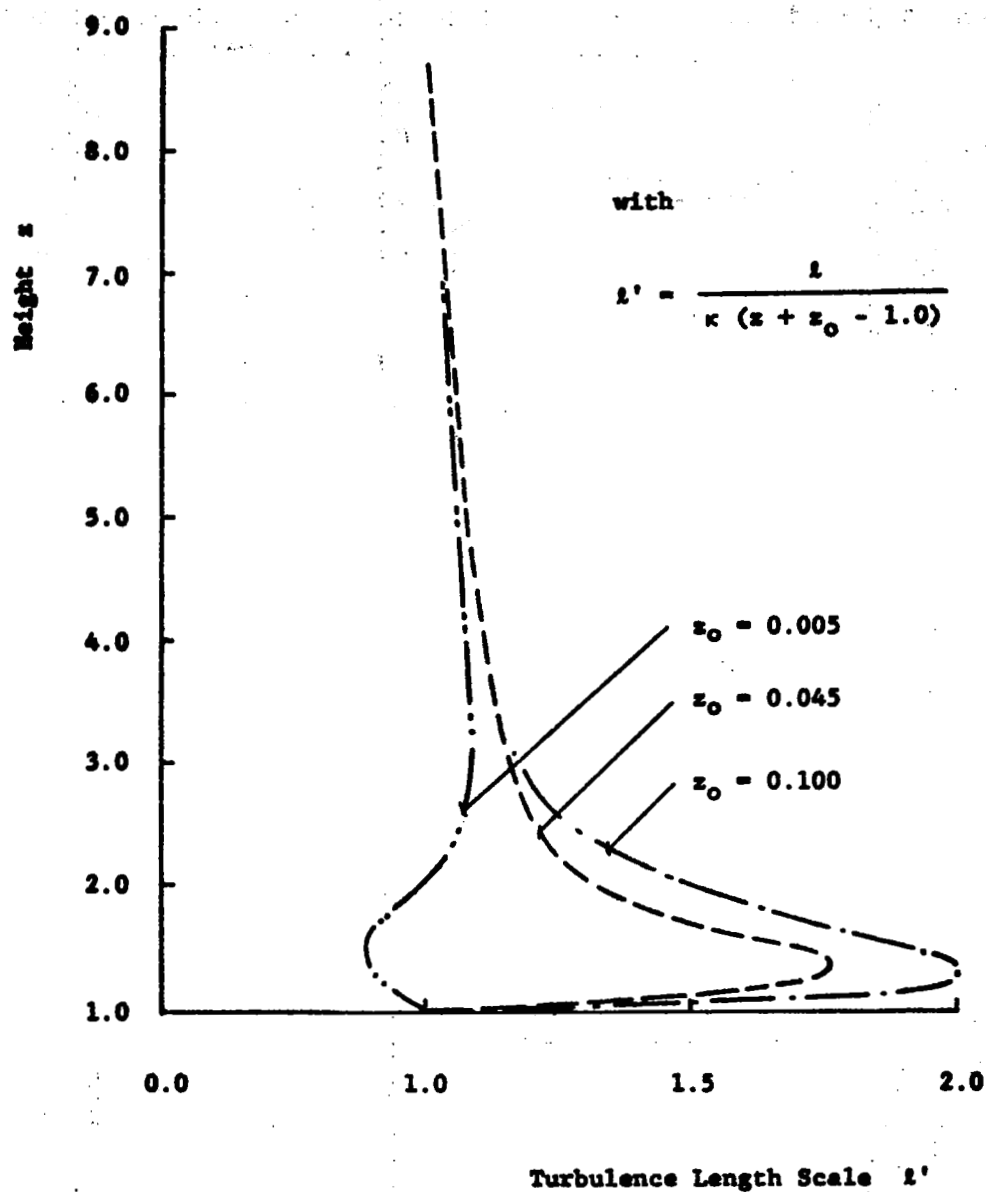


Figure 4.49. Turbulence length scale profiles at  $x = 3.0$  for different  $z_0$ .

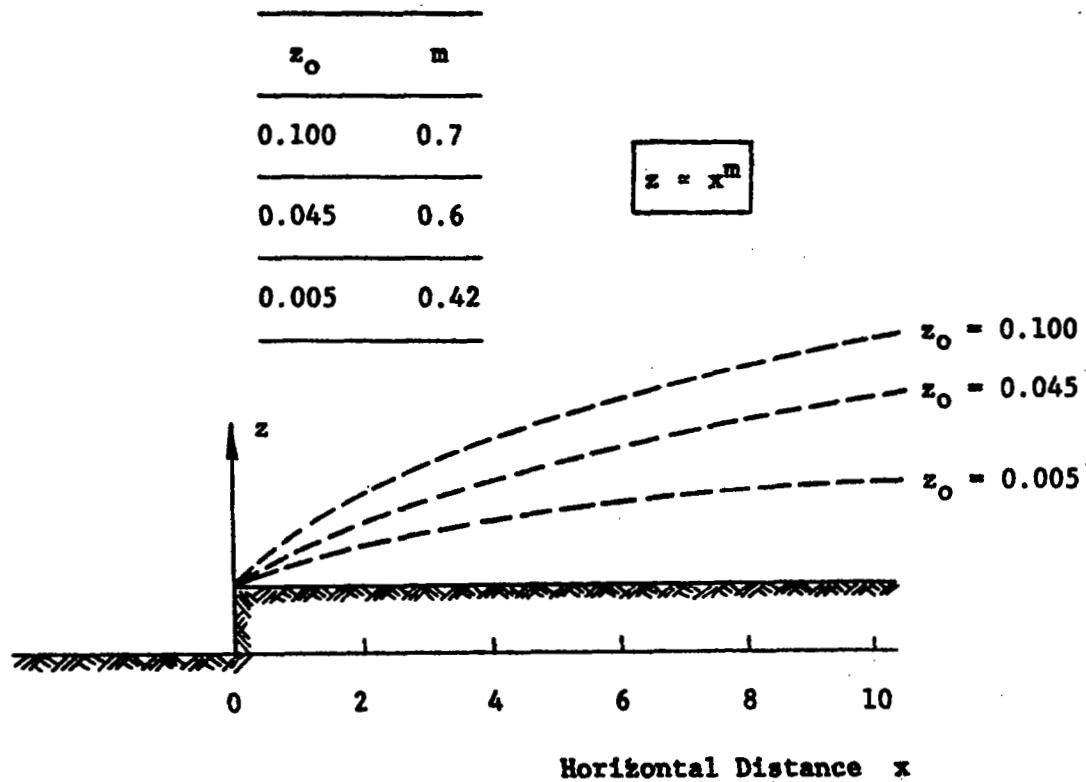


Figure 4.50. Variation of outer edge of vorticity wake region for different  $z_0$ .

this region of high vorticity. It is seen that a  $z_0$ -increase generates a wider spread, possibly as a consequence of the changes in the turbulence structure (larger eddies) of the shear layer, discussed in the previous paragraph.

Concluding this parametric investigation, one may summarize the results by stating that in the downstream flow region an increase in  $z_0$  gives rise to higher turbulence levels in the shear layer originating from the step corner. This, in turn, results in higher shear stress leading to fast reattachment. The typical eddy size in the shear layer increases with  $z_0$  and causes rapid spreading of a region of high streamwise vorticity gradients.

In the upstream flow region changes in  $z_0$  have only moderate influence on the flow parameters. Except for very small surface roughnesses, the front separation bubble grows in size for increasing  $z_0$ .

## BIBLIOGRAPHY

## BIBLIOGRAPHY

1. Harlow, F. H., and J. E. Welch. "Numerical Calculation of Time-Dependent Viscous Incompressible Flow of Fluid with Free Surface," Physics of Fluids, 8:2182-2189, 1965.
2. Harlow, F. H., and J. E. Welch. "Numerical Study of Large Amplitude Free Surface Motions," Physics of Fluids, 9:842-851, 1966.
3. Hirt, C. W. "Heuristic Stability Theory for Finite Difference Equations," Journal of Computational Physics, 2:339-355, 1968.
4. Hirt, C. W. "Computer Studies of Time-Dependent Turbulent Flows," Physics of Fluids, Supplement II, 219-228 (1969).
5. Hotchkiss, R. S. "The Numerical Calculation of Three-Dimensional Flows and Particulates About Structures." Paper presented at the Symposium on Air Pollution, Turbulence and Diffusion, Albuquerque, New Mexico, December, 1971.
6. Deardorff, J. W. "A Three-Dimensional Numerical Investigation of the Idealized Planetary Boundary Layer," Geophysical Fluid Dynamics, 1:377-410, 1970.
7. Deardorff, J. W. "A Three-Dimensional Numerical Study of Turbulent Channel Flow at Large Reynolds Numbers," Journal of Fluid Mechanics, 41:453-480, 1970.
8. Amsden, A. A., and F. H. Harlow. "A Simplified MAC Technique for Incompressible Fluid Flow Calculations," Journal of Computational Physics, 6:332-335, 1970.
9. Nakayama, P. I., and N. C. Romero. "Numerical Method for Almost Three-Dimensional Incompressible Fluid Flow and a Simple Internal Obstacle Treatment," Journal of Computational Physics, 8:230-240, 1971.
10. Schönauer, W. "Numerical Experiments with a Difference Model for the Navier-Stokes Equations (Turbulence Model)," Physics of Fluids, Supplement II, 228-233 (1969).

11. Djurić, D., and J. C. Thomas. "A Numerical Study of Convective Transport of a Gaseous Air Pollutant in the Vicinity of Tall Buildings." Paper presented at the Symposium on Air Pollution, Turbulence and Diffusion, Albuquerque, New Mexico, December, 1971.
12. Ogura, Y., and N. A. Phillips. "Scale Analysis of Deep and Shallow Convection in the Atmosphere," Journal of Atmospheric Sciences, 19:173-179, 1962.
13. Lantz, R. B., and K. H. Coats. "A Three-Dimensional Numerical Model for Calculating the Spread and Dilution of Air Pollutants." Paper presented at the Symposium on Air Pollution, Turbulence and Diffusion, Albuquerque, New Mexico, December, 1971.
14. Sutton, O. G. "A Theory of Eddy Diffusion in the Atmosphere," Proceedings of the Royal Society of London, 135(Series A):36-39, 1932.
15. Bosanquet, C. H., and J. L. Pearson. "The Spread of Smoke and Gases from Chimneys," Transactions of the Faraday Society, 32:63-69, 1936.
16. Pasquill, F. "Estimation of the Dispersion of Wind-borne Material," Meteorological Magazine, 90:174-183, 1961.
17. Hino, M. "Computer Experiment on Smoke Dissufion Over a Complicated Topography," Atmospheric Environment, 2:258-273, 1968.
18. Anderson, G. E. "Mesoscale Influences on Wind Fields," Journal of Applied Meteorology, 10:117-126, 1971.
19. Aziz, K., and J. D. Hellums. "Numerical Solution of the Three-Dimensional Equations of Motion-Convection in Fluids Heated from Below," Physics of Fluids, 10:314-324, 1967.
20. Gosman, A. D., W. M. Pun, A. K. Runchal, D. B. Spalding, and M. Wolfshtein. Heat and Mass Transfer in Recirculating Flows. New York: Academic Press, Inc., 1973.
21. Frost, Walter, J. R. Maus, and W. R. Simpson. "A Boundary Layer Approach to the Analysis of Atmospheric Motion Over a Surface Obstruction," Report prepared under NASA Contract No. CR-2182 by The University of Tennessee Space Institute, Tullahoma, Tennessee, January, 1973.

22. Frost, Walter, W. L. Harper, and G. H. Fichtl. "Analysis of Atmospheric Flow Over a Surface Protrusion Using the Turbulence Kinetic Energy Equation," Boundary-Layer Meteorology, 8:401-417, 1975.
23. Robertson, J. M. Hydrodynamics in Theory and Application. Englewood Cliffs, New Jersey: Prentice-Hall, Inc., 1965.
24. Parkinson, G. V., and T. Jandali. "A Wake Source Model for Bluff Body Potential Flow," Journal of Fluid Mechanics, 40:577-594, 1970.
25. Kiya, M., and M. Arie. "A Free-Streamline Theory for Bluff Bodies Attached to a Plane Wall," Journal of Fluid Mechanics, 56:201-219, 1972.
26. Fraenkel, L. E. "On Corner Eddies in Plane Inviscid Shear Flow," Journal of Fluid Mechanics, 11:400-406, 1961.
27. Good, M. C., and P. C. Joubert. "The Form Drag of Two-Dimensional Bluff-Plates Immersed in Turbulent Boundary Layers," Journal of Fluid Mechanics, 31:547-582, 1968.
28. Csanady, G. T. "On the Resistance Law of a Turbulent Ekman Layer," Journal of Atmospheric Sciences, 24:467-471, 1967.
29. Tverskoi, P. N. Physics of the Atmosphere. United States Department of Commerce. Springfield, Virginia: Clearinghouse for Federal Scientific and Technical Information, 1965.
30. Jackson, P. S., and J. C. R. Hunt. "Turbulent Wind Flow Over a Low Hill," Journal of Fluid Mechanics, 64:519-563, 1974.
31. Frost, Walter, and U. K. Kaul. "Turbulent Atmospheric Flow Over a Backward Facing Step." Report being prepared.
32. Frost, Walter, George Fichtl, J. R. Connell, and M. L. Hutto. "Mean Horizontal Wind Profiles Measured in the Atmospheric Boundary Layer About a Simulated Block Building." Paper presented at the Second U.S. National Conference on Wind Engineering, Colorado State University, Boulder, Colorado, June, 1975.



33. Kolmogorov, A. M. "Equations of Turbulent Motion of an Incompressible Turbulent Fluid." Izv. Akad. Nauk SSSR Ser. Phys. VI, No. 1-2, pp. 56-58, 1942. Translated into English at Imperial College, Mechanical Engineering Department Report ON/6, 1968.
34. Prandtl, L. "Ueber ein neues Formelsystem fuer die Ausgebildete Turbulenz," Nachrichten von der Akademie der Wissenschaften in Göttingen, Math. Phys. Kl., pp. 6-19, Göttingen: Van den Loek und Ruprecht, 1945.
35. Wolfshtein, M. "Convection Processes in Turbulent Impinging Jets." Ph.D. dissertation, Imperial College of Science and Technology Mechanical Engineering Department Report SF/R/I/2, London, England, November, 1967.
36. Ng, K. H., and D. B. Spalding. "Turbulence Model for Boundary Layers Near Walls," The Physics of Fluids, 15(Number 1):20-30, January, 1972.
37. Rodi, W., and D. B. Spalding. "A Two-Parameter Model of Turbulence, and Its Application to Free Jets," Wärme--und Stoffübertragung, 3(Number 2):85-95, 1970.
38. Rotta, J. C. "Statistische Theorie Nichthomogener Turbulenz," Zeitschrift für Physik, 129:547-572, and 131:51-77, 1951. Also English translation at Imperial College Mechanical Engineering Department Reports TWF/TN/38 and TWF/TN/39, London, 1951.
39. Roache, P. J. Computational Fluid Dynamics. Albuquerque, New Mexico: Hermosa Publishers, 1972.
40. Patankar, S. V., and D. B. Spalding. Heat and Mass Transfer in Boundary Layers. London: Morgan-Grampion, 1967.
41. Patankar, S. V., and D. B. Spalding. "A Finite Difference Procedure for Solving the Equations of the Two-Dimensional Boundary-Layer," International Journal of Heat and Mass Transfer, 10:1389-1412, 1967.
42. Taylor, P. A., and Y. Delage. "A Note on Finite Difference Schemes for the Surface and Planetary Boundary Layers," Boundary Layer Meteorology, 2:108-121, 1971.

43. Spalding, D. B. "The Calculation of the Length Scale of Turbulence in Some Turbulent Boundary Layers Remote from Walls." Imperial College, Heat Transfer, Section Report TWF/TN/31, 1967.
44. Launder, B. E., A. Morse, W. Rodi, and D. B. Spalding. "Prediction of Free Shear Flows--A Comparison of the Performance of Six Turbulence Models." National Aeronautics and Space Administration SP-321, Washington, D.C., 1973.
45. Robertson, J. M., and D. B. Taulbee. "Turbulent Boundary Layer and Separation Flow Ahead of a Step," Developments in Mechanics, H. J. Weiss, D. F. Young, W. F. Riley, and T. R. Rogge, editors. Vol. 5. Ames, Iowa: Iowa State University Press, 1969. Pp. 171-183.
46. Taulbee, D. B., and J. M. Robertson. "Turbulent Separation Analysis Ahead of a Step." American Society of Mechanical Engineers Paper No. 71-WA/FE-32, presented at ASME Winter Annual Meeting, Washington, D.C., November, 1971.